Engineering, Synthesis and Characterization of New - π Conjugated (Macro)molecular Architectures for Organic Optoelectronics : application toward ambipolar materials

Yiming Xiao

Université Pierre et Marie Curie

Ecole doctorale Physique et Chimie des Matériaux (ED397)

Institut Parisien de Chimie Moléculaire (CNRS-UMR8232)

Laboratoire de Chimie des Polymères

Engineering, Synthesis and Characterization of New π-Conjugated (Macro)molecular Architectures for Organic Optoelectronics

Application Toward Ambipolar Materials

Par Yiming XIAO

Thèse de Doctorat de Chimie

Présentée et soutenue publiquement le 23 octobre 2014

Devant un jury composé de :

Dr. Laurent LEGRAND	Maître de conférence UPMC Université Pierre et Marie Curie	Examinateur
Prof. Yves GEERTS	Professeur Université Libre de Bruxelles	Rapporteur
Dr. Stéphane MERY	Chargé de Recherche CNRS IPCMS, Université de Strasbourg	Rapporteur
Dr. Eric CLOUTET	Chargé de Recherche CNRS LCPO-ENSCBP, Université Bordeaux 1	Examinateur
Prof. André-Jean ATTIAS	Professeur Université Pierre et Marie Curie	Directeur de thèse
Dr. Fabrice MATHEVET	Chargé de Recherche CNRS Université Pierre et Marie Curie	Co-Encadrant

A mes parents

献给我的父母

Remerciement

Ce travail a été réalisé au sein de l'Institut Parisien de Chimie Moléculaire (UPMC-CNRS-UMR8232), Laboratoire de Chimie des Polymères, dirigé par le Professeur Alain Fradet que je remercie pour son accueil.

Je tiens tout d'abord à remercier mon directeur de thèse, le Professeur André-Jean Attias, pour m'avoir confié ce sujet.

Je tiens à remercier chaleureusement les deux autres membres permanents de l'équipe, Dr. Fabrice Mathevet et Dr. David Kreher. Merci à Fabrice pour être toujours au labo, 7j/7 et 24h/24 disponible sauf quand tu es en Asie ^_^, merci de m'encourager en science et aussi dans ma vie, une vie à l'étranger. Merci à David, en juillet 2008, tu as conduit de Paris à Chantilly pour notre premier rencontre et aussi mon premier contact avec l'équipe quand j'étais en campus d'été de TOTAL.

Mes remerciements s'adressent aussi aux autres membres de l'équipe :

Ibtissam Tahar Djebbar, le pionnier de mon sujet, une collègue et une grande sœur.

Frédéric Lincker, un super chimiste avec un top niveau du français.

Ping Du, un super post-doc, grand (mais petit en taille) chimiste chinois, « roi de synthèse » ^_^.

Danli Zeng, avec toi, j'ai appris beaucoup de chimie en polymère à la façon chinoise, comme j'avais refait un master à Shanghai.

Antoine Colas, super gentil garçon avec plein d'humour.

Leszek Mazur, mon polonais très fort en tous les deux sens de « physique ».

Andrea Castiglione, mon Italiano qui m'a apporté une belle ambiance Italienne.

Mon grand merci aussi à Amina Bakhma, Vincent Jactel, Alice Six, Farid Kameche et Xiaolu SU.

Je voudrais aussi remercier les stagiaires : Lambert Sicard, Yuying He, Jingjing Li, Corrine Peng, Marcin Sleczkowski, Téo Sanchez, Romain Agostinho, et Clément Ravet.

Mes remerciements s'adressent aussi à nos collègues en coopération avec l'équipe :

Les Strasbourgeois, Dr. Benoît Heinrich et Dr. Bertrand Donnio du Département des Matériaux Organiques (DMO) de l'Institut de Physique et Chimie des Matériaux de Strasbourg (IPCMS) qui nous ont donné leur accueil chaleureux pour effectuer l'étude par diffraction des rayons X de mes composés et assuré l'interprétation des résultats. Pendant mon séjour à IPCMS et la session de GIXS en Corée, j'ai énormément appris de Benoît « sur place » : ta patience et nos innombrables discussions ont été plus que précieuses dans ma rédaction de thèse.

Mes collègues de l'Institut de Nanoscience de Paris (INSP) à Jussieu. Merci à Dr. Emmanuelle Lacaze, avec toi, j'ai eu ma première touche de l'AFM et puis j'ai eu ma première image de mon film. Merci au Dr. Jean-Louis Fave avec qui j'ai passé plusieurs jours dans la salle noire pour faire le temps de vol sur mes composés.

Les Coréens, dont la plupart sont Coréennes. Avec votre accueil amical, j'ai effectué trois visites à Ewha Womans University pour caractériser mes produits en OFET. Merci aux Prof. Jeong-Weon Wu, Dr. Kwang-Jin Lee, Dr. Je-Heun Woo, Eun-Young Choi, Eun-Sun Kim et aussi les deux très charmantes et efficientes secrétaires Min-A Kim et Ji-Hye Jung.

Merci à Jean-Charles Ribierre, un normand qui travaille en Corée et au Japon avec sa femme chinoise. JC est en même temps près et loin de moi pour répondre mes question en OFET.

Egalement, je tiens à remercier l'ensemble des personnes au laboratoire : Shaodong, Xiaolu Ma, Martine, Brigitte, Ludovic, Romain, François, Jutta, Laurent, les deux Benjamin, Sandrine, Matthieu, Joël, Georgette, Suzie, Chirine, Gaëlle, Emilie, Stéphanie, Soum, Philippe et tous les autres.

En même temps, je remercie à mes amis et collègue de l'association chinoise (Association des Boursiers de China Scholarship Council en Ile-de-France) et bretonne (Mission Bretonne et Cercle Celtique Dalc'h Mat) : Pinglu Zhang, Sheng Gao, Xiangye Liu, Limin Meng, Ke Wang, Eric, Alex et Anaïs.

Je remercie le China Scholarship Council pour m'avoir conféré une bourse de 5 ans qui couvre mon master et doctorat à UPMC.

Pour finir, merci à toute ma famille huit mille kilomètres à l'est, pour leurs encouragements et amour, sans quels, je n'aurais pas pu réussir mes cinq ans d'études en France.

Glossary

AFM	Atomic Force Microscopy
BC	Bottom Contact
Cr	Crystal phase
DIAD	Diethyl azodicarboxylate
CV	Cyclic voltammetry
DMF	*N*,*N*-dimethylformamide
DP_n	Number-average Degree of Polymerization
DSC	Differential Scanning Calorimetry
E_g	HOMO-LUMO band-gap
*E*opt	Optical band-gap
E^{ox}	Oxidation potential
E^{red}	Redaction potential
EL	Electroluminescence
eV	Electronvolt
Fc	Ferrocene
GIXS	Grazing Incidence X-ray Scattering
HOMO	Highest Occupied Molecular Orbital
I	Isotropic phase
I_p	Polydispersity index
ITO	Indium Tin Oxide
Lam	Lamellar mesophase
LC	Liquid Crystal
LUMO	Lowest Unoccupied Molecular Orbital
M_n	Number average molecular mass
NBS	N-Bromosuccinimide

NMR	Nuclear Magnetic Resonance
n-type	Negative-type (electron-conducting)
OFET	Organic Field-Effect Transistor
OLED	Organic Light-Emitting Diode
OPV	Organic Photovoltaic
OTFT	Organic Thin Film Transistor
OTS	Octadecyltrichlorosilane
p-type	Positive-type (hole-conducting)
P3HT	Poly(3-hexylthiophene)
P3AT	Poly(3-alkylthiophene)
PCBM	phenyl C61-butryic acid methyl ester
POM	Polarized-light Optical Microscopy
ppm	Parts Per Million
PR-TRMC	Radiolysis Time-Resolved Conductivity
RF-ID	Radio Frequency Identification Tag
rr-P3HT	Regioregular P3HT
SCLC	Space Charge Limited Current
SEM	Scanning Electron Microscopy
Sm	Smectic mesophase
TEM	Transmission Electron Microscopy
TC	Top Contact
THF	Tetrahydrofuran
TOF	Time-of-flight
UV-vis	Ultraviolet-visible spectroscopy
XRD	X-Ray Diffraction

Contents

CHAPTER 1 INTRODUCTION

1.1 Organic Semiconductors

In the 1950s, the concept of "organic semiconductor" was introduced to describe π-conjugated organic materials possessing the ability to transport charges. Since then, organic semiconductors have been the focus of numerous investigations in several fields, from chemistry to physics, opening simultaneously many new opportunities and potential industrial applications [1-3] .

In addition and since the discovery of the conductivity property of polyacetylene by A. J. Heeger, A.G. MacDiamid and H. Shirakawa in 1977, more and more attention has been attracted in the past 25 years and very impressive improvements in performance were achieved [4] based on these materials in a wide variety of domains (Organic Light-Emitting Diodes (OLED), Organic Field-Effect Transistors (OFET), Organic Photovoltaics (OPV), Liquid Crystals (LC), sensors, etc.).

1.1.1 π-conjugated systems

The basic electronic configuration of a carbon atom are $(1s)^2$ $(2s)^2$ $(2p)^2$. In order to form covalent bonds with other atoms, these orbitals can be combined (or hybridized) into new orbitals (called "hybrid orbitals").

When only a hybridization of orbitals into σ bonds is observed (sp^3), the whole molecule is insulating as all the electrons are fixed in every bond (no charge transport carriers) (Figure 1.1.a). On the contrary, in the case of a double bond, the 2s orbital and two of the three 2p orbitals ($2p_x$, $2p_y$) hybridize into three sp^2 orbitals in a plane with an angle of 120°C to each other and the $2p_z$ orbital is perpendicular to this plane (Figure 1.1.b). Thus, when two carbon atoms approach to each other, two of the sp^2 orbitals overlap to form a σ bond and the two $2p_z$ orbitals overlap as well to generate this time a bonding molecular orbital π of lower energy and an antibonding molecular orbital π* of higher energy (Figure 1.1.c). In this configuration, the π electrons cannot be attributed to a single atom: we can speak about conjugation.

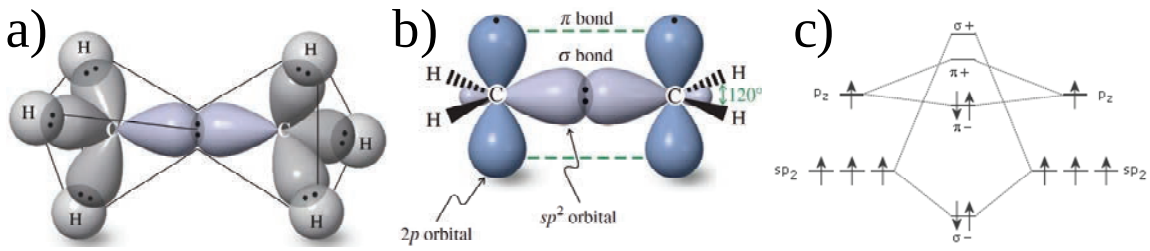

Figure 1.1 Schematic representations of the bonding in a) ethane, b) ethylene and the molecular orbitals in ethylene

By increasing the number of hybridized carbon atoms in a molecule (Figure 1.2), the number of molecular orbitals will increase and the energy gap between each π (or π*) energy levels will decrease. Then the energy level of bonding orbitals (antibonding orbitals) become so close one to the other that they are no more distinguishable but form the so called conduction band and valence band.

In this context, the Highest Occupied Molecular Orbital (HOMO) and Lowest Unoccupied Molecular Orbital (LUMO) play a special role as they are associated respectively to the ionization potential and electronic affinity of the compound, so they can characterize the materials ability to give and/or accept electrons. The energy difference between HOMO and LUMO can also be called as the forbidden band (gap) as in the field of inorganic semi-conductors.

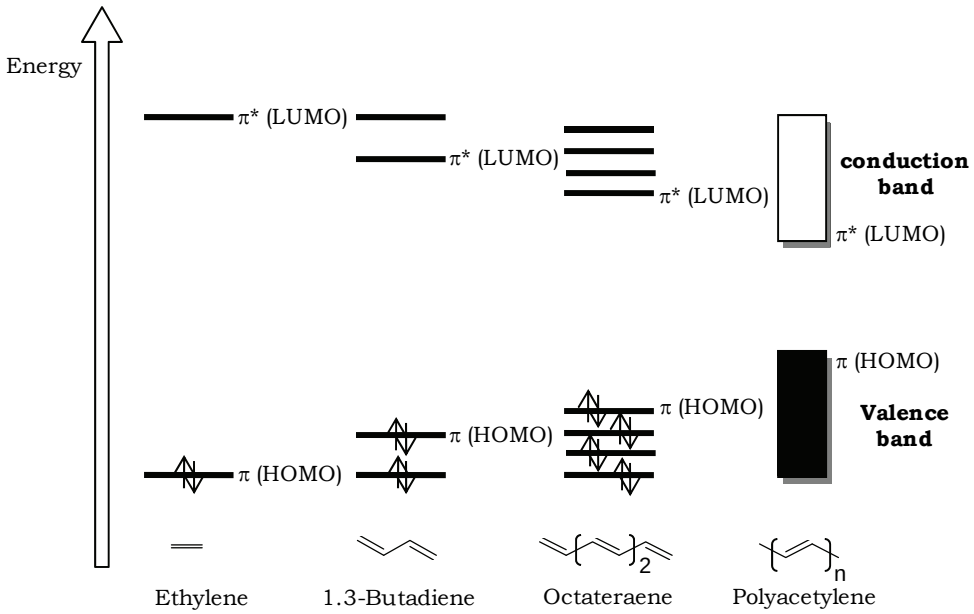

Figure 1.2 Diagram of molecular orbitals

As a consequence, we can now distinguish electron-donor and electron acceptor molecules. In fact, the oxidative process of an electron-donor molecule results in the formation of a hole in the HOMO level after forming a radical cation; on the contrary, the reductive process takes place when an electron is gained in the LUMO level via the formation of a radical anion.

Furthermore, the electron in the LUMO level of a radical anion can be transferred to an adjacent neutral molecule and an adjacent neutral molecule can transfer its electron to the hole in the HOMO level of a radical cation. This is the way a charge transfer (conductivity) can happen and be observed in such π-conjugated materials.

1.1.2 π-conjugated small (single) molecules, oligomers and polymers

In this context, there are several well known examples: anthracene, pentacene, rubrene, etc. as single or small molecules [5]; oligothiophene, benzothiophene, thienothiophene, etc as oligomers [6] and polypyrrole, polyacetylene, poly(3-hexylthiophene) (P3HT), or poly(p-phenylene vinylene) (PPV) as polymers [4] (Figure 1.1).

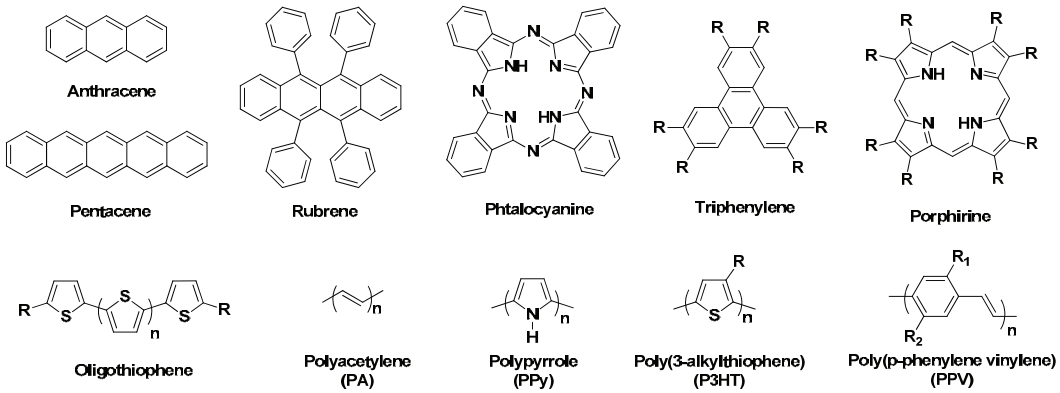

Figure 1.1 Chemical structures of typical small molecule (oligomer) and polymer type organic semiconductors

As a remark, the frontier between the definition of single molecules and the one of oligomers is often very vague; in this manuscript we consider the mono-dispersed single molecules or oligomers as "small molecules (with a well-defined molecular weight, even though the weight might be relatively high)", the multiple dispersed polymers being classified as "polymers" [7].

Both small molecules and/or polymers present advantages and disadvantages.

On the one hand, small molecules offer well defined chemical structures and then can give very precise and reproducible properties. Moreover, they can be readily evaporated to form, for instance, very good defect free thin films and then show excellent electronic or optical properties. Nevertheless, the synthesis should be carried out step-by-step and can be costly as well as the evaporation process itself, even if in some cases small molecules can be easily processed in solution just as the polymers (after introducing solubilizing long alkyl chains for example).[6]

On the other hand, polymers can be obtained by relatively much less costly polymerization reactions directly from the monomers, and their main advantage is their easy and cheap processability (spin coating, dip coating, etc.). But they present always a chain length distribution, thus obliging to several purification steps to remove or decrease the number of inevitable defects formed during the polymerization, defects which could at the end alter the quality of thin films, for instance.

This is why we can say that, between small molecules and polymers, between the evaporation and solution process, it is never easy to make a definitive choice: there are always different strategies to be taken into account.

1.1.3 Charge transport in organic semiconductors

It is complicated as well in terms of transport properties, as the performances of the organic semiconductors critically depend not only on the efficiency with which charge carriers (electrons and/or holes) move within the π-conjugated materials, but also the device configuration in which they will be integrated.

Indeed, in the case of OLED or OFET devices, the charge carriers are either injected from metal (Au, Ag, etc.) or conducting oxide electrodes (ITO); meanwhile, for OPV technology, the charge carriers are generated via photon-induced charge separation at the interface between electron-donor and electron-acceptor components.

In addition and as a remind, the most important classical inorganic semiconductor currently used in such devices belongs to the family of silicon based materials, which can be defined as a highly crystalline three-dimensional solid presenting highly delocalized bands, due to the fact that all the atoms are held together with strong covalent or ionic bonds. As a consequence, the charges transport can occur, coming from the strong interactions of overlapping atomic orbitals, and this process might be remarkably limited by defects, lattice vibrations, or phonon scattering in the solid [5]. On the contrary, the organic semiconductors are composed by single (macro)molecules which are weakly bound together through van der Waals, hydrogen bonding and/or π-π interactions : this gives usually a much less ordered organization in bulk and in this condition, there are two possibilities for the charges to be transported. One way is along the conjugated backbone (intramolecular transport, mostly in the case of polymers); the other way is through the overlapped adjacent molecules π-orbitals (intermolecular transport, observed in both polymer and/or single molecule cases).

In other words, we must remember that in organic semiconductors, it is a hopping from one localized state to another localized state which occurs, and this can be considered as an electron transfer between a charged moiety and another adjacent neutral moiety [8]. Of course, for some very ordered molecule single crystals, weak bands could also be observed [9, 10].

1.1.4 Applications of Organic Semiconductors

As we talked previously, several new “markets” were opened based on the development of these organic semiconductors, in particular in the field of Organic Light-Emitting Diodes (OLED), Organic Photovoltaics (OPV) and/or Organic Field-Effect Transistors (OFET).

1.1.4.1 Organic Light-Emitting Diode (OLED) [11]

Electroluminescence (EL) from organic devices was first reported using single crystals of anthracene in the 1960s [12]: however, the fabricated device required a high drive voltage of 400 V to obtain EL from this blue emitter. Later, the use of vacuum-deposited anthracene thin films led to a significant reduction of this drive voltage [13]. Then in 1987, a doublelayer OLED using thin films of 1,1-bis{4-[di(*p*-tolyl)amino]-n phenyl}cyclohexane (TAPC) as a hole-transporting material and tris(8-quinolinolato)aluminum (Alq3) as an emitting material sandwiched between transparent indium tin oxide (ITO) and an alloy of magnesium and silver was reported to exhibit a luminance of over 1000 cd m^{-2} at a drive voltage of ca. 10 V [14, 15]. Subsequently, a single-layer OLED using a thin film of poly(*p*-phenylene vinylene), ITO/polymer/Ca, was reported in 1990 [16] . These two reports triggered extensive

research and development of OLEDs from the standpoints of both fundamental science and potential technological applications for full-color, flat-panel displays and lightening. Furthermore, the recent finding of triplet emitters led to remarkable improvements in the EL quantum efficiency [17-19]. Today, OLEDs are characterized by low drive voltage, high brightness, full-color emission, rapid response, and easy fabrication of large-area thin-film devices.

Concerning OLEDs functioning, they are current-driven devices that utilize emissions from the electronically excited states of molecules. More precisely, the operation of OLEDs based on an unique emitting layer involves charge injection from the anode and the cathode into the adjacent organic layers, transport of injected charge carriers through the organic layers, exothermic recombination of holes and electrons to generate electronically excited states of molecules (often called excitons), followed by their deactivation via the emission of either fluorescence or phosphorescence light taken out of the device as EL (Figure 1.3.a).

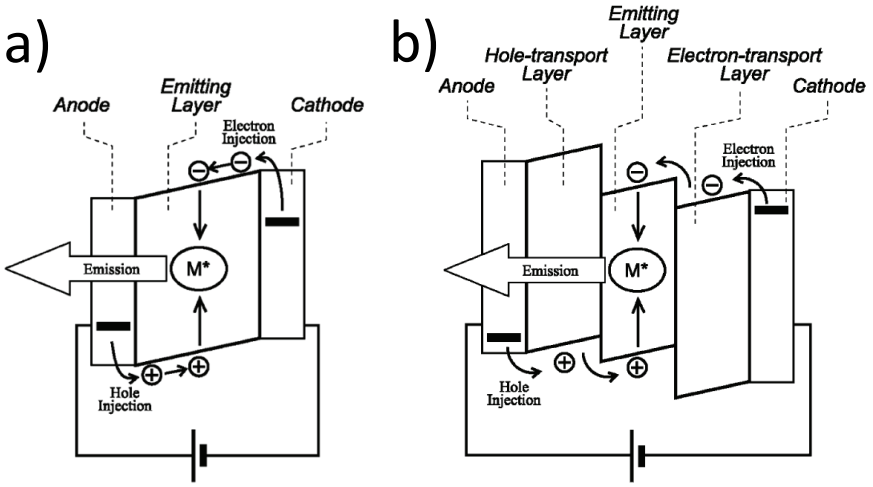

Figure 1.3. Operation principles of monolayer(a) and multilayer (b) OLEDs

But to attain high external quantum efficiency (Φ_{ext}) (see next paragraph) for EL, it is necessary to achieve efficient charge injection from both the anode and the cathode into the adjacent organic layers at low drive voltage, good charge balance, and confinement of the injected charge carriers within the emitting layer to increase the probability of the desired emissive recombination. This is the reason why more recently other structures called “multilayer OLEDs” were developed, consisting of the emitting and hole-, electron-transport layers sandwiched between the ITO anode and the metal cathode, as shown in Figure 1.3.b.

Such OLEDs are characterized by two key parameters: the external quantum efficiency (Φ_{ext}) which is defined as the number of photons emitted per number of injected charge carriers and the luminous power efficiency (L_{eff}) [lm W^{-1}] which is defined as the ratio of luminous flux to power.

Moreover, when fluorescent emitters are employed, only 25% of the generated excitons are utilized. On the contrary, when phosphorescent emitters are used, an internal quantum efficiency up to 100% can be achieved in principle since the phosphorescent emitters, which are usually doped in a host material, can capture both singlet and triplet excitons generated by the recombination of injected holes and electrons[17, 20].

The performance of OLEDs, therefore, depends upon various materials and interfaces having specific roles such as charge-injection and charge-transporting, charge-blocking, and emission. More generally, materials involved in OLEDs should meet the following requirements: (a) suitable ionization potentials and electron affinities, that is to say well-matched energy levels for the injection of charge carriers from the electrodes or the organic layer into the adjacent organic layers; (b) Good ability to form smooth and uniform thin films without pinholes; (c) well controlled morphology and thermal stability. (d) In addition to these general requirements, materials should meet further specialized needs depending upon the roles that they play into the devices, as for example, hole transport, electron transport, charge blocking, and light emission.

1.1.4.2 Organic Photovoltaics (OPV)

Solar energy presents a great potential as a clean and inexhaustible new energy source. By definition, solar cells are devices where light energy is converted into electrical energy.

Such devices allowing photoelectric conversion and based on organic photoactive materials are mainly classified into two categories: photoelectrochemical cells and photovoltaic devices.

First, photoelectrochemical cells consist of two electrodes immersed in an electrolyte solution containing a redox couple. In this domain, Dye-Sensitized organic Solar Cells (DSSC) using nanocrystalline porous TiO_2, on which an organic dye is adsorbed, and I_3^-/I^- redox species in solution or gels, have been topic of recent intensive research and development because of the high conversion efficiencies reached (10%) [21, 22].

Second, organic solid-state photovoltaic devices (OPVs) consist of thin films of organic photoactive materials sandwiched between two metal electrodes. Both Schottky-type and *pn*-heterojunction cells have been studied [11, 23]. Generally, higher quantum yields for the photogeneration of charge carriers are reached for *pn*-heterojunction cells compared to Schottky-type devices because of electron donor-acceptor interactions between the two kinds of organic semiconductors, that is, *p*-type and *n*-type organic semiconductors (p-type and *n*-type organic semiconductors generally meaning electron-donating and -accepting organic materials, respectively). The performance of OPVs is evaluated by comparing the power conversion efficiency (η) and fill factor (FF) parameters.

The mechanisms for OPVs functioning have been interpreted in terms of the energy band model applied for inorganic semiconductor PV devices, which may not be applicable to molecular organic

solids with well-localized energy levels. The basic operation processes of a *pn*-heterojunction OPVs is for example described and divided in five steps (Figure 1.9): (a) light absorption by organic semiconductors to form excitons, (b) diffusion of excitons, (c) charge carrier generation and separation at the organic/organic interface, (d) charge transport through the organic layers, and (e) charge collection at both electrodes.

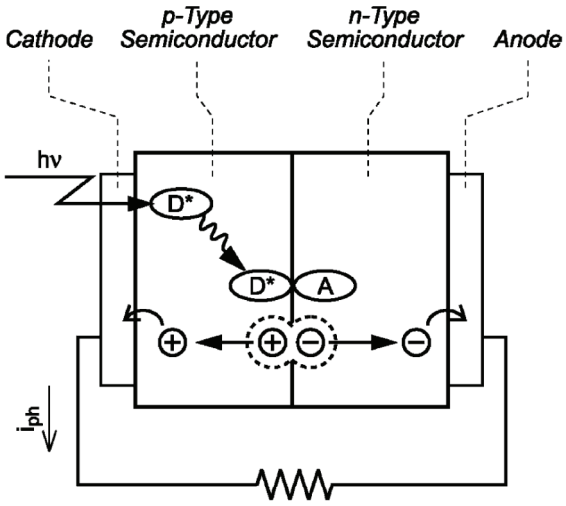

Figure 1.9. Operation processes of pn-heterojunction OPVs.

Note that these processes are just the opposite to those of OLEDs, namely, (a) charge injection from the electrodes into the organic layers, (b) charge transport through the organic layers, (c) charge recombination to form excitons, (d) emission from excitons, and (e) light extraction out of devices.

1.1.4.3 Organic Field-Effect Transistors (OFET)

(As most of the new synthesized materials in this work were characterized by the OFET, this kind of application will be more detailed here in introduction.)

In 1930, the principle of the field-effect transistor (FET) was first proposed by Lilienfeld[24]. However, the first OFETs were not described until 1987. Since their characteristics have undergone spectacular improvements during the last two decades [25], both small organic molecules and conjugated polymers attracted the community of industrial and academic research groups interested in using organic semiconductors as the active layer in transistors [11, 26] .

In fact, an OFET acts essentially as an electronic valve by modulating the semiconductor channel conductance via the gate field. Moreover, transistors are nowadays essential for all electronic applications, including integrated circuits for memories and sensors and also to drive individual pixels in active matrix displays. In particular, one of the most exciting applications of organic electronic circuits is probably in the supply chain area, where radiofrequency-powered elements (e.g. RFID tag) may replace 1D barcodes for identification and be applicable as a backplane drive for displays.

Figure 1.5 shows a typical OFET structure (or more appropriately, a usual thin film transistor). Looking into details, the OFET consists of a gate electrode, a dielectric insulating layer and an organic semiconducting material sandwiched between the source and drain electrodes.

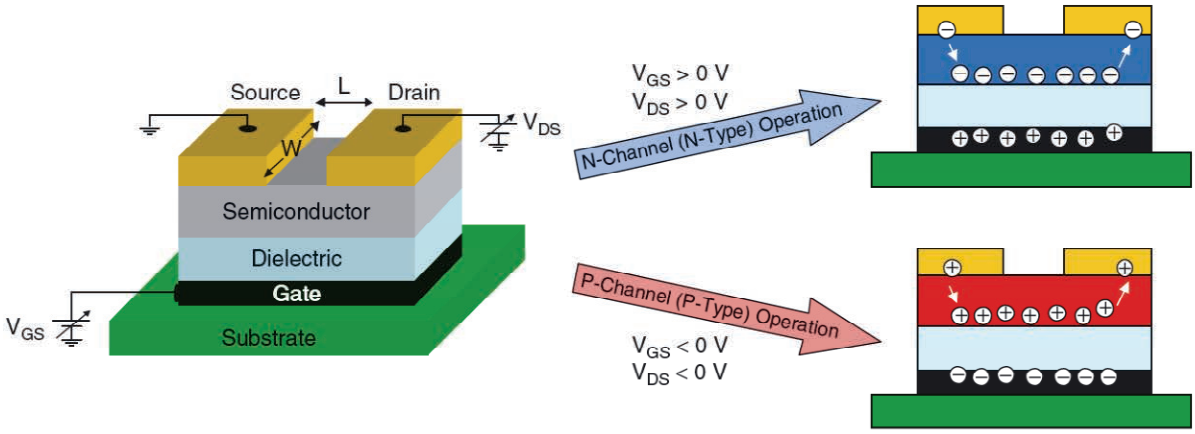

Figure 1.5 Organic field effect (thin-film) transistor structure with highlighted accumulation of electrons and holes for n- and p-channel semiconductors, respectively

Note that the organic semiconductor used in OFETs should not be intentionally doped. Consequently, the semiconductor carrier concentration is very low, usually $<10^{14}$ cm^{-3}. When a voltage is applied between the source and drain electrodes (V_{SD}) and the gate field is zero (source-gate voltage = 0 V), the source–drain current is very low and the device is "off". When the gate field is established by the application of a negative or positive source-gate bias (V_{SG}), accumulation of charges at the interface between the gate dielectric and the semiconductor (carrier concentration $>10^{20}$ cm^{-3}) occurs. Thus, upon application of the positive or negative source-gate bias, electrons or holes, respectively, are accumulated at the interface between the semiconductor and the dielectric and the source-drain current (I_{SD}) increases (Figure 1.5). This is called the 'on' state of the transistor.

The I_{on}:I_{off} ratio is also a useful measure of purity, because high off-currents are indicative of considerable extrinsic doping of the semiconductor. As a consequence, field effect mobilities greater than 0.1 cm^2 V^{-1} s^{-1} and I_{on}:I_{off} > 10^6 are needed [27] to be useful in optoelectronic devices such as active matrix displays that require sharp turn-on and fast switching.

Note also that organic FETs normally operate in the accumulation mode, hence, as described above, the increase in magnitude of V_{SG} enhances channel conductance, in contrast to conventional Si and GaAs transistors. When an organic semiconductor-based FET is active upon the application of negative V_{SG} and V_{SD}, hence accumulation of holes occurs, the organic material is said to be *p-channel* (or p-type) since holes are the majority charge carriers. On the other hand, when a (positive) source-drain current is observed upon the application of positive V_{SG} and V_{SD}, accumulation of electrons occurs, and the semiconductor is *n-channel* (or n-type) since electrons are mobile (Figure 1.5). In a

few cases, OFETs operate for both V_{SG} and V_{SD} polarities and the semiconductor is said to be *ambipolar*.

To end, it must be emphasized that the fundamental difference between n-/p-organic and -inorganic semiconductors is the following: the latter are based on the gate voltage sign at which they are active whereas the former are based on the mobile carrier type due to the (chemical) doping process. Therefore, it is important to stress that the categorization of an organic semiconductor as 'p' or 'n'-channel (or type) is not an absolute meaning but is strongly related to the FET device structure-material combination on which the transport characteristics are measured.

This is why very rapidly, we thought interesting to present below different types of OFETs (Figure 1.6), insisting on each type of device configuration with their own fabrication issues, advantages and disadvantages, due to the fact that we tested as well some of them with our materials.

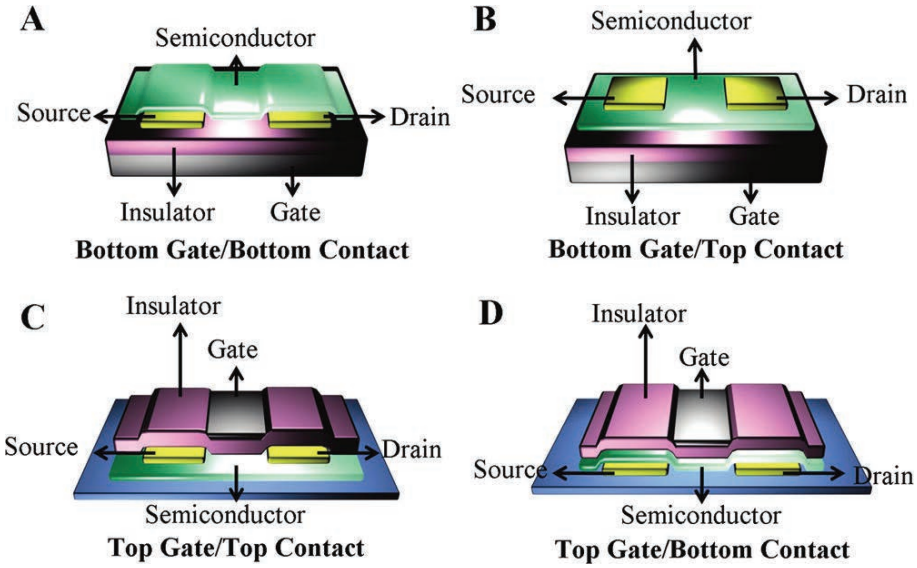

Figure 1.6 Schematic representations of various OFET configurations [28]

In the top-contact/bottom-gate geometry (Figure 1.6 B), the organic semiconductor is deposited on top of the gate dielectric layer and then the source and drain electrodes are deposited on top by either metal evaporation through a shadow mask or by printing. In this device structure, the contact resistance is usually low due to intimate contact between the semiconductor and the source/drain electrodes and the charge carrier mobilities are usually the highest among different FET structures. However, in this type of structure, small channel lengths are difficult to achieve by both metal thermal evaporation and printing (usually $L>>5$ μm channels) and solution-processed metal ink/polymeric contacts may damage the semiconductor.

In the bottom-contact/bottom-gate devices (Figure 1.6 A), the source and drain electrodes are first defined on the insulator with photolithography (allowing very small channel lengths) or other deposition processes and only at the end occurs the organic layer deposition. Bottom-contact devices

typically exhibit greater contact resistance than top-contact devices and high carrier mobility and typical *I* -*V* plots are usually obtained only upon source/drain contact treatment with thiol-based molecules to form a self-assembled monolayer. However, bottom-contact devices may be more easily integrated into low-cost manufacturing processes. Furthermore, smaller device features can be obtained through photolithographic techniques to enhance circuit speed.

Other technologically important OFET structures are the "top-gate" (Figure 1.6 C and D) configurations, where the dielectric and then the gate contact are deposited on top of the organic semiconductor. In the most common device structure, heavily doped silicon is used as both the substrate and the (bottom-) gate electrode; thermally grown SiO_2 with thicknesses of ~100-300 nm act as the dielectric and 30-50 nm thick Au is used as source/drain (top-) contact material. While these silicon-SiO_2 -Au-based devices are extremely important for comparing results among different research groups synthesizing new organic semiconductors, the use of plastic substrates, polymeric insulators and conductive inks as the source and drain electrodes must be developed to allow low-cost/flexible electronic applications.

1.1.5 Charge carrier mobility characterization methods

We precedently presented quickly the different popular devices incorporating organic semiconductors, but in any case the intrinsic charge transport property of the materials must be determined, one key parameter characterizing the materials involved being more precisely the charge mobility μ.

In fact, without any external potential, the transport is merely a diffusive process and can be described as:

$$\langle x^2 \rangle = nDt$$

Here, $<x^2>$ means the mean-square displacement of the charges, *D* is the diffusion coefficient, *t* is the time, and *n* represents an integer number equal to 2, 4, or 6 for one-,two-, and three-dimensional (1D, 2D, and 3D) systems, respectively.

Anyway, the charge mobility μ is related to the diffusion coefficient via the Einstein-Smoluchowski equation:

$$\mu = \frac{eD}{k_B T}$$

where k_B is the Boltzmann constant and e is the electron charge.

When an external electric field is applied, the charge carriers will start to drift; now, the mobility can be described as well as the ratio between the velocity (v) of the charges and the amplitude of the applied electric field, F: the unit of the carrier mobility is then expressed in cm^2/Vs.

$$\mu = \nu/F$$

Importantly, diffusion is the local displacement of the charge around an average position, while drift induces a displacement of the average position. This is the reason why drift is more representative to determine the migration of the charges through the organic semiconductors.

There are several methods to determine experimentally the charge mobility in organic semiconductors [29-31]. Among these methods, Time-of-Flight (TOF), Organic Field-Effect Transistor (OFET), Space-Charge Limited Current (SCLC or "Diode") and Pulse-Radiolysis Time-Resolved Microwave Conductivity (PR-TRMC) are the most wildly used ones. They are presented below.

1.1.5.1 Time-of-Flight (TOF)

The first charge mobility measurement on organic semiconductors was realized by Kepler [32] and Leblanc [33] with a TOF setup, a very suitable technique for measuring the transport properties of organic semiconductors presenting low mobilities [31].

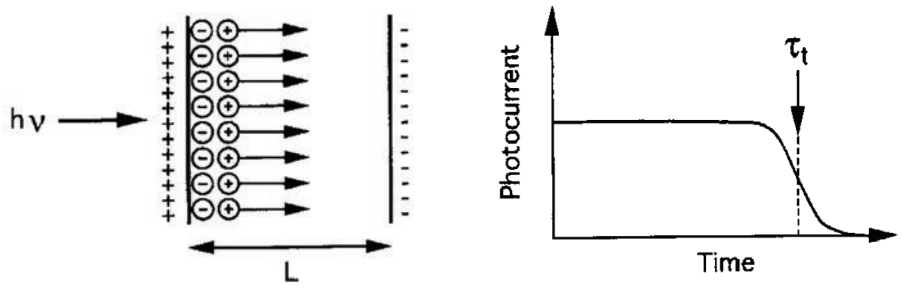

Figure 1.20 Principle of the time of flight measurement. Left: schematic view of the carrier generation and transport. Right: resulting time dependent current [31] .

Here, the sample consists of an organic film or crystal sandwiched between two conducting electrodes. The material is first irradiated by a short laser pulse in the immediate vicinity of one electrode to generate hole-electron pairs. For the above purpose, this electrode is most often constituted by a transparent conductor, such as indium doped tin oxide (ITO), but semitransparent metal electrodes are also often used. Driven by the polarity of the applied bias and the corresponding electric field (in the 10^4-10^6 V/cm range), the photogenerated charges migrate through the material toward the second electrode (see Figure 1.20 Left). This charge transport gives a current recorded in the external circuit. This current is constant, and then falls down to null at the time ***t***, at which the charge sheet arrives at the rear electrode (see Figure 1.20 Right). The transit time is related to the mobility through:

$$\tau_t = \frac{L}{\mu F} = \frac{L^2}{\mu V}$$

Where, L is the distance between the electrodes, F is the electric field in the organic layer, and V is the external voltage across the sample.

In ideal conditions, the signal in the Figure 1.20 right shows a step shape, where the falloff of the current corresponds to the arrival of the charged sheet. But in practical cases, the charge transport is much more complicated from the front electrode to the rear one, knowing that diffusion and trapping are two important features which take place in the TOF experiments: this is the reason why this technique requires working with highly pure and flawless samples.

1.1.5.2 Space-Charge-Limited Current (SCLC, also referred as "Diode Configuration") [30, 31, 34]

SCLC will happen in the materials in which free carrier concentrations are very low. When the tested materials are put into intimate contact with a metal electrode (which means the transport is bulk limited and not contact limited), the metal can be considered as a reservoir of free carriers and these free carriers could diffuse into the material if the Fermi level of the metal is close enough to the allowed levels of this materials. So this mechanism can also be called as "injection". With high work function metals, holes can be injected; on the contrary, using low work function metals, only electrons can be injected.

The experiment is carried on by building diodes where the samples (organic material layers) are sandwiched between two electrodes. The electrodes should be carefully chosen to be sure that only electrodes or holes can be injected at a low voltage. In ideal conditions (traps being negligible), the current density J evaluates quadratically with the applied bias V. In this situation, because of the electrostatic potential preventing the injection of additional charges, the number of injected charges will reach a maximum value, and at this value, the corresponding current is the SCLC:

$$J = \frac{9}{8}\epsilon_0\epsilon_r\mu\frac{V^2}{L^3}$$

with $\varepsilon_0\varepsilon_r$ the permittivity of the polymer and L the device thickness. This formula becomes inaccurate at high electric fields, needing then to be corrected as it becomes a field-dependent function.

1.1.5.3 Pulse-Radiolysis Time-Resolved Microwave Conductivity (PR-TRMC) [30, 35-38]

In the PR-TRMC method, a high energetic electrons pulse goes through the sample to create a low density of free carriers. The conductivity change $\Delta\sigma$ induced by this pulse will be measured by the change in microwave power reflected by the sample and is therefore frequency dependent:

$$\Delta\sigma = e\Sigma\mu N_{e-h}$$

Where $\Delta\mu$ is the sum of hole and electron mobilities and $N_{e\text{-}h}$ is the generated electron-hole pair's density. $N_{e\text{-}h}$ can be estimated by dividing the amount of energy density transferred to the material by the energy required to create one electron-hole pair; this ratio is further multiplied by a survival probability that accounts for possible charge recombination mechanisms during the duration of the pulse. In PR-TRMC, the pulse generates the charges in the bulk of the material. The electric property is obtained very locally (for example, it can be just part of a polymer chain) and the size of this

"information zone" depends on the frequency of the microwave (the lower the frequency, the larger the region that is explored).

With these characteristics, the PR-TRMC method is not much limited by the material purity (no trapping problems), structure (orientation or deposition defects) and the contact. As the tested zone can be so small, this method even can be used to single polymer chain in solution.

The PR-TRMC gives results of the intrinsic AC mobility values of the material in bulk and these values can be taken as the upper limits at low fields. Normally, for a certain sample, the PR-TRMC result is always higher than that obtained by TOF, because the latter is measured with DC probes; it is a macroscopic range test and the carriers crossing the material can be strongly impeded by impurities and structure defects. However, the two methods sometimes can really give quite similar results, for example, in the test of some discotic liquid crystals based on hexathiohexyl triphenylenes (in which the PR-TRMC technique was evaluated) [39].

1.1.5.4 OFET

Different types of device configurations were described before (Paragraph 1.1.4.3).

To remind, upon application of the positive or negative source-gate bias, electrons or holes, respectively, are accumulated at the interface between the semiconductor and the dielectric and the source-drain current (I_{SD}) increases: this is called the "on" state of the transistor.

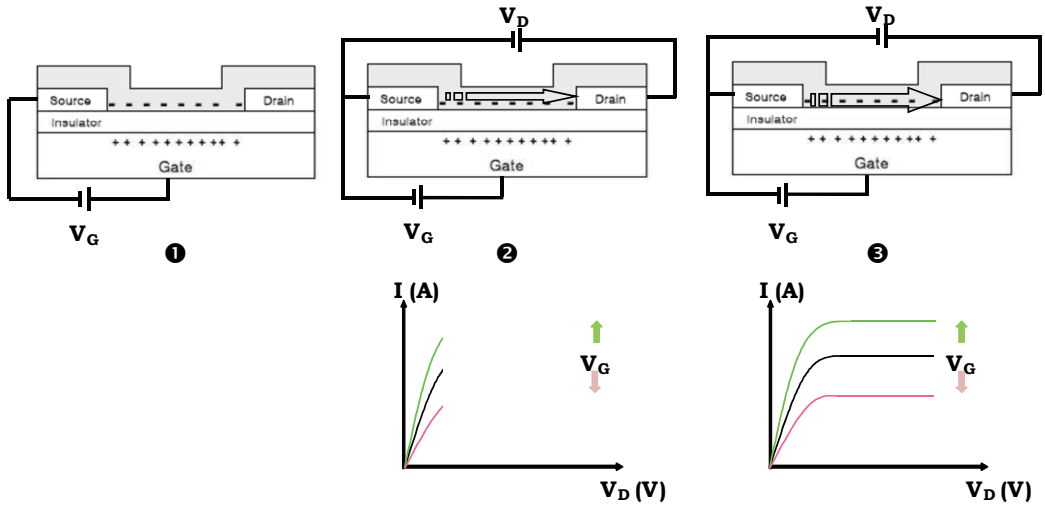

Figure 1.21 Schematic representation of the OFET operation principles: 1) gate voltage applications; 2) application of the voltage between the source and the drain (linear regime,) reaching the saturation regime; 3) I_{DS}–V_{DS} curve at various V_G values when V_D is applied (liner regime and in the saturation regime)

The basic relationships describing the OFET drain currents are the followings [40]:

$$(I_{SD})_{lin} = (W/L)\mu_{FET}C_i(V_{SG} - V_T - V_{SD}/2)V_{SD}$$

$$(I_{SD})_{sat} = (W/2L)\mu_{FET}C_i(V_{SG} - V_T)^2$$

where μ_{FET} is the field effect carrier mobility of the semiconductor (the average drift velocity per unit electric field), W the channel width, L the channel length, C_i the capacitance per unit area of the dielectric and V_T the threshold voltage [41]. By increasing the magnitudes of V_{SD} for a given V_{SG}, a 'linear regime' (Equation 7) is initially observed at low source-drain voltages ($V_{SD} < V_{SG}$) where the current increases linearly, followed by a regime where the current saturates ("saturation regime", Equation 8 when the drain voltage exceeds the gate voltage ($V_{SD} > V_{SG}$)). Note that these equations assume that the field effect mobility of the material is constant. However, the field-effect mobility in organic semiconductors is usually dependent on the gate voltage, which suggests that a larger V_{SG} leads to a higher density of free (or mobile) charge carrier at the dielectric-semiconductor interface, resulting in increased field effect mobility [42].

The temperature dependence of the field effect mobility in some organic semiconductors has been examined as well with mixed results. It has been shown that for sexithiophene, the field effect mobility is thermally activated for temperatures T>25 K but becomes thermally independent for T<25 K [43]. Many models have been suggested to explain this behavior, including the Multiple Trap and Thermal Release (MTR) model and the polycrystalline model where individual grains are assumed to be trap free and all the traps are concentrated at the grain boundaries [44]. Another important device parameter is the current on-off ratio (I_{on}:I_{off}), which is the ratio of the current flow between the source and drain when there is no gate bias and the current flow at maximum gate bias. However, this value is highly dependent on the operating voltages, the device geometry and the dielectric material. Therefore, this parameter provides a qualitative measure of semiconductor performance, but identical device structures and biases ranges must be used to compare the results from different semiconductors.

1.1.6 Ambipolar transport

Recently, an ambipolar charge transport (simultaneous or selective transport of electrons and/or holes) in an organic transistor was highly desirable because it would enable the design of circuits with low power dissipation and good noise margins, similar to those encountered in complementary metal-oxide semiconductor (CMOS) logic circuits [45]. Moreover, for several important applications of organic semi-conductors in devices, it would be better that the ambipolar charge injection and transport could be achieved (for example, light-emitting field-effect transistors [46, 47]).

Nevertheless, organic low molecular weight materials and conjugated polymers are usually either electron or hole semi-conductors, or they are unintentionally n- or p-doped. Consequently, organic field-effect transistors (OFETs) based on a single material as active layer can only be operated as p- or as n-channel device.

This is the reason why various alternative approaches (more complex OFET configurations compare to the "simple" ones) have been recently developed in order to achieve balanced electron and

hole transport as well as efficient injection of both types of carriers, i.e. to obtain such ambipolar devices.

1.1.6.1 Bilayer approach

The first demonstrated ambipolar OFET was obtained by Dodabalapur and co-workers [48, 49] , who combined two layers of n-channel and p-channel semiconducting materials (here meaning semiconductors with high and low electron affinity, respectively) in the same device. In this case, although the mobilities of each n- or p-channel material are lower than its own at independent state, both electron and hole transport were observed in this single device.

As talked before also, it is important to choose the materials carefully according to the relative position of their HOMO and LUMO levels as well as the deposition order for achieving ambipolar characteristics. Indeed, for a long time the difficulty was to find the adequate n-type material, but as more and more n-channel materials were developed recently, the attentions are paid back on this approach [50].

In this field, all examples of bilayer ambipolar transistors use sublimed thin films. In other words and to the best of our knowledge, no ambipolar bilayer transistors based on solution-processed semiconductors have been demonstrated up to now. This seems mainly due to the problem of fabricating well-defined smooth bilayer structures by spinning one polymer on top of another: lamination or spontaneous vertical phase separation could also be big problems.

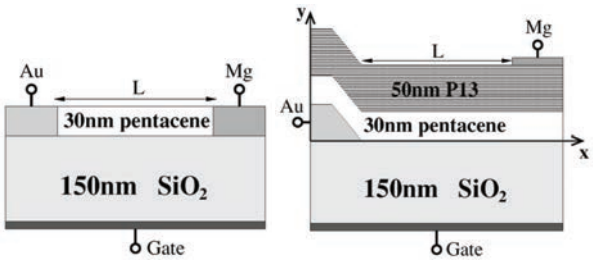

Figure 1.22 Example of a monolayer and a bilayer configuration OFET [47]

1.1.6.2 Multilayer approach

The Organic Light-Emitting field effect Transistor (OLET) (Figure 1.23) is another optoelectronic device having the structure of a thin-film transistor and the capability of light generation [51, 52]. Bright/multicolor OLETs may allow electroluminescent display fabrication with simpler driving circuits. Furthermore, the most advanced OLETs possess a huge technological potential for the realization of intense nanoscale light sources and highly integrated optoelectronic systems, including the long-researched electrically pumped organic laser. However, in the traditional single-layer devices, the charge carrier accumulation and the exciton formation zones largely coincide, which leads to severe excitons charge quenching [53].

Multilayered structures offer the opportunity to individually optimize the different materials parameters in a single device. In this way, the bilayer approach could be modified and controlled by playing precisely the materials design.

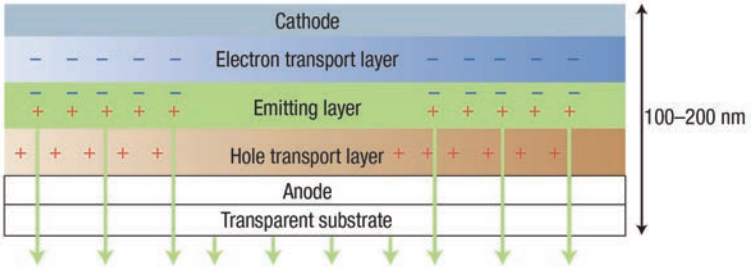

Figure 1.23 Schematic representation of device structures and of main optoelectronic processes occurring in an OLET [51]

1.1.6.3 Blend approach

Although the bilayer and multilayer approaches can yield some impressive device characteristics and interesting insight into the electronic properties of organic semiconductor heterointerfaces, its main disadvantage remains the need to deposit two or several layers on top of each other. Furthermore, cheaper solution processable options for bilayers are challenging due to the need for finding an orthogonal solvent for the deposition of the second layer. An alternative method is consequently to use blends of n- and p-channel materials and thus realize ambipolar transport in a single layer. For the blend approach, both coevaporated and solution-processed films are feasible [50].

For the coevaporation way, Rost et al. showed that coevaporating PTCDI-$C_{13}H_{27}$ and α-quinquethiophene with equal fractions results in good ambipolar characteristics (Figure 14). Here again, the mobilities obtained are smaller than those for the pure materials [54]. This can be understood in terms of interpenetrating networks of n-channel and p-channel materials, which predominantly conduct one or the other carrier due to their different electron affinities and ionization potentials: thus, the effective mobilities of both electrons and holes in a percolating network are lower compared to that of a neat film. In this configuration, by turning the fraction of n- and p channel material, the electron and hole mobilities can even be adjusted [55].

For the solution processable way, thin films of polymer blends can be easily obtained and are thus well suited for application in integrated circuits. Their microstructure can be tuned by the choice of solvents and spin conditions [56].

1.1.6.4 Low band gap approach

As already mentioned, injection of both holes and electrons into a particular semiconductor is one major obstacle to overcome in order to fabricate ambipolar OFET. Most common organic semiconductors (small molecules and polymers) show band gaps between 2 and 3 eV. Thus, injection

from a metal electrode with a given work function (high or low) will always result in high injection barriers (>1 eV) for either electrons or holes. One solution against this is to use a material having low band gaps, generally less than 1.8 eV [57]. Thus, the injection barrier for both charge carriers is lowered and efficient ambipolar transport can take place.

In this context, for several years, more and more organic semiconductors are synthesized and characterized, following different strategies and focusing in particular on chemical modifications: in this way, the band gap can be tuned and designed with precision [58]. As examples, the band gap can be designed through adjusting the following parameters: (1) Bond length alternation; (2) Aromaticity; (3) Conjugation length; (4) Substituent effects; (5) Intermolecular interactions [59]. The detailed design methods (synthetic) are summarized in several review articles [59-61].

1.1.6.5 Other approaches

Fullerene Derivatives

Fullerenes and their derivatives have been known as n-type semiconductors for some time and thus were applied in bilayer and blend ambipolar transistors. Recently, however, they were shown to have ambipolar characteristics as pure materials as well [45, 62].

Single Crystals

Organic single crystals are seen as model systems for charge transport in organic semiconductors, as they are free of grain boundaries, have a low concentration of trap states, and thus show very high field-effect charge transport mobilities. Although most single-crystal FETs till recently only showed p-channel behavior [63], it was reported an electron mobility of 0.01 $cm^2\ V^{-1}\ s^{-1}$ [64] for rubrene as a benchmark molecule for single-crystal p-channel transistors.

High/Low Work Function Electrodes

Another way to avoid the problem of unequal charge carrier injection into a semiconductor is the use of source and drain electrodes with unequal work functions. We have already seen that many organic semiconductors that usually show p-type behavior with standard gold electrodes can also show n-type behavior with low work function electrodes such as calcium or aluminum and suitable trap-free gate dielectrics. Thus, using, e.g., a gold electrode for hole injection and a calcium electrode for electron injection in the same device should lead to ambipolar behavior even for wide band gap semiconductors [50].

1.2 Liquid Crystals

1.2.1 Generalities

Since the discovery of liquid crystals by the botanist Friedrich Reinitzer in the 19th century, this kind of materials has attracted the attention of chemists and physicists alike [65]. The liquid crystal state is an authentic state of matter, intermediate between the classical crystalline solid state and isotropic liquid one. The liquid crystal phases, so-called “mesophases”, became a main research field of soft matter [66]. Their macroscopic behavior is defined by the molecular properties of their constituents: the mesogens. The formation of a liquid-crystalline phase is determined generally by the shape anisotropy of these mesogens.

At present, π-conjugated liquid crystal compounds interest many research groups. Indeed, their self-spontaneous organization (intermolecular interactions) property on large areas should allow a good mobility of the charge carriers, thus making them good candidates for the active layer in electronic components.

1.2.2 Liquid crystal families and mesogens

Two types of liquid crystal are distinguished: lyotropic liquid crystals [67], where the liquid crystal polymorphism results from interactions between one or several solvents and amphiphilic molecules, and thermotropic compounds where the succession of phases is obtained by changing the temperature. In some cases, these two processes can be also combined to obtain amphotropic liquid crystals [68]. As our study involves only thermotropic compounds, we will focus only on this family of materials in the following parts.

Among the organic substances, only certain types of molecules display mesomorphic properties; in fact, not all the molecules are likely to have a mesomorphic state. The existence of these phases (mesophases) is due to the anisotropic shape of the molecules and to their chemical constitution. These mesophases correspond to well-defined molecular organizations that are directly related to the molecular structure of the mesogenic compounds. These compounds are organic molecules made of a rigid part (aromatic ring) and a flexible part (alkyl chains), which are characterized by strong geometric anisotropy. These molecules are formed by an amphipathic structure due to two chemically incompatible constituent parts, which induce segregation and the presence of mesophases.

Generally, the different shapes can be classified as “calamitic” (rod-like), “discotic” (disclike) [69], “sandic” (board-like) [70] and “banana-shaped” [71] mesogens (Figure 1.24).

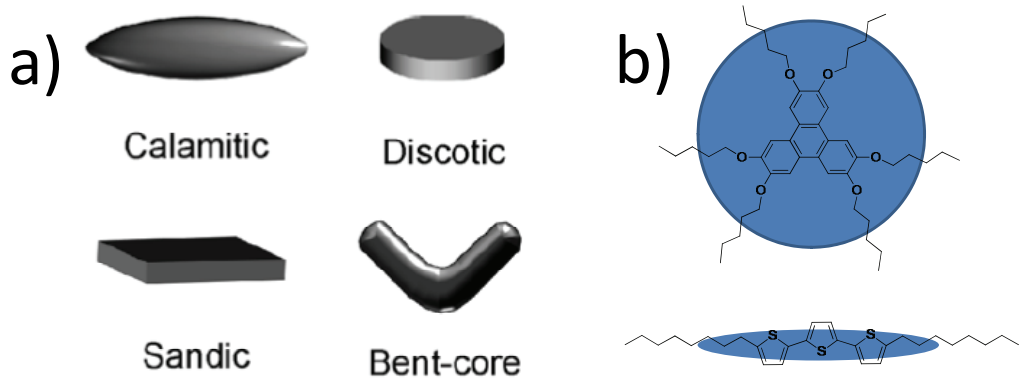

Figure 1.24. a) Different shapes of liquid-crystalline molecules. b) Examples of calamitic and discotic molecules.

1.2.3 Different types of mesophases

1.2.3.1 Nematic phases

The nematic phase, which can be obtained for calamitic or discotic mesogens, is the most disordered mesomorphic phase. It has a structure characterized by an orientational order but no positional order. In fact, the molecules are oriented in parallel to each other along a preferred direction defined (director), but are free to move in space [72] (Figure 1.25).

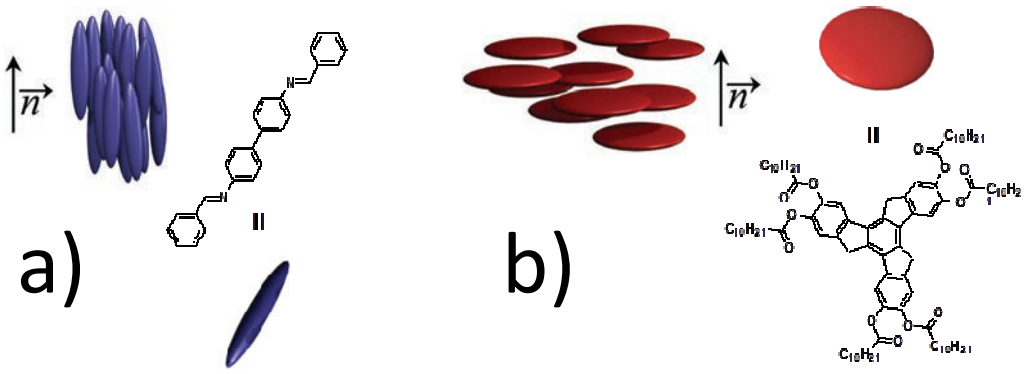

Figure 1.25 Schematic representation of the nematic mesophase in the case of the calamitic (a) and discotic (b) mesogens

The typical schlieren textures observed by polarized optical microscopy for nematic phases are shown in Figure 1.26.

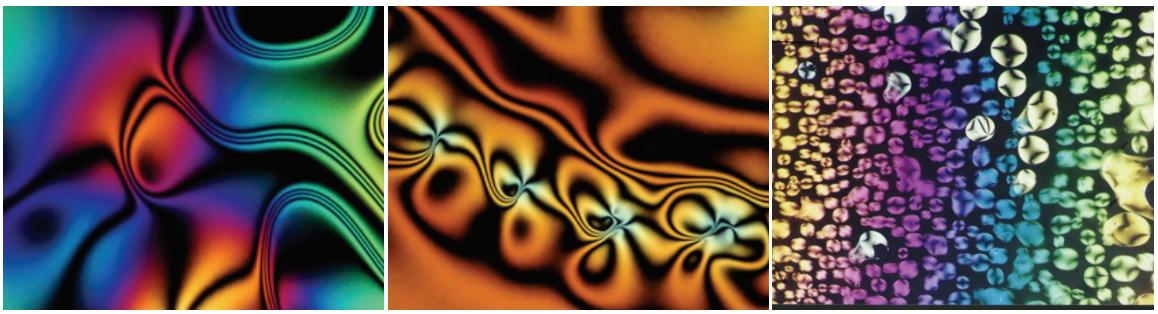

Figure 1.26 Typical schlieren textures observed by polarized optical microscopy for nematic phases

If the molecule is a chiral one, the observed mesophases can be a chiral nematic (N*) or cholesterics (as the first discovered N* molecule was a derivative of cholesterol). In this mesophases, the director varies in direction throughout the medium in a regular way. In any plane perpendicular to the twist axis, the long axes of the molecules tend to align along a single preferred direction in this plane, but in a series of equidistant parallel planes, the preferred direction rotates through a fixed angle (Figure 1.27).

Figure 1.27 Schematic representation of the organization of chiral nematic mesogens

The typical optical textures observed by polarized optical microscopy for chiral nematic phases are given in Figure 1.28.

Figure 1.28 Some examples of cholesteric textures

1.2.3.2 Smectic phases

The smectic phase is characterized by an orientation order and positional order as the molecules are organized in layers [73]. A variety of smectic phases exist, mainly obtained with calamitic molecules. Organization of the mesogens within the layers gives rise to several varieties of the lamellar phases.

In fact, the molecules are, as in the nematic phase, oriented parallel to a preferred direction, but in addition, they are arranged in parallel, equidistant layers, which can be free to slide over each other depending on the nature of the smectic phase. In the smectic A (SmA) phase (Figure 1.29.a), the molecules are oriented parallel to the normal of the layers and form uniaxial phases, while in the smectic C (SmC) phase (Figure 1.29.b), the molecules are inclined at an average angle of θ relative by the normal of the layers.

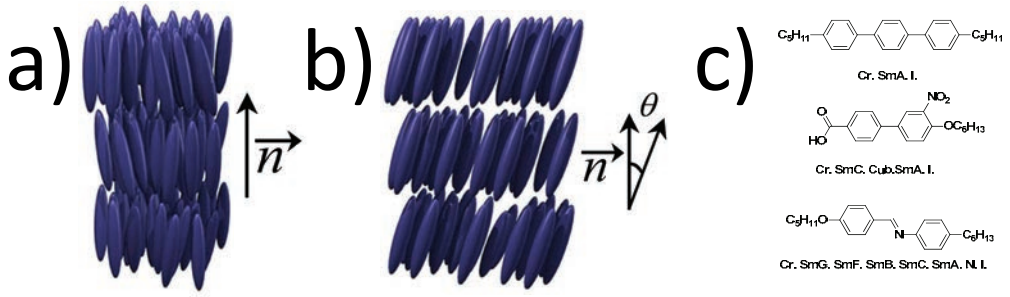

Figure 1.29 Schematic representation of the organizations of the mesogens in (a) Smectic A and (b) Smectic C mesophases and (c) some examples of mesogens which can form smectic phases

Other smectic phases characterized by a positional order within the layers, such as the smectic B (SmB), the smectic F (SmF), and the smectic I (SmI) phase, are shown in Figure 1.30. The smectic B derive from the smectic A, whereas the smectic I and F derive from the smectic C. In these highly ordered phases, the molecules are arranged hexagonally within the layers.

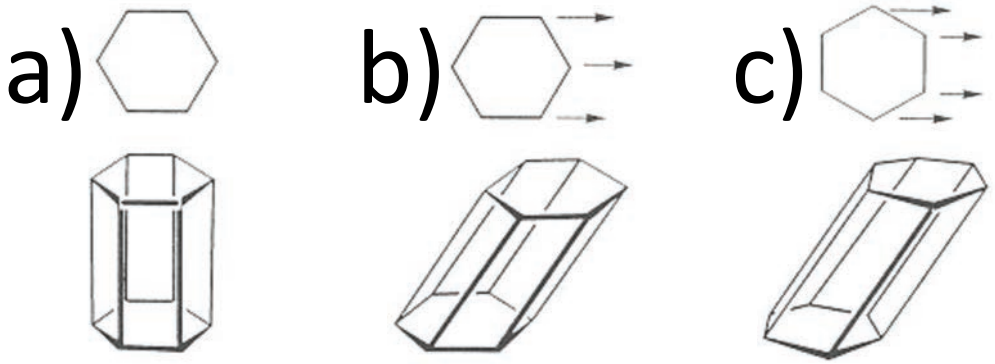

Figure 1.30 Schematic representation of the mesogenic organization within the layer in Smectic B (a) Smectic I (b) and Smectic F (c)

More generally, when a smectic phase sample is placed between two glass slides, the layers become distorted and can slide over one another in order to adjust to the surface conditions and preserve their thickness. The optical properties (focal conic texture) of the smectic state arise from these distortions of the layers. Typical optical textures formed by smectics are shown in Figure 1.31.

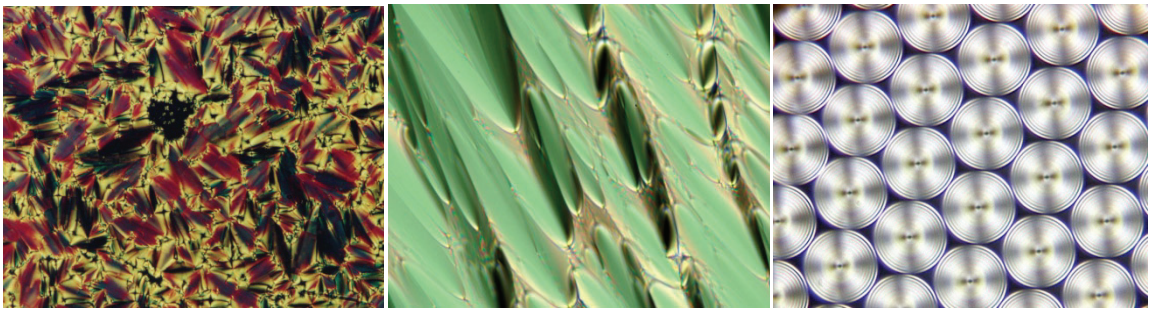

Figure 1.31 Typical focal conic textures of Smectic A phase

1.2.3.3 Columnar phases

The columnar mesophases generally results from stacking of the discotic molecules to form columns (Figure 1.32.a) [73]. These columns are parallel to each other and are organized periodically, thus leading to structures characterized by orientational and two-dimensional positional orders (Figure 1.32.b).

As shown in the Figure 1.32.b and Figure 1.32.c, these networks can adopt mainly hexagonal, rectangular, or oblique symmetry, respectively, forming three classes of columnar organizations: hexagonal (Col_h), rectangular (Col_r), and oblique (Col_o) columnar mesophases. In the hexagonal columnar phase (Col_h), the molecules are stacked to form columns arranged in a hexagonal network.

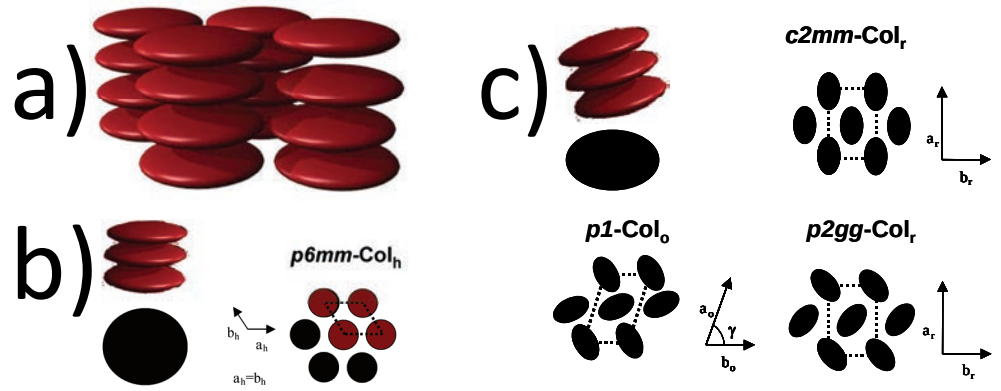

Figure 1.32 Schematic representations of the (a) columnar mesophase; (b) hexagonal (CoI_h) columnar arrangement; (c) rectangular (Col_r), and oblique (Col_o) columnar arrangement

Figure 1.33 shows some typical optical textures of columnar mesophase.

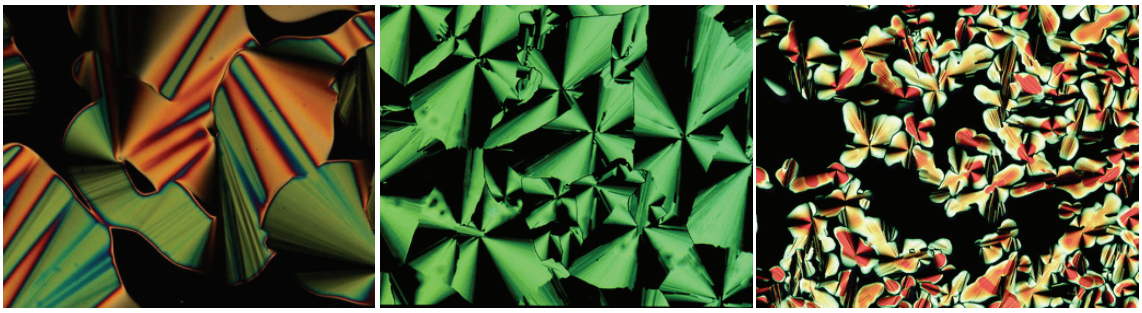

Figure 1.33 Typical optical textures of columnar mesophase

1.2.4 Liquid crystal polymers

The existence of the liquid crystalline state requires rigid and/or shape-anisometric molecules. With the knowledge of these structural principles, the construction of polymers with potential liquid crystalline properties is immediately obvious. The macromolecule as a whole can either have a rigid rod-like or disk-like structure or contain mesogenic groups as monomer units [74]. On the one hand, polymers whose total structures are mesogenic are only achievable when the polymer itself as rod-

shaped, for example, via a rigid, helical secondary structure. On the other hand, numerous structures are conceivable for polymers with mesogenic groups as monomer units, whereby one can differentiate between two fundamentally different types (Figure 1.34).

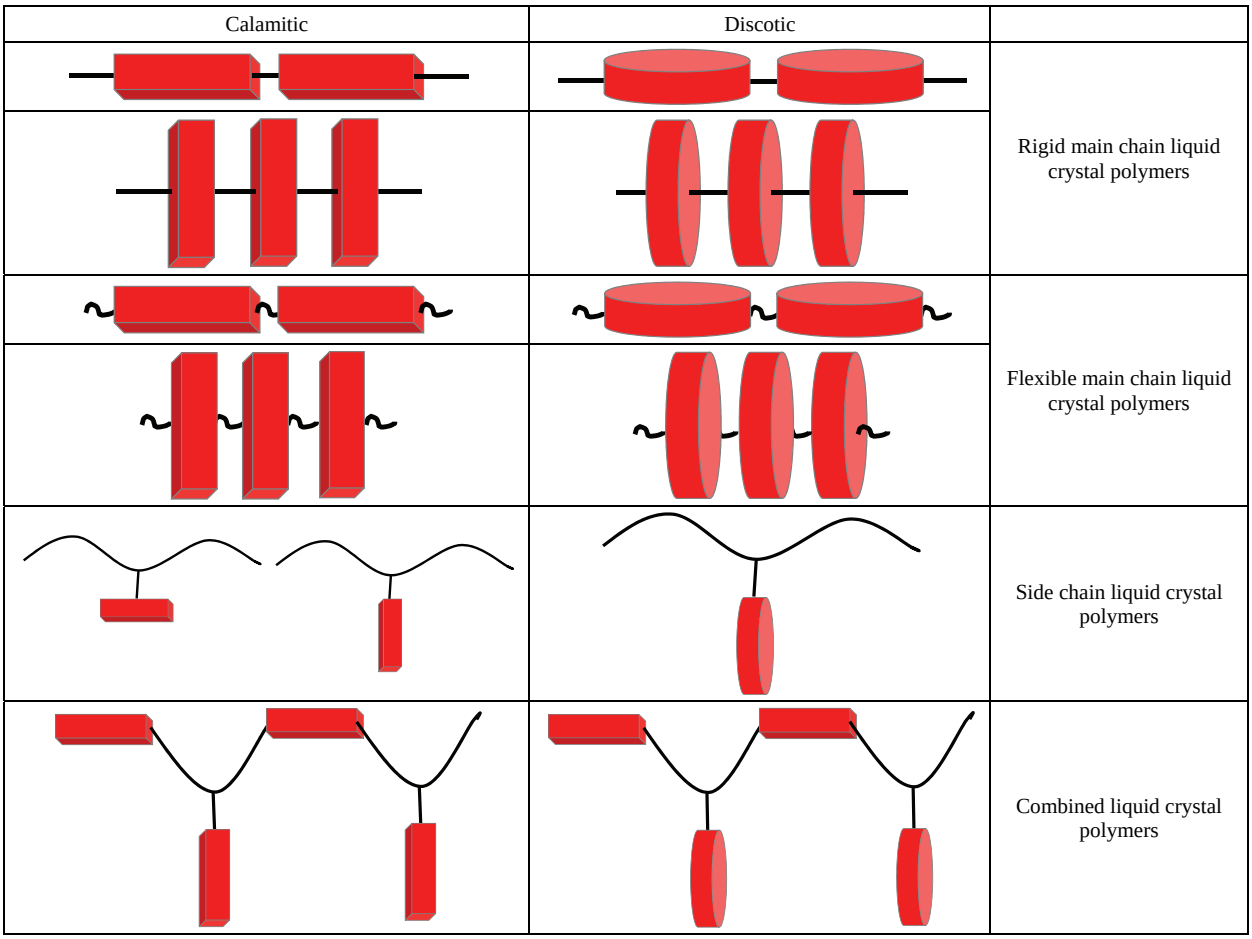

Figure 1.34 Types of liquid crystalline polymers derived from rod-shaped and from disk-shaped mesogenic molecules

1. Those in which the mesogenic groups are located in the polymer main chain are known as liquid crystalline main chain polymers

2. Those in which the mesogenic groups are attached to the polymer main chain in a side-chain-like manner are known as liquid crystalline side chain polymers

In comparison to low molar mass liquid crystals, attachment of the mesogenic groups to the polymer generally restricts the translational and rotational motions of the mesogenic groups. Therefore an influence on the temperature range of existence and a change in the physical properties of the liquid crystalline phase could be directly expected.

1.2.5 Semiconducting liquid crystal small molecules

Apart from other non-conjugated organic materials, the semiconducting small molecules have been widely studied through the past 2 decades since they can be readily purified and form well ordered (often crystalline) thin films for the fabrication of high performance devices. In these molecules, in

general, there exists one or several π-conjugated systems and these "rigid cores" can bring the liquid crystal property through adding one or more alkyl chains. A direct benefit of this is that the good self-organization can be preserved while the alkyl chains can render these materials more soluble and then better solution-processable.

In addition, there are other advantages in using liquid crystalline semiconductors [75]. Liquid crystals are partially ordered molecular materials whose properties, including their conduction properties, lie between those of (fully ordered) crystalline and (fully disordered) amorphous molecular materials. They can consequently combine the best properties of both. More precisely, like amorphous molecular materials they are easily processed and they lack grain boundaries that, in their crystalline counterparts, act as deep traps for the charge carriers. Additionally, most are sufficiently well ordered so that they share some of the advantages of crystalline molecular solids: in theory, charge carrier mobilities could even be almost as high as those in the crystal. Furthermore, at least in the most ordered liquid crystalline phases, impurities that could act as charge traps have limited solubility and then are relatively "forced out of the system".

In order to investigate and develop the advantages of liquid crystalline mesophase to increase the performance of semiconducting properties, numerous semiconducting LC small molecules were designed and reported.

As examples, up to now, it has been reported many different types of liquid crystals exhibiting from good to high mobilities ranging from 10^{-4} cm^2/Vs up to ~1 cm^2/Vs, including triphenylenes [76, 77], phthalocyanines [78, 79], porphirines [80], perylenes [81], phenylbenzothiazoles [82], phenylnaphthalenes [83, 84], oligothiophenes [85, 86], and benzothienobenzothiophenes [87] , etc.

To try to better understand these results, it is necessary to detail a little more the way the charges can move in such small molecules liquid crystal semiconductors, before to give a "state of the art" concerning both p-type and n-type materials.

1.2.5.1 Charge transport in liquid crystal semiconductors

When discussing charge carrier mobility in organic materials, it is essential to recognize that it is not an intrinsic property of organic molecules. It is a material property and requires hopping of charges between the molecules. For this reason, a sufficient interaction of different π-electron systems (π-π stacking) at the local scale is necessary to allow charge transport between neighboring molecules. With typical stacking distances of several Angstroms, this intermolecular hopping process of charges occurs many times before reaching the opposing electrodes, which have a distance of 100 nm (minimum) to several mm. While closely packed crystalline samples facilitate local charge hopping between organic molecules, grain boundaries in polycrystalline samples strongly affect the charge carrier mobility on a macroscopic scale (Figure 1.35). In contrast, amorphous films from organic materials ($\mu=10^{-5}$-10^{-4} cm^2V^{-1} s^{-1}) suffer from poor local order and weak π-orbital overlap between

molecules. Therefore, ideally a mono-domain of a properly packed organic material is needed to achieve (relatively) high charge carrier mobilities [88].

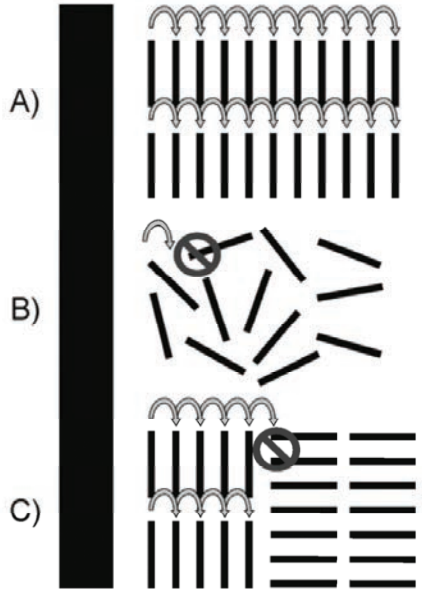

Figure 1.35. Charge transport in different orientations. A) crystalline: good charge transport, B) amorphous: no charge transport, C) polycrystalline: grain boundaries pin the charges on larger length scales.

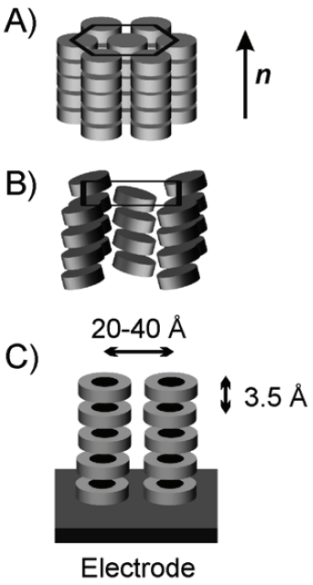

Figure 1.36. A) Hexagonal assembly of discotic columns (Colh). B) Columnar rectangular mesophases (Colr). C) Charge transport in columnar stacked discotics. The aromatic cores (black) form conductive 1D channels, while the surrounding alkyl-chains (gray) act as an insulating layer around the cores.

In this context, liquid-crystalline ordering (Figure 1.36) offers the possibility to easily orient organic semiconducting molecules [89] and to prepare mono-domain samples. But even if LC phases possess a higher degree of order than the isotropic melt (amorphous order) it is however lower compared to the perfectly regular and most dense crystal. Thus π-conjugated molecules with liquid-crystalline phases are attractive to improve the charge carrier mobility.

In the case of the discotic liquid crystals, columnarly stacked aromatic macrocyclic cores can provide coaxially-insulated, conductive pathways which offer a unique possibility for the one-dimensional (1D) transport of charge (Figure 1.37). This is the reason why discotic liquid crystal semiconductors are serious candidates for future applications as organic charge transport layers in a variety of devices such as OFET, OPV and OLED [37].

Differently and interestingly as well, in the case of calamitic liquid crystals, the lamellar organization favors the charge transport in the layers namely, i.e. in a two dimensional (2D) way [90] (Figure 1.37).

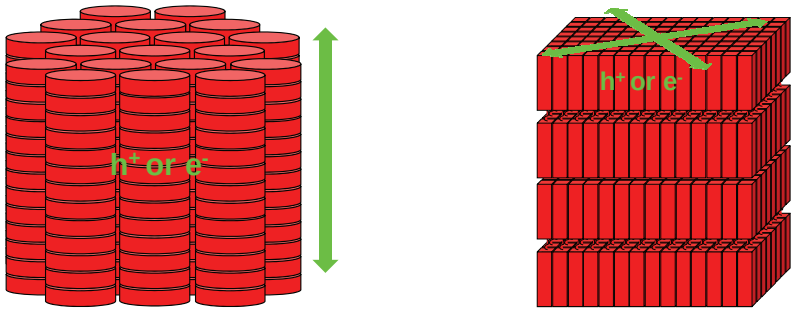

Figure 1.37 Charge transport model in discotic columnar and calamitic smectic liquid crystals, the arrows indicate the direction of electronic charge hopping.

1.2.5.2 P-type semiconducting liquid crystal small molecules

The majority of the semiconducting materials discovered until now are p-type.

(1) Discotic ones

Triphenylene derivatives are among the most widely investigated discotic liquid crystals because they are robust and show a strong tendency for columnar mesophase formation. Two decades ago, Adam et al [76] (Figure 1.38, TS) reported already a 0.1 cm^2/Vs mobility for a triphenylene derivative and made this family very popular in this field. Later, its corresponding hexaalkoxy substituted triphenylenes (Figure 1.38 TO) were studied but gave lower mobilities, between 10^{-4} and $10^{-2} cm^2/Vs$ for both type of carriers, depending on the length of the side-chains [91].

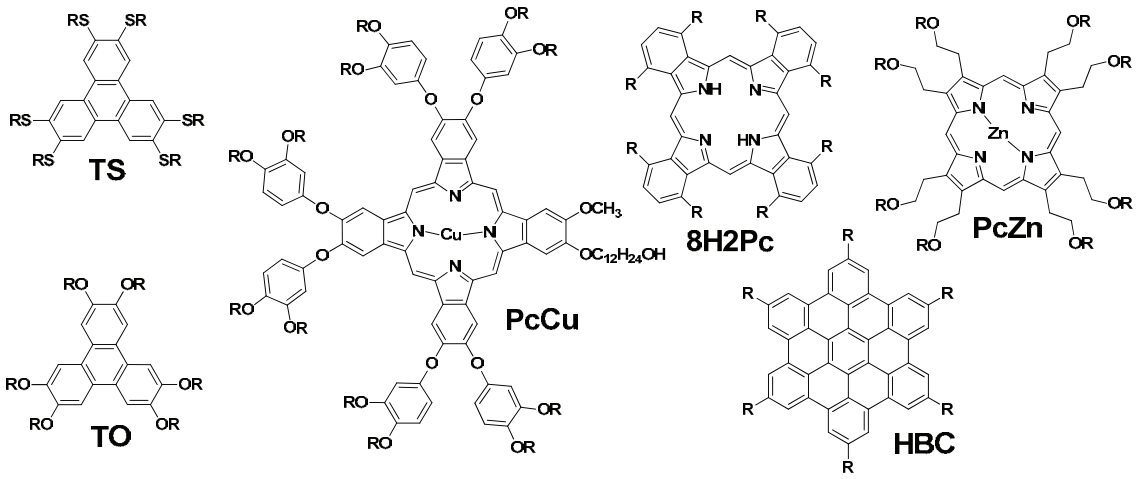

Figure 1.38 Discotic p-type semiconducting liquid crystal small molecules

Phthalocyanine derivatives are another series of discotic p-type liquid crystal semiconducting molecules, a mobility of 0.2 cm^2/Vs in its corresponding columnar phase being for example reported by Hanna et al [79] (Figure 1.38, **8H2Pc**). Besides, some phthalocyanine metal complexes show both high hole and electron mobilities (10^{-3} to 10^{-2} cm^2/Vs) [80, 92] (Figure 1.38 **PcCu** and **PcZn**).

Coronene can also form very ordered columnar liquid crystal mesophases. In the early reports, unity mobility could even be obtained from the hexabenzocoronene (Figure 1.38, **HBC**) [93] and recent

work further evidenced that the well ordered columns can be magnetically orientated and as a result show anisotropy OFET mobilities [94].

(2) Calamitic ones

One of the first reported calamitic p-type liquid crystal molecules is the 2-(4'-heptyloxyphenyl)-6-dodecylthiobenzothiazole (**7O-PBT-S12**) (Figure 1.39) which was described in 1997 by Hanna et al. [82]. A hole mobility of 0.003 cm^2/Vs was obtained by TOF once in its SmA phase. Then later in the same year, Hanna's group reported another calamitic liquid crystal p-type semiconductor, 2-(4'-octylphenyl)-6-dodecyloxynaphthalene (**8-PNP-O12**), which gave a mobility of $1.6x10^{-3}cm^2$/Vs in a lower temperature smectic phase [83].

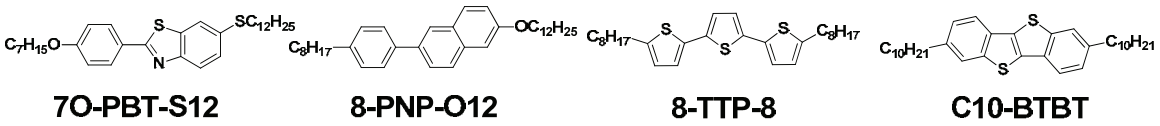

Figure 1.39 Calamitic p-type semiconducting liquid crystal small molecules

Being the simplest calamitic semiconducting liquid crystal material in the oligothiophenes family, the α,ω-dialkylterthiophene was thoroughly studied as well [95]. In the SmG phase of **8-TTP-8** (Figure 1.39), a 0.01 cm^2/Vs mobility value was obtained [85]. Recently, this **8-TTP-8** was again tested as a model molecule to compare with α-benzothienobenzothiophene (**C10-BTBT**) [86] (Figure 1.39). In the new experiment, by using a "in temperature" spin-coating method, the mobility of **8-TTP-8** was increased to 0.2 cm^2/Vs and the **C10-BTBT** showed a higher and remarkable mobility of 3 cm^2/Vs if measured by OFET [86].

Based on the self-healing property of some liquid crystal molecules, Breemen et al. [96, 97] reported also a terthiophene derivative (Figure 1.40 **M1**) forming easily large-area ordered films after thermal treatment in the liquid crystal mesophase, reaching a mobility of 0.02 cm^2/Vs by both TOF and OFET measurements. Another case we can notice is an α-chain modified **C10-BTBT**(Figure 1.39). Méry et al. reported as well a [1]benzothieno[3,2-b][1]benzothiophene-2,7-dicarboxylate (Figure 1.40 **M2**) in which both hole and electron transports were observed [87].

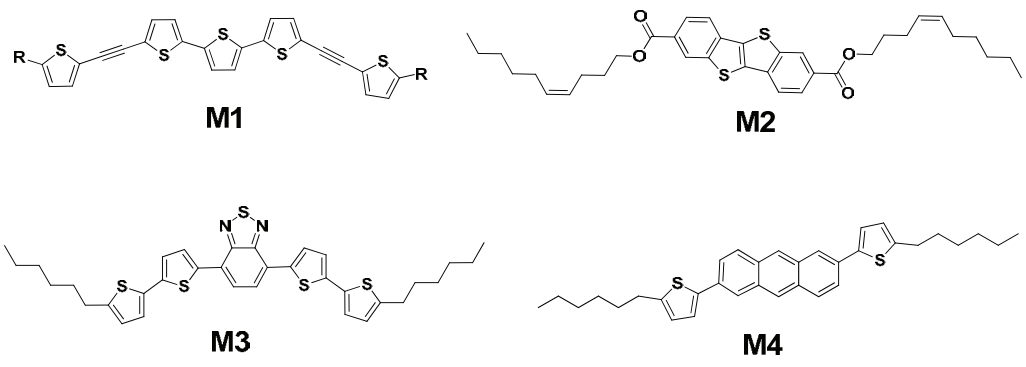

Figure 1.40 Other calamitic p-type semiconducting liquid crystal small molecules

Finally with the modern well-established molecular chemistry, more and more "combined" calamitic liquid crystal molecules can be synthesized by coupling or fusing different basic conjugating bricks (benzene, thiophene, and other heterocyclic rings) (Figure 1.40, **M3, M4**) [98, 99]: thus, we can expect to obtain novel liquid molecules.

(3) Others (glassy-nematics): oligofluorenes

Contrary to their polymer analogues (Paragraph 1.2.5), monodisperse oligofluorenes are capable of self-organization into uniaxially aligned, defect-free films for the realization of strongly polarized and highly efficient organic electroluminescence devices [100]. Furthermore, spun-cast glassy nematic films comprising monodisperse oligofluorenes are stable against recrystallization which is essential to the prevention of device failure.

As an example, Yasuda et al. [100] reported a semiconducting LC oligofluorene F(MB)10F(EH)2 (Figure 1.41) fabricated OFET containing a monodomain glassy-nematic film, a field-effect mobility of 0.012 cm^2/Vs was observed.

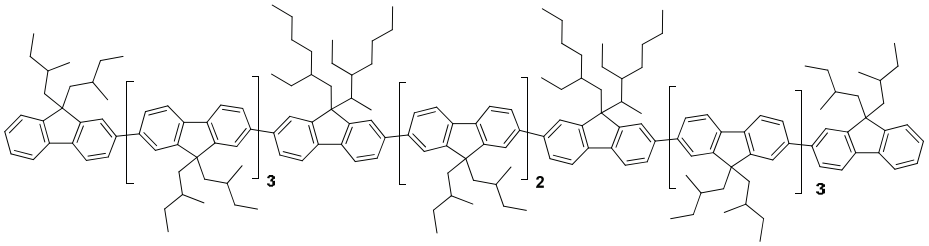

Figure 1.41 An example of oligofuorene

There are more glassy nematic liquid crystal oligoflurene derivatives that are reported for OLED [101] and other optoelectronic devices [102, 103] but this is not our main topic.

1.2.5.3 N-type semiconducting liquid crystal small molecules

In comparison with their numerous p-type homologues, the n-type semiconductors were always and are still not as much developed due to the fact that the transport in n-channel conductors is often degraded easily by air.

Nevertheless, at the moment, rylene and related diimide molecules represent the most important family of n-type semiconducting LC molecules. This is due to the fact that they are a robust, versatile class of polycyclic aromatic electron-transport materials which present excellent thermal and oxidative stability, high electron affinities, and, in many cases, high electron mobilities [104].

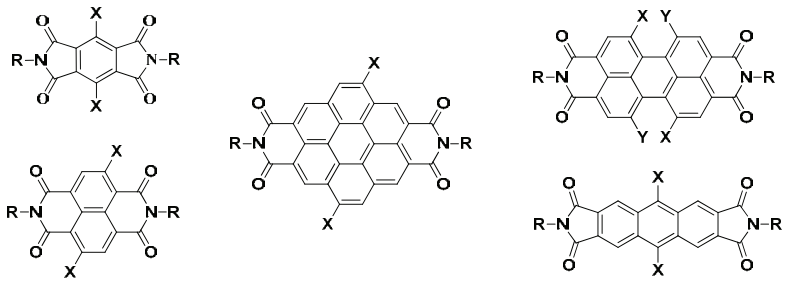

Figure 1.42 some rylene diimide small molecules which give n-type transport properties

In the up-shown family, particularly some perylene diimide molecules can self-assemble into highly ordered one-dimensional columnar stacks, making them promising candidates for use as charge-transport materials in organic electronics.

High electron mobilities were determined by using different characterization methods. Mobilities of 0.11 cm^2/Vs have been for example measured by pulse radiolysis time-resolved microwave conductivity (PR-TRMC) techniques for **M5** in tis liquid crystal phase [81]; on the other side, Marder et al. found that at room-temperature, **M6** displays a space-charge-limited current (SCLC) mobility as high as 1.3 cm^2/Vs under ambient conditions [105] while even higher values (up to 6.7 cm^2/Vs for **M7**) were found for closely related columnar discotic coronene-2,3:8,9-tetracarboxylic diimides [106]. Recently as well, Bao, Würthner, and co-workers reported that OFETs based on **M8** can exhibit mobilities as high as 0.72 cm^2/Vs, which decreases only slightly after air exposure and remain stable for more than 50 days [107].

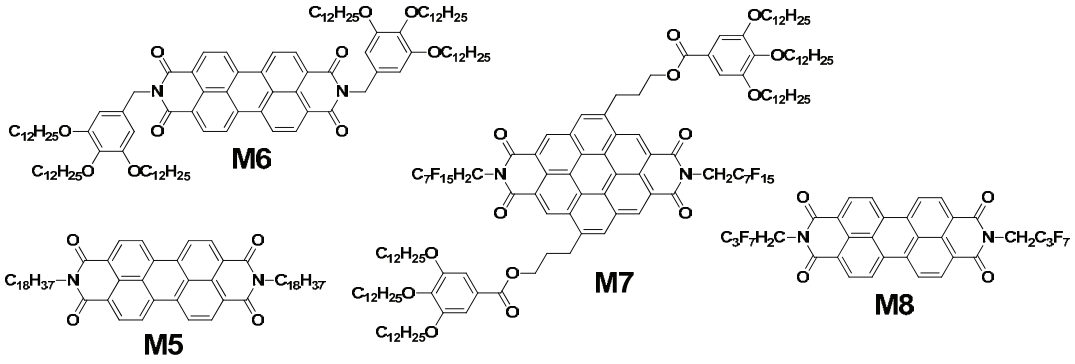

Figure 1.42 Some perylene diimide based n-type semiconducting liquid crystal small molecules

Note that as for n-type materials, chemistry is very usefull: many p-type or ambipolar molecules can be chemically modified into n-type molecules by, for example, introducing one or multiple electron withdrawing groups to adjust the LUMO level. This allow us at the same time to remind that we must be careful with this notion of n or p-type material, as it could change depending the counter material used or the device configuration tested.

1.2.6 Semiconducting Liquid Crystal Polymers

As we presented just before a state of the art concerning mobilities in small molecules, we can do the same for both main-chain and side-chain semiconducting liquid crystal polymers.

In fact, the best way to enhance charge carrier mobility in polycrystalline polymer films is the reduction of grain boundaries to increase the crystalline domain sizes. More precisely, the key idea in achieving this goal is to take advantage of the material's ability to self-heal local defects within the film: compounds exhibiting a liquid crystalline state have the potential for such kind of self-healing [89, 108-110].

1.2.6.1 Main-chain liquid crystal polymers

(1) Polyfluorenes based.

Polyfluorenes (PFO) are rigid rod polymers that can be rendered soluble in organic solvents by appropriate substitution at the C9 bridging position: some of them exhibit high temperature liquid crystalline phases, which can be thermally exploited to achieve optimal thin film microstructures and good transistor performance (Figure 1.43) [111-114].

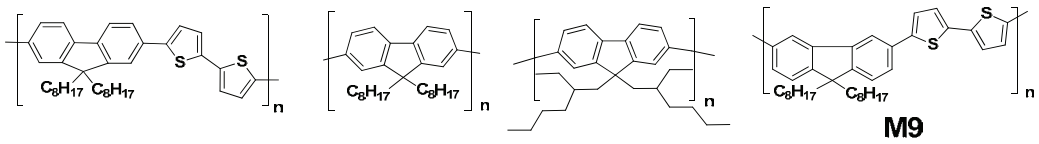

Figure 1.43 Some polyfluorenes based Main-chain liquid crystal polymers

Sirringhaus et al. reported as well a bithiophene implanted alternating copolymer poly(9,9-dioctylfluorene-co-bithiophene) (Figure 1.43, **M9**) resulting in an increase in both HOMO energy level and improved charge transport. In this case, orientation of the polymer backbones can be achieved by a combination of thermal annealing within the mesophase and substrate induced alignment: mobility around 0.02 cm^2/Vs has been observed for this polymer, with good ambient stability [115].

(2) Polythiophene based

Similar to its PFO homologues, several polythiophene based liquid crystal polymers have been reported. Most of these kind of semiconductors are main chain liquid crystal polymers, such as Poly(3,3'''-dialkylquaterthiophene) (Figure 1.44, **M10)** [116] poly(2,5-bis(3-alkylthiophen-2-yl)thieno[3,2-b]thiophene) [117, 118] (Figure 1.44, **M11**), and poly(didodecylquaterthiophene-alt-didodecylbithiazole) (Figure 1.44, **M12**) [119].

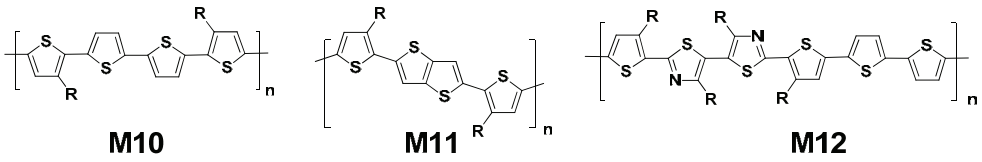

Figure 1.44 Some cases of polythiophene based semiconducting side chain liquid crystal polymers

Through the addition of liquid crystalline side-chains, the (conjugated) polymers can show different specific properties (birefringence, self-orientation, induced anisotropy, etc.)[109, 120] They are typically prospective candidates for elaborating functional materials as well as or even better than main-chain type liquid crystalline conjugated polymers [121].

On the one hand, their electrical and optical properties can be controlled by the various liquid crystalline side chains and on the other hand, furthermore, with their polymeric properties, macroscopic alignment of the molecules can be progressed by an external perturbation such as shear stress, electric or magnetic field [122].

1.2.6.2 Side-chain liquid crystal polymers

Even if main-chain liquid crystal polymers are more numerous, a few side-chain liquid crystal polymers were also synthesized recently, including either calamitic [122] or discotic [123, 124] pending groups as in our research group. One reason is that by designing the backbone and the side-groups, it opens a door for a versatile method towards different kinds of LC polymers with various properties.

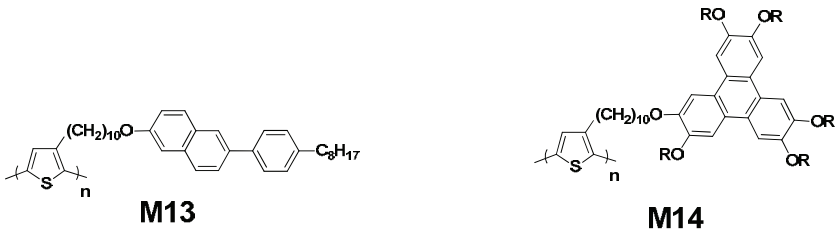

Figure 1.45 Some cases of polythiophene based semiconducting side chain liquid crystal polymers

1.2.7 Ambipolar semiconducting materials

In order to conclude this part on liquid crystals and remembering the high interest actually concerning ambipolar organic semiconductors (Paragraph 1.1.6), it must be said that this is still challenging and, until recently, there were only a few reports showing that a given material can efficiently transport both electrons and holes [125]. Indeed, in order to avoid the phase separation issues such as in multilayer or blend systems, homogenous materials should be developed. Here we present several strategies employed to surpass this challenge.

1.2.7.1 Combined systems: donor-acceptor dyads and triads

A very logic and also simple idea is to link a donor molecule and an acceptor molecule by a covalent manner in a single molecule. Based on their corresponding size and electronic properties, these kinds of molecules are called dyads or triads.

Oligothiophenes, triphenylenes and phthalocyanine are good candidates as donor moieties and perylene diimides and fullerenes are often chosen as acceptors to form these well self-organized (liquid crystal) dyads and triads [126-131] .

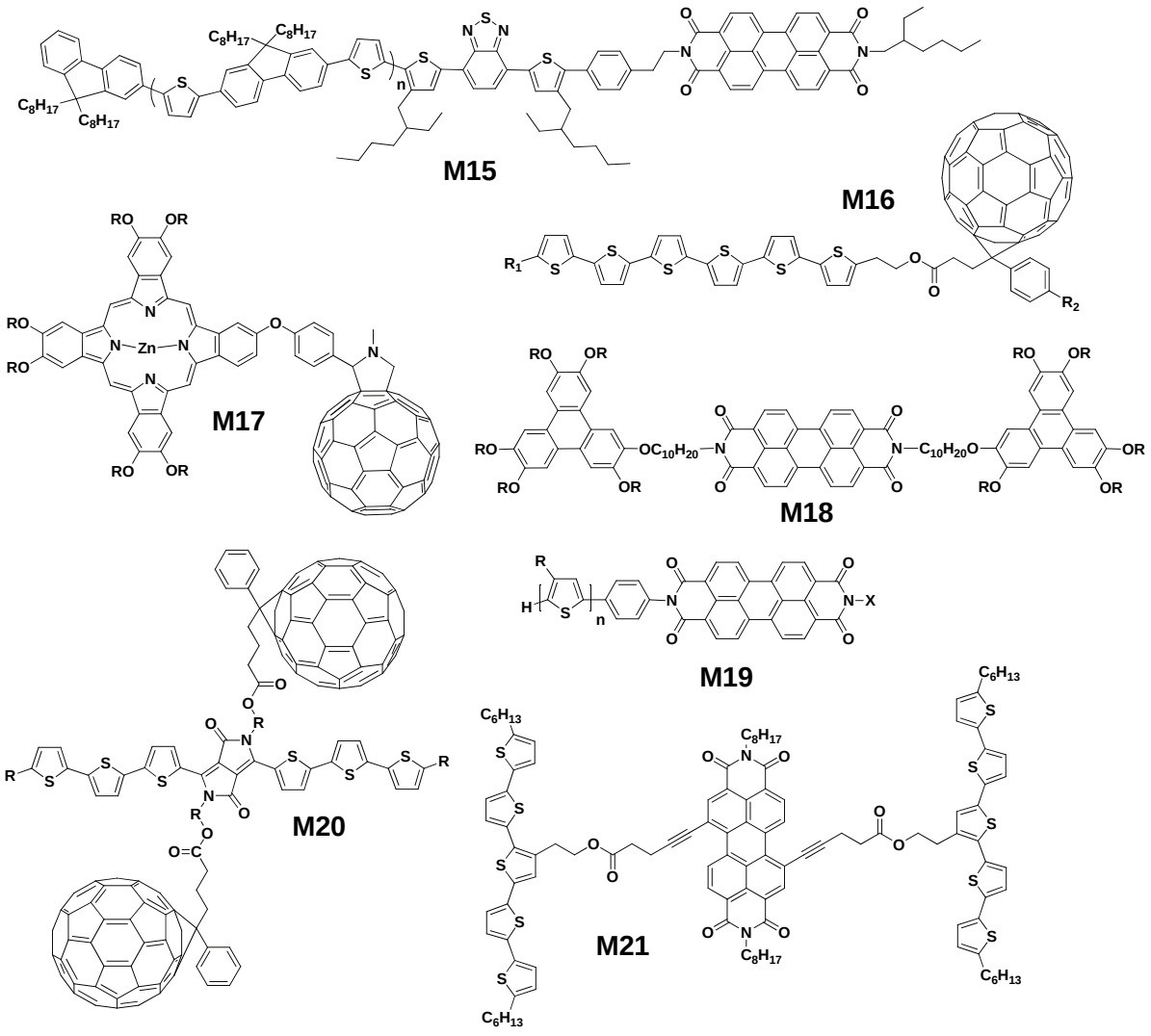

Figure 1.46 Liquid crystal donor-acceptor dyads and triads

1.2.7.2 Combined systems: donor-acceptor polymers

By following a similar concept, the semiconducting polymer backbone can be modified by attaching “opposite type” pending groups to form a “multiade” macromolecule.

Polythiophene, as a classical self-organized high performance p-type polymer, is often chosen as the donor backbone.

As an example, Thelakkat et al. reported a well self-organized crystalline-crystalline D-A block copolymer, by combing one bloc of regioregular polythiophene and a perylene diimide substituted polyacrylate (Figure 1.47 , **M23**) [132, 133].

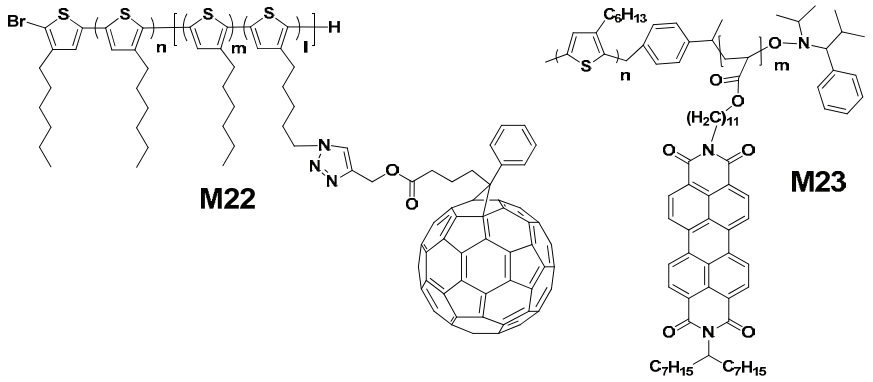

Figure 1.47 Donor-acceptor polymers

Another attempt was reported by Hashimoto et al. on a fullerene grafted block copolythiophene which shows also a well nano-structured self-organization (Figure 1.47, **M22**) [134].

1.2.7.3 Low band-gap systems: small molecules and polymers

On parallel to these "combined systems", notable progress has been made over the past decade in understanding the structure/function relationships governing material performance in the field of organic semiconducting materials: thus, it is possible to adjust the electronic properties (modifying the HOMO/LUMO levels, in particular to decrease the gap) and simultaneously improve the self-organizing characteristics of the materials by designing new aromatic systems based on the existing basic aromatic cores [60, 135]. Note that this is possible both regarding small molecules and/or polymers.

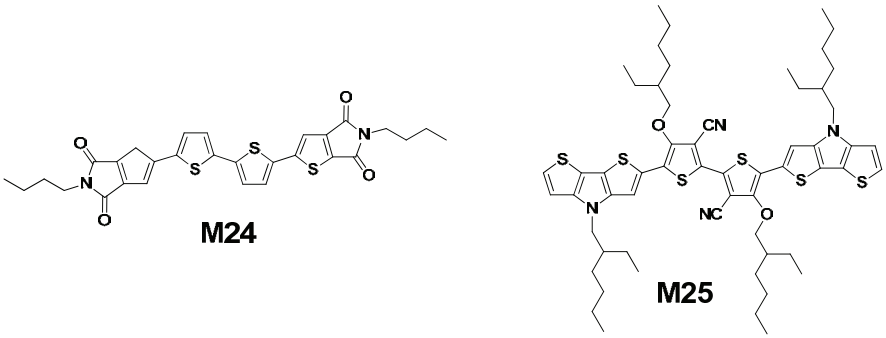

Figure 1.48 Low band-gap liquid crystal small molecules

As an example of small molecule, by introducing some electron withdrawing groups (EWG), the oligothiophenes's LUMO level can be lied down. Muccini et al [136] and Roncali et al. [137] reported

respectively two oligothiophenes derivatives (Figure 1.48) modified by EWGs and these ambipolar molecules showed well self-organized (liquid crystal) properties.

As an example of polymer, by alternatively mixing electron rich and electron poor bricks, the band-gap through the entire all conjugated polymer chain could be reduced. For the polymers presented below, inserting some kind of diimide moieties into the polythiophene chain, the polymers are modified to show ambipolar properties [138].

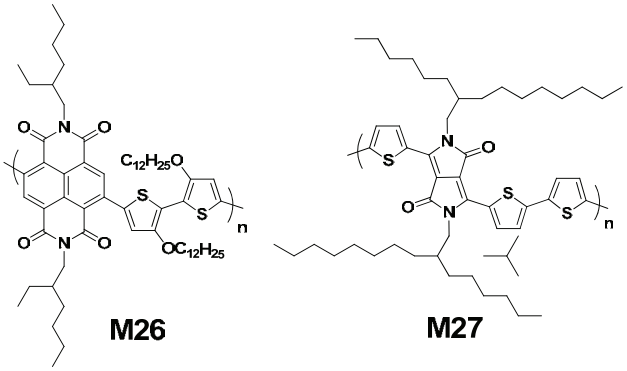

Figure 1.49 Low band-gap self-organized polymers

1.3 Design & synthesis of self-organized (semiconducting) materials

After this introduction to organic semiconductors describing as well some devices and how to determine their mobility, plus a remind concerning liquid crystals and in particular semiconducting liquid crystal materials, here we present few classical synthetic routes we can find in the literature relative to the specific materials we worked with during this PhD, namely triphenylenes, rylenes compounds and oligo-polythiophenes: note that we will insist more on this last family in a separate chapter

1.3.1 Hexaalkyl-Triphenylenes (HAT)

Two decades ago, the triphenylene derivatives became a hot research topic as a discotic liquid crystal semiconducting materials (Paragraph 1.2.4.2) and from then on, several triphenylene based molecules were designed and characterized, such as TS and TO shown in Figure 1.50.

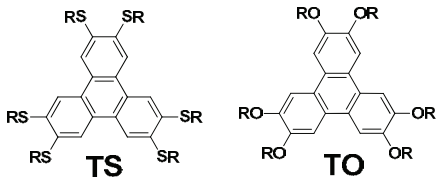

Figure 1.50 Triphenylene based discotic liquid crystal molecules

The symmetric triphenylene derivatives can be easily synthesized through an oxidative cyclization, for example, by $FeCl_3$ [139] or $MoCl_5$ [140] in acidic environment. But in order to modify or to link

triphenylene moities to other structures, a functionalization and/or desymmetrization is necessary. One of the common methods is to activate one position of the core by keeping a residual hydroxyl group to form a monohydroxy-functionalized derivative. Generally, it is realized by following one of the three existing different strategies.

(1) Multi-step

This way includes six steps of synthesis but the purifications are relatively facile and the yield of each step is also good enough [141].

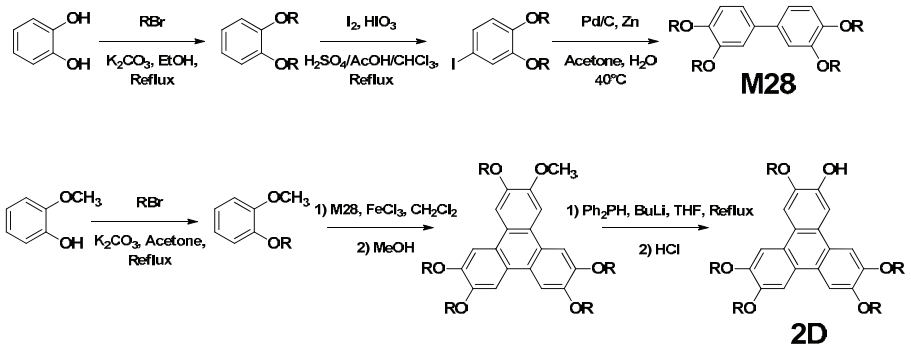

Figure 1.51 The "multi-step" method for the synthesis of monohydroxy-functionalized triphenylene

(2) Post-cleavage

With a proper ratio of the ether cleavage agent, one alkoxyl chain can be cut and render the monohydroxy-functionalized triphenylene derivative [142, 143]. This method is fast but the yield is low (with many bi or tri byproducts) and of course, symmetric triphenylene should be synthesized first.

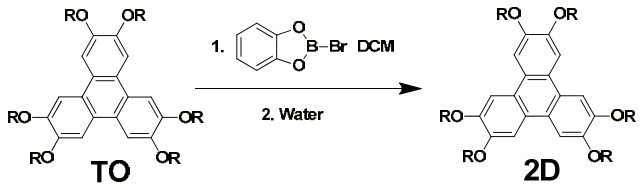

Figure 1.52 The "post-cleavage" method for the synthesis of monohydroxy-functionalized tryphenylene

(3) Statistic direct cyclization

Inspired from the cyclization reaction of the symmetric triphenylene synthesis, with a 1:2 ratio of the two primary bricks (**2B** and **2C**), the target product can also be oxidatively synthesized in one step [144]. In fact, for several cases, the two basic bricks are co-products in their preparation. Although this method's purification is a little more time consuming but in terms of global yield and number of steps, it seems advantageous to follow this way.

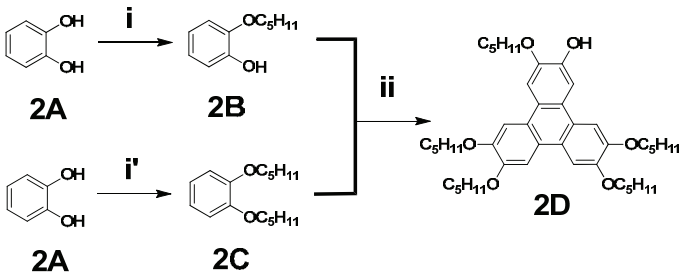

Figure 1.53 The "Statistic direct cyclization" method for the synthesis of monohydroxy-functionalized tryphenylene

Starting from this hydroxyl function, other chemical groups can be easily introduced on the triphenylene core [141], or in another word, this OH allows the triphenylene to be grafted onto other molecules [123] by, for example, a simple Williamson etherification.

1.3.2 Perylenes and other rylene related diimides

The rylene related diimides are a well known family as organic semiconducting small molecules and the perylene diimides were particularly wildly studied during the last two decades [104, 145].

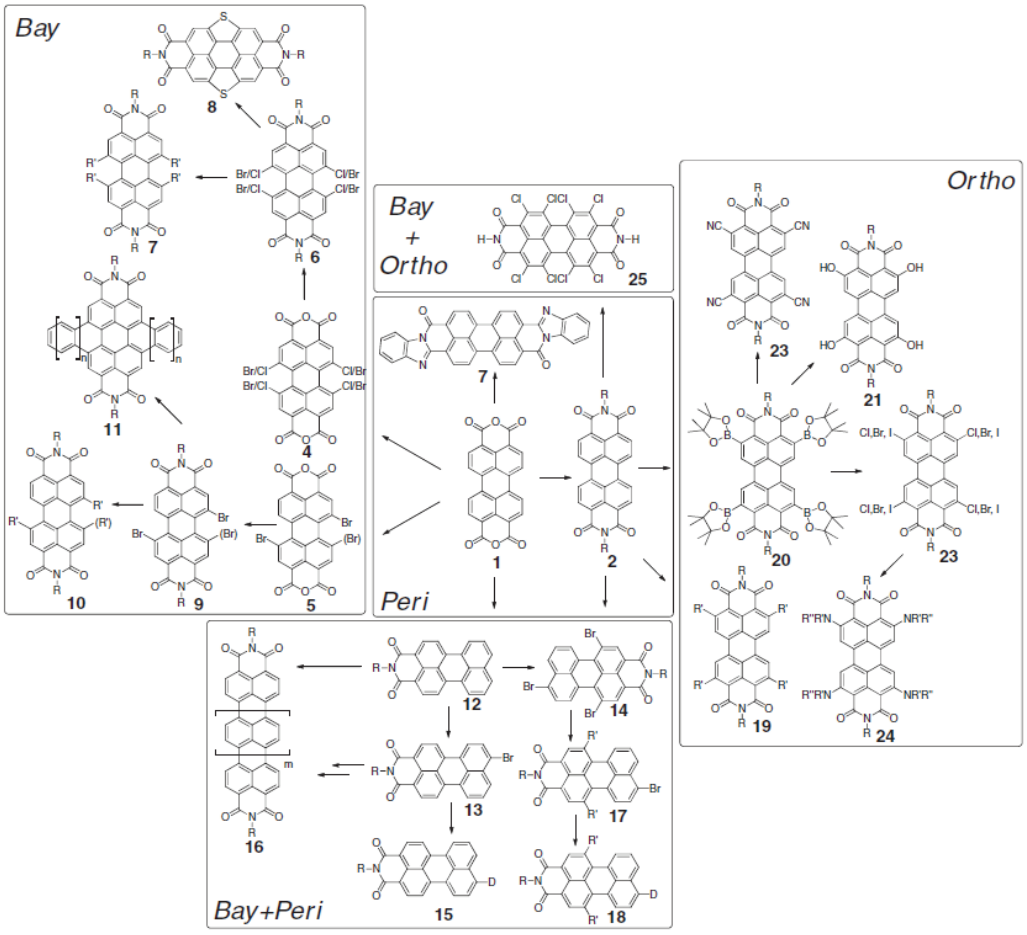

Figure 1.54 Perylene related diimides (Figure extracted from reference [146]

Basically, the chemistry of functionalization of the perylene diimides can be divided into two directions: on the core or on the imide position (Figure 1.54).

Indeed, the strong π-π stacking between two perylene aromatic cores brings it good electronic performances but also several difficulties in synthesis.

Moreover, the first problem comes from the low solubility as the conjugated cores give the molecules a great tendency to aggregate, which makes their purification very difficult. Thus, grafting branched chains onto it is a good way to increase the solubility: the core position branching is more efficient compared with the imide position because it can better decrease the π-π stacking effect. But, this core modification will also get rise to a change of HOMO/LUMO levels. Thus, chemical design can be modified in such a way that we could adjust the final opto-eletronic properties [147].

Another issue is the functionalization. As the anhydride group can be easily reacted with aliphatic amine, it is a good functional position itself and this kind of modification will not dramatically change the core property (HOMO/LUMO for example).

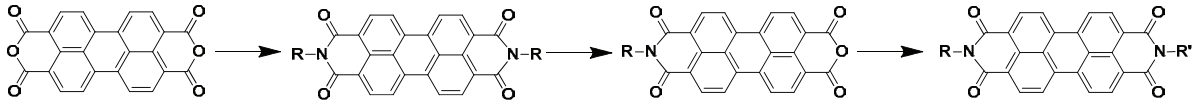

Figure 1.55 Functionalization of perylene imide position

Usually, the Perylene-3,4,9,10-tetracarboxylic dianhydride (PTCDA) is a common starting material for the perylene diimide synthesis but cannot be used directly to reach the corresponding imide-anhydride perylene: in fact, the mono-imidification cannot be controlled but directly go to the diimide derivative. So it is necessary to first isolate this diimide perylene before desymmetrization [148].

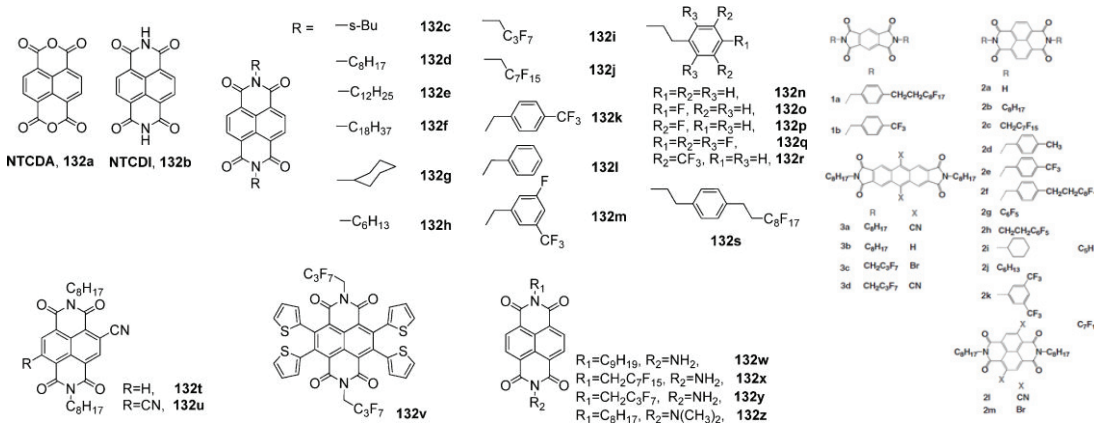

Figure 1.56 Functionalization of smaller rylene imide cores [28]

As the "smaller" members in the rylene family, pyromellitic and naphthalene diimides are also two groups of well studied semiconducting materials (usually as n-type) and the functionalization methods are similar as those of perylene, too [28](Figure 1.56).

1.3.3 Oligothiophenes and regioregular polythiophenes

1.3.3.1 Short introduction: towards regioregular materials

As seen before (see introduction), the field of organic conjugated materials and organic electronics literally exploded recently and a tremendous development took place. The vision to produce cheap (printable) electronics on a large scale triggered as well extensive researches in academia institutes and even more in industry, expecting huge markets and many emerging companies and divisions worldwide [6].

In this context, thiophene based materials are among the most important conjugated materials encountered in organic electronics. More precisely, oligo- and polythiophenes have being widely investigated and most frequently successfully implemented as active component incorporated in organic devices [6, 149-152] such as light-emitting diodes (OLEDs) and lasers, field effect transistors (OFETs), integrated circuits and solar cells (OPVs).

As an example, the most prominent and frequently used materials are doubtless poly(3,4-ethylenedioxythiophene) poly(styrenesulfonate) (PEDOT-PSS) [153-155] in conducting and hole-transport layers of OLEDs and OPVs and also the so-called regioregular or head-to-tail coupled poly(3-hexylthiophene) (P3HT) [156-158] which acts as a semiconductor in OFETs and OPVs. Both are even rather rare examples of commercially produced conjugated polymers today (Figure 1.57).

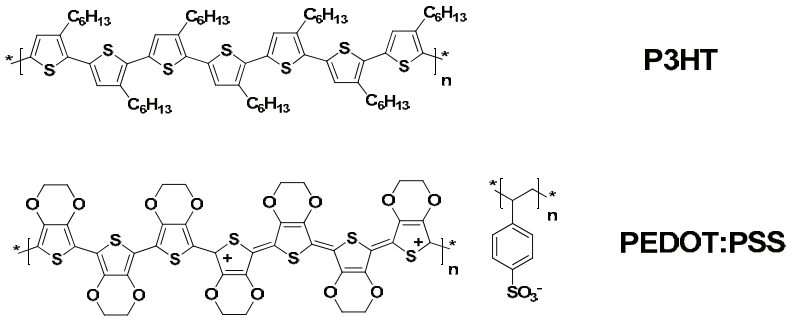

Figure 1.57 Commercially produced thiophene based conjugated polymers

On parallel to the remarkable development of these conjugated polymers with applications in the conducting and semiconducting state, a renaissance of oligothiophenes was launched in 1989 when Garnier and co-workers found that shorter conjugated oligomers such as α-sexithiophene (**6T**) can also be used as a material and active semiconductor in OFETs [159, 160]. Later, the implementation of structurally defined end-capped oligothiophenes (**EC5T–EC7T**) in OLEDs [161] was demonstrated in 1993, as well as the interest of α-quinque (**5T**) and octithiophene (**8T**) in OPVs [162] in 1995 (Figure 1.58).

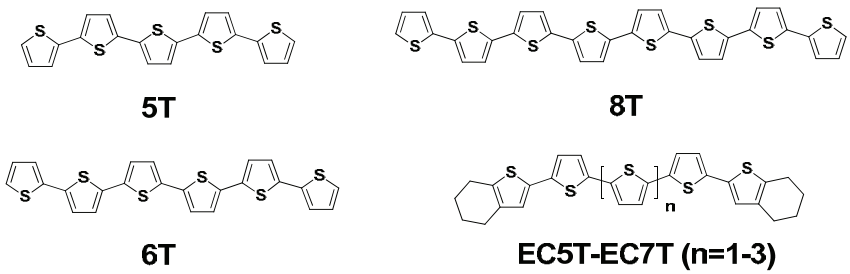

Figure 1.58 Some examples of oligothiophenes based materials widely studied in organic electronics.

Polythiophene (PT) powders were initially prepared by using protic acid, Lewis acid or electrochemical oxidative polymerizations, leading to non-regioregular polymers [163, 164] . Another way to reach PT is to take advantage of electrophilic reactions which favor sites in α position of the sulfur atom, enchaining predominantly 2,5-couplings to form an extended π-system with quasi one-dimensional delocalization: but a strong tendency to associate gives some intermolecular overlap and also renders PT insoluble and intractable. As a result, some efforts have been done by enchaining 2,4 defects but caused backbone twisting, electron localization and widening of the optical bandgap. On the other hand, eliminating couplings β to sulfur resulted in the maximization of effective conjugation length but materials with low processability were obtained by this strategy.

This is why the solubility was improved by adding ring substituents. This way following different polymerization methods, several soluble 3-alkylthiophenes were obtained with moderate [165] or high [166] molecular weight. Moreover, this increase of solubility is crucial in view of preparing low-cost and large area electronic devices.

Consequently, in the next pages we will focus essentially on the solution-processable thiophene derivatives which mean that, in this case, the problem of regiochemistry is reintroduced as it is essential.

Before to precise the different synthetic tools available to obtain regioregular PT, including the carbon-carbon bond-forming and other cross-coupling protocols [163] , it must be remembered that several regioregular structures can be observed (Figure 1.59).

Among them, the head-to-tail has unique and distinct physicochemical properties which make it the most interesting. Indeed, its architecture is preorganized for three-dimensional self-assembly, generating mesoscopic order and intrinsically large magnitude electronic properties. These include efficient two-dimensional charge transport [167, 168] with high mobility (0.1 cm^2 V^{-1} s^{-1}) [169], current density (28 mC m^{-2}) [169] and ambipolar transport [170]. Low-energy (~2.09 eV) inter-chain excitons indicating two-dimensional delocalizations are also most intense in the structure formed by HT-PT [171] , these excitons depending strongly on inter-chain order and being diminished with head-to-head (HH) coupling defects. To sum up, an improved synthesis to obtain highly regioregular HT-PT results usually in enhancing the transport properties of the final semiconducting material.

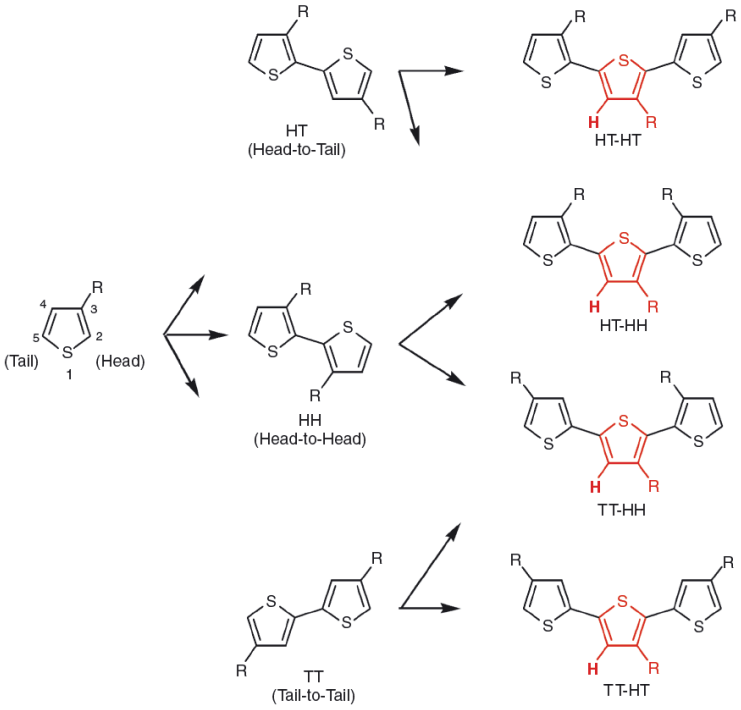

Figure 1.59 Traditional syntheses incorporate multiple regioisomers [163]

1.3.3.2 Brief survey of synthetic strategies to reach regioregular polythiophenes

With this aim, established nickel- and palladium-based cross-coupling technology was quickly adapted to the synthesis of regioregular poly(3-alkylthiophene)s. As an example, McCullough's group developed a **Kumada (organomagnesium)** coupling protocol affording <98% HT product (44-66% yield, Mn = 20000-40000, PDI = 1.4) [158]. Shortly after, Rieke's group reported a **Negishi (organozinc)** protocol (~75% yield, Mn = 24000-34000, PDI = 1.4) [172] . These were later joined by **Stille (organotin)** [173, 174] and **Suzuki (organoboron)** [175, 176] methods.

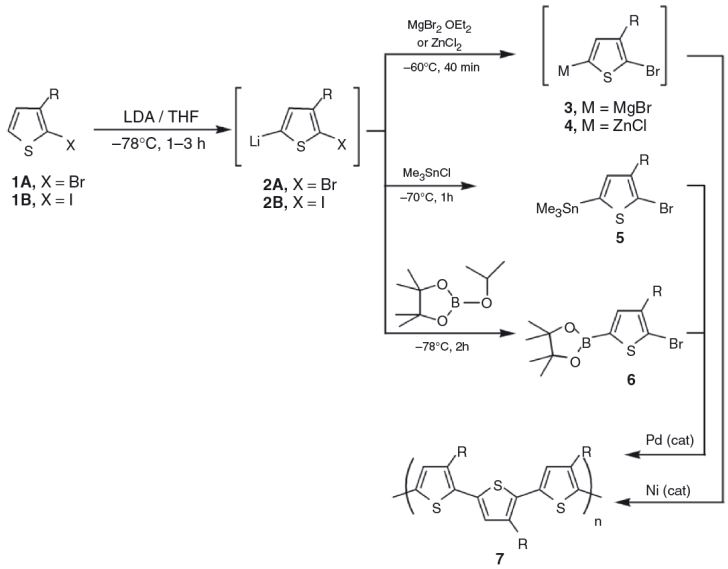

Figure 1.60 The regioselectivity and their corresponding chemistry

Two important features of these cross-coupling reactions are the selective C-C bond formation and, in some cases, the regioselectivity of the catalyst. Regiospecific conversion of an aryl halide monomer to a metal monofunctional monomer (**3–6**, Figure 1.60) followed by selective cross-coupling gives head-to-tail coupled poly(3-alkylthiophene)s. Substituents may be limited by the organolithium intermediates required to access the cross-coupling competent monomer. However, designing for post polymerization functionalization provides a partial solution [177, 178]. Telechelic synthesis [173, 179] or isolable monomers, allowing polymerization in diverse solvents, are as well notable advantages.

On the one hand, with the **Rieke's method** (Figure 1.61 upper), dibromothiophene **8** quantitatively reacts with "Rieke zinc" (Zn*) to generate a ca 9:1 or higher ratio of isomers **9** and **10** [172]. The ratio varies with the reaction conditions, temperature in particular, and in some cases, substituent bulk. Despite this, polymerization affords exclusively HT polythiophene. Rieke group demonstrated that steric congestion on the catalyst determines selectivity in the coupling reaction [172].

On the other hand, a **Grignard metathesis (GRIM)** method was developed by McCullough's group in 1999 [180, 181] (Figure 1.61, lower). This convenient synthesis uses commercially available preformed Grignard reagents to metallate the monomer quantitatively. Magnesium-halogen exchange of a Grignard reagent (alkyl, aryl) with the thienyl halide **8** generates a ca 85:15 mixture of **11** and **12** and an inert alkyl halide. Polymerization with a congested nickel catalyst and purification recovers >99% HT PT in high yields (Mn = 20 000 35000, PDI = 1.2-1.4).

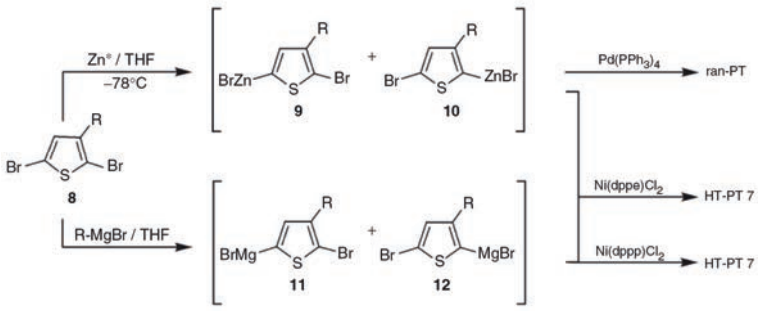

Figure 1.61 The Rieke (upper) and Grignard metathesis (GRIM) (lower) syntheses of regioregular polythiophenes

Some other non-catalytic approaches to regioregular polythiophenes rely on the discovery by Andersson and co-workers that the oxidation of some monomers can be controlled, giving high coupling selectivities. For example, phenyl-substituted thiophene monomers can be regiospecifically polymerized by a slow addition of $FeCl_3$ that maintains a low concentration of radical during the whole process [182] .

But as in our work and study we essentially choose the GRIM strategy, it is necessary to detail the mechanism involved in this specific polymerization.

1.3.3.3 Mechanism of GRIM, a nickel-mediated cross-coupling polymerization

Comparing the well understood bimolecular cross-coupling, the mechanism of polymerization of thiophenes has some very different characteristics. For example, the HT regioregularity increases with Mn for both regioirregular polythiophene (irPT) and regioregular polythiophene (rrPT) [183].

In fact, it is agreed that for a nickel-phosphine complex-catalyzed Grignard coupling reaction with thiophene derivatives, the mechanism follows several steps (1) oxidative addition of an aryl halide to a metal-phosphine catalyst, (2) metathesis (transmetalation) of the catalyst complex with an organometallic reagent to generate a diorganometallic complex and (3) reductive elimination of the coupled product either with regeneration of the metal-phosphine catalyst or concurrent oxidative addition of an aryl halide [184]. More precisely, effective syntheses based on organomagnesium, organozinc, organoboron, organotin or organosilane reagents have been demonstrated [185].

Moreover, it was evidenced that in a GRIM synthesis of a regioregular poly(3-hexylthiophene) (reP3HT), the polymerization proceeds by a chain growth mechanism. Indeed, the conversion vs Mn and conversion vs Mw/Mn plots indicates that an initiator exists [186]. Furthermore, with the ***living*** nature of nickel-mediated cross-coupling polymerization of 3-alkylthiophenes, the degree of polymerization (DPn) increases with monomer conversion and this DPn can be predicted by controlling the molar ratio of the monomer to the nickel initiator [187].

As a consequence and due to this quasi-living processes, the rrPT can be obtained with low polydispersities [188] and furthermore, by adding a new portion of a different monomer at the end of the first polymerization, a further increase in the molecular weight is observed, allowing this way a nice opportunity to obtain block copolymers [189] (Figures 1.62).

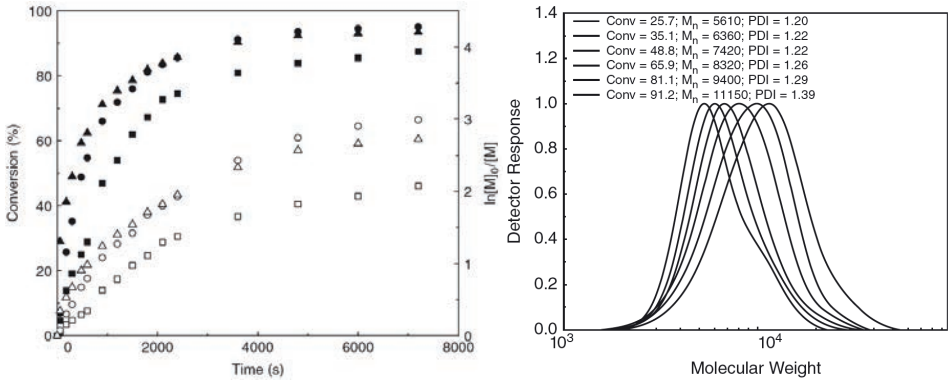

Figure 1.62 **Left** *Conversion (filled symbols) and logarithm of monomer concentration (open symbols) vs time plots for 2-bromo-3-hexylthiophene polymerization at different concentration of Ni(dppp)Cl_2 initiator (23–25 °C); $[M]_0$ = 0.075 mol L^{-1}: (■, □) $[M]_0$:[Ni(dppp)Cl_2] = 136:1; (●, ○) $[M]_0$:[Ni(dppp)Cl_2] = 57:1; (▲, Δ) $[M]_0$:[Ni(dppp)Cl_2]=49:1.* **Right** *GPC traces for 2-bromo-3-hexylthiophene polymerization (23–25 °C); $[M]_0$ = 0.075 mol L^{-1}; $[M]_0$:[Ni(dppp)Cl_2] =57:1. The McCullough method was used for polymerization of 2-bromo-3-hexylthiophene* [187]

Looking into details concerning the mechanism, McCullough's group proposed a mechanism of π-complexation of the nickel(0) with the thiophene growing chain, forming an associated pair that limits

polymerization to one end of the polymer chain (Scheme 2.4). The first step in this mechanism is the reaction of 2 equiv. of 2-bromo-5-chloromagnesium-3-alkylthiophene monomer (**1**) with Ni(dppp)Cl_2 generating a bis-organonickel compound (**2**), which undergoes reductive elimination to form an associated pair of the 5,5'-dibromobithienyl (tail-to-tail coupling) and Ni(0) ([**3**·**4**]), Figure 1.63). It has been proposed that this associated pair is formed by coordination of 1,3-bis(diphenylphosphino)propanenickel(0) to the thiophene ring in an η^2 or η^4 bonded fashion (Figure 1.64). The dimer undergoes then a fast oxidative addition to the nickel(0) center, generating a new organonickel compound. In other word, the polymer chain growth occurs by insertion of one monomer at a time, in which the Ni(dppp) moiety is incorporated into the polymer chain as an end group (polymer **5** in Figure 1.63). Moreover and according to the proposed mechanism, only one structural defect (one tail-to-tail coupling) per polymer chain is generated during the catalytic cycle.

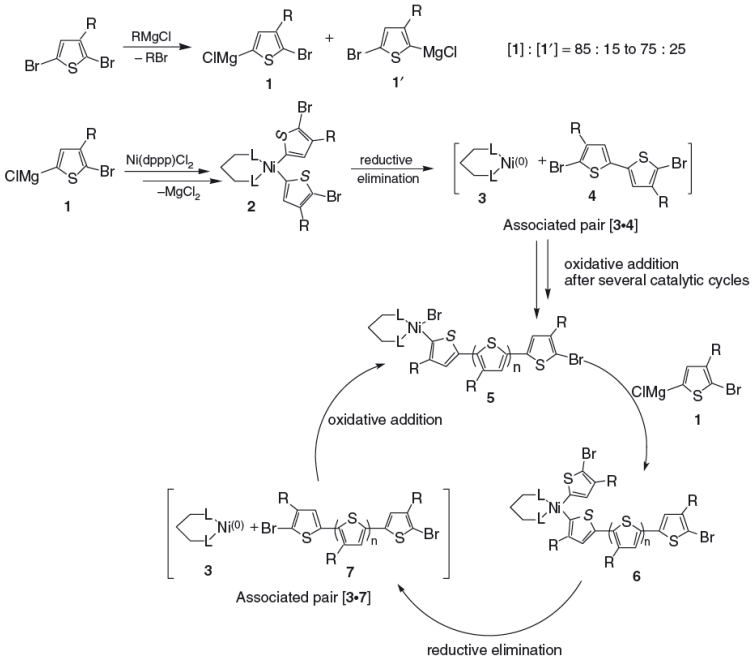

Figure 1.63 Mechanism of Grignard metathesis method for the synthesis of regioregular poly(3-alkylthiophene) [188].

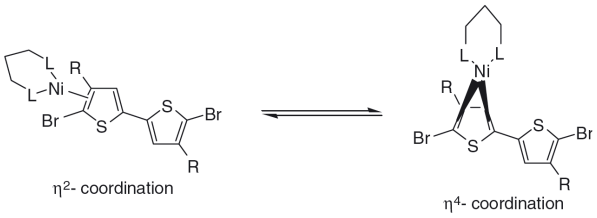

*Figure 1.64 Proposed mechanism for the binding of 5,5'-dibromobithienyl to a low-valent nickel moiety Ni(dppp)^0 (formation of the associated pair [**3**·**4**] in Figure 1.63)* [163]

Beside the McCullough mechanism, Yokozawa and co-workers proposed another possible explanation [177]. In their mechanism, the oxidative addition of the polymer chain occurs selectively, being kinetically slower or thermodynamically less stable for the monomer than for the growing

polymer chain. This effect could be due to a decreased electron density of the thiophene ring on the polymer chain [163] .

1.3.3.4 Polythiophenes chemical modification

Poly(3-alkylthiophene)s are chemically robust, withstanding strong reductants including borane [189] and $LiAlH_4$ [190]. However, the electron-rich backbone can be readily functionalized by oxidative methods. Li and co-workers exploited this to replace the 4-proton with Cl, Br or NO_2 functionality [191, 192] , thus providing the possibilities for the **chain functionalizations**.

For the **end functionalization**, McCullough's group reported a versatile and simple method for *in situ* end-group functionalization of regioregular poly(3-alkylthiophene)s using the GRIM method. This method eliminates the need to synthesize and isolate a polymer bearing predominately H/Br end groups. In the mechanism of the polymerization, the nickel catalyst acts as an initiator and therefore at the end of the reaction, the rrPT chain will be still bound to the nickel initiator, along with a Br group and the phosphine ligand (Figure 1.65).

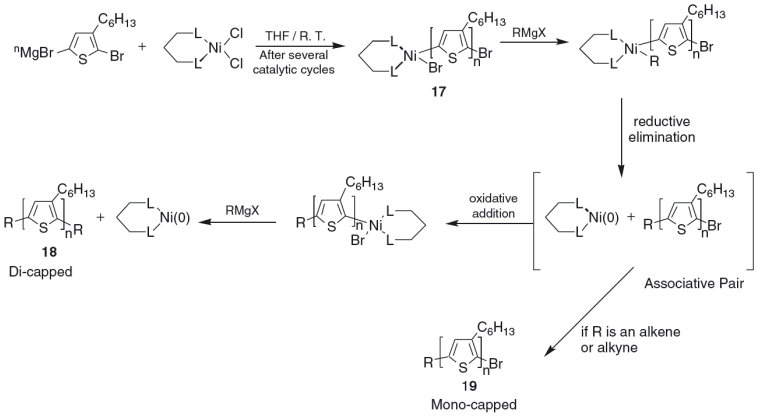

Figure 1.65 Proposed mechanism of end-capping of regioregular poly(3-alkylthiophene) synthesized by GRIM [193]

In addition, this *in situ* chain end functionalization of nickel terminated polymers is perhaps the strongest argument that proves the 'living' nature of GRIM polymerization of 3-alkylthiophenes. Regioregular poly(3-alkylthiophene)s with various end groups are now readily available [193, 194].

Some GRIM tolerated functional groups can be introduced directly from the monomer and then we can talk about **substituent modification**. For example, from the halogenated (often terminal brominated) alkyl chain, various groups can be grafted [123, 124, 177, 195] or can be transformed to continue the derivatization [177, 196, 197]. Another example is that the esters are also tolerated by GRIM and this provides a complementary route to the carboxylic acid [198] (Figure 1.66).

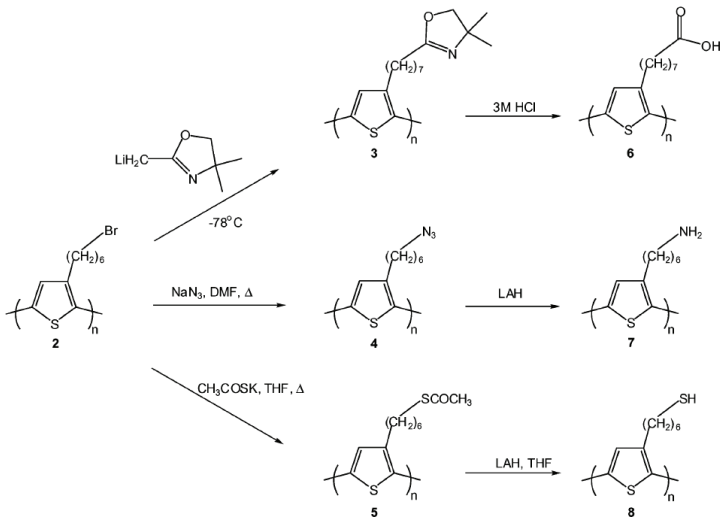

Figure 1.66 Post-polymerization Functionalization of Poly(3-(6-bromohexyl)thiophene) [177]

1.3.3.5 Polymer purification and fractionation

Note that inorganic contaminants may be present in the regioregular polythiophenes synthesized via crosscoupling polymerization protocols. An important stage of purification is consequently required.

More precisely, the crude product of polymerization may contain impurities including inorganic salts, from the catalyst or coupling byproducts, phosphines or other ligands, monomer or low molecular weight oligomers. Bad consequences include alteration of the absorption spectra and the decrease of electronic properties, quenched fluorescence, modification of thermal behavior and ash in the elemental analysis [199-201].

At the same time, it was evidenced that careful purification to a metal content of 10 ppm or less optimizes electronic properties, allowing balanced ambipolar transport in transistors [170] .To this aim, precipitation of crude regioregular polythiophenes from chloroform into methanol, a common purification technique, can occur too rapidly to remove these impurities suitably: dilute solutions and an extended precipitation time are consequently better and crucial to obtaining analytically pure material by this method [201].

Moreover, soxhlet extraction by increasingly ‘good’ solvents conveniently separates oligomers and narrows the molecular weight distribution of fractions from crude, polydisperse samples. Yamamoto *et al.* reported that the solubility of regioregular polythiophenes increased in the following solvent order: methanol < acetone < hexane < dichloromethane < tetrahydrofuran < xylene < chloroform [202]. Successive extractions gave also fractions with increased molecular weights and regioregularity and red-shifting visible absorption λ_{max} [203] . This effect was seen regardless of polymer regiochemistry [163].

Finally, the polythiophenes can also be purified with the preparative GPC [204-206] technique. Based on the hydrodynamic radius (or "the size of the polymer chain"), this can be sometimes even more accurate than the Soxhlet fractionation.

1.3.3.6. Characterizing (regioregular) polythiophenes

In order to characterize these polymers, we use to take advantage of several known experimental techniques devoted to determine the chemical structure and physical-chemical behavior of organic materials, but with some specificities related to this family of regioregular polythiophenes, specificities that we point out and describe quickly below.

NMR spectroscopy

As most of the substituted polythiophenes can be dissolved in common solvents, solution NMR became a very efficient method to characterize the chemical structure and stereochemistry (molar mass, regioregularity, etc). In the NMR spectroscopy, the details of the chain microstructures can hardly be explained by a single coupling motif but a sequence of unities [207] . Commonly studied ^{1}H and ^{13}C nuclei proved sensitivity not only to the connectivity within the monomer ring but also to neighboring ring orientation and substitution. The proton NMR chemical shifts of the polythiophene main chain (aromatic rings) are listed in Table 1.1. Alkyl protons are less sensitive to perturbations of the π-system and give broad, overlapping signals [158].

Regioregular types	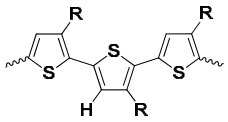 HT-HT R=C8	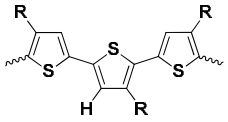 TT-HT R=C10	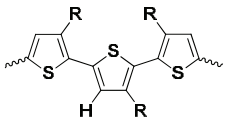 HT-HH R=C10	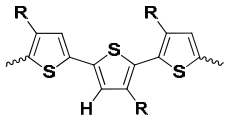 TT-HT R=C10
H (δ ppm)	6.98	7.00	7.02	7.05

Table 1.1 ^{1}H chemical shifts (ppm, $CDCl_3$) of configurational triads in poly(3-alkyl)thiophenes [163]

Analysis of chain ends provides also important information on functionality, as well as an accurate determination of molecular weight. In particular in our case, with the GRIM method, we focus on the polymer chain growth from a homo-coupled dimer giving chains terminated by a tail-to-tail (TT) dyad. The α-CH_2 peak of the TT terminal ring is thus interesting as it shifts upfield by ~0.2 ppm vs that of internal rings. In addition and because only one defect is enchained, this provides a distinct marker for the determination of the absolute molecular weight of regioregular poly(3-alkylthiophene)s (comparing the H/Br- and H/H-terminated chains shows that the former shifted upfield by a further 0.05 ppm, allowing end-group discrimination (Figure 1.67).

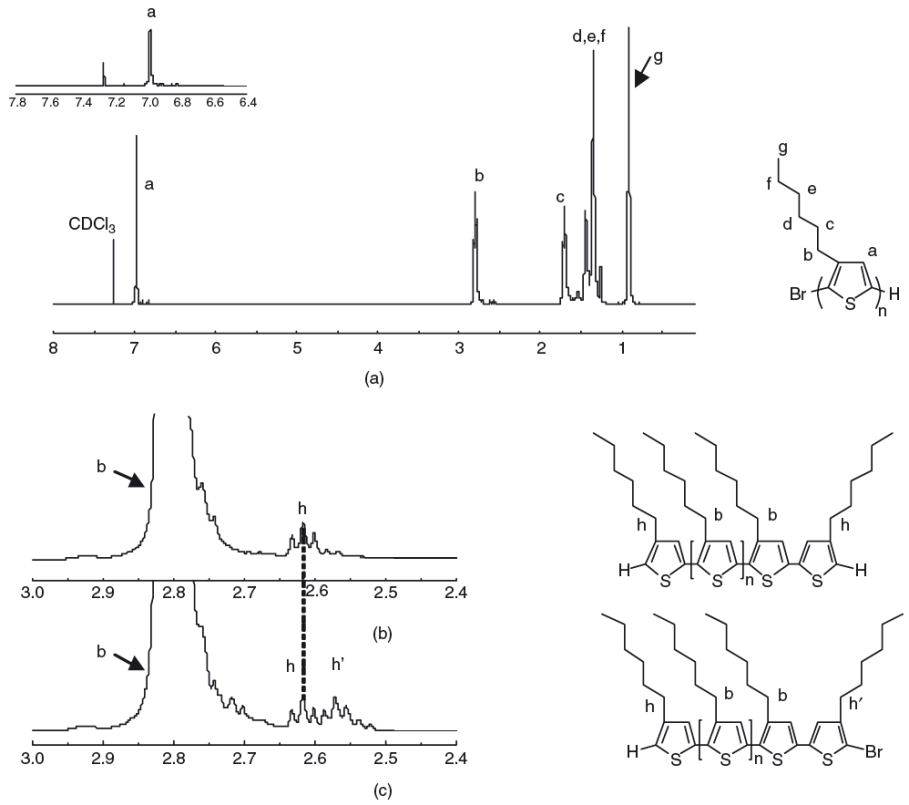

Figure 1.67 ^{1}H NMR (500 MHz) spectra of (a) rr-poly(3-hexylthiophene) H/Br terminated; (b) expansion of rr-poly(3-hexylthiophene) H/H terminated; and (c) expansion of rr-poly(3-hexylthiophene) H/Br terminated.[188]

In Chapter 4 and Chapter 5, the polymers' (or polymer precursors') ^{1}H NMR molar weight were calculated based on comparing the integrations between the terminal α-CH_2 peak (h)with the main peak (b) (Figure 1.67). But this kind of end-group discrimination also happens on the aromatic protons, Table 1.2 shows the thiophene proton chemical shifts of different terminal configurations.

	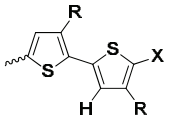 HT R=C6	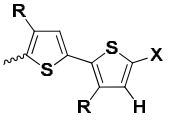 TH R=C6	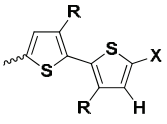 HH R=C6	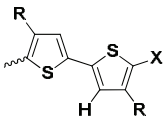 TT
H (δ ppm)	6.90	7.16	7.3	-

Table 1.2 ^{1}H chemical shifts (ppm, $CDCl_3$) of terminal rings in poly(3-alkyl)thiophenes [163]

UV-Vis spectroscopy

The extent of π-electron delocalization within the conjugated backbone is conveniently probed by UV-Vis spectroscopy. Intensely absorbing π →π* transitions, correlating with the HOMO-LUMO gap, provide a qualitative measure of conjugation length in both neutral and oxidized species [208]. Defects, including HH couplings, that limit accessible low-energy conformers reduce the effective conjugation length and blue shift the absorption maxima. The degree of solvation ranging from extended chains through collapsed compact (coiled) structures, or aggregates, to the solid-state likewise has profound

spectroscopic consequences. Study in each regime reveals behavior enhancement in regioregular polythiophenes while it is attenuated or absent in regioirregular samples [163] .

MALDI-TOF mass spectrometry

Matrix-Assisted Laser Desorption-Ionization Time-Of-Flight Mass Spectrometry (MALDI-TOF-MS) is a powerful tool for the analysis of molecular weight distributions and end-group analysis of polythiophenes [209]. Absolute molecular masses can be determined (Figure 1.68), independently of the polymer structure, whereas gel permeation chromatography (GPC) gives molecular weights relative to a calibration standard. GPC correlates the hydrodynamic volume of the randomly coiled polymer chains with polymer molecular weight and is commonly referenced to polystyrene. However, conjugated polymer systems such as poly(3-alkylthiophene)s, adopt a more rod-like conformation in solution, leading to an overestimation of the molecular weight (Figure 1.69) [210].

Narrow polydispersity samples obtained by fractionation of regioregular poly(3-hexylthiophene)s were compared by MALDI-TOF-MS and GPC, with the latter giving Mw values 1.5–2.0 times higher. Polydispersities were often identical; though occasionally the GPC value was lower [209].

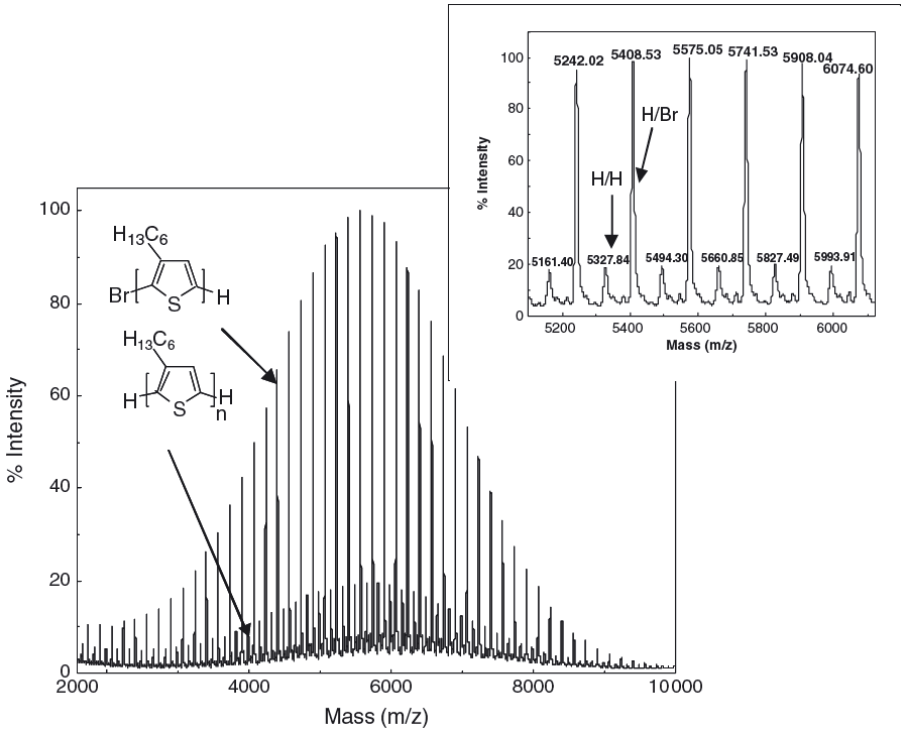

Figure 1.68 MALDI-TOF mass spectrum of rrP3HT synthesized by the GRIM method Á(Mn = 5476 g mol^{-1}; Mw = 5930 g/mol^{-1}; PDI = 1.08) [209]

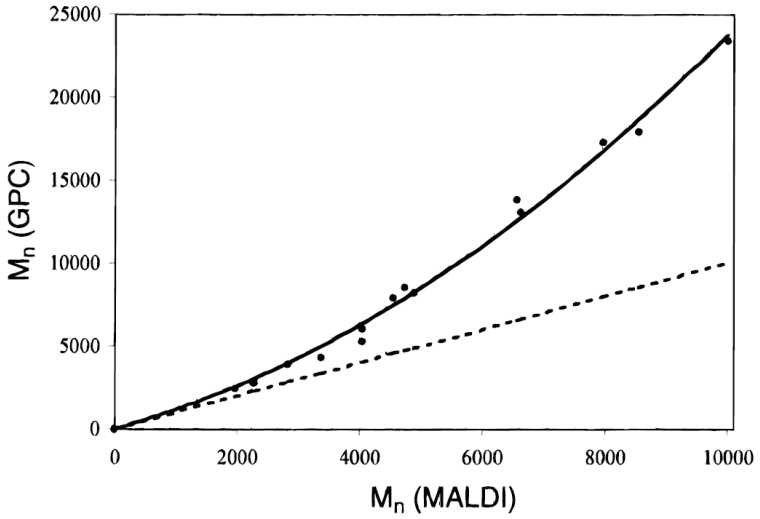

Figure 1.69. Relationship of Mn calculated by MALDI-TOF and GPC. The dotted line serves as a reference (slope =1) [209]

X-Ray studies

To understand the solid-state structure-property relationships of polythiophenes, the X-Ray analysis has been used extensively [124, 211]. Small substituents give little effect on regiochemistry while the orientation of larger substituents can dramatically affect the unit cell dimensions [212]. The prevalent packing model derives from a lamellar structure with rod-like main chains arranged in parallel and alkyl substituents between (Figure 1.70.a and 1.70.b).

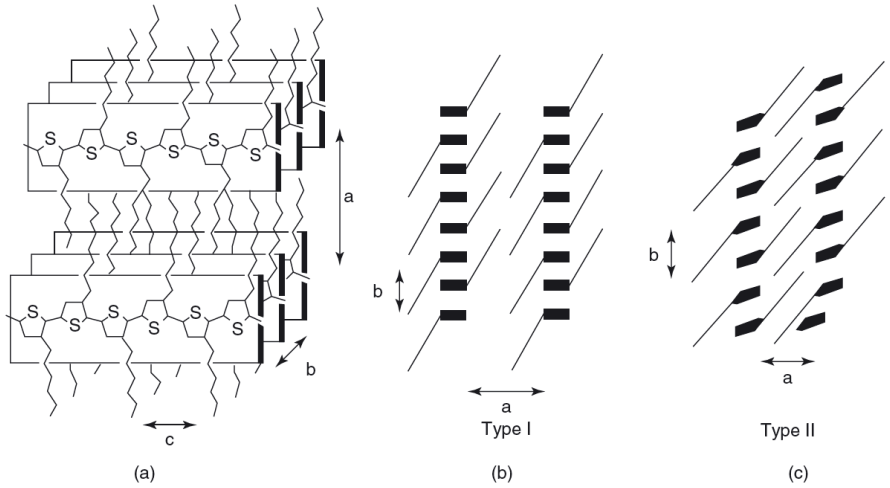

Figure 1.70 Structure of regioregular poly(3-hexylthiophene): (a) orientation of lamellae; (b) common (hightemperature) form; (c) metastable interdigitated polymorph

This form, designated type-I, packs π-systems face-to-face, 3.8–3.9 Å apart [213-215], and staggered within the a-c molecular plane to allow nesting of side-chains. Viewed down the *b* axis (Figure 1.70.b), a similar staggered offset makes the unit cell dimension equal to twice the π-stacking distance and minimizes eclipsing interactions in the stack. The head-to-tail architecture organizes alkyl substituents much like in a hexagonally close-packed solid alkane or polyethylene, promoting highly crystalline

regions with *trans*-planar alkyl conformations [216]. Variations in alkyl length give corresponding expansion or contraction of the unit cell along the *a* axis, with the other dimensions being minimally perturbed [217]. Electron diffraction patterns of crystalline microwires are consistent with the type-I motif, orienting the *b* axis parallel with the long dimension of the "wire" [218, 219]. Directionally crystallized rrP3HT, in contrast, has a fibrous morphology with the stacking axis rotated 90°, orienting the *c* axis parallel to the long axis of the fiber [220].

It is useful to note that the backbone and alkyl chains have competing organizational tendencies, leading sometimes to the observation of polymorphism [221-225]. As an example, a metastable modification, designated type-II, was characterized by Prosa et al. (Figure 1.70.c) [216]: in this phase, alkyl chains are more fully interdigitated, indicating that the side-chain crystallization drives the structure. Additionally, the phase concurrently forms with type-I (Figure 1.70.b) during solvent casting of films. Melting destroys this order while subsequent solidification in the absence of solvent precludes its formation. Moreover, Causin et al. determined that the type-II polymorph could be formed reproducibly by careful crystallization near the melting temperature. On the contrary, heating to the necessary temperatures to melt the side-chains causes reversion to the type-I structure upon cooling [226].

Thermal analysis (DSC, TGA)

Substituted polythiophenes are comb-like polymers, with both backbone and side-chains independently capable of crystallization. This allows complex behavior from competing processes and polymorphic behavior has been noted [202, 216, 221, 223, 227] . DSC data can be combined with the temperature dependent X-ray diffraction to study the different mesophases (mesophases transitions). For example, generally, the low-temperature transitions come from the alkyl substitutions (side chains) and high-temperature transitions are designated to "backbones". Some additional transition (glass temperature) can be observed in rrP3AT, transforming a glassy crystal to a plastic crystal with different inter-ring torsion. This was dubbed a twist-glass transition [228].

Finally, other characterization methods can be cited but were not used during this work, such as solid-state NMR [163], solid-state UV–Vis spectroscopy [229, 230], solid-state vibrational spectroscopy (IR, Raman), a few microscopy techniques (AFM, STM) [124, 231] and light scattering (for studying aggregates) [232].

1.3.3.7 Parameters influencing charge carrier mobility in rrPT

As discussed in the previous paragraphs, the applications of organic semiconductors lay mainly in thin-film transistors, ranging from flat-panel displays to smart cards and electronic identification tags [233]. In particular, solution-processable organic semiconductors could make it easy and cost-effective to fabricate large-area thin films using established printing technologies [234]. Moreover, for organic semiconductors to be valuable in most practical applications, field-effect mobilities of greater than 0.1

$cm^2\ V^{-1}\ s^{-1}$ (with on/off ratio greater than 10^6) are needed for the driving circuits in liquid crystal displays [42], and mobilities approaching that of hydrogenated amorphous silicon (0.5–0.1 $cm^2\ V^{-1}\ s^{-1}$) are desirable. This is the reason why before to present our results, here we conclude our discussion on the importance of controlling several parameters to reach high charge carrier mobility of polythiophenes in OFET configuration (for more about OFET, see Paragraph 1.1.5.4).

About two decades ago, the first relatively high mobility was obtained from rrP3AT as 10^{-2} [235], and recently, much higher mobilities were achieved as 0.2 $cm^2\ V^{-1}\ s^{-1}$ [163]. As expected, regioregularity is critical for good electrical properties and consequently riP3AT has a much lower mobility than rrP3AT, typically ranging between 10^{-4} and 10^{-5} $cm^2\ V^{-1}\ s^{-1}$ [236-238].

In particular, the rrP3ATs are widely used to study the factors which will influence the carrier mobility, such as processing conditions [235, 239, 240], surface treatment [241] and molecular weight [242] and the polymer structure and morphology can be correlated with the carrier mobility results. Generally, the best mobilities are obtained using relatively high molecular weight rrP3ATs (Mn >25 kDa by GPC) under slow evaporating (annealing) conditions on hydrophobic substrates. These conditions promote self-organization of rrP3ATs with the π-π stacking direction perpendicular to the substrate surface, and also good interconnectivity of crystalline domains [242].

Another important factor that influences mobility in conjugated polymers is charge carrier density: mobility tends to increase with charge carrier density as traps become filled [243]. Furthermore, when the charge density is sufficiently high, conjugated polymers can reach the metal-insulator boundary, where very high conductivities are expected [244, 245]. Consequently, the highest field effect mobility ever reported for HT-PHT was obtained using a high-capacitance polymer-electrolyte dielectric that could induce a very large hole density into rrP3ATs.

The influence of the side chain length was studied as well by several groups and the results are summarized in Table 1.3 [163]. It is believed that the alkyl side-chains act as a barrier to charge transport between π-conjugated main chains and shorter side-chain length results in a higher π-stacking density in the charge transport region, leading to higher mobility [246]. In different configurations, it is also possible to find that the hexyl side-chain is optimal for charge transport due to better self-organization than other polymers in the series [247]. So when the mobility values are compared, the different configurations must be taken into account.

Polymer	**Mobility ($cm^2\ V^{-1}\ s^{-1}$)**		
	Kaneto et al	Babel and Jenekhe	Park et al.
rrP3BT	1×10^{-2}	1×10^{-3}	1×10^{-2}
rrP3HT	3×10^{-3}	1×10^{-2}	5×10^{-3}
rrP3OT	-	3×10^{-4}	1×10^{-5}
rrP3DDT	8×10^{-4}	3×10^{-5}	-

Table 1.3 Summary of previous work on effect of side-chain length on field effect mobility for rrP3ATs [163]

Another issue with rrP3HT is its low on/off ratio when exposed to air, which is attributed to its low ionization potential (IP ≈ 4.8 eV). Indeed, although high on/off ratios could be obtained under inert conditions or after "dedoping" the polymer film under vacuum, on/off ratios quickly decrease when the polymer is exposed to ambient air. In fact, both water and oxygen are responsible for the lower on/off ratio, moisture being the dominant factor [248]. Of course, high on/off ratios and good stability can be obtained if rrPHT is kept under an inert atmosphere [234, 249].

Thus, the environmental stability of rrP3ATs is also an issue to be considered. As its ionization potential is relatively low [248], the rrP3ATs are susceptible to be oxidized in wet air [250]. Furthermore, polythiophenes can undergo photochemical reactions and therefore must be protected from the combination of light and oxygen [251]. But interestingly, the environmental stability is quite dependent on the synthesis methods and the different configurations of devices [252-254]. By shortening the conjugated length of the polymer or decreasing the electron density of the backbone, the ionization potential can be increased and in this way, the oxidative stability can be increased (also to reduce the off-state current) [255] .

Eventually, concerning the degradation in OFETs, it is suggested that ozone, not oxygen, is the real cause of polymer degradation [256]. In the absence of light, oxygen was not a strong dopant, instead, ozone was found to be a strong dopant for polythiophene polymers. These results explain the variations in stability reported in the literature and suggest that environmental stability studies should be conducted in controlled environments in order to define realistic limits to stability.

To conclude, developing conjugated polymers with higher mobilities than rrP3HT seems difficult. To date, poly(2,5-bis(3-hexadecylthiophen-2-yl)thieno[3,2-b]thiophene) (PBTTT) is the only conjugated polymer that has a higher mobility than rrP3HT, its high performance being attributed to its highly organized morphology obtained after annealing on silanized (OTS) substrates [117]. As a consequence, more and more efforts are made to achieve a well controlled modification on both the polymer chain and its substituents: the present work deals with these objectives.

1.4 Aim of this work

In this work, we were interested in designing and preparing different self-organized semiconducting architectures in which it could be possible to inject and transport both holes and electrons. Our approach is based on liquid crystalline materials incorporating different kind of electron-donor (p-type) and electron acceptor (n-type) π-conjugated systems in a unique molecular or macromolecular architecture. We expect that these ambipolar materials could present a spontaneous nanosegregation of p-type and n-type entities in bulk, leading to well defined distinct conductive channels for each type of charge carriers.

Concerning the molecular approach, we propose to design two families of small molecular donor-acceptor liquid crystalline dyads or triads in combining either p-type and n-type discotic derivatives or p-type and n-type calamitic derivatives. This strategy should lead to ambipolar columnar or lamellar nanostructured materials presenting respectively one-dimensional or two-dimensional charge transport as illustrated in Figure 1.71.

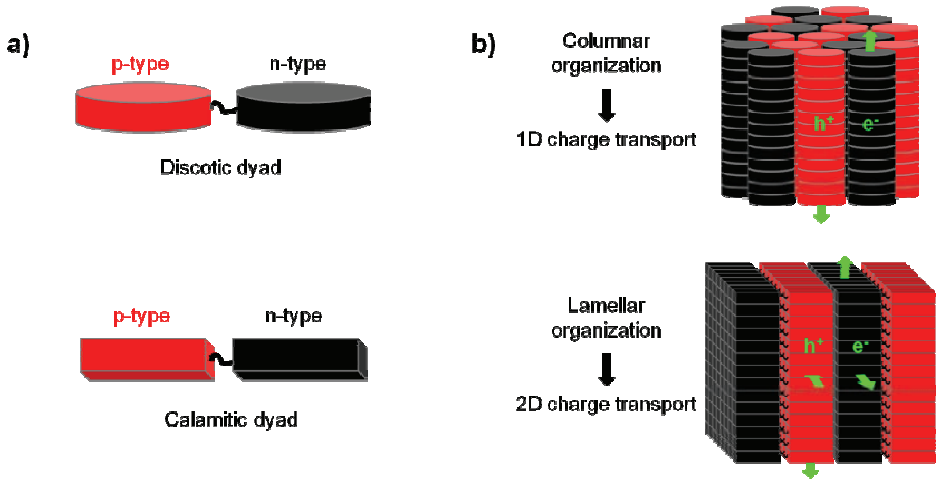

Figure 1.71: a) schematic representation of ambipolar discotic and calamitic dyads. b) Schematic representation of self-organization obtained with discotic and calamitic dyads and expected ambipolar charge transport properties.

The family of discotic donor-acceptor molecules will be based on conventional discotic semiconductors such as triphenylene derivatives as p-type building blocks and perylene or naphthalene derivatives as n-type building blocks. The chemical structures of these ambipolar discotic dyads and triads are given in Figure 1.72.a, and they boil down to one or two alkoxytriphenylenes linked with a perylene or naphthalene diimide by an alkyl chain spacer. This family will be described in the chapter 2 which will focus on the design, synthesis and characterization of these different materials.

The family of calamitic donor-acceptor molecules will be based on usual calamitic semiconductors such as terthiophene derivatives as p-type building blocks and pyromellitic derivative as n-type building blocks. The chemical structures of these ambipolar dyads are given in Figure 1.72 b, and they boil down to an end-capped terthiophene moiety linked with an end-capped pyromellitic diimide

moiety by an alkyl chain spacer. This family will be described in the chapter 3 which will focus on the design, synthesis and characterization of these materials.

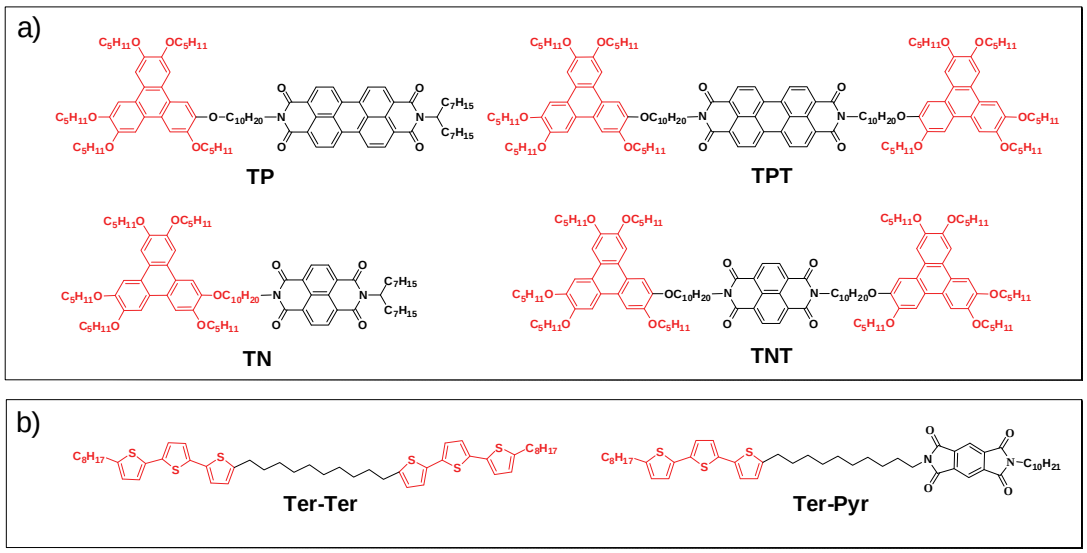

Figure 1.72: a) Chemical structures of discotic donor-acceptor molecule family studied in chapter 2. b) Chemical structures of calamitic donor-acceptor molecule family studied in chapter 3.

Concerning the macromolecular approach, we propose to design a new family of donor-acceptor liquid crystalline side-chain polymer combining a p-type backbone and n-type side-groups in a unique self-organized polymeric architecture (Figure 1.73.a). We expect that this kind of polymer will present a spontaneous phase separation at the nanoscale of the two covalently linked π-conjugated systems in self-organizing in a lamello-lamellar nanostructure, which could produce distinct conductive channels with two-dimensional charge transport properties in the lamellae of backbones and side groups as illustrated in Figure 1.73.b.

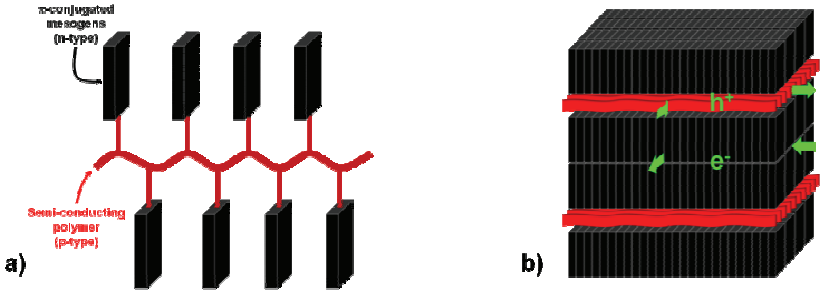

Figure 1.73: a) schematic representation of donor-acceptor liquid crystalline side-chain polymer combining a p-type backbone and n-type side-groups in a unique polymeric architecture. b) Schematic representation of expected self-organization with donor-acceptor liquid crystalline side-chain polymer and of expected ambipolar charge transport properties.

This architecture was inspired by recent works developed in our laboratory [123] and relating to the design and elaboration of a model side chain liquid crystal semiconducting polymer where: (i) the backbone was a π-conjugated polymer and (ii) the side groups were π-conjugated discotic mesogens. More precisely, this polymer was formed by polythiophene backbone and triphenylene-molecule side

groups (Figure 1.74.a). A supramolecular self-assembling of this p-type semiconducting polymer was observed where the backbone and columns were parallel to each other in an intertwined lamello-columnar liquid-crystal structure consisting in the alternation of rows of columns and backbone sub-layers (Figure 1.74.b).

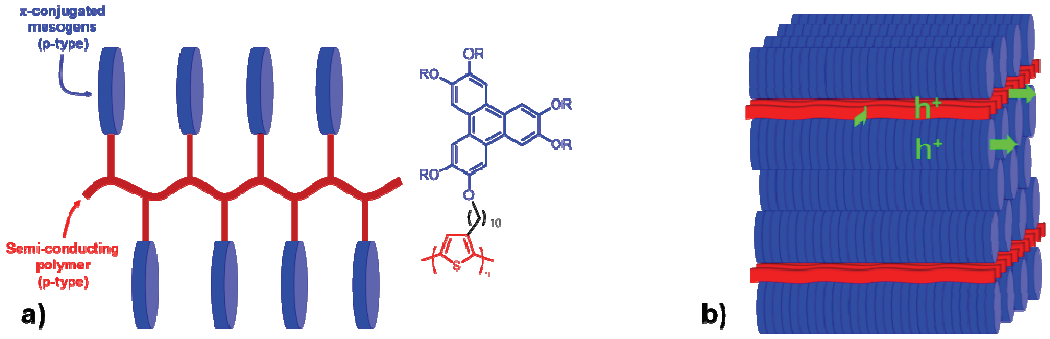

Figure 1.74: a) schematic representation of the model liquid crystalline side-chain polymer combining a p-type backbone and p-type discotic side-groups in a unique polymeric architecture. b) Schematic representation of expected self-organization with this liquid crystalline side-chain polymer and of expected charge transport properties.

In this context, we will first develop and complete the previous work on the model liquid crystalline side-chain polymer in studying and evaluating the influence of the controlled dilution of the mesogenic side groups (i.e. the degree of polymer lateral substitution) on the supramolecular organizations and on charge transport properties. That is why in the chapter 4, we will prepare and study the self-organization properties in bulk and in thin films of a homopolymer comprising triphenylene side groups on every thiophene units with an alternated copolymer with thiophene/triphenylene ratios of 2:1 (Figure 1.75). In addition, the self-organization properties will be also correlated to the charge transport properties of these materials studied in field effect transistor configuration.

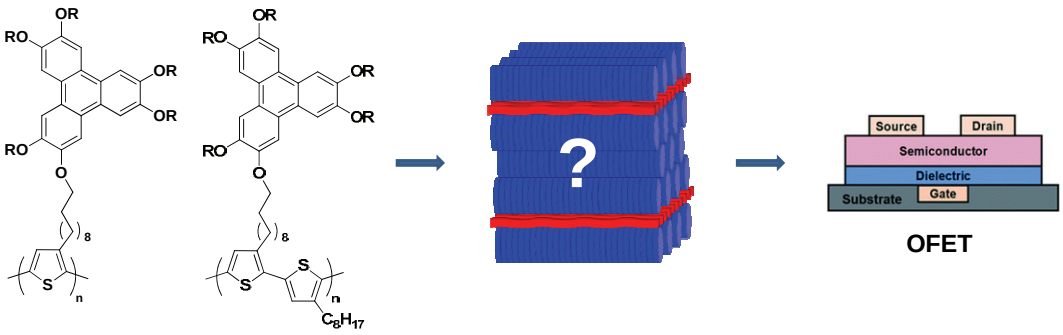

Figure 1.75: Chemical structures of the homopolymer and the alternated copolymer with thiophene/triphenylene ratios of 2:1 studied in chapter 4.

Then, taking advantages of the previous study on model liquid crystalline side-chain polymers (homopolymer and alternated copolymer), we will present in the last part (Chapter 5) the design of a new family of donor-acceptor liquid crystalline side-chain polymers combining a p-type backbone and n-type side-groups in a unique self-organized polymeric architecture. More precisely, these polymers

will be formed by a polythiophene backbone and perylene diimide side groups (Figure 1.76): the synthesis, the self-organization and the charge transport properties of these ambipolar self-organized polymers are discussed in Chapter 5.

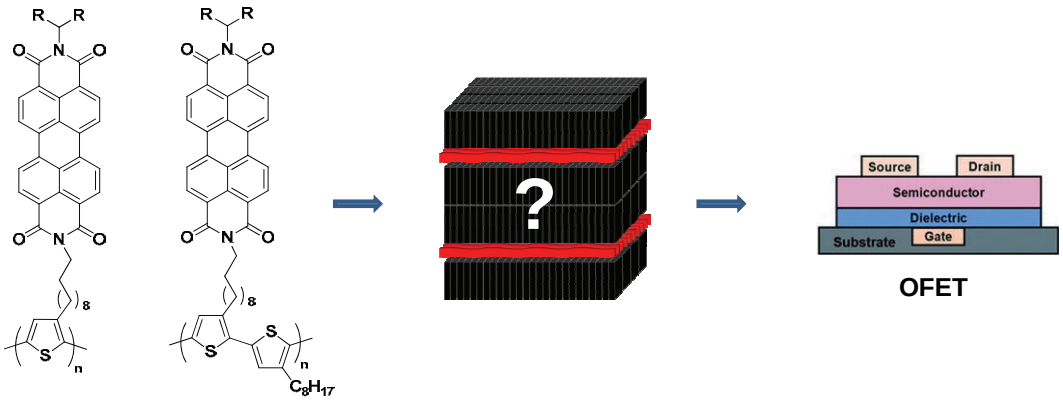

Figure 1.76: Chemical structures of donor-acceptor liquid crystalline side-chain polymers combining a p-type backbone and n-type side-groups in a unique polymeric architecture.

Finally, we will conclude this work and we will give some perspectives that these results open up in the field of the elaboration of self-organized semi-conducting materials, and more generally in the field of organics electronics.

CHAPTER 2 SYNTHESIS AND CHARACTERISATION OF DONOR-σ-ACCEPTOR COLUMNAR LIQUID CRYSTAL DYADS AND TRIADS

In this chapter, we will study a new family of donor-σ-acceptor liquid crystalline dyads and triads, combining p-type and n-type discotic derivatives. These molecules are based on triphenylene derivatives as donor moiety and perylene or naphthalene diimides as acceptor moieties, both entities being linked by alkyl chain spacers. More precisely, the chemical structures of these expected ambipolar discotic dyads and triads are given in Figure 2.1.

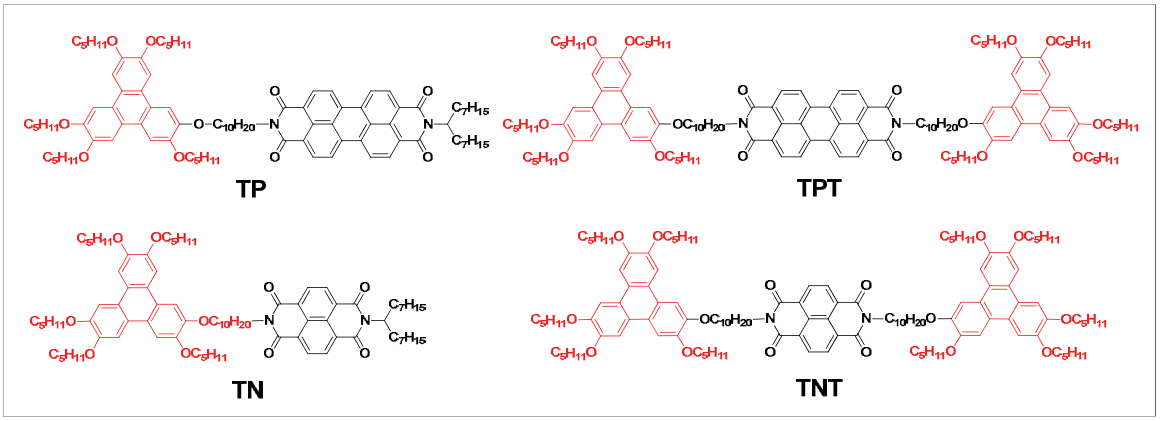

Figure 2.1 Chemical structures of the discotic target donor-σ-acceptor dyads and triads family

In particular, we will describe and discuss the synthesis, the thermal behavior, the self-organization, as well as the optical and electronic properties of this molecules family.

2.1 Synthesis

2.1.1 Synthesis of amino-alkyl-functionalized triphenylene

2.1.1.1 Synthesis of the monohydroxyalkoxy triphenylene

As introduced in Paragraph 1.3.1, we choose the "statistic cyclization" method recently described by Kong et al [144] as the main synthetic route to prepare the monohydroxy-functionalized triphenylene **2D** (Figure 2.2).

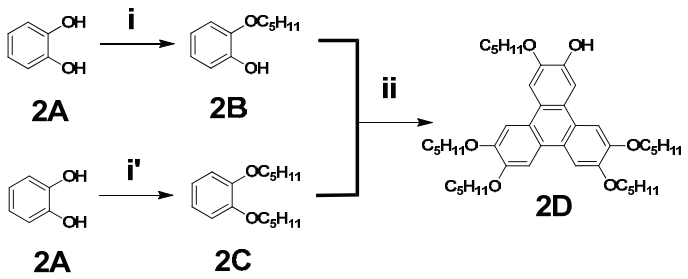

*Figure 2.2 Synthesis of monohydroxyalkoxy triphenylene **2D**. Conditions : i) 1-bromopentane (1 equivalent), K_2CO_3, KI, TBAB, ethanol, reflux, 24h, 79%; i') 1-bromopentane (2.2 equivalent), K_2CO_3, KI, TBAB, ethanol, reflux, 24h, 83%; ii) $FeCl_3$, DCM/MeCN, 0°C, 2h, 22%.*

This synthetic route for the preparation of compound **2D** consists in three steps. The two first ones concern the preparation of building blocks **2B** and **2C** obtained by classical Williamson etherification of catechol through adjusting the ratio of bromoalkane. The last step is a ferric chloride oxidatively catalyzed statistic cyclization. The key point in this "statistic" method is to precisely maintain the ratio between **2B** and **2C** as 1:2 to reduce the byproducts (symmetric, dihydroxy, trihydroxy, etc.).

Even though the yield of the last step is quite low and the purification of compound **2D** is tricky due to the presence of the multiple byproducts formed by the statistic cyclization (mainly the symmetric one), this method is more rapid than the "multi-step" way and more efficient (in total yield) than the "post-cleavage way" (see Paragraph 1.3.1).

2.1.1.2 Synthesis of the amino-alkyl-functionalized triphenylene via Gabriel synthesis

In order to functionalize the monohydroxyalkoxy triphenylene **2D**, we used the Gabriel synthesis to introduce an amino-terminated alkyl chain.

In this context, Figure 2.3 shows one of the different synthetic routes, compound **2D** being involved from the very first step and being trailed in each of the successive three steps.

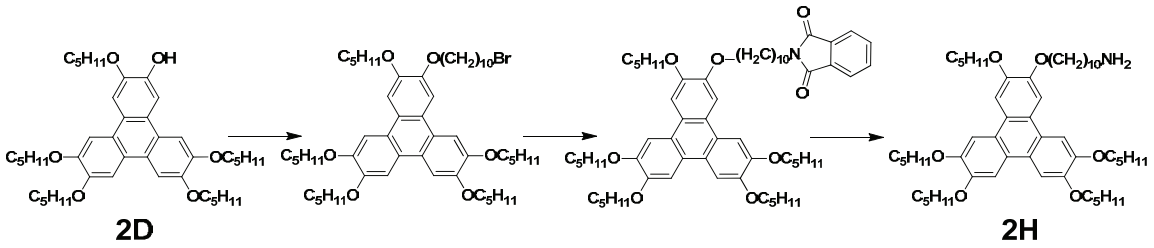

*Figure 2.3 A possible synthetic route towards amino-alkyl-functionalized triphenylene **2H***

To avoid this linear synthetic route which will dissipate the monohydroxy triphenylene, we chose finally another strategy to carry out the Gabriel reaction with the aim of economizing the compound **2D** (Figure 2.4).

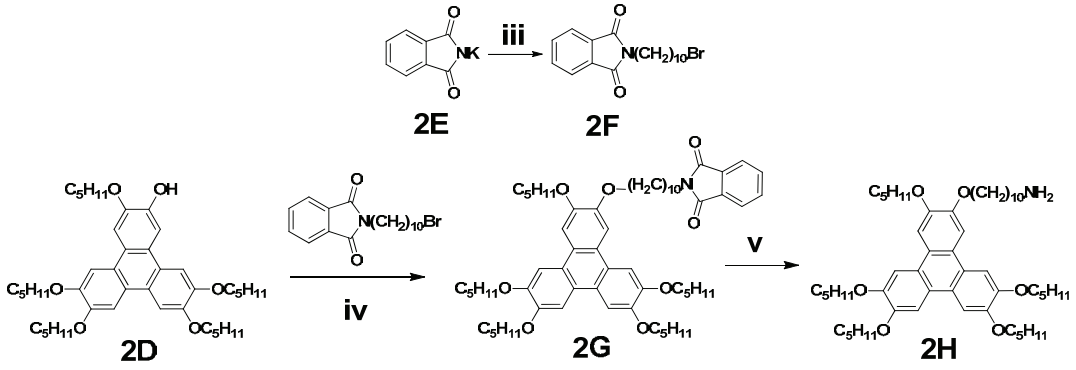

*Figure 2.4 Synthesis of amino-alkyl-functionalized triphenylene **2H**. Conditions; iii) 1,10-dibromodecane, DMF, 100°C, 12h, 92%; iv) K_2CO_3, DMF, 120°C, 12h, 82%; v) NH_2NH_2 (aq), EtOH, reflux, 1.5h, quantitative.*

In this synthetic route, the molecule **2F** bearing a "pre-Gabriel" functional group was first prepared in large quantity by reaction between one equivalent of 1,10-dibromodecane and one equivalent of potassium phthalimide **2E**. Then compound **2F** was grafted onto the triphenylene derivative **2D** by Williamson etherification: here, **2F** was used in large excess to optimize the nucleophilic attack on the precious monohydroxyalkoxy triphenylene **2D** and to obtain the compound **2G** with a high yield. **2G** was finally treated by aqueous hydrazine hydrate to complete the Gabriel synthesis with a quantitative yield and the final compound amine **2H** was purified easily by simple recrystallization.

2.1.2 Synthesis of mono-anhydride mono-imide perylene

In order to improve the solubility of perylene diimide building block, a branched alkyl chain substitution was chosen rather than a linear one [148] . Our choice was consequently the aminoalkyl building block **2J** which presents two long chains of seven carbons directly connected to the carbon bearing the amine group.

As the amine **2J** is not commercially available, it was synthesized from its ketone precursor, i.e. 8-pentadecanone **2I**. The compound **2I** was first reacted with hydroxylamine to form the oxime intermediate, and then was reduced by the mild hydrogenation reagent RedAl to give the target branched amine **2J** in quantitative yield (Figure 2.5).

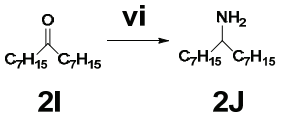

*Figure 2.5 Synthesis of branched amine **2J**. Conditions : vi) NH_2OH, EtOH, Pyridine, 100°C, 2h / RedAl, Toluene, Reflux, 2h, quantitative.*

As the mono-imidification on perylene-3,4,9,10-tetracarboxylic dianhydride (PTCDA) cannot be achieved directly [257] , an alternative route was applied, consisting the symmetric bisimide derivative preparation and then the cleavage of one terminal branched chain to reach the mono-anhydride mono-imide perylene **2M** (Figure 2.6).

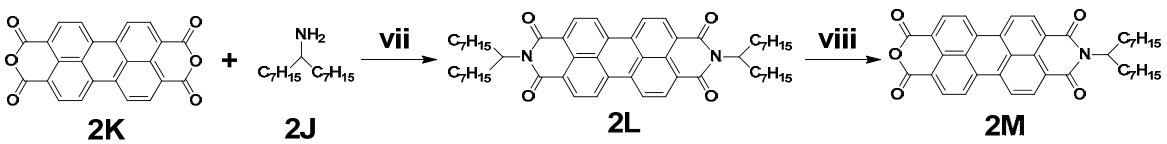

*Figure 2.6 Synthesis of mono-anhydride-functionalized perylene **2M**. Conditions : vii) $Zn(OAc)_2$, imidazole, 160°C, 4h, 81% ; viii) KOH, t-BuOH, Reflux, 1.5h / AcOH / HCl, 43%.*

More precisely, the branched amine **2J** was firstly grafted on commercially available PTCDA **2K** through imidification reaction in melted imidazole, catalyzed by zinc acetate (Lewis acid) according to the literature procedure [258] . Then, the symmetric bisimide compound **2L** was treated in strong basic medium to open the imide ring and to remove the swallow-tail-amine chains statistically. During this

reaction, the progress should be timely followed by TLC in order to stop the alkyl chain cleavage at the optimum moment. The starting material, the over-cleaved (**2K**) and the target molecule (**2M**) can be finally separated easily by silica column chromatography.

2.1.3 Synthesis of the triphenylene/perylene and triphenylene/naphthalene based dyads and triads

The synthetic route to prepare the triphenylene/perylene based dyad and triad is given in Figure 2.7. The synthesis of the dyad **TP** was carried out by the coupling between the mono-anhydride mono-imide perylene **2M** and the amino-alkyl functionalized triphenylene **2H** by following the same procedure as the synthesis of compound **2L**. Similarly, the synthesis of the triad **TPT** can be achieved from the same triphenylene derivative **2H** and the commercially available PTCDA **2K.**

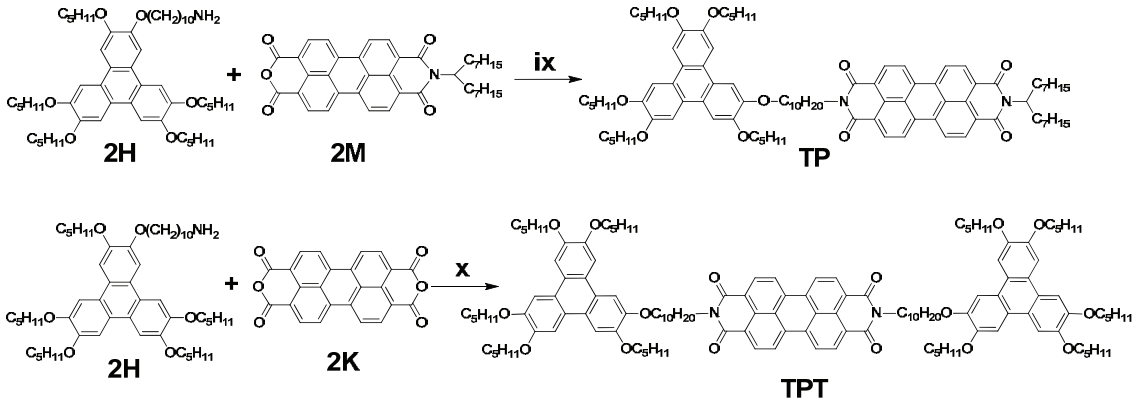

Figure 2.7 Synthesis of triphenylene/perylene based dyad and triad. Conditions: ix) $Zn(OAc)_2$, imidazole, 160°C, 2h, 75% ; x) same as the previous, 45%.

Concerning the synthesis of the triphenylene/naphthalene based dyad and triad, the previous strategy developed for the perylene based compounds couldn't be applied. Indeed, the attempt to prepare the mono-anhydride mono-imide naphthalene derivative failed. On the one hand, as described for the perylene derivatives, the mono-imidification from 1,4,5,8-naphthalenetetracarboxylic dianhydride (NTCDA) is nearly impossible and on the other hand, contrary to the perylene case, the mono-cleavage from the symmetric diimide naphthalene is not possible either. Thus, we were obliged to develop another strategy based on a statistic approach, as described in Figure 2.8.

The imidification of NTCDA was eventually performed in one-pot by adding the two amine derivatives **2H** and **2J** in a 1:1 ratio, assuming that these two amines possess similar reactivities in these experimental conditions. This way, the dyad **TN** and triad **TNT** were obtained in acceptable yields after easy purifications.

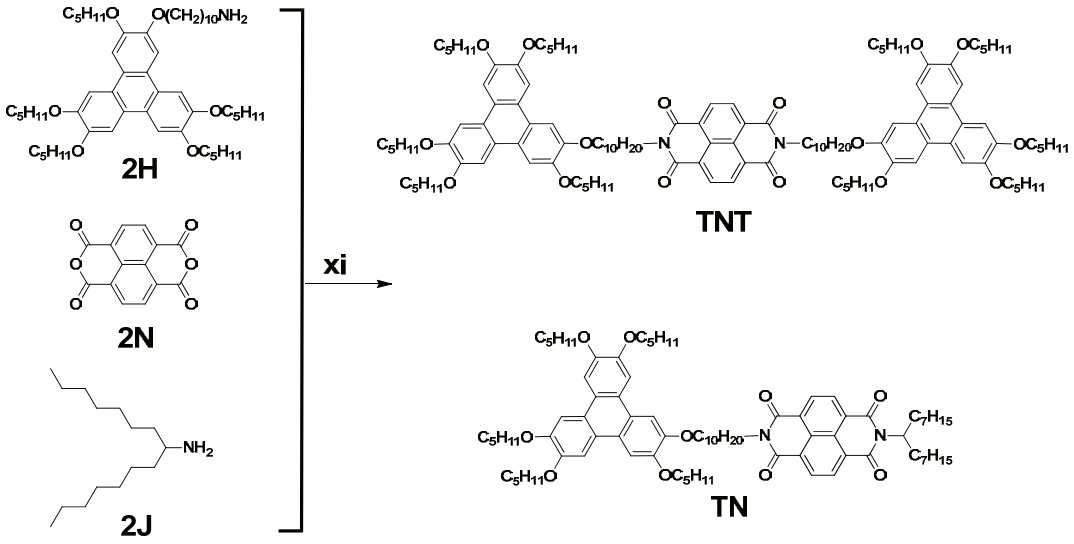

*Figure 2.8 Synthesis of naphthalene based dyad and triad. Condition: ix) same as in ix), 34% for **TN**, 20% for **TNT**.*

2.2 Thermal behavior

The thermal behavior of **TP**, **TPT**, **TN** and **TNT** were investigated by Polarized-light Optical Microscopy (POM) and Differential Scanning Calorimetry (DSC).

2.2.1 Polarized-light optical microscopy

Under POM, the dyad **TP** appeared as a slightly birefringent dark red powder which melted at around 84°C to give a clearly birefringent viscous phase. On further heating, this viscous phase transformed to a non-birefringent isotropic phase at around 146°C. Then on cooling from previous isotropic state, the birefringence phase reappeared at around 140°C, showing a typical pseudo focal-conic characteristic of a columnar hexagonal mesophase (Figure 2.9.a).

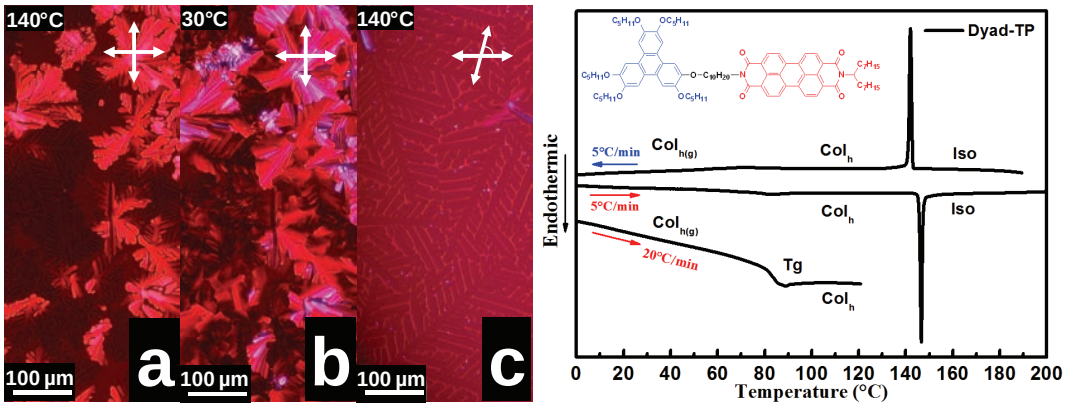

*Figure 2.9. POM microphotographs (left) and DSC thermograms (right) of **TP**. POM microphotographs obtained on cooling: (a) typical pseudo-focal conic texture at 140 °C; (b) preserved pseudo-focal conic texture from the hexagonal columnar mesophase at 30°C (below the T_g); (c) large domain of homeotropic texture at 140°C (slow cooling)*

On further cooling, this pseudo focal-conic texture was clearly maintained until room temperature in a very viscous phase, suggesting the presence of a glass transition at higher temperature and

explaining the freezing of the columnar mesophase (Figure 2.9.b). It is worth noting that, at a very slow cooling rate (0.1 °C/min), it is possible to obtain large (millimeter size) homeotropic domains (Figure 2.9.c).

The triad **TPT** presented a thermal behavior similar to the dyad **TP** with an isotropization temperature around 149°C on heating. However, the dendritic texture obtained on cooling (Figure 2.10.a) and the large oriented mosaic domains obtained with very slow cooling rate (Figure 2.10.b) seem to indicate the presence of a more ordered mesophase that in the case of the **TP** dyad. Moreover and similar to the dyad **TP**, this mesophase can also be preserved on cooling until room temperature.

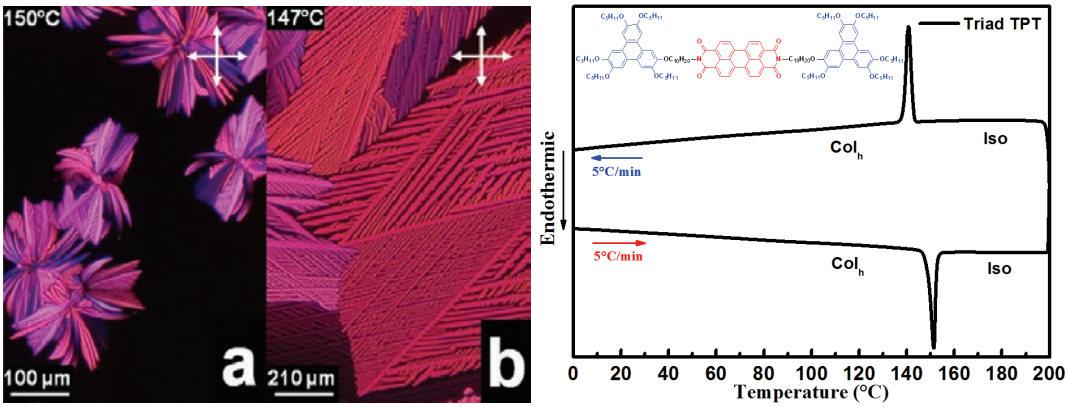

*Figure 2.10. POM microphotographs (left) and DSC thermograms (right) of **TPT**. POM microphotographs obtained on cooling: (a) typical pseudo-focal conic texture at 150 °C. (b) large oriented domains at 147°C*

On the contrary to the triphenylene-perylene dyad **TP**, the triphenylene-naphthalene dyad **TN** presented a fluid phase without any birefringence from room temperature to high temperature indicating its amorphous character (Figure 2.11).

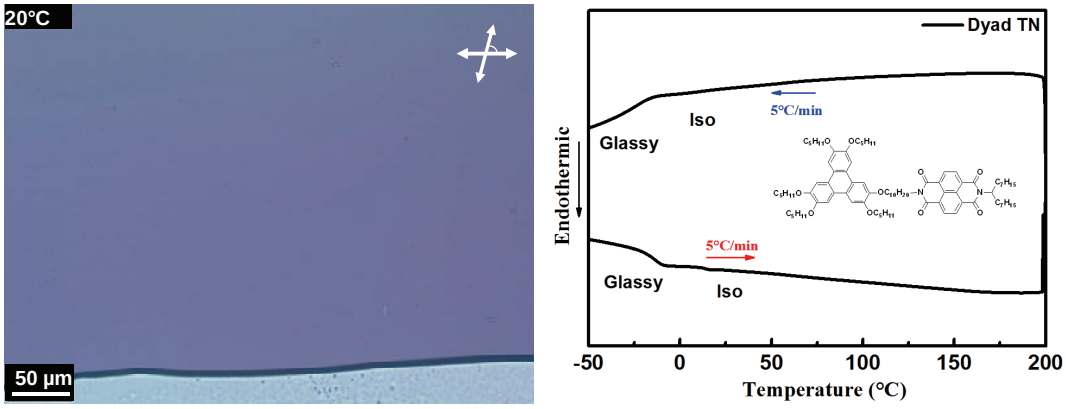

*Figure 2.11. POM microphotographs (left) and DSC thermograms (right) of **TN**. POM microphotograph obtained on room temperature, **TN** is in viscous liquid state and no birefringence observed.*

Nevertheless, concerning the triphenylene-naphthalene-triphenylene triad **TNT**, this compound appeared as a slightly birefringent gray-violet powder when observed under crossed polarizers at room temperature. This powder melted progressively on heating to give a birefringent viscous phase which

transformed into an isotropic phase at around 173°C. On cooling from the isotropic state, the birefringent phase reappeared at around 170°C, showing a mix of homeotropic and typical pseudo focal-conic textures, which is characteristic of a columnar hexagonal mesophase (Figure 2.12.a). Moreover, when being cooled at very low rate, large homeotropic domains were obtained and these domains can be maintained until room temperature in a very viscous phase as illustrated in Figure 2.12.b.

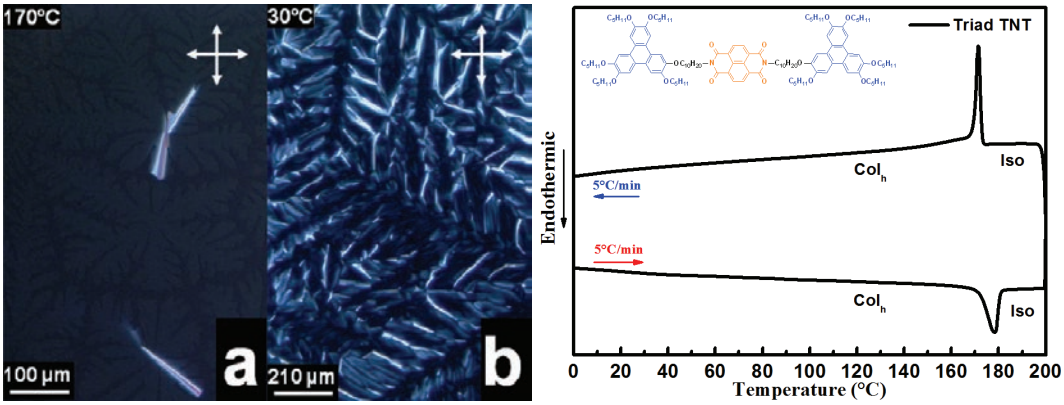

*Figure 2.12. POM microphotographs (left) and DSC thermograms (right) of **TNT**. POM microphotographs obtained on cooling: (a) large domain of homeotropic orientation at liquid crystal mesophase (b) Preserved homeotropic texture of the hexagonal columnar mesophase at 30°C*

2.2.2 Differential scanning calorimetry

The DSC thermograms of **TP**, **TPT**, **TN** and **TNT** are given in Figure 2.9, Figure 2.10, Figure 2.11 and Figure 2.12, respectively. In order to have a better overview of these 4 materials, the transition temperatures, phase sequence, and transition enthalpies are listed in Table 2.1. The DSC thermograms obtained for this family of dyads and triads are quite typical of high-molecular weight compound, containing characteristic signals of glass transitions. At higher temperature, exothermic transitions corresponding to the isotropic liquid phase are in agreement with the results measured by POM.

Compound	T_g[a] (°C)	Transition[b]	T[c] (°C)	ΔH (J g^{-1})
Dyad TP	84.4	$Col_h \rightarrow I$	145.8	4.0
	-	$I \rightarrow Col_h$	142.9	4.3
Triad TPT	-	$Col_o \rightarrow I$	148.9	5.9
	-	$I \rightarrow Col_o$	142.8	6.0
Dyad TN	-9.8	-	-	-
	-23.7	-	-	-
Triad TNT	-	$Col_h \rightarrow I$	172.9	4.8
	-	$I \rightarrow Col_h$	172.2	5.2

*Table 2.1. Phase transition temperatures and enthalpy of **TP**, **TPT**, **TN** and **TNT** .[a] T_g = glass transition determined during heating (rate 20°C/min). [b] Col_h = hexagonal columnar mesophase, Col_o= oblique columnar mesophase. I = Isotropic phase. [c] Indicated temperatures are the onsets of the peaks on heating and on cooling (rate 5 °C/min)*

For instance, the DSC traces of dyad **TP** show a nice reversible transition at around 145°C, corresponding to the transition between hexagonal columnar mesophase (Col_h) and the isotropic phase.

The glass transition of the compound assumed by POM observations can be also clearly detected at 84.4 °C with a high heating rate (20°C/min).

The DSC traces of dyad **TN** also confirmed the amorphous state of the compound at room temperature as no exothermic transitions can be observed on heating. In addition, a clear glass transition at around 9.8°C (5°C/min) can also be detected.

2.3 Self-organization property study

2.3.1 Temperature dependent X-ray diffraction

The temperature dependent X-ray diffraction (TDXRD) is the method of choice to assess the mesophases' formation and identity and to probe the effects of the intimate structural modifications onto the mesophase temperature ranges. As consequences, all the compounds of the discotic dyad and triad family (**TP**, **TPT**, **TN** and **TNT**) were studied by TDXRD in the temperature ranges determined by DSC and POM studies. The measurements were carried out at the Institut de Physique et de Chimie des Matériaux de Strasbourg (IPCMS) in collaboration with Dr. B. Heinrich and Dr. B. Donnio.

2.3.1.1 TP

To begin, the Figure 2.13 shows the typical X-ray patterns of the dyad **TP** recorded at room temperature (pristine state), at 140°C and at room temperature after annealing. The pristine state pattern (Figure 2.13.a) presents one simple slightly broadened reflection in the small-angle region and two diffuse halos in the wide-angle region. The repeat distances ***d*** associated with these reflections can be calculated in using the Bragg's law:

$$\lambda = 2d \sin\theta$$

where λ is the wavelength of incident X-ray and θ is the angle incidence. Thus, in the wide angle, the very broad halo centered at 4.5 Å (h_{ch}) indicates the molten state of the aliphatic chains and the other broad halo around 3.5 Å (h_T+h_{PDI}) evidences the short range ordered π-π stacking of the segregated discotic mesogens. This X-ray pattern suggests the amorphous characteristic of the material with columnar cybotactic pre-organization in the pristine state. On heating and just above the Tg at 84.4°C (detected by DSC), we can observe a sudden self-organization enhancement of the compound to a hexagonal columnar (Col_H) mesophase, resulting in a strong increasing of the small angle reflection (Figuer 2.13.b). The Col_H phase was maintained on cooling until room temperature as proved by the X-ray pattern given in Figure 2.13.c. This pattern presents: i) in the wide angle region, the broad diffuse halo centered at 4.5 Å (h_{ch}) corresponding to the liquid-like disorder of the aliphatic chains and the broad peak around 3.5 Å (h_T+h_{PDI}) corresponding to the stacking period in the columns; ii) in the small angle region, a sharp and intense reflection assigned to (10) with a Bragg spacing of 16.5 Å, followed by a set of weak reflections with a ***d***-spacing ratio of $1:\frac{1}{\sqrt{3}}:\frac{1}{\sqrt{4}}:\frac{1}{\sqrt{7}}:\frac{1}{\sqrt{9}}:\frac{1}{\sqrt{11}}$

corresponding to (10), (11), (20), (21), (30) and (12) reflections of a hexagonal columnar phase. Based on this study, we can propose a packing model for the dyad **TP** where the two moieties (one triphenylene and one perylene) segregate into two individually separated columns with a correlation distance ξ of ~ 100 Å (calculated from Scherrer formula [126, 259]) isolated by the peripheral aliphatic chains as illustrated in Figure 2.13.d.

However, the nearly same size of columns in the Col_H lattice associated with the limited correlation distance (around 30 times of the mesogens stacking distance) induce a macroscopic un-differentiation of columns [260], implying that the segments of stacked identical mesogens frequently exchange with preserving the segregation of any mesogen from the columnar periphery.

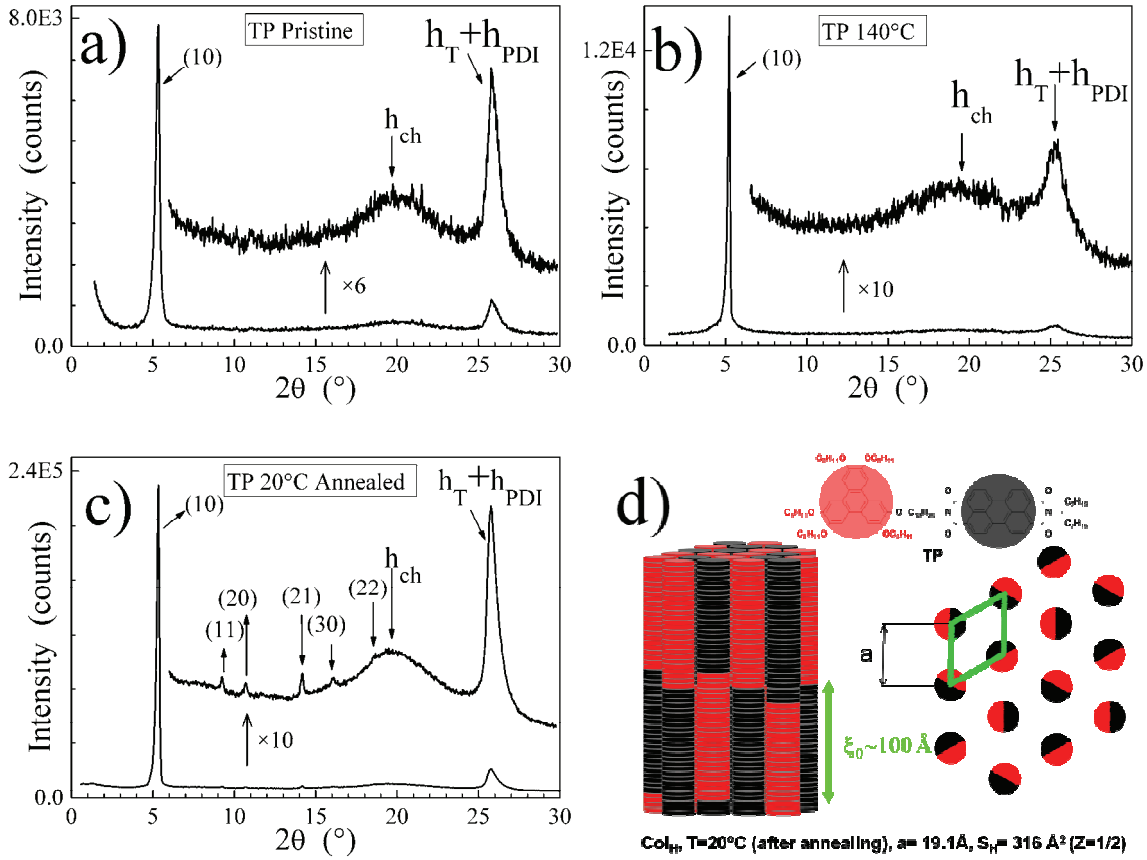

*Figure 2.13 X-ray diffraction patterns of dyad **TP**: (a) in pristine state at 20°C; (b) in liquid crystal state at 140°C; (c) in glass state of liquid crystal phase at 20°C on cooling. d) schematic representation of the Col_H mesophase and the lattice parameters. PDI=perylene diimide; T=triphenylene; ch=aliphatic chains, a=lattice constant, S_H=area of the bidimentianl lattice, Z=number of molecules per lattice, ξ=correlation length*

2.3.1.2 TPT

The Figure 2.14 shows the typical X-ray patterns of the triad **TPT** recorded at room temperature (pristine state), at 140°C and at room temperature after annealing.

The pristine state pattern (Figure 2.14.a) contains slightly broadened reflections in the small-angle region and the superposition of two diffuse halos in the wide-angle region. The usual very broad halo centered at 4.5 Å (h_{ch}) results from the lateral packing of the molten aliphatic chains and the narrower

halo centered at 3.5 Å (h_T + h_{PDI}) evidences the short-range ordered π-π stacking of the segregating discotic mesogens.

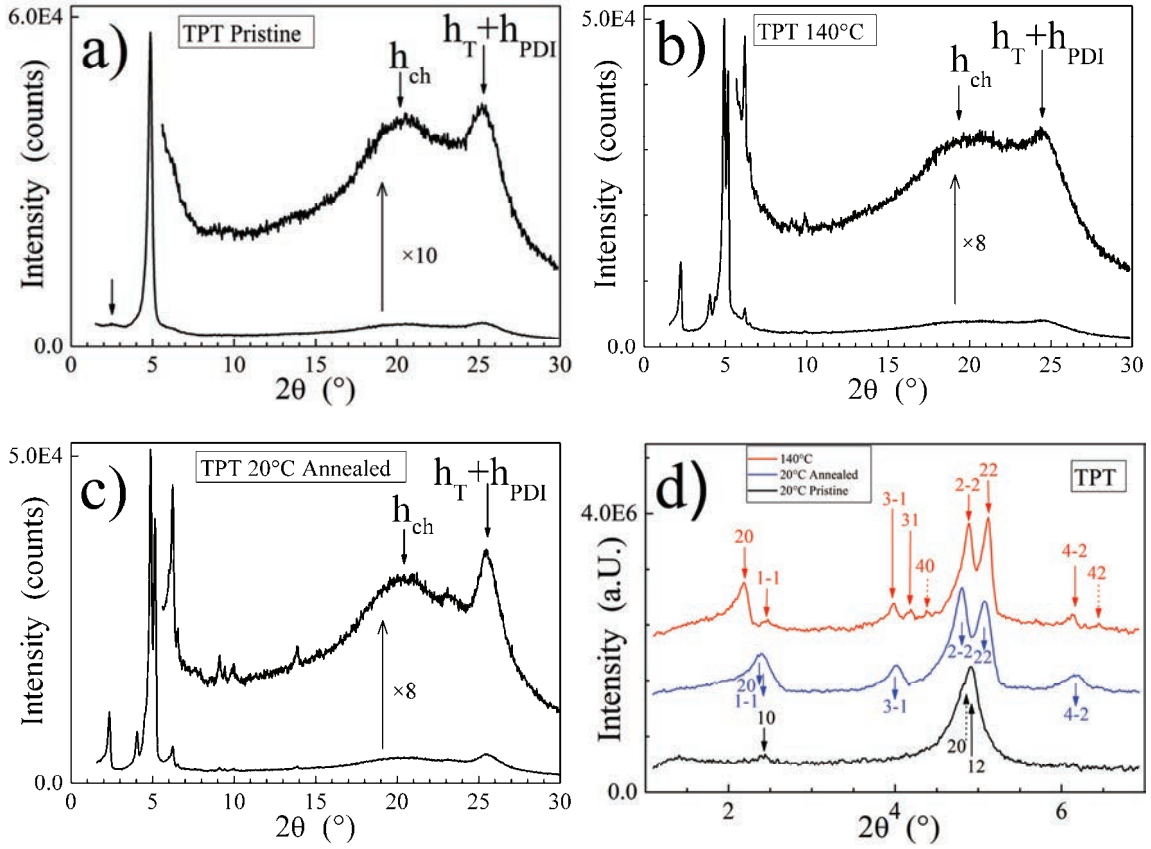

*Figure 2.14 X-ray diffraction patterns of dyad **TPT**: (a) in pristine state at 20°C; (b) in liquid crystal state at 140°C; (c) in glass state of liquid crystal phase at 20°C on cooling. (d) enlargement of small angle region of X-ray patterns at 20°C (pristine), 20°C (annealed) and 140°C. PDI=perylene diimide; T=triphenylene; ch=aliphatic chains*

This pristine pattern is indicative of a mesomorphic organization where very likely the two triphenylenes and the perylene mesogens of **TPT** segregate into three stacks, separated by the aliphatic periphery and arranged in a large columnar lattice. Indeed, the broadened reflection in the small region centered at 36.4 Å (2θ=2.42°) corresponds to the fundamental periodicity of a medium-range correlated rectangular lattice (Col_R) with two molecules per lattice and pseudo-hexagonal coordinates. This rectangular pseudo-hexagonal geometry ($a/b = \sqrt{3}$, γ =90°, with ***a***, ***b*** and γ the lattice parameters) suggests that the triphenylene columns are distributed all around the perylene columns as illustrated in the schematic packing model in Figure 2.15.a.

This model comes down to an alternation along ***b*** axis of intercalated rows of triphenylenes and perylenes. On heating, the X-ray patterns evidence an irreversible re-organization of the columnar lattice taking place around 80°C, likely in connection with enhanced sample fluidity. This re-organization leads to a long-range correlated oblique lattice (Col_O) revealed by the presence of eight sharp reflections in the small angle region (Figure 2.15.b).

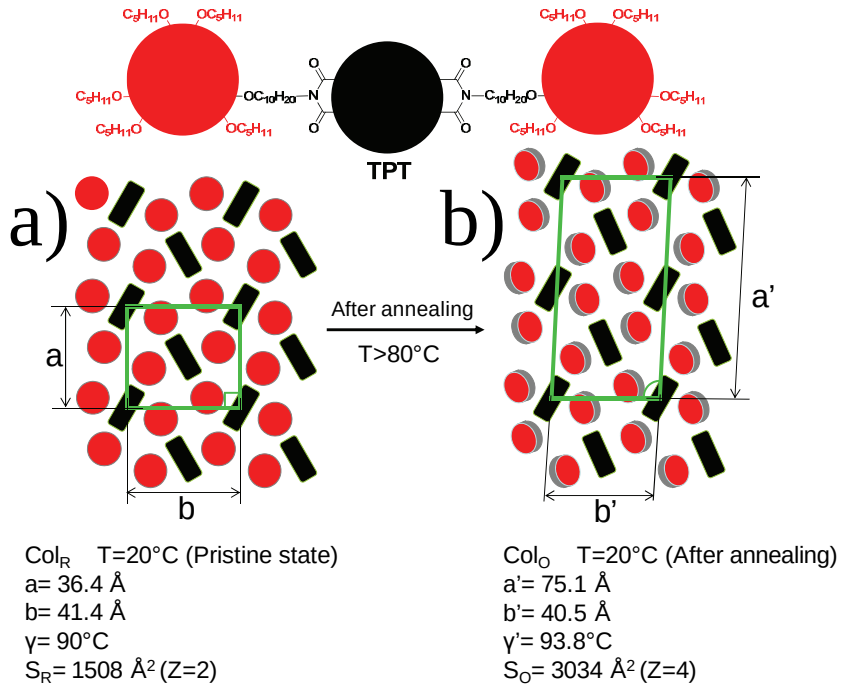

*Figure 2.15 Schematic representations of the Col$_R$ (a) and Col$_O$ (b) phases observed for the triad **TPT** and lattice parameters*

As expected, the oblique lattice vanished at the isotropization temperature but is restored by re-entering the mesophase and is finally maintained on cooling until room temperature as proved in Figure 2.14.c. This oblique columnar mesophase (Col$_O$) is characterized by a slightly deformed lattice ($\frac{a'}{b'}$=1.85-2, γ'≈93.8°) compared to the pristine rectangular pseudo-hexagonal mesophase ($\frac{a}{b} = \sqrt{3}$), γ=90°). However, in comparison to the pristine state, the lattice doubles along an axis and thus includes 4 triad molecules corresponding to 4 perylene and 8 triphenylene columns. Nevertheless, the a/b ratio of oblique lattice close to pseudo-hexagonal suggests that triphenylene columns are distributed all around the perylene columns as well, whilst the parameter is close but different to right angle likely results from different and partially compensating in-plane tilt directions of discotic in the lattice, as illustrated in the schematic packing model (Figure 2.15.b). This model considers also an alternation along ***b*** of intercalated rows of triphenylenes and of perylenes, with this time, opposite in-plane tilts within successive triphenylene rows. The lattice doubling may then be attributed to clusters of 4 triphenylene columns connected to one side of neighboring perylene columns: their distribution in the lattice and maybe the common orientation of their out-of-plane tilts would differ from the next cluster of triphenylenes.

2.3.1.3 TN

On the contrary but also as expected, the typical X-ray patterns recorded at room temperature of the isotropic oily liquid phase observed for the dyad **TN** is presented in Figure 2.16.

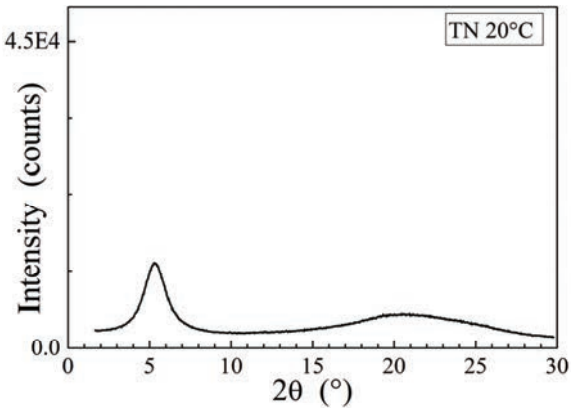

*Figure 2.16 X-ray diffraction pattern of dyad **TN** at 20°C*

Indeed, this pattern only contains broad halos from a local-range columnar-like packing. More precisely the wide-angle scattering signal shows a shoulder around 3.5 Å, due to lateral interactions between neighboring mesogens, while the intense small-angle scattering results from distances between clusters of molecules in lateral interaction, what prefigures the columnar lattice. The lack of mesomorphic properties for the dyad **TN** can be explained as this compound combines two features detrimental for mesomorphism, such as the 1:1 ratio forcing mesogen piles to mix and the small size naphthalene mesogens piling in a less cohesive way.

2.3.1.4 TNT

Figure 2.17 shows the typical X-ray patterns of the triad **TNT** recorded at room temperature in the pristine state, at 140°C and at room temperature after annealing.

The pristine state pattern (Figure 2.17.a) is quite similar to the pristine pattern of dyad **TP** and contains a slightly broadened reflection in the small-angle region and the superposition of two diffuse halos (centered at 4.5 Å and 3.5 Å) in the wide-angle region. As described previously, this pattern is indicative of a columnar mesomorphic organization where very likely the two triphenylenes and the naphthalene mesogens of **TNT** segregate as well into three stacks, separated by the aliphatic periphery and arranged in a hexagonal columnar lattice.

With increasing temperature and reinforcing thermal fluctuations, the π-π stacking distance logically increases and the associated correlation length along the columns decreases as shown in the X-ray pattern at 150°C (Figure 2.17.b) with the important shift and decreasing of the halo centered at around 3.5 Å. On cooling, the Col_H mesophase is maintained until room temperature as proved by the X-ray pattern given in Figure 2.17.c. This pattern presents, in the wide-angle region, the usual very broad halo centered at 4.5 Å (h_{ch}) and the narrower halo centered at 3.5 Å (h_T + h_{NDI}); in the small angle region, a sharp and intense reflection assigned to the fundamental periodicity (01) of the hexagonal lattice with a Bragg spacing d of 15.76 Å, followed by a weak reflection with a d-spacing ratio of $1:1/\sqrt{3}$. Based on this study, we can propose for the triad **TNT** a packing model quite similar

to the dyad **TP** model, where the three moieties (2 triphenylenes and 1 naphthalene) segregate locally into 3 individually separated columns isolated by the peripheral aliphatic chains as illustrated in Figure 2.17.d, but undifferentiated macroscopically.

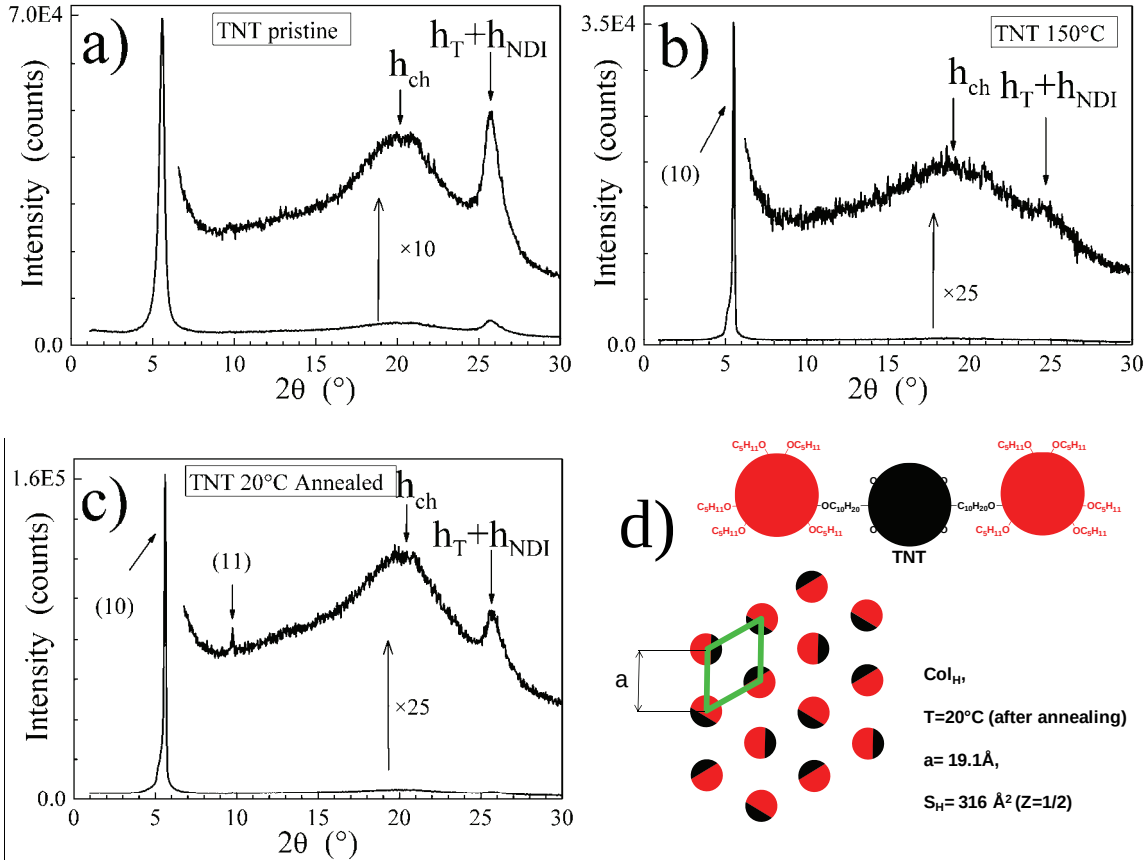

Figure 2.17 X-ray diffraction patterns of dyad TNT: (a) in pristine state at 20°C; (b) in liquid crystal state at 150°C; (c) in glass state of liquid crystal phase at 20°C on cooling. (d) schematic representation of the Col_H mesophase and the lattice parameters. NDI=naphthalene diimide; T=triphenylene; ch=aliphatic chains, a=lattice constant, S_H=area of the bidimentianl lattice, Z=number of molecules stacking forming the bidimentional lattice

In comparison with the triad **TPT**, the crossing from a differentiated to an undifferentiated columnar packing is obviously related to the smaller size of naphthalene core compared to perylene core, translating into weaker interactions within stacks, and thus, into reduced segregation tendency. Conversely, perylene stacks exhibit strong cohesion that leads to the presence of numerous higher order reflections in the dyad **TP**, evidencing the well confinement of mesogens in columns separated from the aliphatic periphery by sharp interfaces. The degree of segregation of perylenes and triphenylenes into different stacks is presumably comparable to triad **TPT**, and the loss of the differentiation in the dyad **TP** is just the consequence of the different molecular geometry. Whilst in the triad the 1 to 2 ratio allows the optimal segment segregation at the nodes and centers of a honeycomb lattice, the 1 to 1 ratio in the dyad only permits first neighbor segregation into bookshelf layers formed by alternating column rows. Unlike the rigid honeycombs, the direction in parallel to the column row alternation is intrinsically different from the perpendicular in-plane direction, and layers

may therefore bend and refold within columnar domains. This mechanism would then mix positions of locally segregated columns to an average lattice apparently constituted of undifferentiated columns.

2.3.2 Atomic force microscopy

Due to lack of time, we choose the dyad **TP** as example: its morphology of thin films was studied by tapping mode Atomic Force Microscopy (AFM). These measurements were carried out at the Institut des NanoSciences de Paris (INSP) in collaboration with Dr. E. Lacaze.

The **TP** films were prepared by spin-coating from a chloroform solution of material (1% w/w, 2000 rpm) onto silicon wafer substrates. The thickness is around 85 nm as determined by profilometer. The film samples were studied before and after annealing (120 °C for 2 hours in vacuum). The typical topography images are given in Figure 2.18.

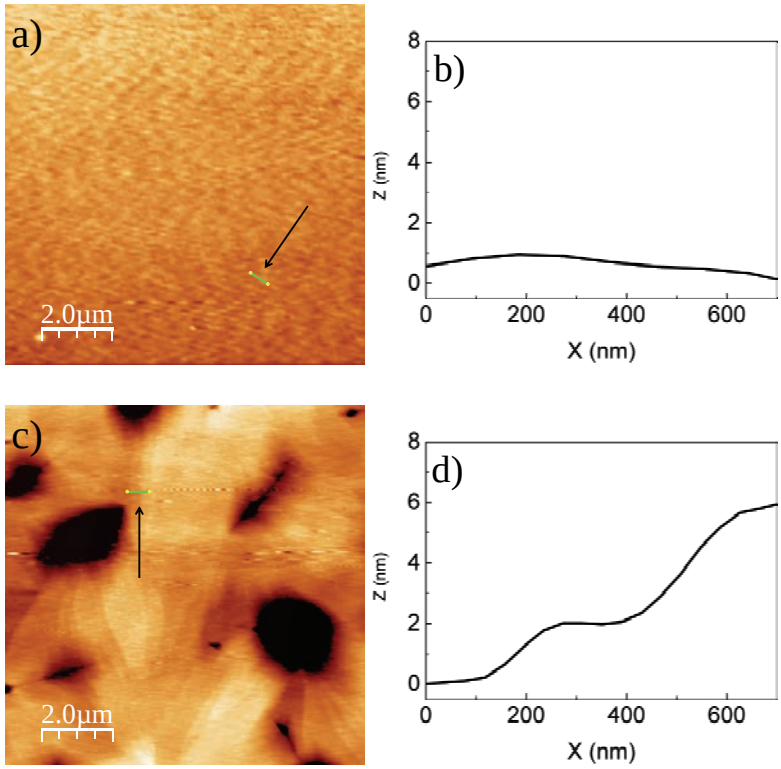

*Figure 2.18 Topography AFM images and corresponding height profiles of **TP** thin films on silicon wafer before (a, b) and after (c, d) annealing*

Before thermal treatment, the film surface appeared relatively uniform with no specific nanostructures (Figure 2.18.a) and the roughness was less than 1 nm as shown in the height profile given in Figure 2.18.b. After being annealed in its liquid crystal mesophase, a clear nanostructured film with terraces could be observed (Figure 2.18.c). The heights of the terraces determined from topography images were about 20 nm, or multiples of 20 nm as shown in Figure 2.17.d.

These values are well consistent with the inter-columnar distance (***a***= 19.1 Å) and more particularly with the Bragg spacing ***d*** around 17 Å measured from X-ray patterns of **TP** Col_H mesophase (Figure

2.19.a). These observations indicate that a well defined frozen columnar organization of dyad **TP** can be obtained in thin films after annealing with the columns lying down on the surface. Thus, the annealing induces likely a planar orientation of the columns and an edge-on orientation of molecules which could be quite interested in organic electronics [89, 261] (Figure 2.19.c).

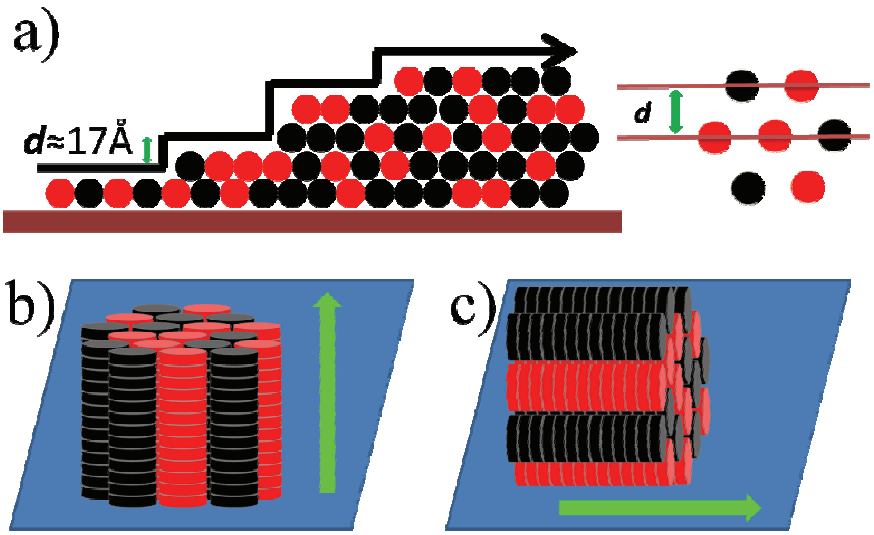

*Figure 2.19 Schematic representation of the dyad **TP** film surface morphology (a) "terrace type" nanostructure; (b) homeotropic orientation (face-on orientation of molecules); c) planar orientation (edge-on orientation of molecules)*

2.3.3 Grazing-incidence X-ray scattering

The Grazing Incidence X-ray Scattering (GIXS) is the method of choice to probe the structure and the morphology of organic thin films. Indeed, the X-ray scattering cross section of organic materials is small in comparison with inorganic materials such as metals because organic materials are mostly consisted of low-Z elements such as C, O and H. Therefore, X-ray scattering signals are week in organic thin layers. To overcome this problem, grazing incidence technique is used to investigate organic thin films systems. GISX technique requires actually small incident angle of X-rays to the surface of the sample, which increases the penetration depth of X-rays in the sample. GIXS is a reflection mode, which provides the information of the surface of a sample. A 2D detector is generally used to simultaneously measure the vertical and the horizontal alignments of atoms or molecules. Therefore, the GIXS measurements allow to determine the orientation of molecules in thin films as for example the "face-on" or "edge-on" orientations, as illustrated in Paragraph 2.3.2. The vertical diffraction peaks of 2D images correspond to the *(0k0)* in the face-on crystallites; whereas they correspond to the *(h00)* in the edge-on crystallites.

Thus the film structure and morphology of dyad **TP** were studied by GIXS. These measurements were carried out at Pohang Accelerator Laboratory (PAL), in collaboration with Prof. H-J Kim (Pusan National University).

The **TP** thin film samples were prepared on silicon wafer substrates by spin-coating with the same conditions as for AFM samples (see Paragraph 2.3.2).

The two dimensional GIXS image of annealed **TP** film is given in Figure 2.20.a.

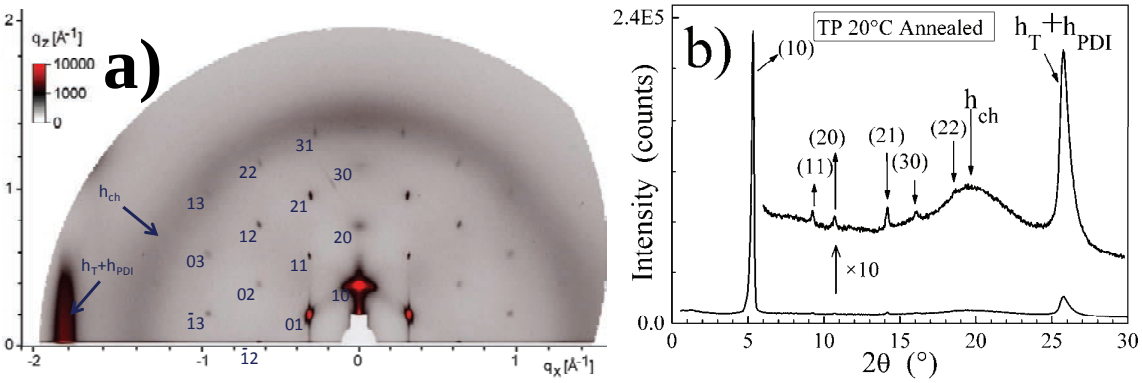

*Figure 2.20 (a) GIXS patterns (with different contrast, red and black) of **TP** film (spun cast on silicon wafer from 1% w/w chloroform solution, annealed at 120°C for 2 hours in vacuum); grazing angle=0.12°.(b) bulk XRD pattern of **TP** (cooled to 20°C from liquid crystal mesophase)*

In addition to the very diffuse halo around 1.4 Å^{-1} (4.5Å), corresponding to the liquid-like disorder of the aliphatic chains (h_{ch}), this pattern presents one broad and intense in-plane reflection at around 1.82 Å^{-1} (along q_x), corresponding to the π-π stacking (3.5 Å) of the segregating discotic mesogens (h_T+h_{PDI}); a vast number of sharp reflections in and out of specular plane (along q_z) can be assigned to the usual reflections of the hexagonal columnar phase (Col_H), already described in the bulk X-ray diffraction study (Figure 2.20.b).

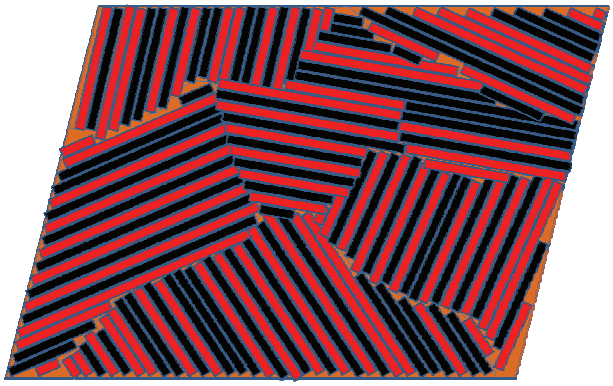

*Figure 2.21 Schematic representation of in plane random orientation (top-view) of dyad **TP** (columns in parallel with the substrate)*

This typical GIXS pattern confirms the hexagonal columnar organization of the dyad **TP** in the annealed film and the edge-on orientation of the molecules on the substrate with the columns oriented in parallel with the surface. These results are perfectly consistent with the terrace nanostructure observed by AFM on the annealed thin film of dyad **TP** (Paragraph 2.3.2, Figure 2.18). It is worth noticing that no specific changes of the GIXS patterns were observed in rotating the sample during the

GIXS measurements. That indicates no preferential alignment of columns and we can consider that there is no macroscopic orientation of the columnar domains in the plane of the thin film (as illustrated in Figure 2.21), which can be a problem for charge transport in an OFET channel as for instance.

2.4 Optical properties (absorption and emission)

2.4.1 Optical properties in solution

The absorption and emission properties of this family of discotic dyads and triads and their corresponding building block molecules were studied in diluted chloroform solutions (ca. 10^{-6} M). In this condition, these molecules can be considered as adequately isolated, i.e. the aggregation and the intermolecular interactions can be neglected.

First, Figure 2.22 shows the absorption and emission spectra of the three isolated building blocks: triphenylene derivative **T** (Figure 2.22.a), perylene diimide **P** (Figure 2.22.b) and naphthalene diimide **N** (Figure 2.22.c).

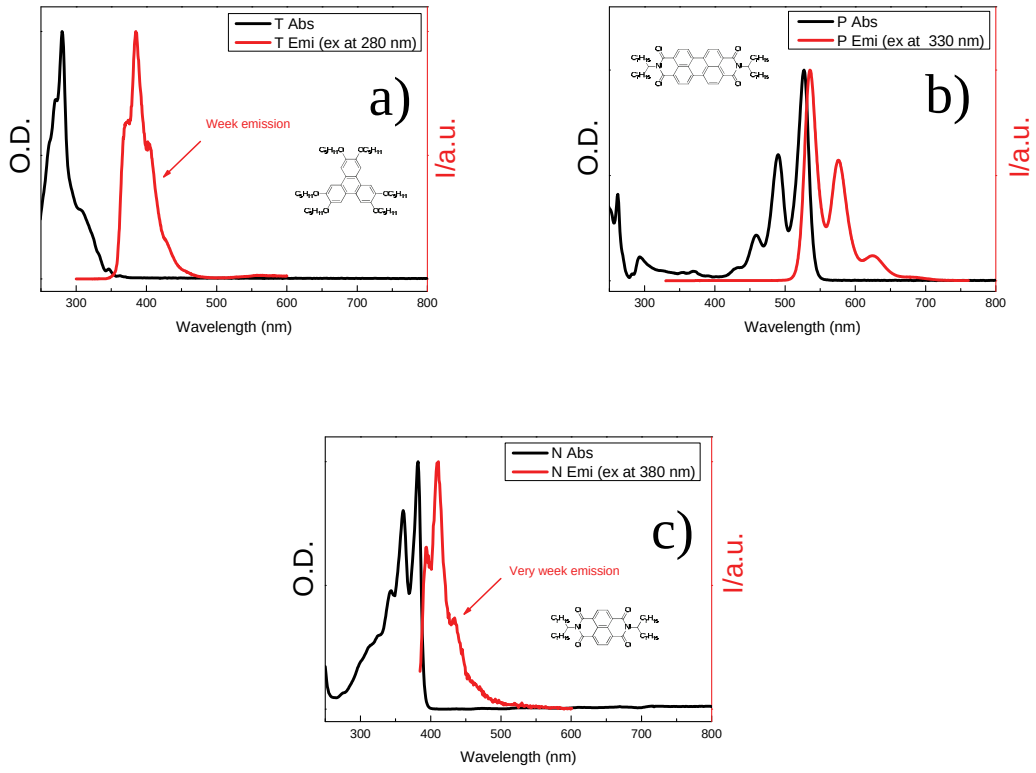

*Figure 2.22 UV-vis and fluorescence spectra of three building blocks triphenylene derivative **T** (a), perylene diimide **P** (b) and naphthalene diimide **N** (c) in chloroform (ca. 10^{-6} M)*

In the case of the triphenylene derivative **T**, the absorption maximum occurs at about 280 nm and the fluorescence appears mainly in the region between 360 and 420 nm. Concerning the optical properties of perylene diimide **P**, three characteristic absorption vibronic peaks can be observed at 459,

490 and 526 while in the fluorescence spectrum the mirror symmetric peaks arise at 537, 575 and 627 nm, respectively. For the naphthalene diimide **N**, its optical behaviors are similar to those of perylene diimide but strongly blue shifted (342, 361 and 382 nm for the absorption; 393, 410 and 434 nm for the fluorescence). It should be also noted that compound **T** and compound **N** present very low fluorescence quantum yields [262, 263] contrary to compound **P** whose quantum yield is close to unity [146] .

The absorption and emission spectra of dyad **TP** and triad **TPT** were carried out and are given in Figure 2.23. In the case of dyad **TP** (Figure 2.23.a), the absorption spectrum is the sum of the isolated triphenylene and perylene absorbances taken separately.

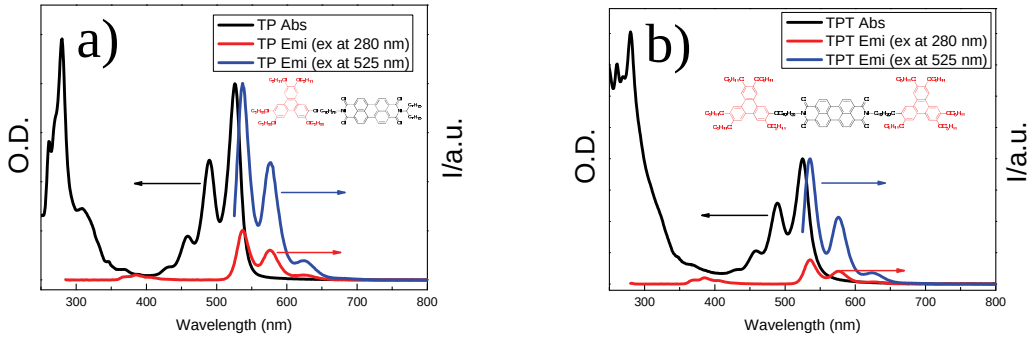

*Figure 2.23 UV-vis and fluorescence spectra of dyad **TP** (a) and triad **TPT** (b) in chloroform (ca. 10^{-6} M)*

More precisely, the absorption band at wavelengths shorter than 400 nm is due to the triphenylene unit while the absorption in the visible region of the spectrum is due to the perylene moiety [264]. The maximum of the absorption from the triphenylene unit appears at about 280 nm, which can be attributed to the symmetry-allowed S0-S4 electronic transition [265-267] . Low intensity peaks at 345 and 360 nm are related to the symmetry-forbidden S0-S1 transition. Regarding the contribution from the perylene moiety, the absorption peak at 525 nm corresponds more particularly to the (0,0) vibronic transition while the peak at 488 nm is attributed to the (0,1) transition. Peak-to-peak ratio between the (0,0) and (0,1) peak intensities is around 1.6, which indicates that there is no aggregation between the perylene moieties in the diluted solutions [267, 268]. The absorption spectrum of triad **TPT** (Figure 2.22.b) is quite similar to that of dyad **TP** but evidently, as the triphenylene/perylene ratio is of 2/1, the absorption spectrum in the range of triphenylene is doubled.

Concerning now the emission properties, dyad **TP** and triad **TPT** are strongly fluorescent in chloroform solutions. The emission spectra are in fact dominated by the emission from perylene as proved by the presence of the three peaks at 537, 575 and 627 nm which can be attributed to isolated perylene moieties, confirming that there is no aggregation [269, 270]. When excited at 280 nm, a weak signal around 390 nm from the triphenylene moieties is also visible [265-267]. Not surprisingly, the emission signal coming from triphenylene unit in triad **TPT** is slightly stronger than that in dyad **TP**.

Concerning these two compounds, it is worth noticing that energy transfer may occur in **TP** and **TPT** solutions, due to the overlapping of triphenylene (donor) emission spectra with perylene (acceptor) absorption spectra.

After describing the optical properties of dyad and triad incorporating the perylene diimide unit, we realized the same study for the corresponding materials involving the naphthalene diimide unit. Thus, the absorption and emission spectra of dyad **TN** and triad **TNT** are given in Figure 2.24. Here also, their absorption spectra are the sum of the isolated triphenylene and naphthalene absorbances.

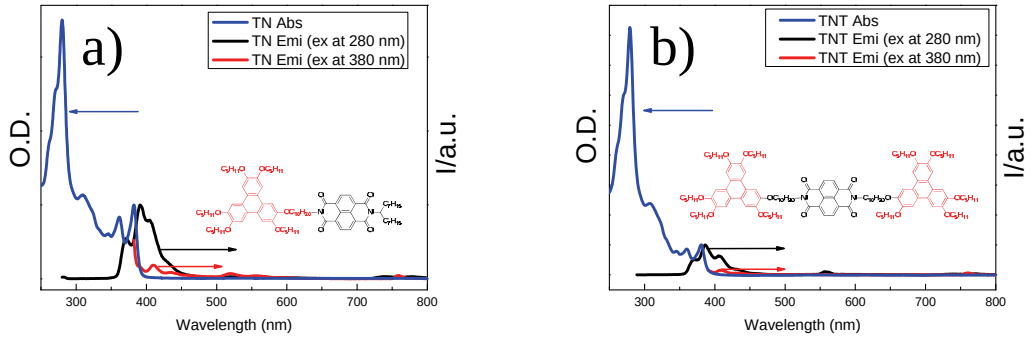

*Figure 2.24 UV-vis and fluorescence spectra of dyad **TN** (a) and triad **TNT** (b) in chloroform (ca. 10^{-6} M)*

However, the weak naphthalene moiety's absorption band at higher energy (λ_{max} located at 380 nm) is slightly overlapped with the triphenylene's and consequently, it is not very visible especially for triad **TNT** where the triphenylene band intensity is doubled.

The dyad **TN** and triad **TNT** are also fluorescent in chloroform solution (even though much weaker compared to the corresponding perylene based dyad **TP** and triad **TPT**). However, this time, the emission spectra are dominated by the emission from triphenylene (fluorescence quantum yield is about 6% [262] for **T** and between 0.2%-0.6% for **N** [271, 272]) as proved by the presence of the vibronic band at around 390 nm, characteristic of triphenylene band.

2.4.2 Concentration dependent absorption and emission

To better understand the intermolecular interaction and aggregation phenomena, the dyad **TP** was taken as an example to further investigate the influence of concentration on absorption and emission properties in a poor solvent such as methylcyclohexane [273]. The result, i.e. the "concentration dependent normalized absorption spectra" is shown in Figure 2.25.

At very low concentration, the absorption spectra are similar to those in diluted chloroform (Figure 2.23.a). When the concentration increases, due to the molecular stacking of both perylene units and triphenylene units, the apparent absorption coefficients of both chromophores decreased and the

absorption bands are shifted and broadened. This can be attributed to the electronic coupling between the perylene moieties and the triphenylene moieties.

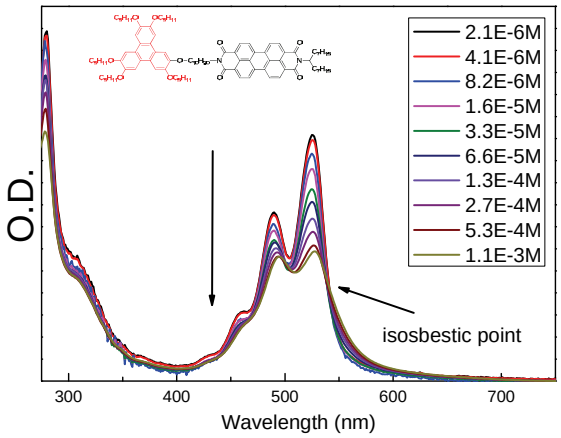

*Figure 2.25. Concentration-dependent absorption spectra of dyad **TP** in methylcyclohexane solutions (c= 1.1x10^{-3}M to 2.1x10^{-6}M). Arrows show the changes when increasing the concentration.*

Concerning the contribution from the perylene moiety, it can be seen that an isosbestic point appears at about 530 nm, which suggests the formation of π-π face-to-face aggregates at high concentration.

Finally, in the photoluminescence spectra, at low concentration, we can find the same emission spectra as in the diluted chloroform (Figure 2.26.b). As the concentration increased, the fluorescence was gradually quenched until almost completely disappeared. This confirms again the molecular aggregations.

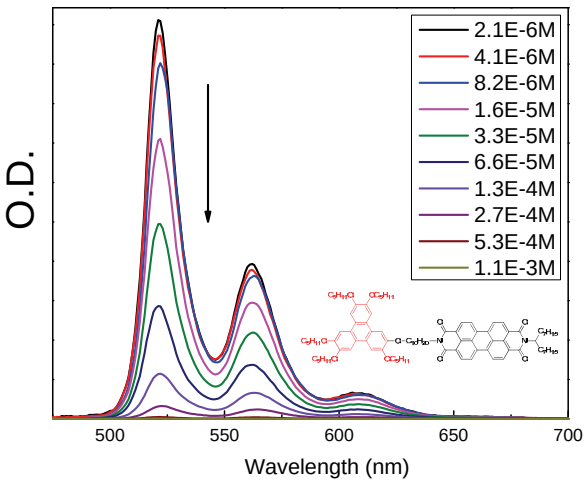

*Figure 2.26. Concentration-dependent fluorescence spectra of **TP** in methylcyclohexane solutions (excited at 450 nm, c= 1.1x10^{-3}M to 2.1x10^{-6}M) Arrows show the changes when increasing the concentration.*

2.4.3 Optical properties in solid state

As an extension of the concentrated solution to extreme and to provide some additional information about the thin film properties (including thermal treatment effects), the dyad **TP** film absorption properties were studied as well. Indeed, the solid state can be considered as an extremely concentrated solution (concentration → 100%).

A thermal treatment (similar to the annealing conditions in AFM and GIXS measurements, 120 °C for 2 hours in vacuum, namely in liquid crystal mesophase) was also carried out to evaluate its influence on the optical properties which are correlated with the intimate molecular organization changes with temperature. Figure 2.27 shows the absorption spectra of dyad **TP** thin film before and after annealing.

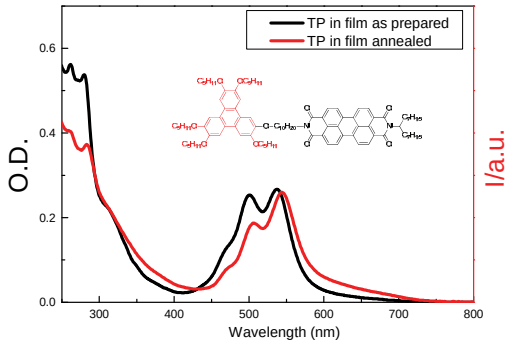

*Figure 2.27 Absorption spectra measured in dyad **TP** thin film, before (black) and after (red) annealing*

The as-prepared film's absorption is consistent with the spectrum observed at high concentration in the previous concentration-dependent absorption study in solution (Figure 2.25). It is obvious that the peak-to-peak ratio between the (0,0) and (0,1) peak approaches to unity.

After annealing, it can be observed that all the vibronic peaks from the perylene moieties are about 5 nm red-shifted with a shape-regression to the isolated molecules case, suggesting a little increase of π-π intermolecular interactions between perylene units due to small changes in molecular packing upon annealing. Regarding the position of the absorption peaks of the triphenylene moieties, a small red-shift of about 2 nm was observed after annealing. This result, together with a little increase of the absorption tail in the range 350-400 nm, suggests a little increase of the aggregation of the triphenylene units in the annealed dyad **TP** films which coincides with the temperature dependent X-ray diffraction experiments.

It should be noted that, in the solid state, there is almost no fluorescence observed in **TP** (neither in **TPT** nor in **TNT**, **TN**) and that is the reason why the emission properties were not further studied.

2.5 Electrochemical behavior and HOMO/LUMO energy levels

The electrochemical behaviors of **TP**, **TPT**, **TN** and **TNT** were studied using cyclic voltammetry. All the experiments were carried out at room temperature in chloroform solutions (concentrations around 10^{-3} M, n-Bu_4NPF_6 0.05 M being added as supporting electrolyte), at a scan rate of 100 mV s^{-1}, with Pt as the working and counter electrodes and Ag/AgCl electrode (saturated KCl) as the reference electrode. Note that oxidation and reduction potentials were determined as an average value between each anodic and corresponding cathodic potentials: $E_{1/2}^{red/ox} = ½ (E_{pa} + E_{pc})$.

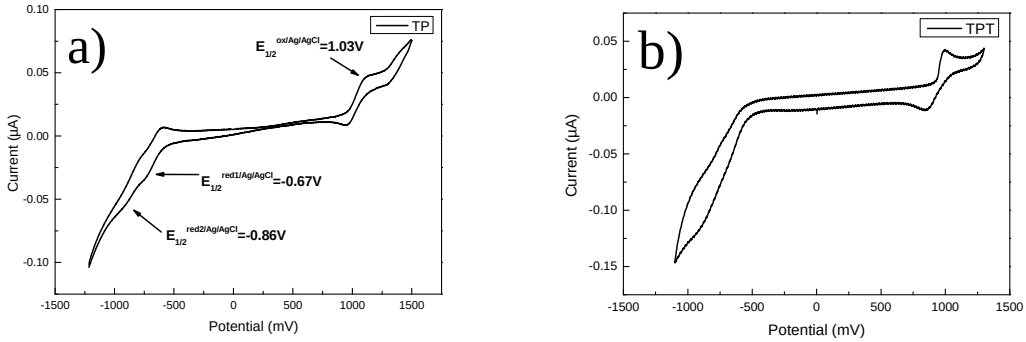

*Figure 2.28. Cyclic voltammetry of **TP** (a) and **TPT** (b) in chloroform solution of n-Bu_4NPF_6 (c (n-Bu_4NPF_6 = 0.05 M, c (**TP** and **TPT**) = ca. 10^{-3} M, 0.05 V/s, room temperature)*

Figure 2.28.a presents the voltammogram of **TP** which shows on one hand two well-separated, reversible, one-electron reduction waves at -0.67 and -0.86 V (vs Ag/AgCl) corresponding to the formation of the radical anion and dianion characteristic of the perylene acceptor moiety, and on the other hand a unique one-electron reversible oxidation wave corresponding to the triphenylene donnor moiety radical cation at 1.03 V (vs Ag/AgCl). The **TPT** showed similar redox profiles with a doubled oxidation from the two triphenylene parts (Figure 2.28.b).

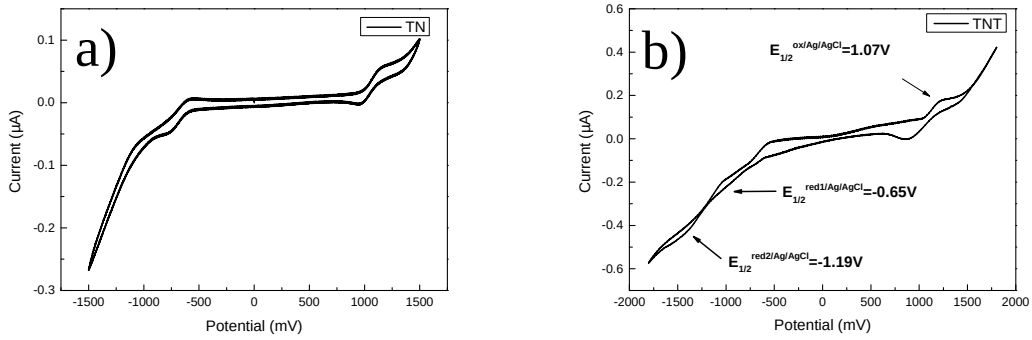

*Figure 2.29. Cyclic voltammetry of **TN** (a) and **TNT** (b), in chloroform solution of n-Bu_4NPF_6 (c (n-Bu_4NPF_6 = 0.05 M, c (**TN** and **TNT**) = ca. 10^{-3} M, 0.05 V/s, room temperature)*

In the case of triad **TNT** (Figure 2.29.a), the reversible oxidation happened at 1.07 V (vs Ag/AgCl) and this is in agreement with the triphenylene moiety characteristic as seen previously in dyad **TP** and triad **TPT**. As the acceptor core was replaced from perylene to naphthalene, the two reductions appeared at -0.65 V and -1.19 V (vs Ag/AgCl), respectively. In the dyad **TN** (Figure 2.29.b) the oxidation wave from the triphenylene decreased by a half. All the potential values are listed in Table 2.2.

Compound	$E_{1/2}^{red2}$ (V/Ag/AgCl)	$E_{1/2}^{red2}$ (V/Fc/Fc$^+$))	$E_{1/2}^{red1}$ (V/Ag/AgCl)	$E_{1/2}^{red1}$ (V/Fc/Fc$^+$))	$E_{1/2}^{ox1}$ (V/Ag/AgCl)	$E_{1/2}^{ox1}$ (V/Fc/Fc$^+$)
TP	-0.86	-1.35	-0.67	-1.16	1.03	0.54
TPT	-0.81	-1.26	-0.63	-1.09	0.93	0.47
TN	-0.66*	-1.19*	-0.66*	-1.19*	1.05	0.52
TNT	-1.19	-1.68	-0.65	-1.15	1.07	0.68

*Table 2.2. Redox potentials of **TP**, **TPT**, **TN** and **TNT** measured in Solution Cyclic Voltammetry: $E_{1/2}^{Fc}$ = 0,49 V vs Ag/AgCl*

Based on these redox potential values, the HOMO and LUMO energies of **TP**, **TPT**, **TN** and **TNT** were estimated (see Table 2.2) on the basis of the reference energy level of ferrocene (4.8 eV below the vacuum level [274]) and taking into account the empirical relationships which has been proposed by Brédas et al.[275] and widely used by others [274, 276]:

$$E^{HOMO} = -4.8 - E_{1/2}^{ox1}(\text{vs Fc}) \qquad E^{LUMO} = -4.8 + E_{1/2}^{red1}(\text{vs Fc})$$

Where $E_{1/2}^{ox}$(vs Fc) and $E_{1/2}^{red}$(vs Fc) are, respectively the first potentials values for oxidation and reduction of the studied material relative to the Fc/Fc$^+$ internal standard.

For all the molecules, the HOMO values are mainly issued from the first oxidation potential of the triphenylene moiety, as the LUMO energies are determined mainly from the oxidation potential of the perylene (**TP** and **TPT**) or naphthalene (**TN** and **TNT**) moiety.

Moreover and as an important remark, these HOMO/LUMO values do not represent any absolute solid-state or gas-phase ionization potentials but can be used to compare different compounds relative to one another. Note as well that the calculated band gap reported in Table 2.3 is not an optical band gap but an electrochemical band gap (even if in our experimental conditions both gaps should be quite close).

The values of HOMO/LUMO energies of all the four molecules and the basic building bricks are summarized in Table 2.3.

	TP	TPT	TN	TNT	TriPh*	Naph*	Pery*
E^{HOMO} (eV)	-5.47	-5.43	-5.46	-5.45	-5.4	-7.04	-6.3
E^{LUMO} (eV)	-3.77	-3.87	-3.75	-3.73	-1.7	-3.41	-4.1
E_g^{CV} (eV)	1.7	1.56	1.71	1.72	3.7	3.63	2.2

*Table 2.3. HOMO/LUMO values of **TP**, **TPT**, **TN** and **TNT** *The HOMO/LUMO values of the corresponding triphenylene moiety [277], naphthalene moiety [278], and the perylene moiety [105] are published in previous reports.*

In this context, by comparing all these HOMO/LUMO values with the ones of each donor and/or acceptor taken alone (free), we can observe that generally **TP** and **TPT** have similar HOMO/LUMO values as in isolated model perylene diimide and triphenylene, respectively. Similarly, **TN** and **TNT** show typical HOMO/LUMO values regarding the ones of an isolated model naphthalene diimide and isolated triphenylene as well. These results evidence that donor and acceptor units don't interact in solution, as it was expected, because the covalent linker is long and not conjugated as observed for the other similar systems [126, 279] .

2.6 Preliminary results on charge transport properties

The charge transport properties of dyad **TP** were investigated by temperature-dependent time-of-Flight technique (Experimental 2.7.1 for more details). The measurements were carried out at the Institut des NanoSciences de Paris (INSP) by M.Sc. Leszek Mazur in cooperation with Dr. Jean-Louis Fave (for more details about the sample preparation and measurements conditions, see Experimental 2.7.1)

The dyad **TP** was characterized in bulk by conventional TOF configurations: 8 μm thick **TP** films (sandwiched between two ITO electrodes) were excited by nanosecond pulses at 337 nm, where the sample strongly absorbs light. The measurements were first carried out in the Col_h mesophase. Unfortunately, even if the sample was carefully orientated into large, homeotropic liquid crystal domains in the TOF cells (as in Figure 2.9.c), the obtained photocurrent stayed very low (range of nA). Moreover, the deflection point did not shift with applied voltage, indicating that it cannot be considered as the transit time. As a result, the charge carriers mobility in the mesophase can hardly be evaluated by TOF technique.

However, in isotropic state, the TOF experiments gave some exploitable results. The sample was photo-excited by lasers in using two different beam wave lengths (337 nm and 508 nm), close to the maximum absorptions of triphenylene and perylene moieties, respectively.

When the sample was excited by the laser beam at 337 nm with applied negative voltage, untypical transient photocurrent curves were recorded, as displayed Figure 2.30.a. First of all, the UV laser pulse should excite triphenylene core, which behaves like a p-type semiconductor, i.e. is able to conduct only holes. Thus, applying negative voltage should result in no photocurrent curve. In contrast, when the negative voltage was applied, the signal of electrons was detected, corresponding obviously to the hopping between perylene diimide cores.

In the TOF method, the absorption of light pulse leads to creation of excitons. Then, due to the electric field they dissociate into free electrons and holes. Depending on the sign of voltage applied, one kind of carriers flow through the sample and the other ones were absorbed by the first electrode. Thus, after initial rise, the photocurrent should only decrease, as all the carriers were created

immediately after the pulse. However, a clear increase of the **TP** photocurrent in the 1-20 µs range could be observed, after a fast decay, when excited by 337 nm laser pulse (see inset in Figure 2.30.a). Moreover, the transit time was clearly visible, even in *lin-lin* scale, which is highly uncommon for such experimental conditions.

This uncommon increase of transient photocurrent did not occur when the sample was excited at 508 nm which is directly in the perylene absorption band. The electron mobility was determined to be equal to $5.3X10^{-5}$ cm^2/Vs irrespectively of the excitation wavelength, and remained independent on the electric field within the experimental range of 125-250 kV/cm. The energy of 508 nm laser pulse was significantly lower than the pulse emitted at the wavelength of the pump laser (337 nm), which explains why the photocurrent in Figure 2.30.b is lower than in Figure 2.30.a.

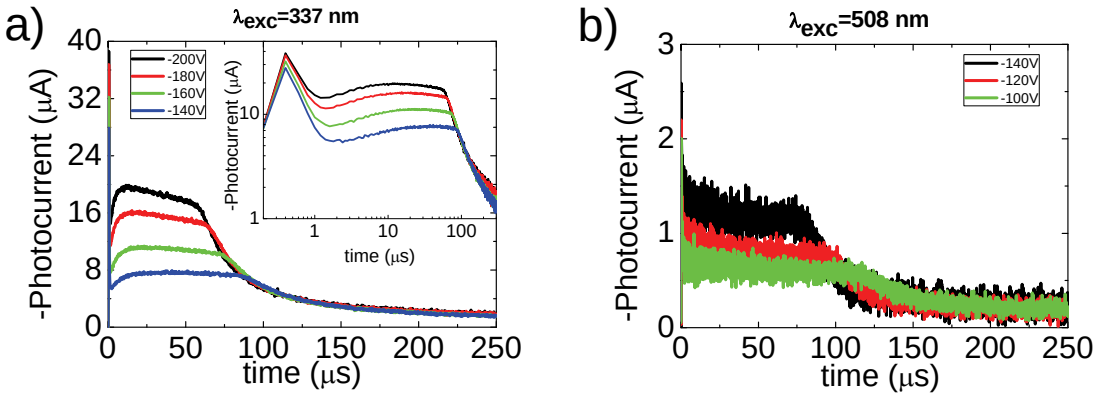

*Figure 2.30. Dyad **TP** photocurrent curves excited at a) 337 nm and b) 508 nm wavelength, recorded at 200°C in the isotropic phase. The inset in a) displays the curves in log-log scale.*

Based on these observations, a model was proposed to explain this uncommon behavior of transient photocurrents in the isotropic state of **TP**. The model is based on the assumption that the 377 nm laser beam creates excitons in triphenylene sites. These excitons can either move to another triphenylene moiety or transfer energy to perylene moiety then move to another perylene site. Here, it should be noticed that the triphenylene excitons are singlets while perylene excitons decay into long-lived triplet states. In case of organic semiconductors, generally, charge separation can occur only at the metal-organic semiconductor interface, after exciton diffusion. However, we postulated that in the case of **TP**, the exciton dissociation can also occur at the **TP**-ITO electrode interface, or in the bulk between triphenylene and perylene diimide, which has been previously reported for molecules with similar structure [262, 280] . The bulk dissociation would result in the observation of two components in the transient photocurrent, for holes and electrons flow, respectively. In electric field the carriers flow in opposite directions, but their currents sum up.

The electrochemical study (see Paragraph 2.5) on **TP** confirms that after charge separation, electrons tend to stay on perylene moieties and holes on triphenylene moieties. This is another positive proof for the previous model.

2.7 Conclusion

In this chapter, the design and synthesis of a family of discotic liquid crystal molecules were described. Their thermal behaviors, self-organization properties, optical and electronic properties are discussed.

The triphenylene-perylene based dyad **TP** and triad **TPT** together with the triphenylene-naphthalene based triad **TNT** present liquid crystalline properties. All of these three liquid crystalline molecules self-organize into well defined columnar nanostructures and these organizations can be preserved after cooling to room temperature. That means the organization could be self-healed in the liquid crystal phase and then be maintained until room temperature.

Then studies were carried out both in solid state films and in solutions particularly on the triphenylene-perylene dyad **TP**. AFM and GIXS measurements on **TP** solid films prove that this dyad can self-organize into hexagonal columnar structures and orientated on parallel to the silicon wafer substrate surface. This is a promising property in the domain of organic transistors where the 2D orientation is a key factor for the transistor performance. Then through the absorption/emission spectra in solution, a photon transfer from triphenylene moiety to perylene moiety was observed. Combining the concentration dependent absorption spectra in a bad solvent and absorption spectra of solid state film, the molecular aggregation properties was further studied.

The electrochemical behaviors of these molecules confirmed their ambipolar properties. As the donor and acceptor moieties are linked by long alkane chains, their initial electrochemical properties can be preserved. With the columnar self-organization, we can then envisage a separate ambipolar charge transport inside of this material.

With a preliminary time of flight study on dyad **TP**, an untypical charge transport was observed in its isotropic state which could be explained by the same photon transfer in solution absorption. Unfortunately, in the liquid crystal and solid state, neither TOF nor OFET have revealed any mobility. The short correlation distance in the columnar and non-optimized orientation could be the two main reasons. To surmount this, chemical modifications can be done onto the individual moieties to prolong the correlation distance and other deposition methods can be tried to have a better control on 3D orientation.

Thus, we can conclude that, via this design strategy, a family of self-organized liquid crystalline ambipolar molecules was prepared. With their self-organization and orientation properties, photon transfer properties, this family of molecules can be interesting candidates in the domains of organic electronics and potonics.

2.7 Experimental

2.7.1 TOF configurations

The TOF measurements carried out in this chapter were in the most fundamental configuration, i.e. no CGL was used. Standard liquid crystal cells with Indium-Tin-Oxide (ITO) as semitransparent electrodes with thickness of 8 μm were purchased from Instec Inc. The compound **TP** (in powder) was placed in the vicinity of one entrance of the cell and heated to isotropic state. Then, it flowed into the cell by capillary forces.

The samples are then mounted in the TOF setup, using a home-built polarizing microscope and a microscopic hot stage (Instec HCS302). Multiple in-situ transitions between the liquid crystalline and isotropic states are carried out to significantly increase the domain size and to be able to reduce the effects of the grain boundaries on the charge transport. The samples are excited by a nitrogen nanosecond pulsed laser (LTB Lasertechnik Berlin GmbH, model MNL 205-L) emitting at 337 nm with a repetition rate of 1.8 Hz. The photogeneration of a sheet of photocarriers in the samples leads to a transient photocurrent signal, which is amplified and then recorded by a Tektronix TDS 5034 350 MHz digital oscilloscope.

2.7.2 Synthesis

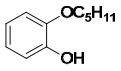

Chemical Formula: $C_{11}H_{16}O_2$
Molecular Weight: 180.2435

2B

Prepared as **2C** except the feeding ratio between catechol and 1-bromopentane which was modified as 1:1 to give the title compound (12.8 g, 79%) as a yellow oil; NMR δ_H (ppm) (200 MHz, $CDCl_3$) 6.90 (4H, m, H_{arom}), 5.67 (1H, s, -OH), 4.04 (2H, t, $-OCH_2-$) 1.84 (2H, m, H_{aliph}), 1.44 (4H, m, H_{aliph}), 0.94 (3H, t, J 6.9, $-CH_3$).

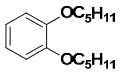

Chemical Formula: $C_{16}H_{26}O_2$
Molecular Weight: 250.3764

2C

Catechol (10 g, 0.09 mol), 1-bromopentane (25 mL, 0.20 mol), potassium carbonate (50 g, 0.36 mol), potassium iodide (0.94 g, 6 10^{-3} mol) and a catalytic amount of tetrabutylammonium bromide were added to absolute ethanol (200 mL) under an atmosphere of argon. The light pink mixture was heated at reflux for 24h, cooled down to room temperature and extracted with dichloromethane (100 mL). The organic layer was successively washed with water (3 x 50 mL), dried over $MgSO_4$, filtered and the solvent removed under reduced pressure. The crude product was filtered through a short plug

of silica gel using a 1:1 mixture of DCM/Hexane to yield **2C** (18.79 g, 83%) as a yellow oil; NMR δ_H (ppm) (250 MHz, $CDCl_3$) 6.90 (4H, s, H_{arom}), 4.01 (4H, t, J 6.6, -OCH_2-), 1.84 (4H, m, H_{aliph}), 1.44 (8H, m, H_{aliph}), 0.94 (6H, t, J 6.9, -CH_3).

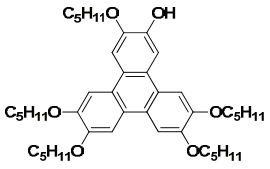

Chemical Formula: $C_{43}H_{62}O_5$
Molecular Weight: 674.9488

2D

Acetonitrile is added drop-wisely to a well-stirred suspension of Iron (III) trichloride (3.24 g, 20 mmol) in anhydrous dichloromethane (20 mL) until the initially observed suspension becomes solution. This new solution is cooled by an ice bath to about 0°C. 30 minutes after, a solution of **2B** (1.0 g, 4 mmol) and **2C** (0.36 g, 2 mmol) in 15 mL of anhydrous dichloromethane was added carefully, drop by drop at 0°C. The reaction was continued for 2 h at 0°C. MeOH (15 mL) was added to stop the reaction and the mixture was washed twice with HCl (5%, 20 mL) and brine (20 ml). The organic layer was dried with $MgSO_4$, and the solvents were removed under reduced pressure. The crude product was purified by column chromatography (silica gel, DCM/hexane 1:1) and afforded **2D** (0.3 g, 22%); NMR δ_H (ppm) (200 MHz, $CDCl_3$) 7.98-7.75 (6H, m, H_{arom}), 5.91 (1H, s, OH), 4.23 (10H, m, -O-CH_2-), 1.95 (10H, m, H_{aliph}), 1.65-1.35 (20H, m, H_{aliph}), 0.97 (15H, t, J 6.9, -CH_3); δ_C (50 MHz, $CDCl_3$) 149.23, 149.08, 148.90, 148.83, 145.94, 145.35, 124.03, 123.78, 123.72, 123.65, 123.32, 123.08, 107.6, 107.42, 107.25, 106.51, 104.39, 69.97, 69.94, 69.68, 69.21, 69.17, 29.30, 19.25, 29.16, 29.12, 28.51, 28.48, 28.45, 28.42, 22.71, 22.68, 22.67, 14.26, 14.23, 14.20.

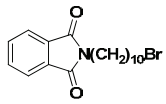

Chemical Formula: $C_{18}H_{24}BrNO_2$
Molecular Weight: 366.2927

2F

2E (3.7 g, 20 mmol) and 1,10-dibromodecane (30 g, 100 mmol) were mixed in DMF (50 mL) and heated at 100 for 12 hours. The condenser was then changed to a set for distillation, and the excess of 1,10-dibromodecane and DMF were distilled off under reduced pressure. The crude product was finally purified by column chromatography (silica gel, ethyl acetate/petroleum ether 1:4) to afford a colorless solid (5.27 g, 72%). NMR δ_H (ppm) (200 MHz, $CDCl_3$): 7.84 (m, 2H), 7.71 (m, 2H), 3.68 (t, 2H), 3.40 (t, 2H), 1.87-1.63 (m, 4H), 1.43-1.28 (m, 12H).

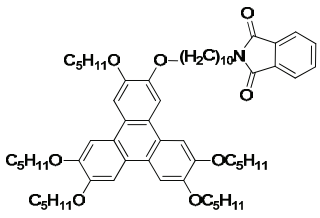

Chemical Formula: $C_{61}H_{85}NO_8$
Molecular Weight: 960.3295

2G

A mixture of **2D** (2.2 g, 3.26 mmol), **2F** (2.39 g, 6.52 mmol), and potassium carbonate (4.5 g, 32.6 mmol), KI (cata), TBAB (cata) in DMF (30 ml) was heated under reflux for 2 days. After cooling to room temperature, 100 ml of dichloromethane was added. The organic solution was washed with water (200mL) twice, and brine (100 ml) and dried over $MgSO_4$. After the solvent was removed under reduced pressure, the resulting residue was purified by column chromatography (silica gel, ethyl acetate / petroleum 1:9) to give **2G** (2.57 g, 82%) as a pale yellow solid. NMR δ_H (ppm) (200 MHz, $CDCl_3$) 7.83 (m, 8H), 7.71-7.67 (m, 2H), 4.23 (t, 12H), 3.67 (t, 2H), 2.02-1.88 (m, 12H), 1.60-1.39 (m, 34H), 0.97 (t, 15H).

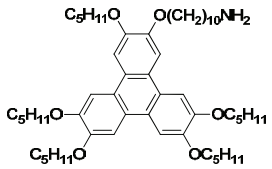

Chemical Formula: $C_{53}H_{83}NO_6$
Molecular Weight: 830.2292

2H

2G (1.3 g, 1.35 mmol) was dissolved in hot ethanol (20 ml) and the mixture was refluxed. Hydrazine hydrate (80 mg) was added to the mixture, and the reaction mixture was refluxed for 1h. The reaction mixture was allowed to cool and neutralized with 5 wt% aqueous HCl, and then, refluxed again for 30 min. The reaction mixture was cooled, and the precipitate was filtrated off. The solvent was evaporated, and the obtained residue was poured into 5 wt% aqueous KOH, then the product was extracted with $CHCl_3$, dried (MgSO4) and concentrated. **2H** was obtained quantitatively as a colorless solid. NMR δ_H (ppm) (200 MHz, $CDCl_3$) 7.83 (s, 6H), 4.23 (t, 12H), 2.68 (t, 2H), 2.02-1.88 (m, 12H), 1.66-1.32 (m, 36H), 0.97 (t, 15H).

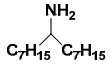

Chemical Formula: $C_{15}H_{33}N$
Molecular Weight: 227.4292

2J

A solution of **2I** (4.5 g, 20 mmol) in 60 mL of ethanol and 30 mL of pyridine was added by 2.8 g (40 mmol) of hydroxylamine hydrochloride and then heated to 100°C for 2 h. The resulting mixture was concentrated by rotary evaporation and the residue was extracted between 5% HCl (aq) and

hexanes. The organic layer was then dried over $MgSO_4$ and after evaporating the solvent again, yielded to 4.6 g (95%) of 8-pentadecanone oxime as yellowish viscous liquid.

The oxime was dissolved in 80 mL of toluene. About 10 mL was distilled off to dry the system, and then the system was protected under nitrogen atmosphere. RedAl (Sodium bis(2-methoxyethoxy)aluminum hydride, 70% in toluene) were added over 5 min then the reaction mixture was refluxed for 2 h. The resulting mixture was carefully added, under stirring, by 100mL of 5% HCl; then more concentrated HCl was introduced to dissolve aluminum salts and render the mixture acidic to litmus. The solution was extracted by hexane and the organic layer was washed with 5% NaOH, dried, and the solvent was removed by rotary evaporation to yield 4.3 g (99%) of **2J**. NMR δ_H (ppm) (200 MHz, $CDCl_3$): 2.68 (m, 1H), 2.14 (br, 2H), 1.20 (m, 32H), 0.81 (t, 6H).

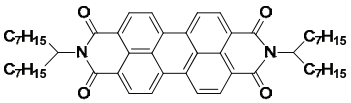

Chemical Formula: $C_{54}H_{70}N_2O_4$
Molecular Weight: 811.1446

2L

A mixture of **2K** (3g, 7.56 mmol), $Zn(OAc)_2$, (1.0 g, 5.67 mmol), imidazole (15 g) and **2J** (4.3g, 18.9 mmol) was stirred at 160 °C for 4 h. After cooling to room temperature, the mixture was dissolved in minimum amount of chloroform and purified directly by column chromatography (silica gel, chloroform) to give **2L** (4.94 g, 81%) as a red solid. NMR δ_H (ppm) (200 MHz, $CDCl_3$): 8.64 (m, 8H), 5.20 (m, 2H), 2.25 (m, 4H), 1.86 (m, 4H), 1.21 (m, 40H), 0.85 (m, 12H).

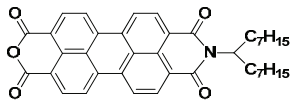

Chemical Formula: $C_{38}H_{39}NO_5$
Molecular Weight: 601.7307

2M

To a mixture of **2L** (1.1g, 1.36 mmol) and *t*-BuOH (34 mL) was added 85% KOH powder (0.45 g). The resulting mixture was refluxed at 90°C and the conversion was monitored via TLC ($CHCl_3$/AcOH). After complete disappearance of **2L**, the mixture was poured slowly (under stirring) into AcOH (34 mL) and stirred for 2h. Then 2N HCl (14 mL) was added and stirring was continued for additional 30 min. The resulting precipitate was collected by filtration, washed with water until the washings were neutral and dried at 80 °C in vacuum. The crude product was further purified by column chromatography on silica gel with $CHCl_3$ to remove bisimide and then with $CHCl_3$/AcOH 10:1 to elute the product. 2**I** was obtained as a dark red solid: 0.35 g, 43%. NMR δ_H (ppm) (200 MHz, $CDCl_3$): 8.66 (8H, m), 5.20 (m, 1H), 2.25 (m, 2H), 1.86 (m, 2H), 1.21 (m, 20H), 0.85 (m, 6H).

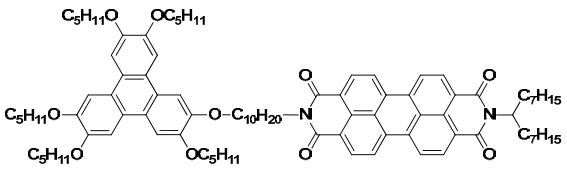

TP

2H (300 mg, 0.36 mmol), **2M** (217 mg, 0.36 mmol) zinc acetate (66.3 mg, 0.36 mmol) and imidazole (2.0 g) were added under stirring. The mixture was heated to 160°C for 2 h under Ar before it was cooled to room temperature. The solid mixture was dissolved in chloroform and was purified by column chromatography (silica gel, ethyl acetate/hexane, 1:3-1:4), and recrystallized from chloroform to methanol to give **TP** (381 mg, 75%) as a dark violet solid. NMR δ_H (ppm) (500 MHz, $CDCl_3$) 8.52-8.11 (8H, m, H_{arom}), 7.54-7.37 (6H, m, H_{arom}), 5.19 (1H, m, N-CH), 4.16-4.00 (14H, m, -O-CH_2-, N-CH_2), 2.27 (2H, m, H_{aliph}), 1.94 (14H, m, H_{aliph}), 1.73 (2H, m, H_{aliph}), 1.64-1.24 (54H, m, H_{aliph}), 1.01-0.96 (15H, m, H_{aliph}), 0.96-0.84 (6H, m, H_{aliph}); δ_C (ppm) (125 MHz, $CDCl_3$) 163.126, 148.733, 134.178, 134.006, 130.679, 129.333, 128.814, 125.996, 125.943, 123.340, 123.270, 123.231, 123.161, 122.912, 122.627, 122.478, 107.001, 106.894, 106.698, 106.604, 106.573, 106.492, 69.705, 69.660, 69.511, 69.429, 69.347, 54.892, 40.642, 32.545, 32.004, 29.750, 29.440, 29.404, 29.286, 29.005, 28.905, 28.811, 28.657, 28.553, 28.517, 27.795, 27.280, 26.866, 25.874, 22.770, 22.749, 14.293, 14.268, 14.222. HRMS calcd. for $C_{92}H_{120}N_2O_{10}Na^+$: 1435.884; found 1435.882. Elemental Analysis: calcd.for $C_{92}H_{120}N_2O_{10}$: C, 78,15; H, 8.55; N, 1.98; O, 11.32. Found: C, 78.58; H, 8.74; N, 1.92; O, 11.06.

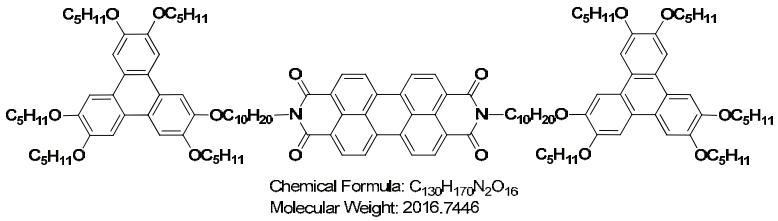

TPT

2H (300mg, 0.36 mmol), and zinc acetate (27 mg, 0.123 mmol) were dissolved in 2g of imidazole at 160°C under stirring. Then compound **2K** (64.4 mg, 0.164 mmol) was added. After 2 hours, the mixture was cooled to room temperature, and extracted with 150 mL of chloroform, washed by 100 mL 20% HCl and then washed by 100 mL brine successively. The organic phase was then dried over anhydrous $MgSO_4$ and concentrated under reduced pressure. The crude product was submitted to column chromatography on silica gel using DCM/MeOH=10/1 as eluant to yield the **TPT** (150 mg, 45%). NMR δ_H (ppm) (200 MHz, $CDCl_3$) 8.22-8.18 (4H, H_{arom}, perylene), 7.87-8.83 (4H, H_{arom}, perylene), 7.50-7.42 (12H, H_{arom}, triphenylene), 4.16-4.01 (28H, m), 1.93 (28H, m, H_{aliph}), 1.49 (62H, m, H_{aliph}), 0.97 (30H, t, H_{aliph}); MALDI-TOF: calcd. for $C_{130}H_{170}N_2O_{16}+Na^+$ 2039.734; Found

2039.545. Elemental Analysis: calcd. for $C_{130}H_{170}N_2O_{16}$: C, 77,42; H, 8.50; N, 1.40; O, 12.70. Found: C, 77.32; H, 8.89; N, 1.71; O, 12.79.

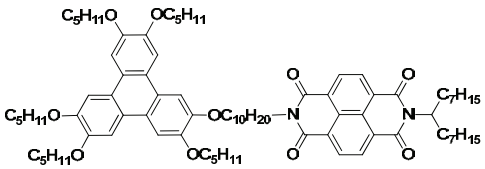

TN

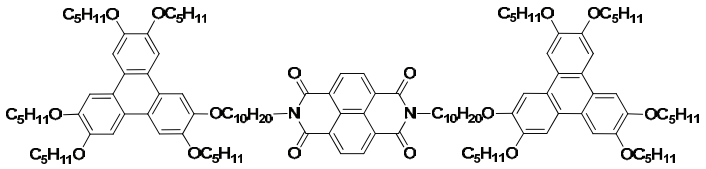

TNT

A mixture of **2N** (269 mg, 1.0 mmol), **2H** (830mg, 1.0 mmol), **2J** (227 mg, 1.0 mmol), and zinc acetate (147 mg, 0.8 mmol) in 3.0 g of imidazole was stirred at 160°C for 2.5 hours. After being cooled to room temperature, this mixture was extracted with 150 mL of chloroform and the organic phase was washed by 100 mL 20% HCl then, by 100 mL brine successively. The organic phase was dried over anhydrous $MgSO_4$ and concentrated under reduced pressure. The crude product was submitted to column chromatography over silica gel using dichloromethane as eluant to yield the **TNT** (373 mg, 20%) and the **TN** (430 mg, 33%).

Triad TNT

NMR δ_H (ppm) (200 MHz, $CDCl_3$) 8.41 (4H, s, H_{arom}), 7.68-7.71 (12H, m, H_{arom}), 4.21 (24H, t, O-CH_2), 4.05 (4H, t, N-CH_2), 1.89-2.02 (28H, m, H_{aliph}), 1.40-1.59 (64H, m, H_{aliph}), 0.98 (30H, t, H_{aliph}); δ_C (ppm) (25 MHz, $CDCl_3$) 162.71, 149.05, 149.01, 123.50, 107.11, 69.70, 29.29, 28.53, 22.74, 14.27. MALDI-TOF: calcd. for $C_{120}H_{166}N_2O_{16}H^+$ 1892.232; Found 1892.057. Elemental Analysis: calcd. for $C_{120}H_{166}N_2O_{16}$: C, 76,15; H, 8.84; N, 1.48; O, 13.53. Found: C, 76.46; H, 9.33; N, 1.43; O, 13.57.

Dyad TN

NMR δ_H (ppm) (200 MHz, $CDCl_3$) 8.66 (4H, H_{arom}, naphthalene), 7.80-7.73 (6H, H_{arom}, triphenylene), 5.15 (1H, m, N-CH), 4.26-4.07 (14H, m), 2.23-2.16 (2H, m, H_{aliph}), 2.02-1.88 (14H, m, H_{aliph}), 1.64-1.20 (54H, m, H_{aliph}), 0.98 (15H, t, H_{aliph}); 0.82 (6H, t, H_{aliph}); δ_C (ppm) (25 MHz, $CDCl_3$) 162.91, 149.08 149.05, 130.86, 126.43, 123.63, 107.25, 69.75, 32.43, 31.90, 29.60, 29.33, 29.29, 28.53, 27.10, 22.73, 14.27, 14.19. MALDI-TOF: calcd. for $C_{82}H_{166}N_2O_{10}H^+$ 1289.871; Found 1289.371. Elemental Analysis: calcd. for $C_{82}H_{116}N_2O_{10}$: C, 76,36; H, 9.07; N, 2.17; O, 12.40. Found: C, 77.12; H, 9.59; N, 2.08; O, 12.50.

CHAPTER 3 SYNTHESIS AND CHARACTERISATION OF DONOR AND DONOR-σ-ACCEPTOR SMECTIC LIQUID CRYSTAL DYADS

In this chapter, we will study two liquid crystalline dyads, combining p-type and n-type calamitic derivatives. This strategy could lead to ambipolar lamellar nanostructured materials presenting two-dimensional charge transport in the sublayers. These architectures are based on terthiophene derivatives as donor moiety and pyromellitic diimide as acceptor moiety linked by alkyl chain spacers.

Thus, two dyads have been designed: the first one is a donor-σ-donor model dyad based on calamitic terthiophene building blocks [86, 255] in order to demonstrate that we can achieve a lamello-lamellar organization; the second one is a donor-σ-acceptor dyad in order to obtain a lamello-lamellar organization exhibiting ambipolar charge transport properties. The chemical structures of these calamitic dyads are given in Figure 3.1.

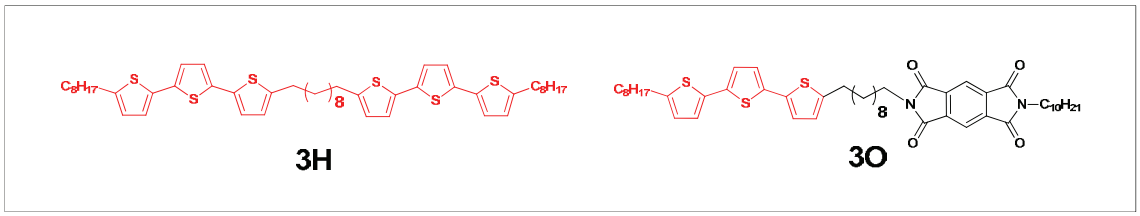

Figure 3.1 Chemical structures of the target calamitic dyad series

In this work, we will describe and discuss the synthesis, the thermal behavior, the self-organization, the optical, electrochemical and charge transport properties of this molecule family.

3.1 Synthesis

3.1.1 Synthesis of model donor-σ-donor calamitic dyad based on terthiophene moieties

The convergent synthetic route of the model calamitic dyad **3H** is shown in Figure 3.2.

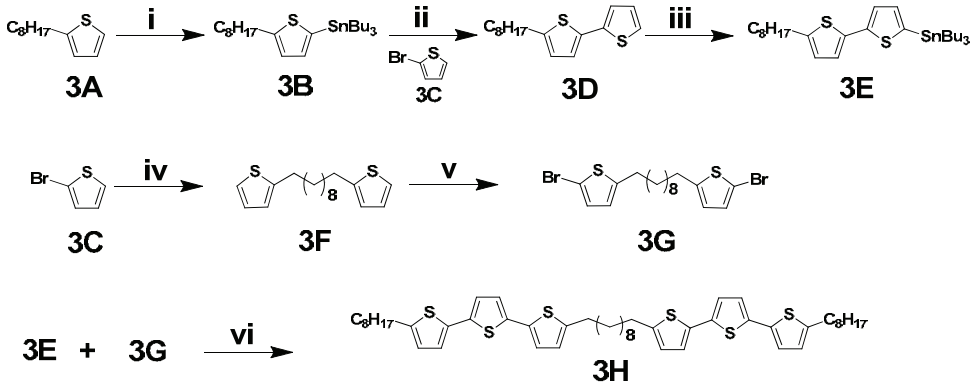

*Figure 3.2 Synthesis of the model calamitic dyad **3H** based on terthiophene moieties. Conditions: i) n-BuLi, THF, -78°C; $ClSnBu_3$, 81%. ii) $Pd(OAc)_2$, PPh_3, THF; DMF, 85°C, 39%. iii) n-BuLi, THF, -78°C; $ClSnBu_3$, 83%. iv) n-BuLi, 0°C, 1,10-dibromodecane, 29%. v) NBS, DMF, 70%. vi) $Pd(OAc)_2$, PPh_3, THF; DMF, 85°C, 47%.*

The building block **3E** was prepared from the commercially available 2-octylthiophene **3A**, which was first converted into its stannane derivative in quantitative yield before a Stille coupling with the 2-

bromothiphene **3C** [281-284], leading to the 2-octylbithiophene **3D**. **3D** was finally converted into its stannane derivative to lead to the building block **3E**.

Concerning the building block **3G**, it was prepared from the commercially available 2-bromothiophene **3C** which was first linked to another 2-bromothiophene by lithiation with n-butyllithium followed by quenching with a long dibromoalkane, to lead to the intermediate **3F**. Then, with N-bromosuccinimide (NBS), the building block **3G** was obtained in a satisfactory global yield.

Finally, the two previous building blocks **3E** and **3G** were combined through a Stille coupling reaction, to reach the target dyad **3H** based on terthiophene moieties.

3.1.2 Synthesis of donor-σ-acceptor calamitic dyad based on terthiophene and pyromellitic diimide moieties

The synthetic route of the donor-σ-acceptor calamitic dyad **3O** is shown in Figure 3.3.

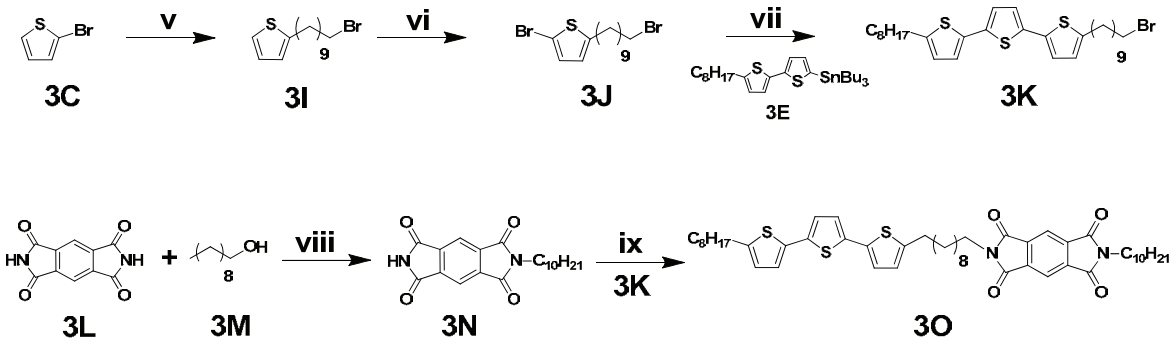

*Figure 3.3 Synthesis of the donor-σ-acceptor calamitic dyad **3O** based on terthiophene and pyromellitic diimide moieties. Conditions: v) n-BuLi, 0°C; 1,10-dibromodecane, 66%. vi) NBS, DMF, 67%. vii) $Pd(OAc)_2$, PPh_3, THF; DMF, 85°C, 58%.viii) 1-Decanol, DIAD, PPh_3, THF, 0°C; DMF, RT, 12%. ix) K_2CO_3, DMF, 120°C, 54%.*

The building block **3K** was prepared from the commercially available 2-bromothiophene **3C** which was first treated with n-butyllithium followed by being quenched with a large excess of a long dibromoalkane, to lead the intermediate **3I**. Then, **3I** was brominated with NBS to give the next intermediate **3J** which was finally combined through a Stille coupling with the building block **3E** previously prepared, to reach the donor building block **3K** with a satisfactory global yield.

The building block **3N** was simply prepared from the commercially available pyromellitic diimide **3L** which was attacked by the 1-decanol **3M** via a Mitsunobu reaction.

Finally, the two previous building blocks **3K** and **3N** were combined in a mild condition to lead to the donor-σ-acceptor calamitic dyad **3O**.

3.2 Thermal behavior

The thermal behavior of dyads **3H** and **3O** were investigated by Polarized-light Optical Microscopy (POM) and Differential Scanning Calorimetry (DSC).

3.2.1 Polarized-light Optical Microscopy

Under POM with crossed polarizers, the model dyad **3H** appeared as a birefringent yellowish powder which melted at around 121°C to give a birefringent and very viscous phase. On further heating, this viscous phase transformed at around 137°C into an isotropic fluid phase presenting no birefringence. On cooling from the isotropic state, the birefringent phase reappeared at around 134°C showing torical focal conic textures characteristic of a lamellar mesophase (Figure 3.4.a). On further cooling, the transition from the lamellar mesophase to crystal phase was clearly observed at around 110°C (Figure 3.4.b) and the crystal phase texture was then maintained unchanged until room temperature (Figure 3.4.c).

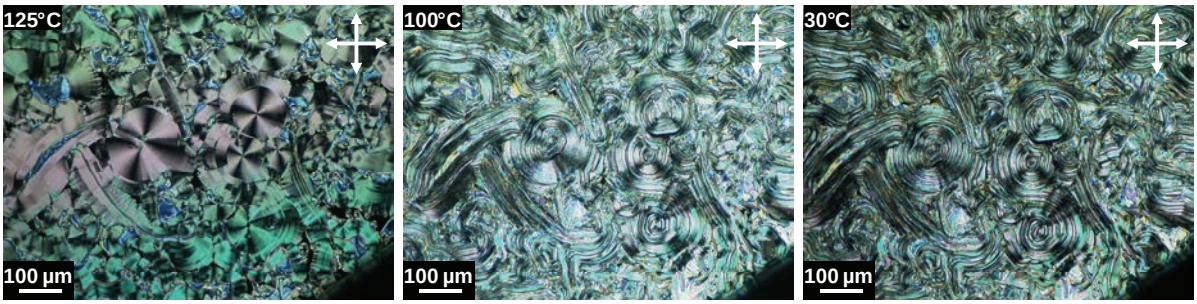

*Figure 3.4 Optical textures of the model calamitic dyad **3H** obtained on cooling from the isotropic state*

In the case of the donor-σ-acceptor calamitic dyad **3O**, this compound appeared as a birefringent slightly yellow powder under POM with crossed polarizers. On heating, the birefringent powder melted at around 149°C to give an isotropic fluid phase. On cooling from the isotropic state a highly viscous birefringent phase is observed at about 156°C showing a crystal-like texture and indicating the presence of a very ordered mesophase (Figure 3.5). On further cooling, this mesophase seems to be maintained until room temperature.

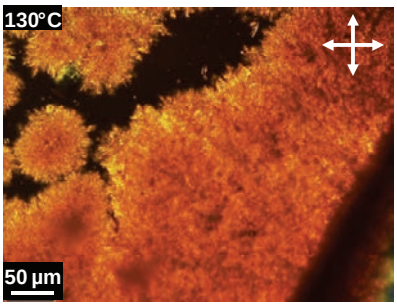

*Figure 3.5 Poptical texture of the donor-σ-acceptor calamitic dyad **3O** obtained at 150°C, cooling from the isotropic state.*

3.2.2 Differential Scanning Calorimetry

The DSC thermograms obtained for the dyads **3H** and **3O** coincide the typical thermal behavior of low-molecular weight liquid crystal molecules, containing endothermic transitions at high temperature and corresponding to crystalline phase/mesophase or mesophase/isotropic phase transitions in

agreement with the POM observations. The DSC traces of **3H** and **3O** are given in Figure 3.6 and the phase transition temperatures and enthalpy changes data are summarized in Table 3.1.

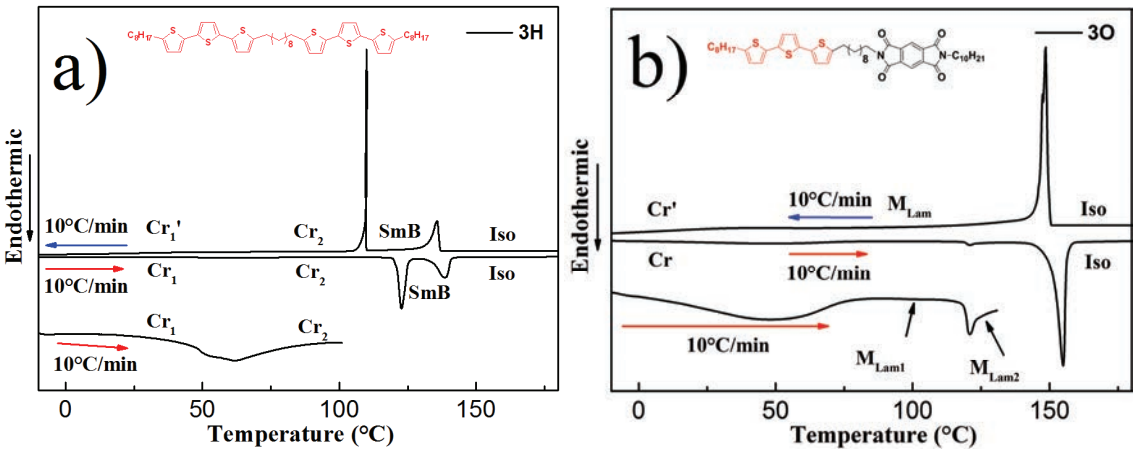

*Figure 3.6 DSC thermograms of dyads **3H** (a) and **3O** (b)*

The DSC thermogram of **3H** recorded on heating shows three endothermic peaks (Figure 3.6.a, table 3.1). The first weak and broad peak at 60.7°C (ΔH=1.5 J g^{-1}) can be attributed to a crystal/crystal transition ($Cr_1 \rightarrow Cr_2$). The large second peak at 120.9°C (ΔH=46.0 J g^{-1}) corresponds to the transition from the Cr_2 to the Smectic B phase ($Cr_2 \rightarrow SmB$, see the following paragraph), as also detected by POM. The last peak at 136.7°C (ΔH=29.2 J g^{-1}) can be associated to the transition from the SmB to the isotropic phase (SmB→Iso). On cooling and in agreement with observations on heating, the DSC trace shows also three peaks at 134.1°C (ΔH=29.2 J g^{-1}), 109.9°C (ΔH=45.7 J g^{-1}) and 44.2°C (ΔH=3.6 J g^{-1}) which can be attributed respectively to the Iso→SmB, SmB→Cr_2 and $Cr_2 \rightarrow Cr_1$' transitions. It is worth noticing that the high enthalpy value of the SmB→Iso transition and the slight delay for the SmB→Cr_2 transition temperature on cooling are fully consistent with the presence of ordered smectic mesophase such as SmB.

The DSC thermograms of **3O** recorded on heating shows three endothermic peaks (Figure 3.6.b, Table 3.1). The first weak and very broad peak at 45.0°C (ΔH=10.0 J g^{-1}) can be attributed to a progressive crystal/mesophase transition ($C_r \rightarrow M_{Lam1}$). The second weak peak at 119°C (ΔH=1.4 J g^{-1}) can be attributed to a mesophase/mesophase transition ($M_{Lam1} \rightarrow M_{Lam2}$). The last large peak at 148.9°C (ΔH=45.0 J g^{-1}) corresponds to the transition to the isotropic phase.

On cooling, the isotropic-mesophase transition took place at 148.9°C with hysteresis effect. Also, differently from heating, the tiny transition between two M_{Lam} disapeared, and only a very large mesophase-crystalline transition was observed at about 32.3°C.

The thermal behavoirs of both dyads are sammerized in Table 3.1.

		T (°C)	ΔH_{LC} (J g^{-1})	Transition	T (°C)	ΔH_{LC} (J g^{-1})	Transition	T (°C)	ΔH_{iso} (J g^{-1})	Transition
Dyad p-p 3H	Heating	60.7	1.5	$Cr_1 \rightarrow Cr_2$	120.9	46.0	$Cr_2 \rightarrow SmB$	136.7	29.2	$SmB \rightarrow Iso$
	Cooling	44.2	3.6	$Cr_2 \rightarrow Cr_1$'	109.9	45.7	$SmB \rightarrow Cr_2$	134.1	29.2	$Iso \rightarrow SmB$
Dyad p-n 3O	Heating	45.0	10.0	$Cr \rightarrow M_{Lam1}$	119.0	1.4	$M_{Lam1} \rightarrow M_{Lam2}$	148.9	45.0	$M_{Lam2} \rightarrow Iso$
	Cooling	32.3	10.1	$M_{Lam} \rightarrow Cr$	-	-	-	145.9	42.8	$Iso \rightarrow M_{Lam}$

*Table 3.1. Phase-transition temperatures and enthalpy changes of dyads **3H** and **3O***

3.3 Self-organization property study

3.3.1 Temperature dependent X-ray diffraction

To assess the unambiguous mesophases formation and probe the effects of the intimate structural modifications onto the mesophase temperatures ranges, the model and donor-σ-acceptor calamitic dyads **3H** and **3O** were studied by temperature dependent X-ray diffraction (TDXRD). The measurements were carried out in collaboration with Dr. B. Heinrich and Dr. B. Donnio at Institut de Physique et de Chimie des Matériaux de Strasbourg (IPCMS).

3.3.1.1 Model dyad **3H**

The Figure 3.7 shows the typical X-ray patterns of the model calamitic dyad **3H** recorded at room temperature (pristine, Cr_1), at 100°C (Cr_2) and at 125°C (SmB). The pristine state pattern (Figure 3.7.a) presents a great number of very sharp reflections indicative of a well-developed three-dimensional crystal lattice (Cr_1). The two reflections located at the small-angle region with a **d**-spacing ratio of 1:2 indicate that the molecules are arranged in a lamellar fashion in the pristine crystalline phase. The corresponding layer spacing at around 56 Å calculated with the Bragg's law from the first reflection, is compatible with an untilted parallel packing of mesogens in the layers. On heating above the transition detected by DSC at 51.4°C, we can also observe a clear reorganization of the pristine crystalline phase into a new crystalline phase Cr_2 as shown by the structure spacing (d≈41 Å) and by the appearance of a second small-angle periodicity (d'=15 Å) in the X-ray pattern recorded at 100°C (Figure 3.7.b). On further heating, the crystalline phase Cr_2 melted at 120°C to give a typical Smetic B phase (SmB), as shown by the X-ray pattern at 125°C (Figure 3.7.c). Indeed, this pattern contains in the small-angle region two sharp reflections related to the smectic layering of molecules, and in the wide-angle region, a diffuse halo and a broad peak both centered at 4.5 Å corresponding respectively to the liquid-like conformation of the alkyl chains and to the existence of a short-range hexagonal order within mesogen sublayers. The inter-lamellar spacing **d** of 54 Å, calculated from the first small-angle reflection, is

compatible with untilted or nearly untilted lamellae, confirming the SmB nature of the mesophase. A schematic representation of the organization of **3H** in SmB mesophase is given in Figure 3.7.d.

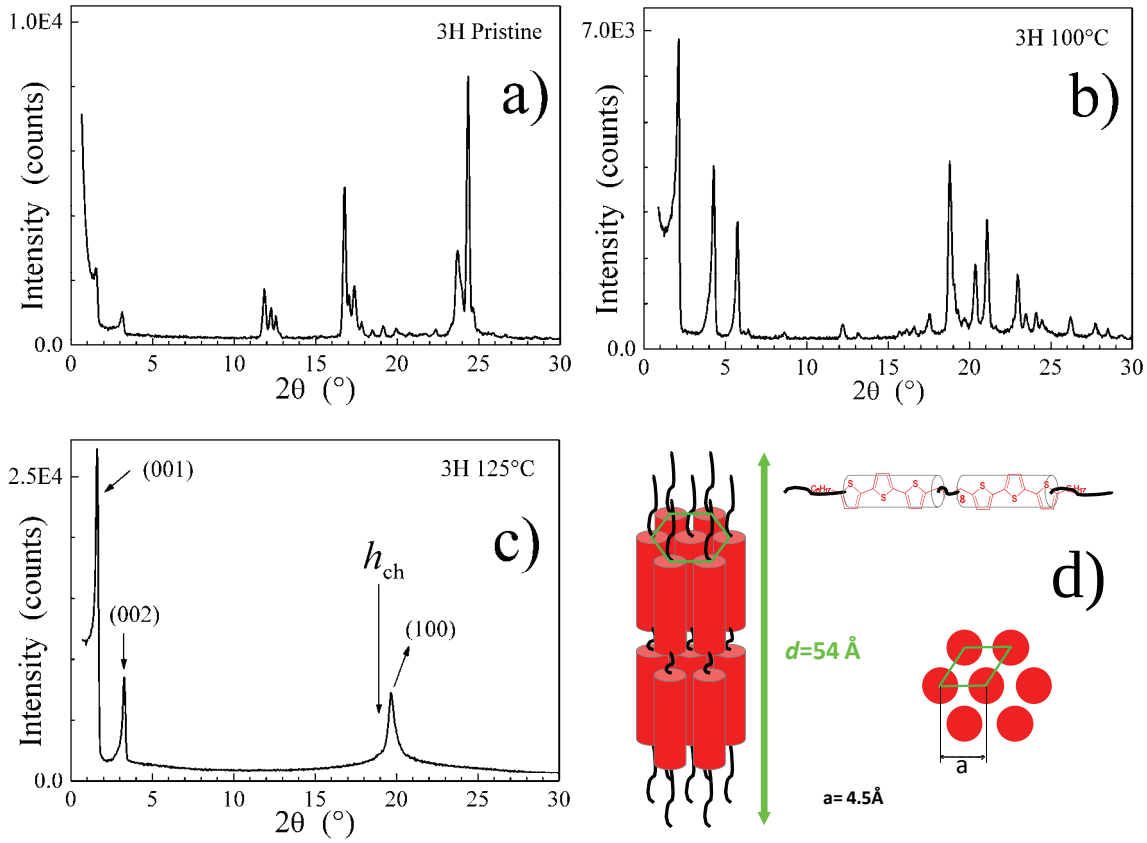

*Figure 3.7 X-ray diffraction patterns of model calamitic dyad **3H**: (a) Cr1 phase (pristine) at 20°C; (b) Cr2 phase at 100°C; (c) SmB phase at 125°C; (d) schematic representation of the SmB mesophase and the lattice parameters. ch=aliphatic chains, a=lattice constant.*

3.3.1.2 Model dyad **3H**

The Figure 3.8 shows the typical X-ray patterns of the donor-σ-acceptor calamitic dyad **3O** recorded at room temperature (pristine, Cr), at 80°C (M_{Lam1}) and at 120°C (M_{Lam2}). In the pristine state pattern (Figure 3.8.a), we can observe that the wide angle reflections are evidently broader compared to the model dyad **3H** and that numerous lamellar orders simultaneously appear in the small-angle region. This means the replacement of one terthiophene unit by pyromellitic diimide decreases the crystallinity of the lateral packing but still preserves the general crystalline lamellae organization presenting a good nano-segregation of molecular segments in well-defined sub-layers with flat interfaces. The layer spacing at around 52 Å, calculated from the first reflection, is compatible with a slight tilt of calamitic moieties in the layers.

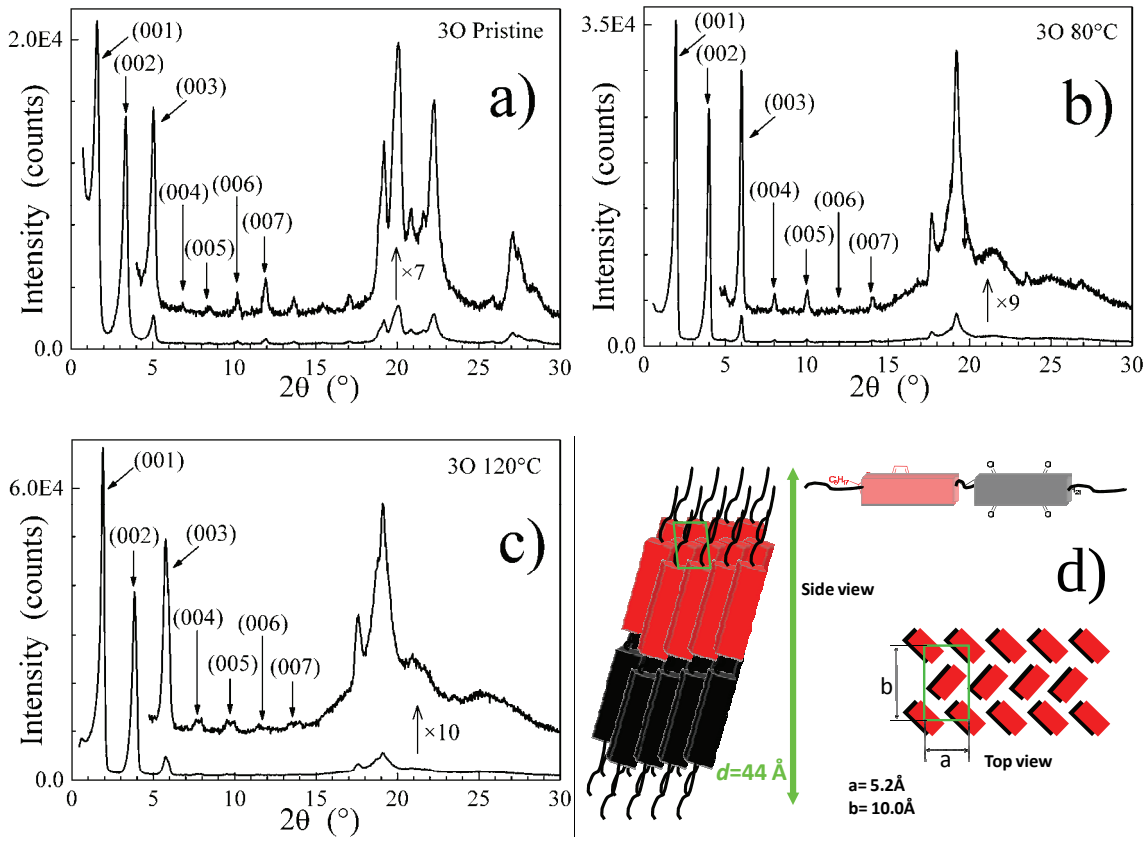

*Figure 3.8 X-ray diffraction patterns of donor-σ-bridge-acceptor calamitic dyad **3O**: (a) pristine, 20°C; (b) M_{Lam}1state, 80°C; (c)M_{Lam}2 state, 120°C; (d) schematic representation of the M_{Lam}1mesophase and the lattice parameters. a,b=lattice constants*

On heating above the broad transition detected by DSC at 45°C, we can observe as well a clear change of the X-ray pattern (Figure 3.8.b), characterized by the reduction of the layer spacing at around 44 Å, indicating a more compact interlayer organization and revealing the transition to a mesophase by the appearance of broad wide-angle scattering. With the melting process of the aliphatic chains, two residual broadened reflections around 5.0 and 4.6 Å might correspond to the bidimensional rectangular sub-lattice (a = 5.2 Å; b = 10.0 Å; Z = 2) of a 3D lamellar mesophase (M_{Lam1}). On further heating above the weak transition at 119°C, the new observed mesophase M_{Lam2} presents nearly the same mesomorphic structure as $M_{Lam}1$ except a slightly larger spacing (around 46 Å) due to tilt angle variation (Figure3.8.c). A schematic representation of the 3O organization is given in Figure 3.8.d.

3.3.2 Grazing-Incidence X-ray Scattering

The thin film structure and morphology of the calamitic dyads **3H** and **3O** were also studied by Grazing-Incidence X-ray Scattering (GIXS). These measurements were carried out at Pohang Accelerator Laboratory (PAL, Korea), in collaboration with Prof. H-J Kim (Pusan National University).

The **3H** and **3O** films were prepared by spin coating or thermal evaporation from a chloroform solution of material (0.25% w/w. 3000 rpm) onto bare silicon wafer. The thickness of films varies from 50 to 100 nm as evaluated by profilometer. These samples were studied after annealing (120°C for 2 hours in vacuum).

The typical two dimensional GIXS images of annealed samples of **3H** and **3O** are given in Figure 3.9.a and Figure 3.9.c., respectively. They both present several peaks in the specular plane (along q_z), corresponding to the (00l) reflections of the lamellar organizations. They also present numerous in-plane (along q_x) and out of plane peaks which can be assigned to the (hk0) and (hkl) reflections observed as well in the wide-angle region of the bulk X-ray diffraction patterns of **3H** and **3O** crystalline phases after annealing (Figure 3.9.b et 3.9.d).

These typical GISX patterns confirm the lamellar organization of both dyads in the polycrystalline annealed thin films and the edge-on orientation of molecules on the substrate with the layers parallel to the surface, as illustrated in schematic models in Figure 3.9.a and Figure 3.9.c.

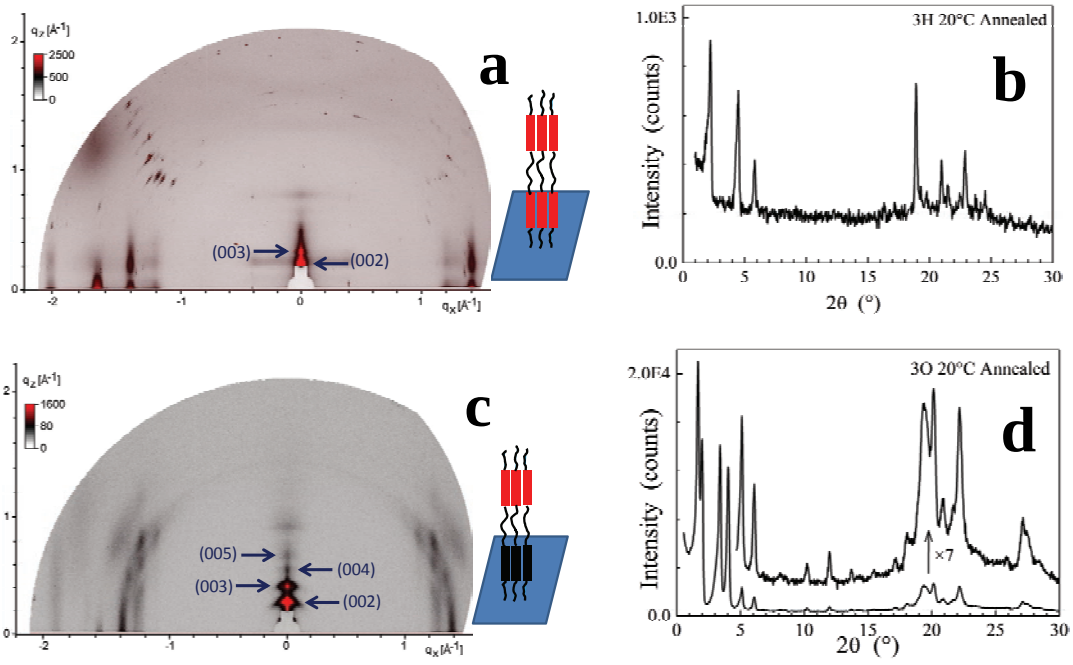

*Figure 3.9 Spin cast film GIXS patterns after annealing at 120°C (2 hours) of a) **3H** and c) **3O** on silicon wafer (with different contrast, red and black); grazing angle=0.12°. X-Ray diffraction patterns at 20°C on cooling of b) **3H** and d) **3O***

GIXS measurements were also performed on a thermal evaporated thin film of the model dyad **3H** on silanized (OTS) substrate with the same parameters as in the fabrication of OFET (Experimental 3.5.1). The elaboration of the thin film is described in the OFET experimental part. The two dimensional GIXS image is given in Figure 3.10 and presents lamellar peaks at once in-plane (along q_x) and out-of-plane (along q_z). That confirms the similar 3D crystalline organization which was observed previously with **3H** spin cast film, but also the presence of two different preferential lamellar orientations with the layers parallel and perpendicular to the substrate as illustrated in Figure 3.10.

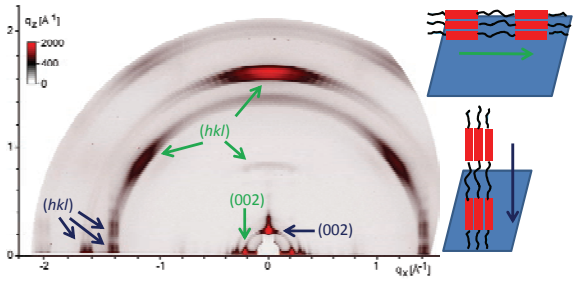

*Figure 3.10 GIXS patterns (with different contrast, red and black) of a thermal evaporated **3H** film on silanized (OTS) surface; grazing angle=0.12°*

3.4 Optical properties (absorption and emission)

The absorption and emission spectra of the terthiophene building block **3K**, the model pyromellitic diimide **3P** and the two dyads **3H** and **3O** in diluted solutions are given in Figure 3.11.

Not surprisingly, the absorption and emission spectra of the model dyad **3H** (Figure 3.11c) composed of two terthiophene moieties linked by an alkyl spacer chain presents very similar optical properties to the terthiophene moiety alone **3K** (Figure 3.11.a).

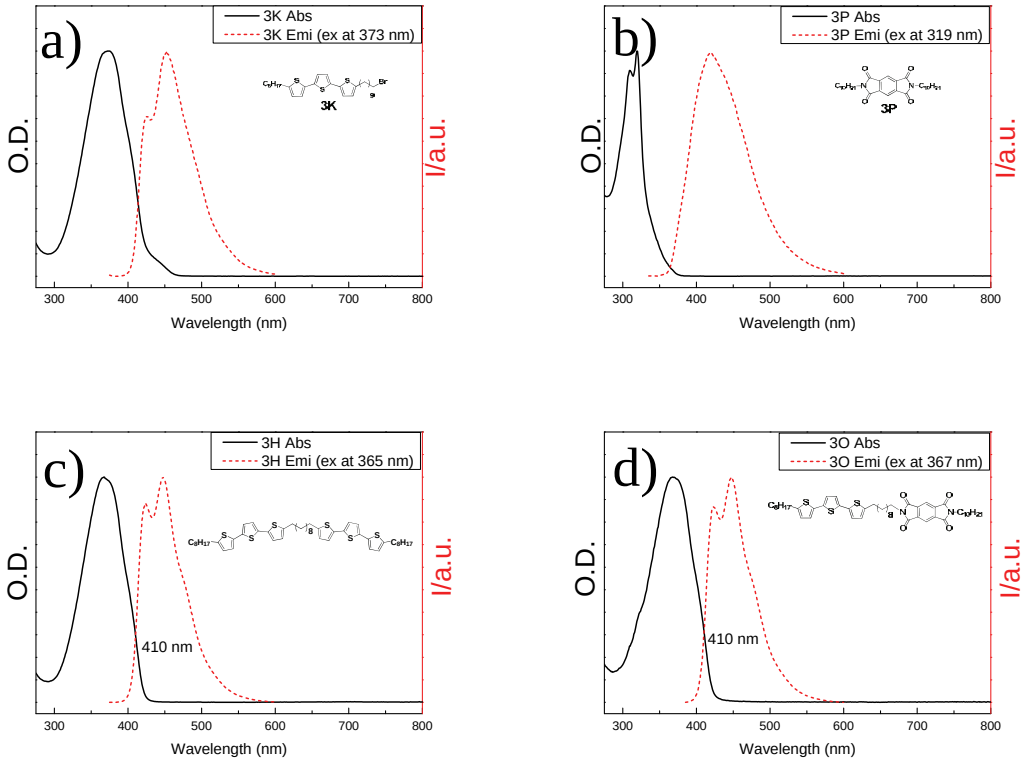

*Figure 3.11 Normalized absorption and emission spectrum of a) **3K (terthiophene)**, b) **3P (pyromellitic diimide)**,c) **3H** and d) **3O** in chloroform (c.a. 10^{-6} mol L^{-1})*

The absorption and emission spectra of the donor-σ-acceptor dyad **3O** (Figure 3.11.d) is quite similar to the model dyad **3H**. Indeed, the terthiophene moiety presents a stronger absorption than

pyromellitic diimide (Figure 3.12), and that is the reason why the absorption spectrum of **3O** is dominated by the terthiophene with just a tiny shoulder at around 320 nm which corresponds to the weak pyromellitic diimide absorption. Consequently, the absorption and emission maxima were measured at 378 nm and 447 nm for both dyads, respectively.

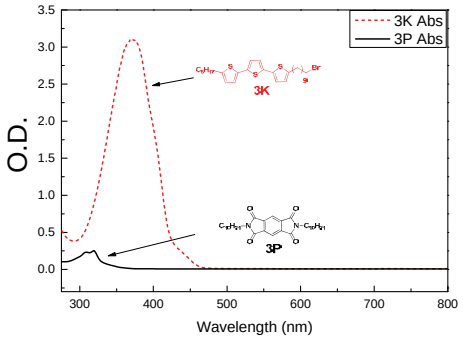

*Figure 3.12 Absorption spectrum of **3K** (terthiophene) and **3P** (pyromellitic diimide) in chloroform ($1.1x10^{4}$ mol L^{-1})*

3.5 Electrochemical behavior and HOMO/LUMO energies

The electrochemical behaviors of the model calamitic dyad **3H** and the donor-σ-acceptor calamitic dyad **3O** were studied using cyclic voltammetry (CV). The experimental conditions and optimized test parameters used are identical to those already described in Paragraph 2.5.

The voltammogram of the model dyad **3H** (Figure 3.13.a) shows only one reversible oxidation wave centered around 1.0 V (vs Ag/AgCl), which corresponds to the formation of the radical cations of terthiophene moieties. Concerning the donor-σ-acceptor calamitic dyad **3O** (Figure 3.13.b) constituted of one terthiophene (donor moiety) and one pyromellitic diimide (acceptor moiety), as expected we observe the same reversible oxidation wave around 1.0 V but also an additional reversible reduction wave around -0.87 V (vs Ag/AgCl), evidencing that both the acceptor and donor moieties behave separately.

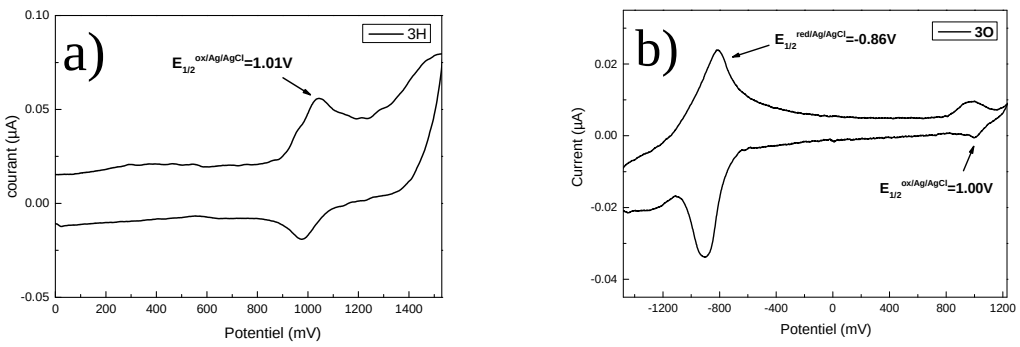

*Figure 3.13 Cyclic voltammograms of **3H** and **3O** (10^{-4} M) in 0.05 M Bu_4NPF_6 chloroform solution (scan rate: 0.05 V/s. Ferrocene as internal standard)*

Nevertheless, even though different kinds of experimental optimizations were carried out, there was always a difference in terms of integrated areas of oxidative and reductive waves in this voltammogram, as we should have a 1 to 1 ratio.

Thus, we can follow the same strategy and methodology described in Paragraph 2.5 to determine the HOMO and the LUMO energy levels of the donor-σ-acceptor dyad **3O** (Table 3.2).

But concerning the model dyad **3H**, as there is no acceptor moiety, the band gap cannot be determined by cyclic voltammetry. As a consequence, here we assume that its electric band gap equals to its optical band gap (E_g^{opt}) which can be approximately determined based on the intersection of its absorption and emission spectra, which is around 410 nm. Thus, the E_g^{opt} was estimated to be 3.00 eV in using the following equation:

$$E_g^{opt} = hv = \frac{hc}{\lambda} = \frac{(4.1 \times 10^{-15} eVs) \times (2.998 \times 10^{8} ms^{-1})}{\lambda}$$

where *h* is the Planks constant = 6.626 x 10^{-34} J s, *c* is the speed of light = 3.0 x 10^{8} m/s, and λ is given in nanometers (410 nm).

Consequently, its LUMO energy level can only be estimated by assuming that the electrochemistry gap is approximately equal to the optical gap (in this way, $E^{LUMO} = E^{HOMO} + E_g^{opt}$).

Compound	$E_{1/2}^{ox}$ **(V/Ag/AgCl)**	$E_{1/2}^{red}$ **(V/Ag/AgCl)**	E^{HOMO} **(eV)**	E^{LUMO} **(eV)**	E_g^{CV} **(eV)**	E_g^{opt} **(eV)**
3H **(p-p)**	1.01	-	-5.32	-2.32*	-	3.00
3O **(p-n)**	1.00	-0.86	-5.31	-3.94	1.37	-

*Table 3.2 Redox potentials and HOMO/LUMO values of the model and D-A dyads (*estimated)*

These values determined here are coherent with the corresponding values for terthiophene [255, 281-285] and pyromellitic diimide [286] reported in literature or other previous works [287].

3.6 Charge transport property study (OFET)

The charge transport properties of both model and donor-σ-acceptor dyads were investigated in OFET configurations. These measurements were carried out at CNRS-Ewha International Research Center (CERC, Korea), in collaboration with Prof. J.-W. Wu and Prof. J.-C. Ribierre (Ewha Womans University). The details about the transistor fabrication and measurement parameters are given in Paragraph 3.5.1.

3.6.1 Preliminary results of the model calamitic dyad 3H

As a preliminary measurement, the thin films of model calamitic dyad were spun cast on bare silicon wafer (SiO_2 surface) in bottom contact (BC) configuration. The output and transfer characteristics are shown in Figure 3.14.

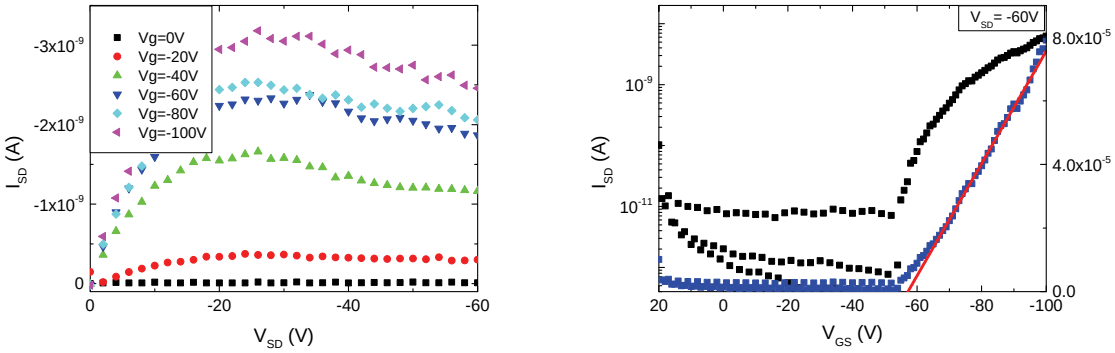

*Figure 3.14 Output (left) and transfer (right) characteristics (BC, SiO_2, **spun cast)** of* **3H**

The results of **3H** in this configuration gave a very low hole mobility of 8.3×10^{-7} $cmV^{-1}s^{-1}$ with very weak source-drain currents, probably due to a small grain size and a large density of boundaries in the solution-processed film [284]. The effect of annealing (at 120°C for 2 hours) on the transistors was not significant and no evident changes in output and transfer characteristics were observed.

Then thin film OFETs prepared by thermal evaporation on SiO_2 substrates were fabricated. Vacuum deposition is a film formation known to reduce the defects and thus improve the mobility. The output and transfer characteristic of evaporated devices are shown in Figure 3.15.

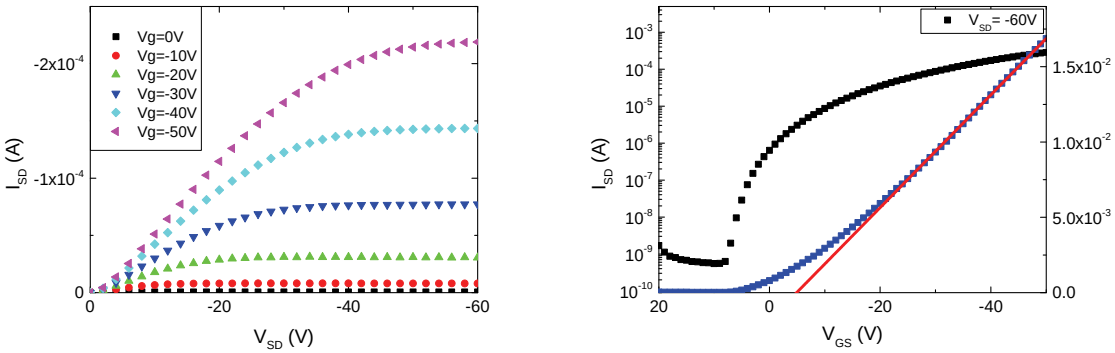

*Figure 3.15 Output (left) and transfer (right) characteristics (BC), SiO_2, **thermal evaporated)** of* **3H**

The results of evaporated thin film of **3H** on SiO_2 substrates gave a significant improvement on mobility with 5 orders of magnitudes to reach 1.9×10^{-2} $cmV^{-1}s^{-1}$.

Further, with the purpose to study the influence of thermal treatment of the thin film, the same OFET chips were then annealed at 120°C, namely in the SmB phase, during 2 hours (Figure 3.16) under nitrogen.

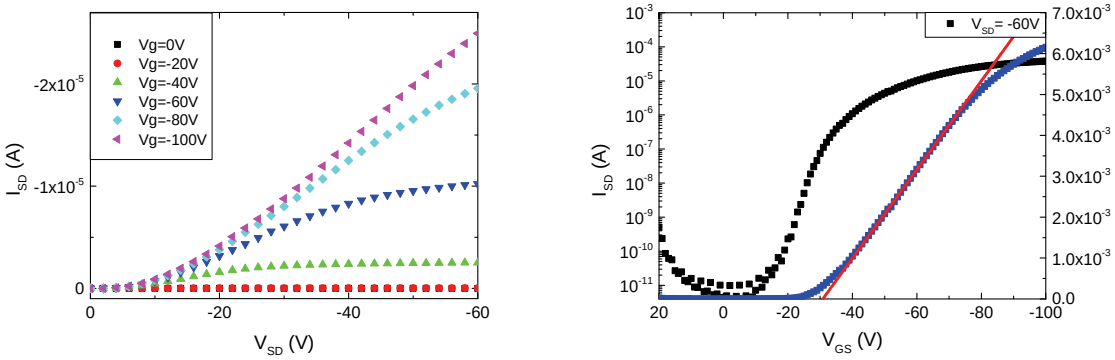

*Figure 3.16 Output (left) and transfer (right) characteristics (BC, SiO_2, **thermal evaporated, annealed)** of* **3H**

After annealing, the mobility decreased slightly around one order of magnitude to $1.6x10^{-3}$ $cmV^{-1}s^{-1}$ and the output gives a worse saturation with higher resistance of contact, indicating a reorganization of the thin film at the substrate surface.

Since the surface property of the substrate plays a very important role on the thin film molecular organization quality [288, 289] and thus can affect the charge transport properties, so further, OFETs based on silanized (OTS) SiO_2 substrates were fabricated and investigated as well (Figure 3.17).

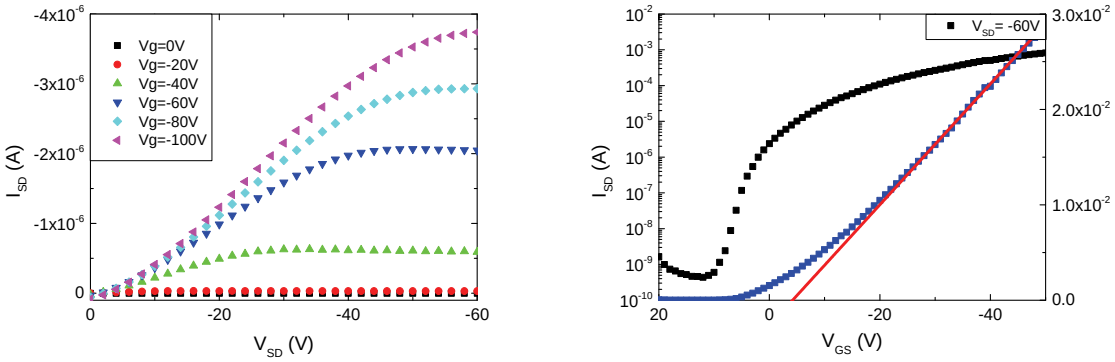

*Figure 3.17 Output (left) and transfer (right) characteristics (BC, OTS, **thermal evaporated)** of* **3H**

The mobility of evaporated thin film of **3H** on OTS surface was increased of one order of magnitude comparing to that on bare SiO_2 surface, to reach 0.1 $cmV^{-1}s^{-1}$. However, as already observed on the bare SiO_2 surface, the annealing decreased slightly the mobility to $5.2x10^{-3}$ $cmV^{-1}s^{-1}$. Top contact configurations were also attempted on both surfaces by evaporation, but no better OFET performances were obtained.

In order to better understand the thermal treatment influence in detail, more GISX and other measurements should be systematically carried out. This work is still in progress and further results will be discussed and published elsewhere in the soon future.

Mobilities, threshold voltage (V_{th}) and on/off current ratio ($I_{on}/_{off}$) deduced from the device characteristics of **3H** in their corresponding configurations are summarized in Table 3.3.

	Configuration	Annealing	Gate dielectric surface	Hole mobility ($cm^2V^{-1}s^{-1}$)	Threshold voltage (V)	I_{ON}/I_{OFF} ratio
SP*	BC	N	SiO_2	$8.3x10^{-7}$	-57.4	$1.2x10^4$
Eva*	BC	N	SiO_2	$1.9x10^{-2}$	-5.2	$5.4x10^5$
	BC	Y	SiO_2	$1.6x10^{-3}$	-31.0	$7.2x10^6$
	BC	N	OTS	$1.0x10^{-1}$	-4.4	$1.3x10^6$
	BC	Y	OTS	$5.2x10^{-3}$	-5.3	$3.0x10^4$
	TC	N	SiO_2	$1.9x10^{-2}$	-1.4	$1.3x10^6$
	TC	N	OTS	$2.1x10^{-3}$	-51.8	$5.3x10^5$

Table 3.3 OFET performances of model calamitic dyad **3H** ** SP=spun cast; Eva=evaporated*

3.6.2 Preliminary results of the donor-σ-acceptor calamitic dyad 3O

Based on the previous results obtained on model dyad **3H**, the charge transport properties of donor-σ-acceptor dyad **3O** thin films were studied in OFET devices directly prepared by thermal evaporation in bottom contact (BC) configuration on a self-assembled monolayer of OTS at the surface of the SiO_2 gate dielectric layer.

The typical output and transfer characteristics of evaporated OTS-treated devices with no annealing are given in Figure 3.18.

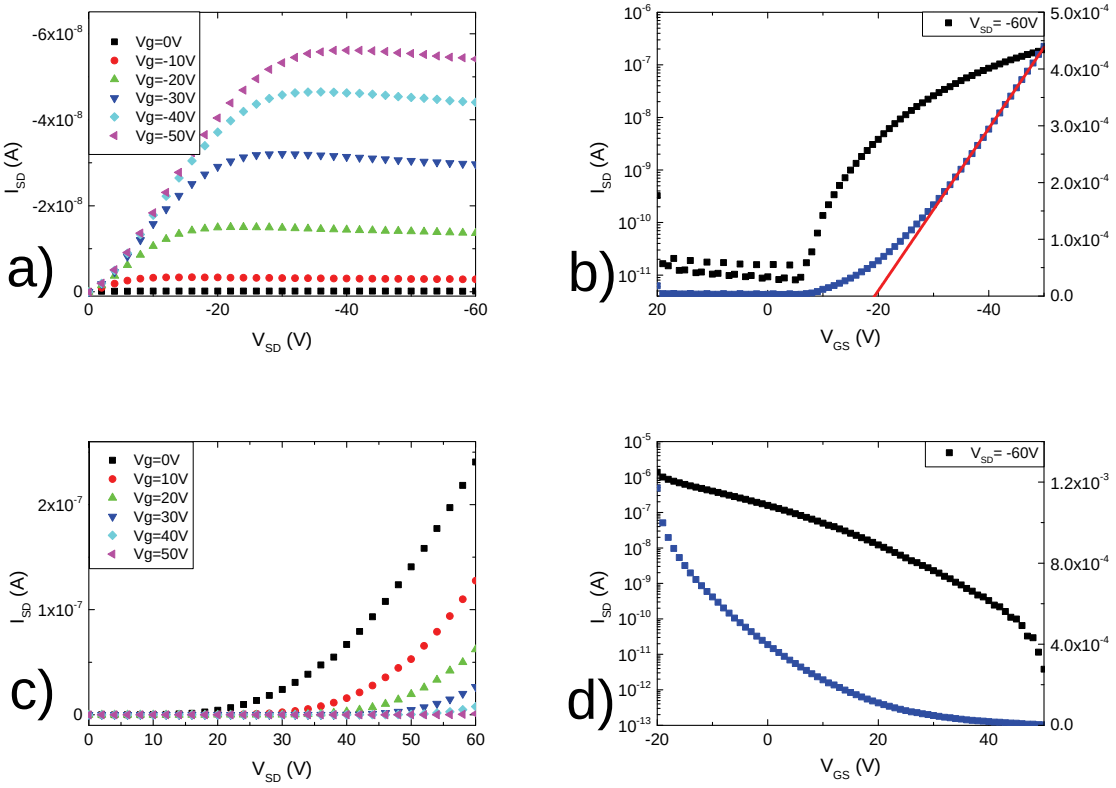

Figure 3.18 (a) hole output, (b) hole transfer, (c) electron output and (d) electron transfer characteristics (BC, OTS, ***thermal evaporated)*** *of* **3O**

It can be found that the devices exhibit hole mobilities of around $5.4x10^{-5}$ $cmV^{-1}s^{-1}$ (Figure 3.18.a and 3.18.b). However, no electron transport was detected based on the output and transfer results (Figure 3.18.c and 3.18.d).

Contrary to the model dyad 3H, the annealing process at 135°C for 2 hours of **3O** thin films have a beneficial effect on the charge transport properties. Indeed, the hole mobility was increased of almost 2 orders of magnitudes to reach $1.0x10^{-3}$ $cmV^{-1}s^{-1}$, probably due to a favorable reorganization in the thin film (Figure 1.19.a and 3.19.b). In addition, the appearance of n-type conduction can be observed in the electric characteristics and more particularly, in the transfer curve (Figure 1.19.d), which presents a typical V-shape of both the hole and electron transport [290, 291] . However, no value of electron mobility could be extracted due to the absence of linear or saturation regimes in the output characteristics (Figure 1.19.c), which could be explained by an important unbalance of hole and electron mobilities. This unbalance could be explained by the fact that the morphology in the thin films is not optimized or by the fact that the LUMO level of acceptor moiety in dyad **3O** (around -3.9 eV) is still too high for an optimum electron injection in the nanostructured layer from Au electrodes (work function of -5.1 eV).

To solve the later problem, a stronger acceptor moiety could be introduced in the donor-σ-acceptor dyad in order to present a lower LUMO level.

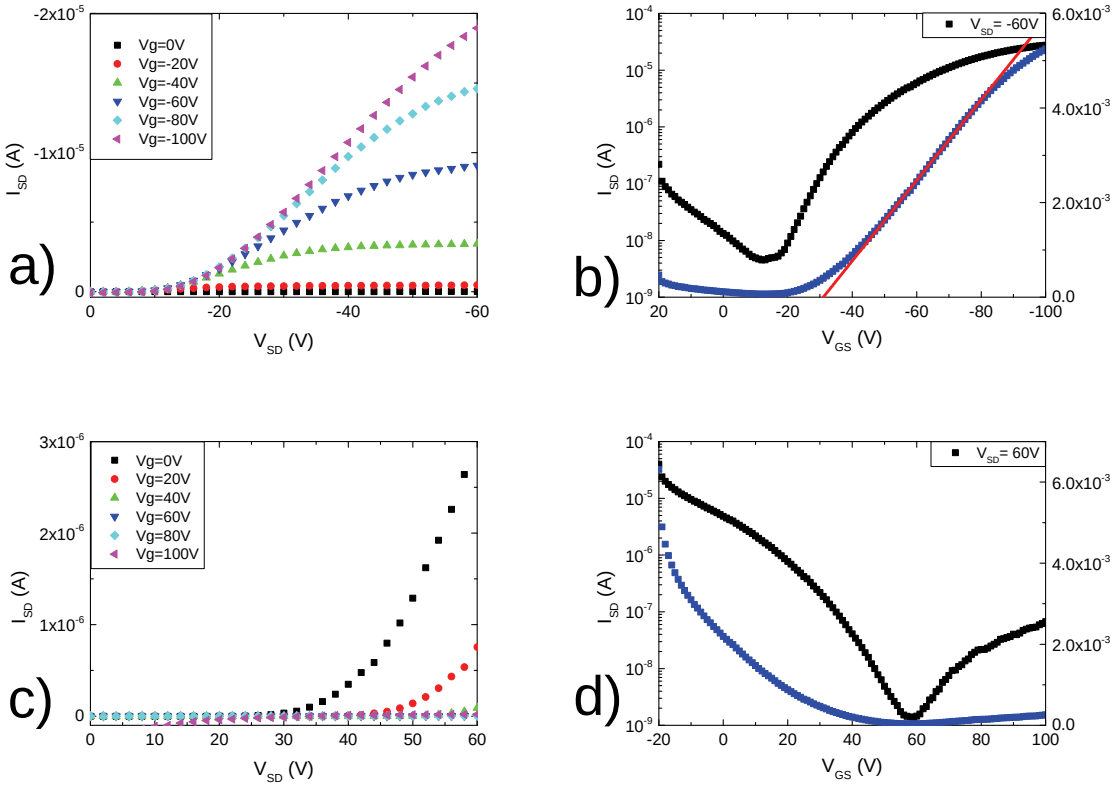

Figure 3.19 (a) hole output, (b) hole transfer, (c) electron output and (d) electron transfer characteristics (BC, OTS, ***thermal evaporated, annealed)*** *of* **3O**

Mobilities, threshold voltage (V_{th}) and on/off current ratio ($I_{on}/_{off}$) deduced from the device characteristics of **3O** are summarized in Table 3.4.

Annealing	Hole mobility ($cm^2V^{-1}s^{-1}$)	Electron mobility ($cm^2V^{-1}s^{-1}$)	Threshold voltage (V) *	I_{ON}/I_{OFF} ratio *
No	$5.4x10^{-5}$	-	-19.6	$2.3x10^4$
Yes	$1.0x10^{-3}$	not determined	-31.5	$5.8x10^3$

Table 3.4 OFET performances of donor-σ-acceptor calamitic dyad **3O** (BC, OTS, thermal evaporated) * for hole transport

3.7 Conclusion

The model calamitic dyad **3H** based on terthiophene-terthiophene and donor-σ-acceptor calamitic dyad **3O** based on terthiophene-pyromellitic diimide were designed, synthesized and characterized. The main results confirmed that the target lamello-lamellar organizations were obtained. They consist on alternating sub-layers containing each building block of these dyads, as demonstrated by POM, DSC and XRD. These organizations should be favorable for 2D charge transport of electrons and holes in the case of the donor-σ-acceptor dyad.

After different thermal and surface treatments, a relatively high hole transport mobility of 0.1 $cm^2V^{-1}s^{-1}$ was obtained from the model dyad **3H** and a hole-electron transport for the donor-σ-acceptor dyad **3O**.

Nevertheless, the electron transport in the donor-σ-acceptor dyad cannot be clearly characterized with the OFET parameters described in this chapter. This limitation could be explained by the mismatching between the electrode (Au) work function and the LUMO level of the acceptor moiety and/or the non-optimized nanostructures in the thin films. As a consequence, the future work on this promising design will be concentrated first on the optimization of the n-type semiconducting building block.

3.5 Experimental

3.5.1 OFET sample preparation and configurations

For the spun cast OFETs, the parameters used were identical in the GIXS sample preparations (see Paragraph 3.3.2 for details).

For thermal evaporation, the product was used directly without further purification or treatment. The deposition rate used was 0.5 Å/s and the thickness was fixed as 50 nm. The annealing was effected in glove-box, for 2 hours: at 120°C for the model calamitic dyad **3H** and at 135°C for the donor-σ-acceptor calamitic dyad **3O**.

The Bottom-Gate (BG) OFETs in both Bottom Contact (BC) and Top Contact (TC) configurations were fabricated and characterized. The BC OFETs were commercialized Fraunhofer FET chips (thermally grown 230 nm SiO_2 as dielectric layer) and the TC transistors were fabricated using the same Fraunhofer wafers.

The substrates were sonicated in acetone and isopropanol and then placed in a piranha solution to remove the residues of organic materials and to induce OH groups in the vicinity of the surface. After rinsing the substrates again in isopropanol and tried by nitrogen flow. Then they were cleaned in a UV cleaner during 20 minutes. For the preparation of the OTS-treated substrates, the silanization was carried out in a 3 mM OTS (octyltriethoxysilane) solution of dry hexane for 90 min. All solvents were purchased from Sigma Aldrich and were used without further purification.

Gold electrodes were used in all the OFET measurements.

For the fabrication of BC devices, the product was deposited (by spin-coating or evaporation) directly to the commercialized Fraunhofer chips. This test chip gives four types of transistors. The channel lengths are 2.5, 5, 10 and 20µm respectively and the channel width is always 1 cm.

In the case of TC devices, the product was deposited on the substrate (wafer, OTS or bare silica), annealed (in some cases) and then the electrodes were deposited by thermal evaporation of the metal (gold) through a shadow mask: deposition rate, 0.5 Å/s; channel length, 40µm; channel width 1.6 cm.

OFET characteristics were measured using a double channel source meter unit (Keithley 2600) and all the tests were realized in glove-box. All the field effect mobilities were calculated on the saturation regime (see Paragraph 1.1.4.3).

3.5.2 Synthesis

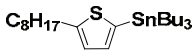

Chemical Formula: $C_{24}H_{46}SSn$
Molecular Weight: 485.3970

3B

Under argon atmosphere, 80.2 mmol of n-BuLi (2.5 M in hexane) was added drop by drop to a solution of 76.4 mmol of 2-octyl-thiophene in 60 ml dry THF which was cooled to -78°C previously. At this temperature, the mixture was stirred during one hour. Then, 91.7 mmol of tributyltin chloride was added drop by drop during about 45 min. The temperature was increased slowly to room temperature. After 16 hours, the mixture was filtrated; the filtrate was diluted with DCM (about 150 ml) and washed thoroughly by a saturated aqueous solution of ammonium chloride. After extraction, the organic phase was dried by magnesium sulfate, filtrated and the solvent was evaporated by Rotavapor. After a distillation, the small molar mass impurities were eliminated and yellowish oil was obtained. Yield, 81%. NMR, δ_H (ppm) (200 MHz, $CDCl_3$): 6.97(d, 1H), 6.89(dt, 1H), 2.84(t, 2H), 1.08-1.68(m, 33H), 0.85-1.06(m, 9H) ; δ_C (ppm) (50 MHz, $CDCl_3$): 151.65, 135.18, 133.71, 125.25, 31.88, 31.83, 30.93, 29.96, 29.37, 29.29, 29.25, 29.00, 27.32, 22.68, 14.12, 13.70, 10.78.

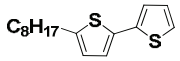

Chemical Formula: $C_{16}H_{22}S_2$
Molecular Weight: 278.4759

3D

(Stille Reaction)

Under argon protection, triphenylphosphine (7.12 mmol) and palladium(II) acetate (1.78 mmol) were dissolved in 110ml of dry THF in order to form the tetrakis(triphenylphosphine)palladium(0) catalyst in situ. Then this catalyst was added to a DMF solution (175 ml) of **3B** (42.73mmol) and 2-bromothiophene (35.61 mmol) before the temperature was increased to 85°C and maintained for 12 hours. The solvent was removed by Rotavapor and the residue was dissolved in DCM (about 200 ml) and was washed by Mili-Q water. The organic phase was extracted, dried by magnesium sulfate, filtrated and the solvent was evaporated again by Rotavapor. Then the crude was purified by column chromatography (silica gel, cyclohexane/DCM, 9:1) and afforded the **title compound** (39%) as a green crystal. NMR δ_H (ppm) (200 MHz, $CDCl_3$) 7.16(dd, 1H), 7.08(dd, 1H), 6.98(dd, 2H), 6.73 (dt, 1H), 2.78 (t, 2H), 1.28-1.42 (m, 10H), 0.88(t, 3H) ; δ_C (ppm) (50 MHz, $CDCl_3$) 145.56, 138.13, 134.90, 127.80, 124.85, 123.86, 123.54, 123.14, 32.01, 31.76, 30.30, 29.47, 29.36, 29.24, 22.86, 14.36.

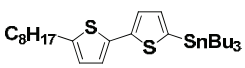

Chemical Formula: $C_{28}H_{48}S_2Sn$
Molecular Weight: 567.5207

3E

With the same procedure, the stannylation was carried out on 3D to give 3E as a yellow-orange oil (83%). NMR δ_H (ppm) (200MHz, $CDCl_3$): 7.13(d, 1H), 7.04(d, 1H), 6.97(d, 1H), 6.66(d, 1H), 2.79(t, 2H), 1.15-1.72 (m, 33H), 0.86-0.99 (m, 14H)

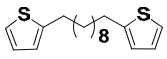

Chemical Formula: $C_{18}H_{26}S_2$
Molecular Weight: 306.5290

3F

At 0°C under argon atmosphere, 2-bromothiophene (0.143 mol) was dissolved in 280 ml dry hexane. The n-BuLi (2.5M in hexane) (0.137 mol) was added drop by drop. After 10 min, about 50 ml of dry THF was added drop by drop until a precipitation appeared. Then the temperature was slowly increased to room temperature and 1 hour later, 1,10-dibromo-decane solution (0.0715 mol in 55 ml dry hexane) was added drop by drop. The reaction continued for another 2 hours and then was quenched by Mili-Q water. This mixture was extracted by ether, washed by water and the organic phase was dried by magnesium sulfate, filtrated and the solvent was evaporated by Rotavapor. The crude product was purified by column chromatography (silica gel, chloroform) and afforded the **title compound** (29%) as a yellowish power. NMR δ_H (ppm) (200 MHz, $CDCl_3$) 7.10(d, 2H), 6.91(t, 2H), 6.77(d, 2H), 2.82(t, 4H), 1.66(t, 4H), 1.28(m, 16H).

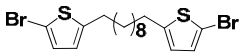

Chemical Formula: $C_{18}H_{24}Br_2S_2$
Molecular Weight: 464.3212

3G

Under argon atmosphere, **3F** (21.33 mmol) was dissolved in 200ml of DMF at room temperature. NBS (N-bromosuccinimide) (46.93 mmol) was added in one time and this mixture was stirred during all the night. The majority of DMF was removed by Rotavapor and the final residue was dissolved in DCM (150 ml). After being washed by Mili-Q water, the organic phase was dried by magnesium sulfate, filtrated and the solvent was evaporated by Rotavapor. The crude product was purified by column chromatography (silica gel, petroleum ether) and afforded the **3G** (70%) as a yellow powder. NMR δ_H (ppm) (200MHz, CDCl3) : 6.83(d, 1H), 6.51(dt, 1H), 2.72(t, 2H), 1.66(quin, 4H), 1.26(m, 13H) ; δ_C (50MHz, $CDCl_3$) : 147.76, 129.52, 124.49, 108.86, 31.57, 30.47, 29.59, 29.41, 29.08.

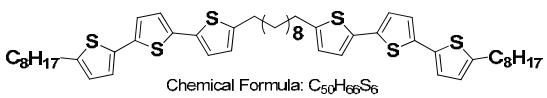

Chemical Formula: $C_{50}H_{66}S_6$
Molecular Weight: 859.4490

3H

(Stille Reaction)

With the same synthesis procedure as **3D**, from **3E** and **3G**, the compound **3H** was obtained as a yellow powder with a yield of 47%. NMR δ_H (ppm) (200MHz, $CDCl_3$) : 6.95-6.96(m, 8H), 6.66(d,

4H), 2.78(t, 8H), 1.67(t, 8H), 1.28(m, 32H), 0.88(t, 6H) ; δ_C (ppm) (75MHz, o-DCB-d4, at 70°C): 146.84, 137.95, 136.26, 126.30, 124.96, 124.82, 33.36, 33.02, 31.69, 31.03, 30.86, 30.71, 30.67, 24.13, 15.39 ; MALDI-TOF: calcd. for $C_{50}H_{66}S_6H^+$ 859.3568; Found 859.0650.

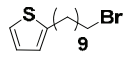

Chemical Formula: $C_{14}H_{23}BrS$
Molecular Weight: 303.3014

3I

At 0°C under argon atmosphere, 2-bromothiophene (0.143 mol) was dissolved in 280 ml dry hexane. The n-BuLi (2.5M in hexane) (0.137 mol) was added drop by drop. After 10 min, about 50 ml of dry THF was added drop by drop until a precipitation appeared. Then the temperature was slowly increased to room temperature and 1 hour later, the mixture was added in one portion to a solution of 1,10-dibromo-decane solution (0.572 mol in 55 ml dry hexane). The reaction continued for another 2 hours and was quenched by adding Mili-Q water. This mixture was then extracted between ether and water. The organic phase was dried by magnesium sulfate, filtrated and the solvent was removed by Rotavapor. The crude product was purified by column chromatography (silica gel, chloroform) and afforded the ***title compound*** (66%) as yellow-brown oil. NMR δ_H (ppm) (200MHz, $CDCl_3$): 7.10(d, 1H), 6.92(t, 1H), 6.77(d, 1H), 3.41(t, 2H), 2.82(t, 2H), 1.84(quin, 2H), 1.66(quin, 2H), 1.28(m, 13H) ; δ_C (ppm) (50MHz, CDCl3) : 145.84, 126.80, 124.24, 122.62, 34.22, 32.97, 31.92, 30.05, 29.64, 29.53; 29.43, 29.22, 28.88, 28.30.

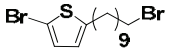

Chemical Formula: $C_{14}H_{22}Br_2S$
Molecular Weight: 382.1975

3J

Under argon atmosphere, **3I** (21.33 mmol) was dissolved in 200ml of DMF at room temperature. NBS (N-bromosuccinimide) (21.33 mmol) was added in one time and this mixture was stirred during all the night. The DMF was removed essentially by Rotavapor and the residue was dissolved in DCM (150 ml) before being washed by Mili-Q water. The organic phase was dried by magnesium sulfate, filtrated and the solvent was evaporated by Rotavapor. The crude product was purified by column chromatography (silica gel, petroleum ether) and afforded the ***title compound*** (67%) as colorless oil. NMR δ_H (ppm) (200MHz, $CDCl_3$): δ 6.82(d, 1H), 6.51(dt, 1H), 3.40(t, 2H), 2.72(t, 2H), 1.84(quin, 2H), 1.66(quin, 2H), 1.28(m, 13H) ; δ_C (ppm) (50MHz, $CDCl_3$) : 147.58, 129.41, 124.40, 108.60, 34.02, 32.90, 31.48, 30.38, 29.45, 29.32, 29.02, 28.81, 28.23.

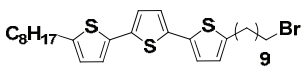

Chemical Formula: $C_{30}H_{43}BrS_3$
Molecular Weight: 579.7614

3K

(Stille Reaction)

With the same synthesis procedure as **3D**, from **3E** and **3J**, the compound **3K** was synthesized. The crude was purified by column chromatography (silica gel, petroleum ether/DCM, 7/3) and afforded the **title compound** (58%) as colorless oil. NMR δ_H (ppm) (200MHz, $CDCl_3$): 6.95-6.97(m, 4H), 6.67(d, 2H), 3.40(t, 2H), 2.78(t, 4H), 1.86(quin, 2H), 1.67(t, 4H), 1.28(m, 22H), 2.89(t, 3H) ; δ_C (ppm) (50MHz, $CDCl_3$) :145.57, 145.48, 136.30, 134.81, 134.77, 124.94, 124.92, 123.60, 123.31, 123.30, 34.19, 32.99, 32.01, 31.76, 31.69, 30.32, 29.54, 29.47, 29.44, 29.37, 29.24, 29.16, 28.92, 28.33, 22.81, 14.24.

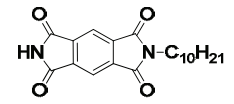

Chemical Formula: $C_{20}H_{24}N_2O_4$
Molecular Weight: 356.4156

3N

Under argon atmosphere, the pyromellitic diimide (**3L**) (9.26 mmol), 1-decanol (**3M**) (4.35 mmol) and PPh_3 (5.21 mmol) were mixed in 100 ml DMF at 0°C. Then diisopropyl azodicarboxylate (DIAD, 5.21 mmol) was dissolved in 30 ml THF and this solution was added to the previous mixture drop by drop. The reaction was continued at room temperature for all night. After removing the solvent by Rotavapor, the residue was directly purified by column chromatography (silica gel, EtOAc/DCM, 1/9) and recrystallized in EtOAc to give the **title compound** (12%) as colorless crystalline powder. NMR δ_H (ppm) (200MHz, $CDCl_3$):8.30(s, 2H), 7.94(s, 1H), 3.74(t, 2H), 1.70(t, 2H), 1.24-1.32(m, 14H), 0.88(t, 3H); δ_C (ppm) (50MHz, $CDCl_3$): 166.28, 137.71, 118.90, 32.05, 29.66, 29.61/,29.42, 29.27, 28.70, 28.58, 26.99, 22.82, 14.35.

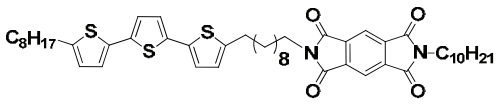

Chemical Formula: $C_{50}H_{66}N_2O_4S_3$
Molecular Weight: 855.2650

3O

Under argon atmosphere, compound **3K** (0.54 mmol) was dissolved in DMF (30 ml) at 120°C. Meanwhile, **3N** (1.62 mmol) was dissolved also in DMF (40 ml) at 40°C, then K_2CO_3 (1.62 mmol) was added. About 10 minutes later, the later solution/suspension was withdrawn by a syringe and then added to the previous **3K** solution. The mixture was further maintained at 120°C for one night. The solvent was removed by Rotavapor and the residue was purified directly by column chromatography (silica gel, DCM) and afterwards recrystallized in EtOH to give the ***title compound*** (54%) as yellow-brown powder. NMR δ_H (ppm) (200MHz, $CDCl_3$): 8.25(s, 2H), 6.95(s, 2H), 6.93(s, 2H), 6.66(s, 2H), 3.71(t, 4H), 2.78(t, 4H), 1.66(t, 8H), 1.24-1.27(m, 36H), 0.87(t, 6H); δ_C (ppm) (50MHz, $CDCl_3$): 166.43, 145,41, 137.38, 136.18, 134.65, 124.80, 123.54, 123.24, 118.27, 38.86, 32.03, 31.75, 30.38,

29.58, 29.46, 29.41, 29.35, 29.30, 29.21, 29.11, 29.05, 28.49, 26.92, 14.59 ; MALDI-TOF: calcd. for $C_{50}H_{66}N_2O_4S_3H^+$ 855.4265; Found 855.5660.

CHAPTER 4 SYNTHESIS AND STRUCTURE-CHARGE TRANSPORT PROPERTIES RELATIONSHIP STUDY OF SIDE-CHAIN LIQUID-CRYSTALLINE π-CONJUGATED POLYMERS

4.1 Introduction

The control of the nanoscale morphology of π-conjugated polymeric architectures, providing long-range order, and the establishment of reliable structure-properties relationships remain the major and fundamental issues in the field of organic semiconductors. In this context, recent works were developed in our laboratory [123, 292] and relating to the design and elaboration of a side chain liquid crystal semiconducting polymer where: (i) the backbone was a π-conjugated polymer and (ii) the side groups were π-conjugated discotic mesogens. More precisely, this polymer was composed of polythiophene backbone and triphenylene-molecule side groups. A supramolecular self-assembling of this p-type semiconducting polymer was observed where the backbone and columns were parallel to each other in an intertwined lamello-columnar liquid-crystal structure, consisting in the alternation of rows of columns and backbone sub-layers.

In this chapter, we developed and completed the previous work on the liquid crystalline side-chain polymer structure by studying and evaluating the influence of the controlled dilution of the mesogenic side groups (i.e. the degree of polymer lateral substitution) on the supramolecular organizations and on charge transport properties. In this aim, we prepared three polythiophene derivatives, a model poly(3-alkylthiophene) **4B,** a homopolymer comprising triphenylene side groups on every thiophene units **4G** and an alternating copolymer with thiophene/triphenylene ratios of 2:1 **4M**, as illustrated in Figure 4.1a. The chain lengths (in number of thiophene unity) are chosen around 50 and the spacer length between the polymer backbone and the pending groups is fixed as 10 carbons. Their self-organization properties in bulk and in thin films were investigated and correlated to the charge transport properties, studied in field effect transistor configuration (Figure 4.1.b).

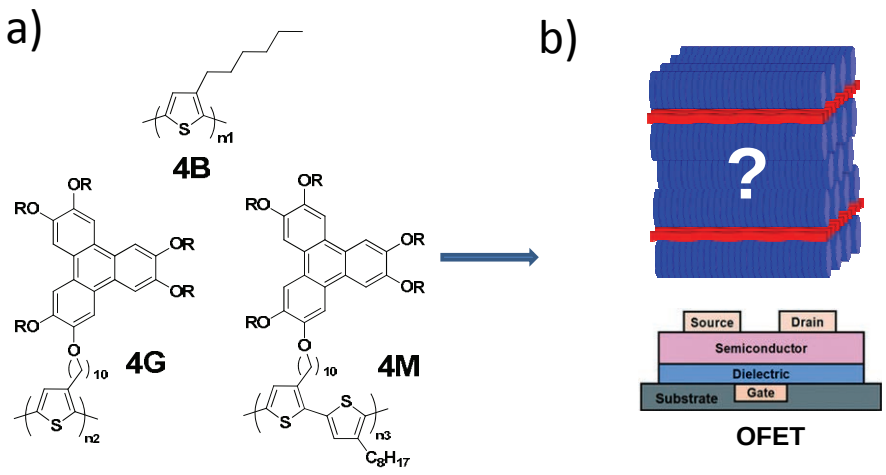

Figure 4.1: a) Chemical structures of the target polymers. b) Influence of the degree of polymer lateral substitution on the self-organization and the charge transport properties

4.2 Synthesis

All the regioregular poly(3-alkylthiophene) backbones were prepared according to the McCullough procedure, namely the Grignard Metathesis (GRIM) [163, 180, 293]. This method is detailed in Paragraph 1.3.3.3.

4.2.1 Synthesis of the model poly(3-hexylthiophene) 4B

The model short regioregular poly(3-hexylthiophene) **4B**, which will be used as reference in charge transport studies was synthesized in from commercially available monomer **4A** by GRIM polymerization in one step (Figure 4.2).

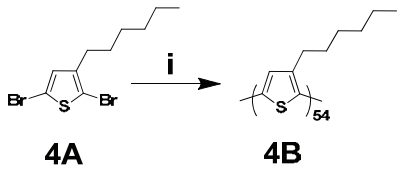

*Figure 4.2: Synthesis of the model short regioregular poly(3-hexylthiophene) **4B**. Conditions: (i) (a) iPrMgCl, THF, 0 °C; (b) Ni(dppp)Cl_2, 0 °C/room temperature, HCl; 64%*

4.2.2 Synthesis of the precursory regioregular poly(3-alkylthiophene)s

According to previous works [123], the synthesis of side-chain polymers **4G** and **4M** is based on a post-functionalization method which requires first the preparation of precursory regioregular poly(3-alkylthiophene)s (**4F** and **4L**, respectively) with a brome at the end of the alkyl chains, followed by the grafting of the triphenylene derivatives **T** on the polymer. The synthetic pathway for **4F** is summarized in Figure 4.3.

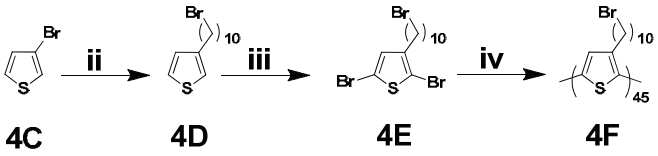

*Figure 4.3: Synthesis of the precursory homopolymer **4F**. Conditions: (ii) (a) n-BuLi, hexane/THF, −40°C; (b) Br$(CH_2)_{10}$Br, −10°C/room temperature; 37%; (iii) NBS, DMF, room temperature, 81%; (iv) Same as "(i)", 50%*

In this synthetic route, the 3-(ω-bromodecyl)thiophene **4D** was first prepared by lithiation with n-butyllithium of commercially available 3-bromothiophene **4C**, followed by quenching with an excess of dibromodecane. After purification by distillation to remove the excess of dibromodecane and silica chromatography to remove the α-substituted byproduct inevitably produced, the compound **4D** was dibrominated in a mild condition by N-bromosuccinimide (NBS) to lead to the monomer **4E**, which was then polymerized via GRIM method to form the precursory homopolymer **4F**.

The synthesis of the precursory alternating copolymer **4L** which presents one in two alkylchains with a brome at the end, is described in Figure 4.4. In this polymer, the 3-octylthiophene was chosen

to play the role of the "diluent" and was first converted in its boronate ester **4I** by the selective attack on the 4-position due to the steric hindrance of lithium tetramethylpiperidide (LiTMP) in the step (vi). The building block **4I** reacted then via a Suzuki coupling with the monobrominated 3-(ω-bromodecyl)thiophene **4E'**, obtained by a regioselective bromination of **4D** onto the 2-position with a slightly sub-stoichiometric amount of NBS, to lead the key head to tail bithiophene **4J**. Finally, the "pre-regioregular" bithiophene was dibrominated by NBS to give the monomer **4K**, which was then polymerized via GRIM method to form the precursory alternating copolymer **4L**.

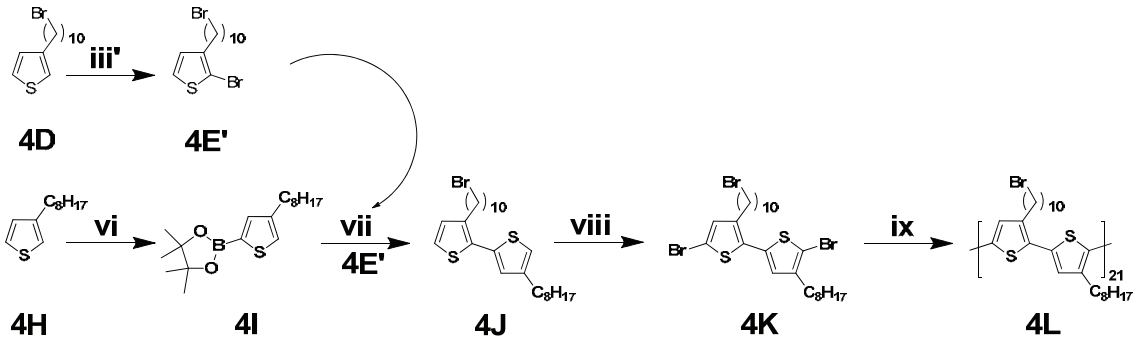

*Figure 4.4: Synthesis of the precursory alternating copolymer **4L** . Conditions: (iii') NBS, DMF, room temperature, 96%; (vi) LiTMP, dioxaborolane, THF, −78 °C, 68.2%; (vii) $Pd(PPh_3)_4$, 1 M $NaHCO_3$, DME, reflux, 82%; (viii) NBS, DMF, room temperature, 67%; ix) Same as "(iv)", 67%*

4.2.3 Synthesis of the side chain polymers 4G and 4M

The side chain homopolymer **4G** and alternating copolymer **4M** were prepared by the post-functionalization of their respective precursory polymers **4F** and **4L**, respectively, with the monohydroxy triphenylene **T** (see Chapter 2) as described in Figure 4.5.

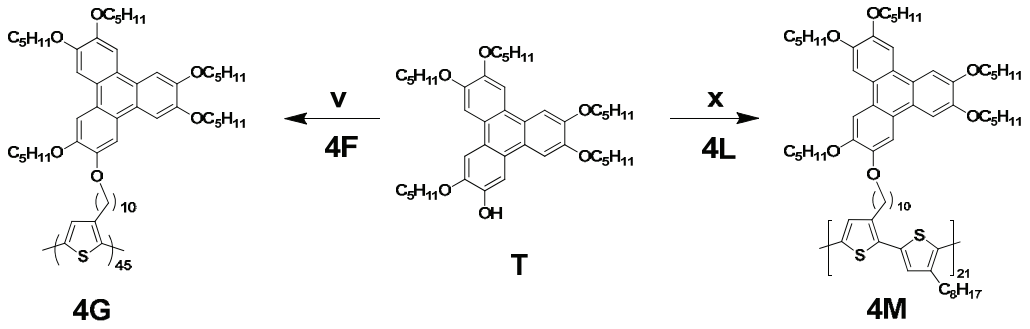

*Figure 4.5: Synthesis of the side chain homopolymer **4G** and alternating copolymer **4M**. Conditions: (v) (a) K_2CO_3, DMF, **T**, 80°C; (b) **4F**, 120 °C; 73%; x) (a) K_2CO_3, DMF, **T**, 80°C; (b) **4L**, 120 °C; 37%*

4.3 Polymers characterizations

The polymers **4B**, **4G** and **4M** were characterized by Size-Exclusion Chromatography (SEC), NMR spectroscopy and elemental analysis. The detailed chemical structure informations such as molecular weights and polydispersity indexes (PDI) are listed in Table 4.1.

Polymer	type	M_n (SEC) (KDa)	DP_n (SEC)	DPI (SEC)	M_n (NMR) (kDa)	DP_n (NMR)
4B	Model	13.4	80	1.2	9.0	54
4F	Homopolymer precursor	14.7	47	1.2	14.0	45
4G	Homopolymer grafted	31.9	36	1.2	40.3	45
4L	Copolymer precursor	10.6	43*	1.4	10.4	42*
4M	Copolymer grafted	17.8	33*	1.6	23.1	42*

*Table 4.1 Chemical structure informations of the polymers repeating unit of **4B**, RU(**4B**)=166.3 g mol^{-1}, RU(**4F**)=310.3 g mol^{-1}, RU(**4G**)=895.3 g mol^{-1}, UR(**4L**)=495.6 g mol^{-1}, UR(**4M**)=1089.7 g mol^{-1}. *Here we consider each thiophene unity in the backbone is equal.*

It can be noticed that as expected, the synthesis used to prepare the polymers led to well-defined polymeric architectures with narrow PDIs (ranging from 1.2 to 1.6) and highly controlled molecular-weights (degree of polymerization, DPn around 45).

Concerning the two side-chain polymers **4G** and **4M**, the quality of the substitution was confirmed by the ^{1}H NMR (Figure 4.6.a and 4.6.b). In the NMR spectrums, it can be observed that after the grafting, the signal of the methylene groups (δ = 3.40 ppm) in the α-position to the terminal bromine atom has completely vanished. This confirms that the substitution is almost quantitative, considering the sensitivity of the NMR spectroscopy. Also, the composition change from elemental analysis (see experimental part of this chapter) evidences the quasi-complete substitution.

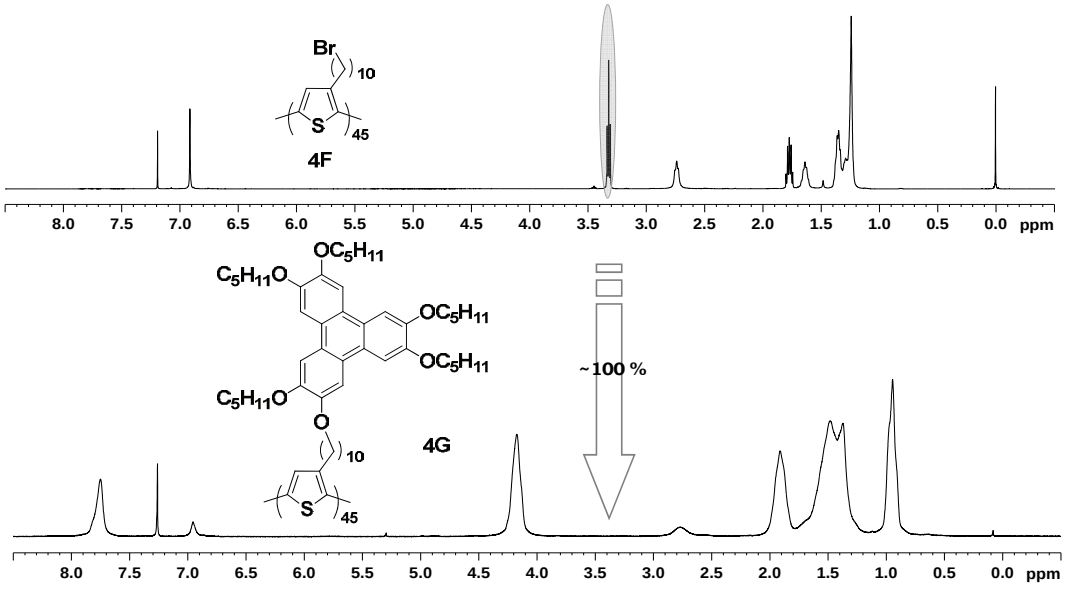

Figure 4.6.a ^{1}H NMR spectra of precursory and grafted homopolymer.

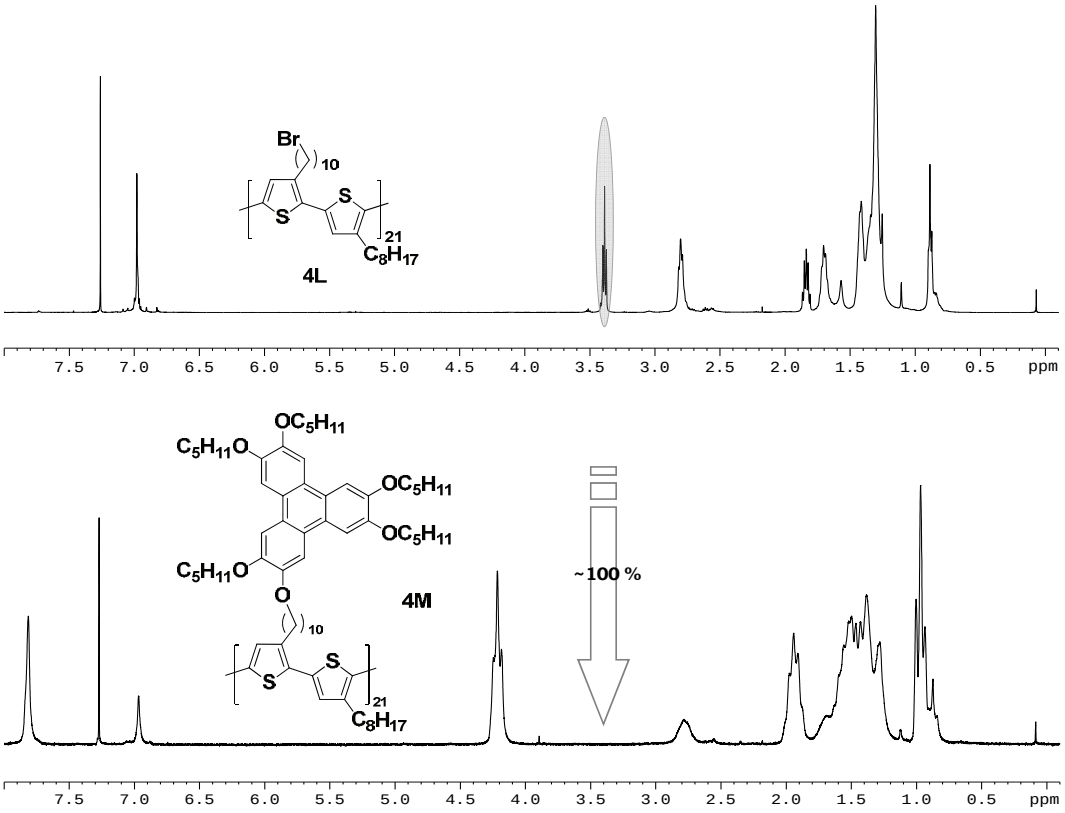

Figure 4.6.b ^{1}H NMR spectra of precursory and grafted alternating copolymer.

It should be taken into account that the polythiophene backbone is much more rigid than the polystyrene one (standard used to determine M_n by SEC), so for a polythiophene with a similar repeating unit mass to the polystyrene, the hydrodynamic radius of polythiophene will be much bigger than the polystyrene one. That is why, in our case, the molecular weight of the model short P3HT **4B** measured by SEC is much more overestimated [209, 294]. Nevertheless, based on the results of Liu et al [209], the M_n from SEC and the true M_n (obtained by Maldi-Tof) can be correlated (Paragraph 1.3.3.6). Thus, in the case of the model polymer **4B**, the M_n (SEC) found of around 13.4 kDa (DPn=80), is overestimated by a factor of around 1.5, explaining the more realistic value of 9 kDa (DPn=54) determined by NMR [DPn (SEC) ≈ 1.5 x DPn (NMR)].

4.4 Thermal behavior

The thermal behavior of **4B**, **4L** and **4M** were investigated by Polarized-light Optical Microscopy (POM) and Differential Scanning Calorimetry (DSC).

4.4.1 Polarized-light optical microscopy

When observed under POM, the two substituted polymers **4L** and **4M** did not develop characteristic optical textures. Nevertheless, on heating, birefringent and homogeneous textures gradually appeared with the increase of temperature (Figure 4.7). Then with the further temperature

increase, the birefringence disappeared. This indicates the existence of mesophases for both substituted polymers.

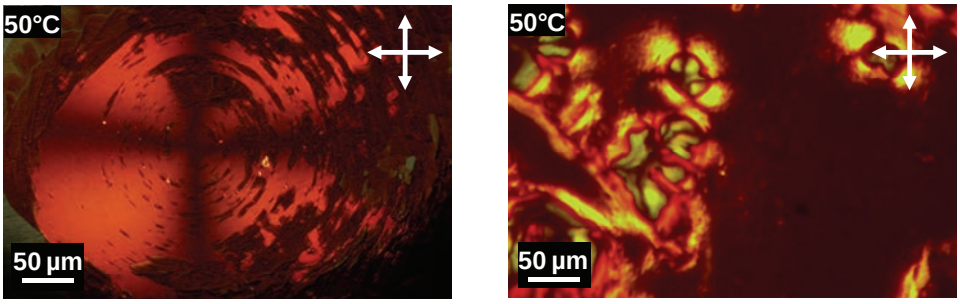

*Figure 4.7 POM images of **4G** (a) and **4M** (b) at 50 °C by heating*

4.4.2 Differential scanning calorimetry

The DSC thermograms of the polymers **4B**, **4L** and **4M** are given in Figure 4.8 and show typical behaviors of macromolecular systems, containing characteristic signals of glass transition, and at higher temperature, exothermic transitions corresponding to the transitions into the isotropic liquid phase, in agreement with the observations from POM.

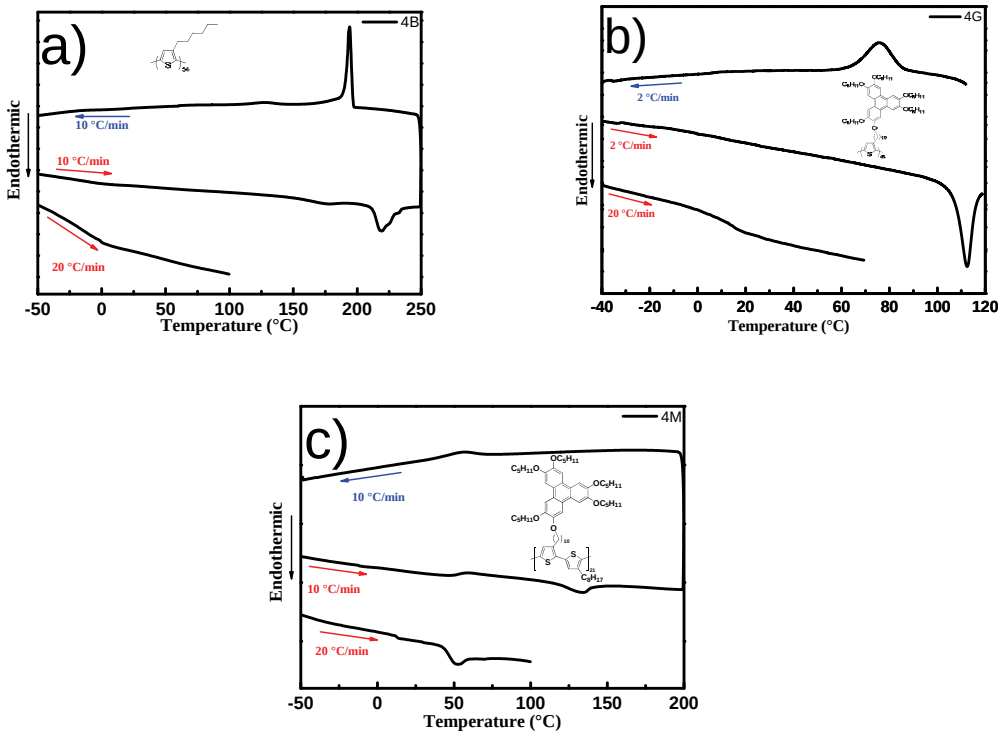

*Figure 4.8 DSC thermograms of polymers **4B** (a), **4G** (b) and **4M** (c)*

More precisely, the thermogram of model short poly(3-hexylthiphene) **4B** (Figure 4.8.a) presents first on heating a glass transition (T_g) at around 0°C. On further heating, an endothermic peak at

211.7°C, associated with a quite large enthalpy change (ΔH=23.8 Jg^{-1}), is observed, which is characteristic of the melting point (T_{iso}) of the polymer. On cooling, this transition is reversible at 196.5°C with a substantial hysteresis of about 15°C. Such results are typical of regioregular P3HT thermal behaviors except that the values of T_g and T_{iso} of **4B** are slightly lower than the values generally reported for regioregular P3HT [295, 296], probably due to the short length of the polymer.

In the case of the substituted homopolymer **4G**, on heating, the T_g appears at a slightly higher temperature (14.5°C) and the isotropization (T_{iso}) takes place at 107.3 °C with an enthalpy change of 7.5 Jg^{-1}. On cooling, the endothermic peak of the reversible transition is shifted to 85.6 °C and no T_g was observed even at a high cooling rate (20°C min^{-1}).

The substituted alternating copolymer **4M** presents similar thermal behaviors to the substituted homopolymer **4G**. However, the T_g appears at higher temperature (46.1°C) as well as for the isotropization (T_{iso}), which is observed at 116.2°C with an enthalpy change of 4.8 Jg^{-1}. On cooling, the reversible transition is observed at 71.4°C and no clear T_g was detected.

The summary of the polymer thermal behaviors characterized by DSC is given in Table 4.2.

Polymer	T_g [a] (°C)	Transition [b]	T_{iso} (°C)	ΔH (J g^{-1})
Model polymer 4B	0.0	Cr → I	211.7	23.8
	-	I → Cr	196.5	29.5
Homopolymer 4G	14.5	Lamcol → I	107.3	7.5
	-	I → Lamcol	85.6	7.2
Alternating copolymer 4M	46.1	Lamcol → I	116.2	4.8
	-	I → Lamcol	71.4	2.9

*Table 4.2. Phase transition temperatures and enthalpies of **4B**, **4G** and **4M**.[a] T_g = glass transition determined during heating (20°C min^{-1}; [b] Transition temperatures are the onsets of the peaks on heating and on cooling, Cr=Crystalline phase, I=Isotropic phase, Lamcol=lamello-columnar phase.*

4.5 Self-organization property study

4.5.1 Temperature dependent X-ray diffraction

The substituted polymers **4L** and **4G** were studied by Temperature Dependent X-ray Diffraction (TDXRD) in the temperature ranges determined by DSC and POM studies. The measurements were carried out at Institut de Physique et de Chimie des Matériaux de Strasbourg (IPCMS) in cooperation with Dr. B. Heinrich and Dr. Bertrand Donnio.

The typical X-ray pattern of the homopolymer **4G** in the mesophase at 50°C, obtained on cooling from the isotropic state is given in Figure 4.9. In this pattern, several sharp and intense Bragg reflections in the small-angle region and two scattering halos in the wide-angle region can be observed. In the wide-angle region, the very broad and diffuse halo centered at 4.5 Å (h_{ch}) indicates the molten state of the aliphatic chains and the other broad reflection around 3.5 Å (h_T) evidences the short range ordered π-π stacking of piled disk-like aromatic cores of the triphenylene pending groups, indicative of

the development of an intermolecular stacking into the columns with a possible very week contribution of the π-conjugated polymer chains.

In the small-angle region, the sharp reflections can be described as a combination of to interlocked systems: on the one hand, a first set of layered structure reflections with a periodicity ***d*** of 50.8 Å, and on the other hand, a second set of reflections indexed in a 2D lattice of columns. The sharpness of these small-angle reflections indicates the long-range correlation of the lamellar ordering and the 2D arrangement of the columns. This organization can be described as a lamello-columnar structure (Lamcol mesophase) consisting in the alternation of triple rows of columns and of polymer backbone sublayers as illustrated in Figure 4.9. The detailed structure characterization of 4G was published previously [124].

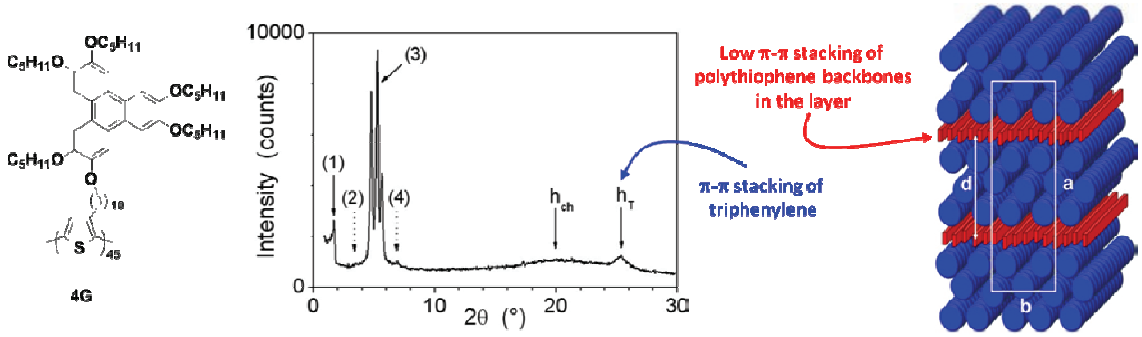

*Figure 4.9 X-ray powder diffraction patterns and schematic representation of self-organization of homopolymer **4G** in the lamello-columnar mesophase at 50°C (on cooling from the isotropic state)*

The X-ray pattern of the alternating, copolymer **4M** (Figure 4.10) which presents half of triphenylene side-groups, does not evidence any change for the Lamcol mesophase organization, for which, very similar geometrical parameters were retrieved (the inter-lamellar distance ***d*** increase slightly of 2%). The main differences with respect to the homopolymer **4G** consist in the appearance, next to the h_T scattering at 3.5 Å, of an additional scattering at 3.8 Å, attributed to h_{PT}, and in the extension of the visible lamellar order series up to the eighth order.

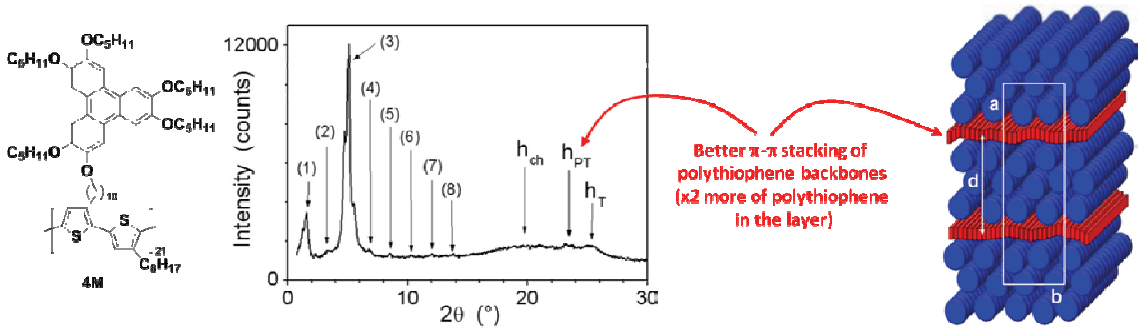

*Figure 4.10 X-ray powder diffraction patterns and schematic representation of self-organization of copolymer **4M** in the lamello-columnar mesophase at 50°C (on cooling from the isotropic state)*

These results attest now the regular stacking of polythiophene backbones, leading to a much improved segregation in sublayers with sharper interfaces and then to a reinforced stability of the organization, as also confirmed by the extension of the mesophase range to higher temperature (see Paragraph 4.4.2). A schematic representation of the alternating copolymer **4M** in the Lamcol mesophase is illustrate in Figure 4.10.

4.5.2 Atomic force microscopy

The thin film morphology on surfaces of the homopolymer **4G** was studied by tapping mode Atomic Force Microscopy (AFM). These measurements were carried out at the Institut des NanoSciences de Paris (INSP) in collaboration with Dr. E. Lacaze.

The **4G** thin films were prepared by flow casting process from an octane hot solution (75 µg ml^{-1}) on silanized (OTS) silicon wafer substrates [297], and these films were then annealed at 90°C for 20 min. The typical AFM images of **4G** thin films are given in Figure 4.11.

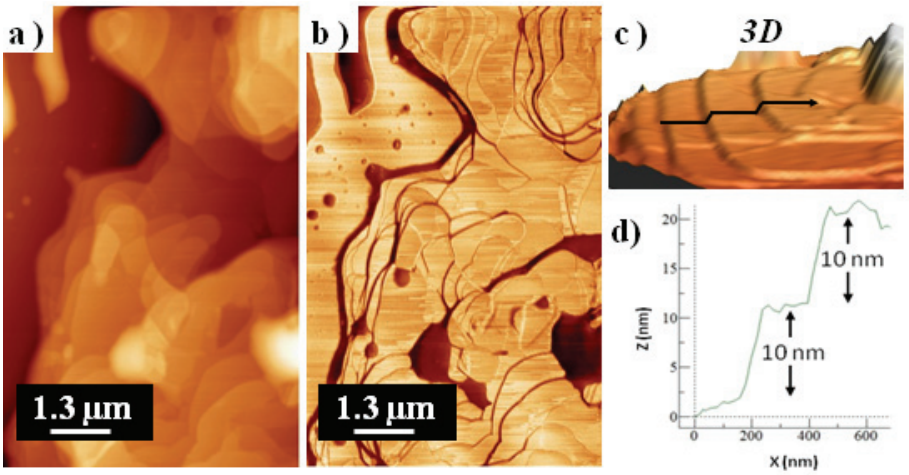

*Figure 4.11 AFM a) topography and b) phase images of substituted homopolymer **4G** thin film on OTS silanized silicon wafer. c) 3D image of terrace structure of the film on OTS-treated wafer. d) Terrace step profile of the **4G** film on OTS treated wafer determined from topography of c)*

The AFM topography and phase images show a nanostructured film with terraces (Figure 4.11. a 4.11.b), indicative of extended flat lamellae oriented parallel to the substrate surface. The heights of the terraces determined from topography images were about 10 nm, 5 nm or multiples of 5 nm as shown in Figure 4.11.c and Figure 4.11.d. They coincide well with the lamellar periodicity (***d***=50.8Å) of the bulk structure measured from the previous small angle X-ray diffraction study.

3.3.2 Grazing-Incidence X-ray Scattering

The thin film structure and morphology of the homopolymer **4G** were studied by Grazing-Incidence X-ray Scattering (GIXS). These measurements were carried out at Pohang Accelerator Laboratory (PAL, Korea), in collaboration with Prof. H-J Kim (Pusan National University).

The **4G** films were prepared by spin coating from a chloroform solution of material (1% w/w. 3000 rpm) onto an OTS treated silicon wafer. The thickness of film varies from 60 to 100 nm as evaluated by profilometer. These samples were studied after annealing (90°C for 2 hours in vacuum).

The typical two dimensional GIXS image of annealed samples of **4G** is given in Figure 4.12.a. It presents several small-angle peaks in the specular plane (along q_z), corresponding to the (00l) reflections of the lamellar organization, and several out of plane peaks which can be assigned to the (0kl) reflections of the 2D lattice of columns, as observed in the small-angle region of the bulk X-ray diffraction patterns of **4G** after annealing at 50°C (Figure 4.12.c). In the wide-angle region, in addition to the very diffuse halo around 1.4 $Å^{-1}$ (4.5Å), corresponding to the liquid-like disorder of the aliphatic chains (h_{ch}), this pattern presents one broad and intense in-plane reflection (along q_x) around 1.82 $Å^{-1}$ corresponding to the π-π stacking (3.5 Å) of the segregating discotic mesogens (h_T), as also observed in the bulk X-ray diffraction study.

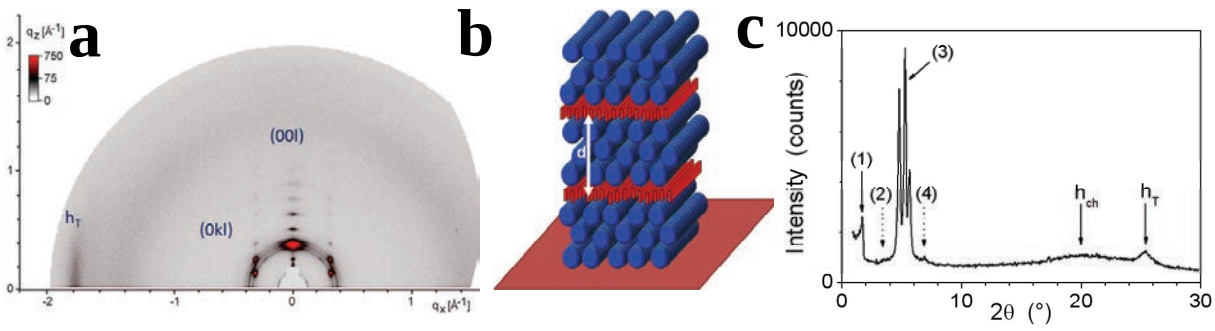

*Figure 4.12 Spin cast film GIXS patterns after annealing at 90°C (2 hours) of the homopolymer **4G** a), schematic representation of the structure and orientation of the Lamcol organization on OTS treated surface b), and bulk X-Ray diffraction pattern at 50°C on cooling of **4G**.*

This typical GIXS pattern confirms the lamello-columnar organization of the homopolymer **4G** in the annealed film and the edge-on orientation of triphenylene side-groups and polythiophene backbones on the substrate with the lamellae and columns oriented in parallel with the surface as illustrated in Figure 4.12 b. These results are perfectly consistent with the terrace nanostructure observed by AFM on the annealed thin films of **4G** (Paragraph 4.5.2, Figure 4.11). It is worth noticing that no specific changes of the GIXS patterns were observed in rotating the sample during the GIXS measurements. That indicates no preferential alignment of columns, and consequently of the polymer backbones, and we can consider that there is no macroscopic orientation of the lamella-columnar domains in the plane of the thin film.

4.6 Absorption properties in solution and solid state

The UV-Vis absorption characterizations of the homopolymer **4G** and the alternating copolymer **4M** were carried out both in solution and in solid state. For the solid state, the annealing effect was also studied in film.

The normalized absorption spectra of homopolymer **4G** and **4M** in chloroform solution at low concentration (≈10^{-6} M in repeating units) are given in Figure 4.13. Two characteristic absorption bands can be observed for both polymers at the same wavelength: the sharp peaks at around 280 nm distributed to the triphenylene side-groups [130] and the broad bands at around 450 nm from the polythiophene backbones [208]. These absorption spectra are the sum of the isolated triphenylenes and the polythiophene absorptions taken separately. When the spectrum is normalized by the polythiophene absorption band, it is obvious that the corresponding integration of triphenylene absorption band of **4G** was doubled compared with **4M**. This is consistent with the "50% dilution" of the triphenylene side-groups in the copolymer **4M** in comparison with the homopolymer **4G.**

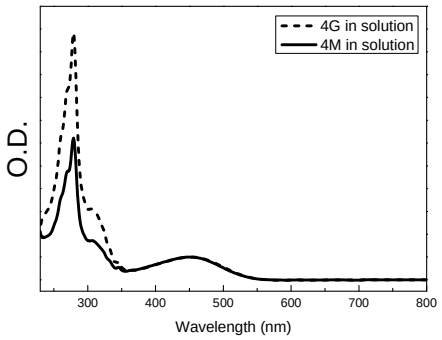

*Figure 4.13 Comparison of absorption properties of **4G** (dashed line) and **4M** (solid line) in dilute chloroform solution (≈10^{-6} M in repeating units)*

In solid state, the absorption spectra of as prepared thin films of **4G** and **4M** present a broadening of the triphenylene bands and the classical red-shift of the polythiophene bands, indicating the aggregation of both side-groups and polymer backbones (dashed lines in Figure 4.14.a and 4.14.b). Thus, the maximum wavelengths of polythiophene bands can be observed at 507 nm and 531 nm for **4G** and **4M**, respectively. The annealing of thin films (90°C, 2 hours) induces a strong effect on the absorption spectra, and more particularly on the polythiophene bands which are red-shifted again of several degrees of nanometers, with the appearance of vibronic structures characteristic of the reorganization of polythiophene backbones in an improved packing [298], as also observed in temperature dependent X-ray diffraction study. Nevertheless, this reorganization appears more pronounced for the alternating copolymer **4M**, as proved by the comparison of the two annealed spectra of **4G** and **4M** in Figure 1.14.c. Indeed, the polythiophene band of **4M** presents a clear vibronic structure and is slightly more shifted in comparison with the **4G** one, indicating a better

aggregation and better π-π stacking interactions of polythiophene backbones. This observation is perfectly consistent with the presence of the additional scattering at 3.81Å (h_{PT}) already observed with X-ray pattern of **4M** (Figure 4.10).

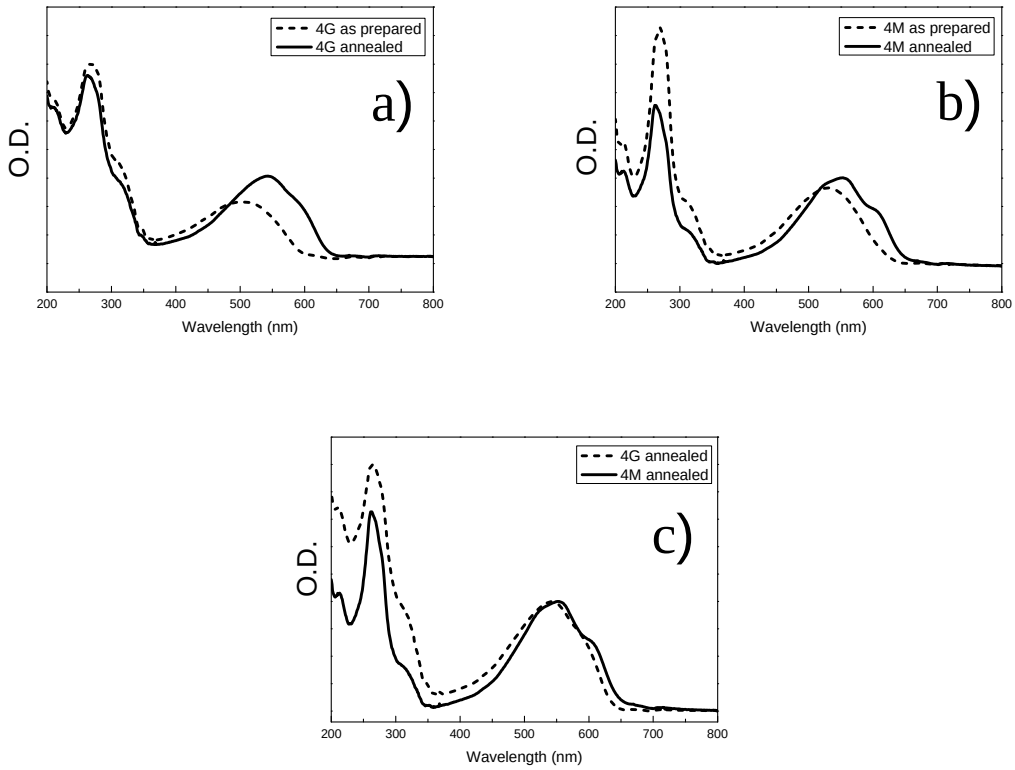

*Figure 4.14 Absorption properties in solid state of the homopolymer **4G** and the alternating copolymer **4M** and the annealing (90°C, 2 hours) effect on film absorptions*

4.7 Charge transport property study (OFET)

The charge transport properties of the model poly(3-hexylthiophene) **4B**, the homopolymer **4G** and the alternating copolymer **4M** were investigated in OFET configurations. These measurements were carried out at CNRS-Ewha International Research Center (CERC, Korea), in collaboration with Prof. J.-W. Wu and Prof. J.-C. Ribierre (Ewha Womans University).

All the transistors have been prepared with Bottom-Gate (BG) and Top Contact (TC) configurations, same channel lengths, silanized (OTS) substrates and annealed thin films in order to limit the parameters. The details about the transistor fabrication and measurement parameters are given in Paragraph 4.9.2.

The output and transfer characteristics of the model polymer **4B**, homopolymer **4G** and alternating copolymer **4M** are shown in Figure 4.15, Figure 4.16 and Figure 4.17, respectively.

In the case of the model short regioregular poly(3-hexylthiophene) **4B**, the hole mobility obtained was 6.1×10^{-2} $cm^2V^{-1}s^{-1}$, which is consistent with the mobility values of the classical regioregular P3HT

published previously [298, 299]. Nevertheless, such high values are generally obtained for high molecular weight P3HTs, and short polymer chains give generally lower mobilities of one or two orders of magnitudes (10^{-4}-10^{-3} $cm^2V^{-1}s^{-1}$) [299]. This indicates that the **4B** films of our transistors present probably an optimized structure. This value of $6.1x10^{-2}$ $cm^2V^{-1}s^{-1}$ can be consequently taken as an internal reference in the discussion of the mobility-structure relationship of the following cases.

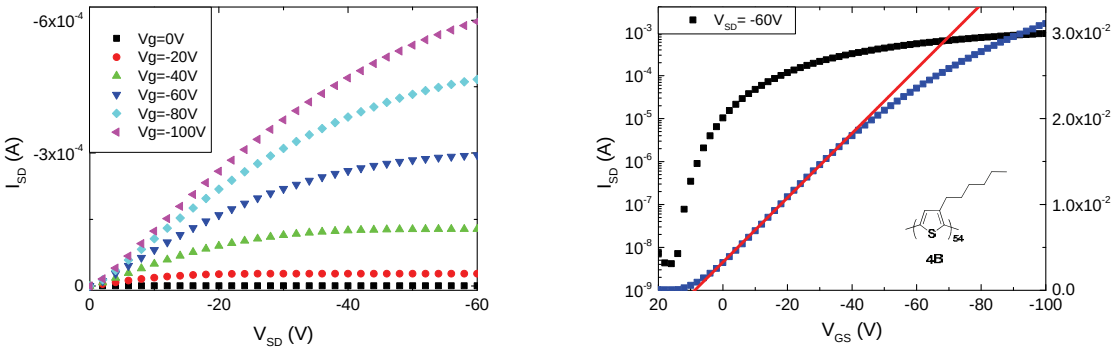

*Figure 4.15 Output and transfer characteristics of the model short poly(3-hexylthiophene) **4B***

In the case of the homopolymer **4G**, the hole mobility was measured about $1.4x10^{-5}$ $cm^2V^{-1}s^{-1}$, which is almost three orders of magnitude lower than the model poly(3-hexylthiophene) **4B**. This low value can be explained by the introduction of the triphenylene side-groups in the polythiophene lamellar structure and by their organization in a long-range correlated columnar superstructure. The triphenylenes being connected with the polymer backbone via unstretchable linkers, that introduce geometric constraints leading to disorder and periodic undulations of the layers as proved by the absence of the scattering at 3.8 Å in the X-ray pattern of **4G** which indicates with the lack of π-π interactions between polythiophenes.

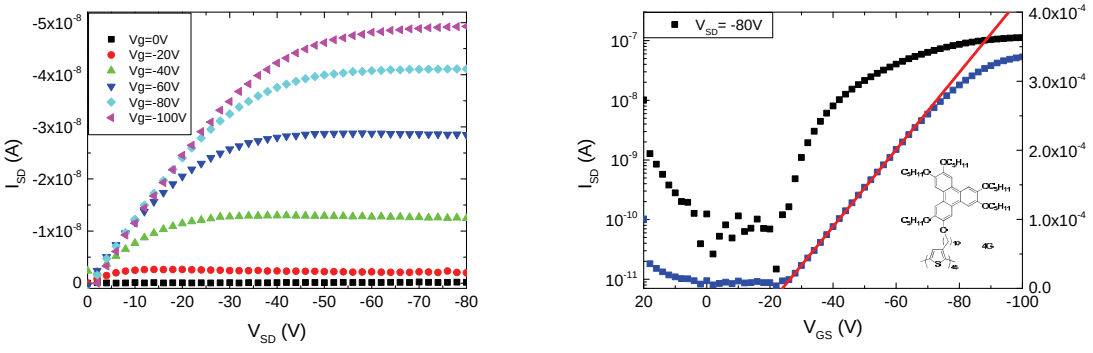

*Figure 4.16 Output and transfer characteristics of the homopolymer **4G***

In the case of the alternating copolymer **4M**, the hole mobility was measured about $1.6x10^{-3}$ $cm^2V^{-1}s^{-1}$, which is two orders of magnitude higher than the previous homopolymer **4G**, and only one order of magnitude lower than the model poly(3-hexylthiophene) **4B**. This relatively high value can be

explained by the different thiophene/triphenylene ratio in the alternating copolymer **4M** in comparison with homopolymer **4G**. Indeed, as the self-organization of the polymers **4G** and **4M** are nearly the same, namely a lamello-columnar structure, the density of thiophene backbones is consequently doubled in the layers of **4M**. That induces a more regular stacking of backbones with better π-π interactions between polythiophenes, and therefore, an improvement of charge transport properties not so far from the model P3HT **4B**. This interpretation is also well consistent with the presence of the scattering at 3.8 Å in the X-ray pattern (Figure 4.10) and the red-shifted solid state absorption (Figure 4.14.c) of **4M**.

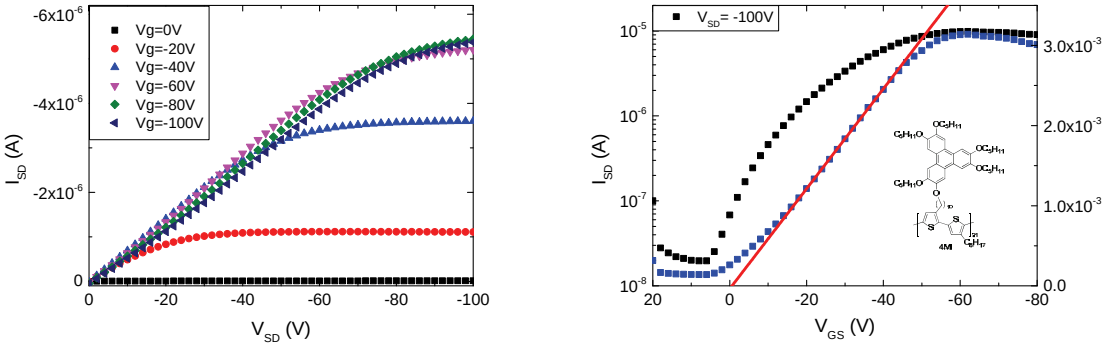

*Figure 4.17 Output and transfer characteristics of the alternating copolymer **4M***

It is worth noticing that these results indicate that in both polymers **4G** and **4M**, the charge transport is probably operated almost exclusively by the polythiophene sublayers. This result could be explained by the two-dimensional charge transport of the polythiophene sublayers which will be always more efficient than the one-dimensional one of the triphenylene sublayers (columnar organization), as long as the orientation of the columns in the plane of the film could not be mastered.

Mobilities, threshold voltage (V_{th}) and on/off current ratio ($I_{on}/_{off}$) of these polymers deduced from the device characteristics of these polymers are summarized in Table 4.3.

Polymers	Hole mobility ($cm^2V^{-1}s^{-1}$)	Threshold voltage (V)	I_{ON}/I_{OFF} ratio
Model polymer 4B	$6.1x10^{-2}$	8.5	$2.3x10^5$
Homopolymer 4G	$1.4x10^{-5}$	-24.1	$7.3x10^3$
Copolymer 4M	$1.6x10^{-3}$	-0.7	$5.3x10^2$

*Table 4.3 OFET performances of the model polymer **4B**, homopolymer **4G** and alternating copolymer **4M***

4.8 Conclusion

In order to study and evaluate the influence of the controlled dilution of the mesogenic side groups (i.e. the degree of polymer lateral substitution) on the supramolecular organizations and on charge transport properties of side chain liquid crystal semiconducting polymeric architectures, we synthesized three different regioregular polythiophene derivatives: a model poly(3-alkylthiophene) **4B,** a homopolymer comprising triphenylene side groups on each thiophene unit **4G** and an alternating

copolymer with thiophene/triphenylene ratios of 2:1 **4M.** They were prepared by Grignard metathesis-based methodology in order to control the chain lengths (in number of thiophene unities) at around 50.

The thermal and self-organization behaviors of these polymers were investigated by polarized-light optical microscopy, DSC, temperature-dependent X-ray diffraction, AFM, GIXS and temperature-dependent UV-vis spectroscopy. Both the substituted homo- and copolymer self-organize into mesophases possessing intertwined lamello-columnar structure (Lamcol mesophase), consisting in the alternation of triple rows of columns and of polymer backbone sublayers.

The hole transport mobility of polymers was tested in OFET configuration. The results indicate that first, in the case of homopolymer **4G**, the disorder introduced by the triphenylene presence in the sublayers of polythiophene backbones induces low mobility ($1.4x10^{-5}$ $cm^2V^{-1}s^{-1)}$, and second, that in the case of the alternating copolymer **4M** with thiophene/triphenylene ratios of 2:1, the increasing of the density (double) of thiophene backbones in the layers leads to a better packing in polythiophene sublayers, and consequently to the improvement of the mobility ($1.6x10^{-3}$ $cm^2V^{-1}s^{-1}$), not so far from the model poly(3-alkylthiophene) **4B** (6.1x10-2 $cm^2V^{-1}s^{-1}$).

These results underline the important impact of the molecular structure design of semiconducting polymeric architectures based on two chemically different moieties on the charge transport properties of these self-organized complex semi-conducting materials.

4.9 Experimental

4.9.1 SEC parameters

Two apparatus were used: 1) an Agilent 1100 Series SEC equipped with a 300 mm x 7.5 PL Gel Mixed-D 5 µm 10^{-4} Å, an refractive-index (RI) detector and Diode-Array UV-vis Detector (DAD); 2) a assemblied SEC constituted by three PL Gel Mixte-C 5µm columns (7.5 X 300 mm; separation limits: 0.2 to 2000 kg.mol^{-1}) coupled with a solvent and sample delivery module Viscotek GPCmax and 2 modular detectors: a differential refractive index (RI) detector Viscoteck 3580 and a DAD Shimadzu SPD20-AV. In both cases the column temperature was fixed at 40°C and the flow rate at 1ml min^{-1} in THF (HPLC-Grade). Both SEC were calibrated by polystyrene standards.

4.9.2 OFET sample preparation and configurations

As **4B**, **4G** and **4M** are polymers (macromolecules), the thermal evaporation method could not be applied in the thin film preparation, and thus only the spin-coating was used.

The parameters used during the spin-coating procedure were similar with those used in Chapter 3: spin speed=2000 rpm, ramp time=0.1 s, spin time= 60 s. The concentration used was 1% weight for the homopolymer **4G** and copolymer **4M** but for the model polymer **4B**, as its solubility is limited, the saturated chloroform solution (<0.5%) was used.

The profilometer confirms that the films thicknesses were all below 100 nm (varies from 40 to about 100 nm). The annealing was carried out in glove-box: 150°C, 30 min for the model polymer **4B**; 90°C, 20 min for both the substituted homopolymer **4G** and substituted copolymer **4M**.

The Bottom-Gate (BG) OFETs in Top Contact (TC) configurations were fabricated and characterized. The wafers used were purchased from MicroChemicals (thermally grown 300 nm SiO_2 as dielectric layer) and then silanized (OTS). The gold electrodes were deposited by thermal evaporation through a shadow mask at a slow rate (0.5 Å/s) directly on top of thin films to give a 40µm channel length and 1.6 cm of channel width.

The substrate cleaning method, silanization procedures, probe-station type and transistor performance calculation methods were identical to those described in Paragraph 3.5.1.

4.9.3 Synthesis

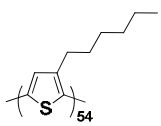

Chemical Formula (repeating unit) : $C_{10}H_{14}S$
Molecular Weight (repeating unit) : 168.2830

4B

Synthesized from the 2,5-dibromo-3-hexylthiophene in using the GRIM method. The procedures are the same as in the synthesis of **4F**.

$[M]_0/[Ni(dppp)Cl_2]_0$= 56 ; Yield : 64%. M_n = 15500, PDI = 1.16 (SEC-THF, PS Standard); DP_n(NMR)=54. NMR, δ_H (ppm) (500 MHz, $CDCl_3$): 6.98 (s, 54H), 2.80 (t, 104H), 2.60 (m, 4H), 1.73 (m, 108H), 1.41 (m, 324H). 0.94 (m, 162H). Anal. Calcd for $(C_{10}H_{14}S)_{54}Br$: C 71.59 %; H 8.42 %; Br 0.88 %; S 19.11 %; found: C 71.32 %; H 8.32 %; Br 0.71 %; S 16.69 %.

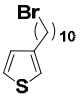

Chemical Formula: $C_{14}H_{23}BrS$
Molecular Weight: 303.3014

4D

3-Bromothiophene (**4C**) (3ml, 3.1 x 10^{-2} mol) was dissolved in 50 ml of freshly distilled hexane under an argon atmosphere. The resulting solution was cooled down to -40°C and stirred for 10 minutes. n-BuLi (19.4 ml, 3.1 x 10^{-2} mol, 1.6 M in hexane) was added drop wise via syringe at this temperature. 5 ml of THF was added to the pale yellow solution which was further left stirring for 1h then the resulting white suspension was allowed to warm to -10°C. 1,10-Dibromodecane (28.7 ml, 0.12 mol) was added in one portion at -10°C and the mixture was warmed to room temperature and stirred for another 2 h. The reaction was quenched by pouring 15 ml of water into the flask and extracted with diethyl ether (2 x 30 ml). The organic phase was washed with water (3 x 30 mL) and dried over anhydrous $MgSO_4$. A pale yellow oil was obtained as a crude product after removing the solvent. The crude was purified by fractional distillation under reduced pressure. After the first distillate (the excess dibromodecane) was removed, the residue was purified by the column chromatography (silica gel, petroleum ether) and afforded a colorless oil (3.52 g, 37%); NMR, δ_H (200 MHz, $CDCl_3$) 7.24 (1 H_{arom}, dd, J 2.9 and 4.9), 6.93 (2H_{arom}, m), 3.41 (2H, t, J 6.8, -CH_2-Br), 2.63 (2H, t, J 7.6, -CH_2-Ar), 1.86 (2H_{aliph}, m), 1.62 (2H_{aliph}, m), 1.40-1.25 (12H_{aliph}, m); δ_C (50 MHz, $CDCl_3$) 143.31, 128.38, 125.16, 119.88, 34.20, 32.95, 30.66, 30.39, 29.58, 29.53, 29.42, 28.87, 28.83, 28.28. Anal. Calcd for $C_{14}H_{23}BrS$: C, 55.44; H, 7.64; Br, 26.34, Found: C, 55.80; H, 7.68; Br: 25.98.

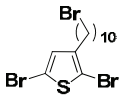

Chemical Formula: $C_{14}H_{21}Br_3S$
Molecular Weight: 461.0935

4E

3-(10-Bromodecyl)thiophene (**4D**) (1.61 g, 5 x 10^{-3} mol) was dissolved in 5 ml of DMF under an atmosphere of nitrogen. N-Bromosuccinimide (2.3 g, 1.3 x 10^{-2} mol) in 10 ml of DMF was added drop wise to this solution at room temperature. After stirring the reaction mixture overnight, the reaction mixture was poured into cold water (50 ml) and extracted with 3 x 30 ml of diethyl ether. The organic

phase was washed with water (3x30 ml), dried over anhydrous $MgSO_4$ and concentrated under reduced pressure. The crude product was submitted to column chromatography over silica gel using hexane as eluant to yield the title compound (1.98 g, 81%); NMR, δ_H (ppm) (200 MHz, $CDCl_3$) 6.77 (1 H_{arom}, s), 3.41 (2H, t, J 6.8, -CH_2-Br), 2.50 (2H, t, J 7.5, -CH_2- Ar), 1.86 (2H_{aliph}, m), 1.65-1.25 (14H_{aliph}, m); δ_C (ppm) (75 MHz, $CDCl_3$) 142.00, 131.97, 109.05, 107.64, 34.20, 32.96, 30.56, 29.56, 29.50, 29.48, 29.32, 29.01, 28.87, 28.30. Anal. Calcd for $C_{14}H_{21}Br_3S$: C, 36.47; H, 4.59; Br, 51.99, Found: C, 36.70; H, 4.42; Br: 51.15.

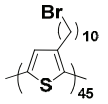

Chemical Formula (repeating unit) : $C_{14}H_{21}BrS$
Molecular Weight (repeating unit) : 301.2854

4F

All glasswares and solvents were carefully dried before use. 2,5-dibromo-3-(10-bromodecyl)thiophene (**4E**) (4 g, 8.7 x 10^{-3} mol) was poured into 100 ml of dry THF at 0°C under argon atmosphere. A solution of isopropyl magnesium chloride (4.3 ml, 8.7 x 10^{-3} mol, 2.0 M in THF) was added drop by drop through a syringe and the resulting pale yellow solution was stirred for 1h at 0°C. A suspension of Ni(dppp)Cl_2 (75 mg, 1.48 x 10^{-4} mol, 1.6 mol %) in THF (5 ml) was quickly injected into the flask. The resulting red solution was gently warmed to room temperature and left overnight under constant stirring. The polymerization was quenched by pouring a 6 M solution of HCl (100 ml) followed by extraction with chloroform (100 ml). The organic layer was successively washed by water (3 x 100 ml), dried over $MgSO_4$ and concentrated under reduced pressure. The crude product was precipitated using methanol and the resulting purple solid was filtered through a Soxhlet thimble. The title compound was obtained (1.31 g, 50%) after successive extraction with methanol; M_n = 14200, PDI = 1.15 (SEC-THF, PS Standard); NMR, δ_H (ppm) (300 MHz, $CDCl_3$): 6.98 (1H, s, Harom), 3.39 (2H, t, J 6.8, -CH_2-Br), 2.80 (2H, m, -CH_2-Ar), 1.90-1.60 (4H, m, H_{aliph}), 1.50-1.31 (12H, m, H_{aliph}); δ_C (ppm) (75 MHz, $CDCl_3$) 139.98, 133.80, 130.59, 128.73, 34.16, 34.14, 32.95, 30.64, 29.64, 29.59, 29.56, 28.91, 28.31. Anal. Calcd for $C_{14}H_{21}BrS$: C, 55.81; H, 7.03; Br, 26.52, Found: C, 55.43; H, 6.94; Br: 26.21.

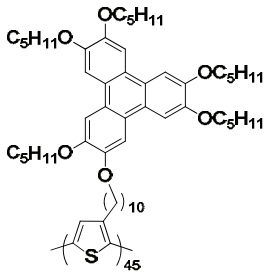

Chemical Formula (repeating unit) : $C_{57}H_{82}O_6S$
Molecular Weight (repeating unit) : 895.3223

4G

2,3,6,7,10-Pentakis(pentyloxy)-11-hydroxytriphenylene (**T**) (0.45 g, 6.6 x 10^{-4} mol), potassium carbonate (0.18 g, 1.3 x 10^{-3} mol) in DMF (20 ml) was heated at 80°C under an atmosphere of nitrogen. One hour later, poly[3-(10-bromodecyl)thiophene] (**4F**) (0.1 g, 3.3 x 10^{-4} mol) in THF (15 ml) was added slowly to the green mixture. The resulting orange solution was left under heating at 120°C for 3 days. The reaction mixture was then cooled down and filtered to remove the excess of base followed by extraction with chloroform (100 ml). The organic layer was successively washed with water (3 x 100 ml), dried over $MgSO_4$ and concentrated under reduced pressure. The crude product was precipitated from chloroform to an abundant volume of methanol and the resulting purple solid was filtered through a Soxhlet thimble. The title compound was obtained (0.22 g, 73%) as a dark red powder after successive extraction with methanol; M.p. 107 °C (Lcol - Iso), NMR, δ_H (ppm) (250 MHz, $CDCl_3$) 7.73 (6H_{arom}, s), 6.94 (1 H_{arom}, s), 4.16 (12H, br. s, OCH_2), 2.76 (2H, br. s, CH_2-Ar), 1.90 (12H_{aliph}, br. s), 1.50-1.30 (34H_{aliph}, m), 0.93 (15H, br. s, -CH_3). Anal. Calcd for $C_{57}H_{82}O_6S$: C, 76.29; H, 9.23. Found: C, 75.75; H, 9.13.

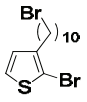

Chemical Formula: $C_{14}H_{22}Br_2S$
Molecular Weight: 382.1975

4E'

To a solution of 3-(10-bromodecyl)thiophene (**4D**) (1.8 g, 5.9 mmol) in 20 ml of DMF, NBS (0.95 g, 5.3 mmol) in 15 ml DMF was added slowly. The mixture was slightly heated up to 35°C for 5 h and then poured into 200 ml of water. The organic materials were extracted by dichloromethane and washed with brine and dried over anhydrous $MgSO_4$. After removal of the solvents, the crude product was purified by column chromatography on silica gel (5% dichloromethane in hexane) to give **4E'** as colorless oil: 1.95 g, yield of 96%. NMR δ_H (ppm) (200 MHz, $CDCl_3$): 7.19 (1H, d, J = 5.6 Hz), 6.79 (1H, d, J = 5.8 Hz), 3.41 (2H, t, J = 6.7 Hz), 2.56 (2H, t, J = 7.5 Hz), 1.86 (2H, mbr), 1.61 (2H, mbr), 1.27 (12H, mbr); δ_C (ppm) (50 MHz, $CDCl_3$): 141.9, 128.2, 125.1, 108.8, 34.0, 32.8, 29.7, 29.4, 29.4, 29.4, 29.3, 29.2, 28.7, 28.2.

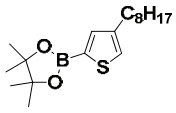

Chemical Formula: $C_{18}H_{31}BO_2S$
Molecular Weight: 322.3135

4I

To a solution of 2,2,6,6-tetramethylpiperidine (3.6 g, 25.5 mmol) in 50 ml of dry THF, 10.2 ml n-BuLi (2.5 M in hexane) was added drop wise at -10°C. The mixture was stirred for another 30 min at -10°C and then cooled down to -78°C. A solution of 3-octylthiophene (**4H**) (5.0 g, 25.5 mmol) in 20 ml of dry THF was then added slowly and the system was kept under -78°C for 1 h. After stirring at -40°C for another 2.5 h, 2-isopropoxy-4,4,5,5-tetramethyl-1,3,2-dioxaborolane (5.2g, 28.0 mmol) was

added drop wise at -78°C, and then the mixture was allowed to warm to room temperature and stirred overnight. Then the mixture was poured into 200 ml of water and the organic materials were extracted by dichloromethane and washed with brine and dried over anhydrous $MgSO_4$. After removal of the solvents, the crude product was purified by column chromatography on silica gel (5% ethyl acetate in hexane) to give **4I** as colorless oil: 5.6 g, yield of 68.2%. NMR δ_H (ppm) (200 MHz, $CDCl_3$): 7.48 (1H, s), 7.21 (1H, s), 2.62 (2H, t, J = 7.7 Hz), 1.59 (2H, mbr), 1.24-1.27 (22H, sbr), 0.88 (3H, t, J = 6.5Hz); δ_C (ppm) (125 MHz, $CDCl_3$): 144.7, 138.5, 133.7, 127.5, 84.0, 31.9, 30.7, 30.1, 29.4, 29.3, 29.2, 24.7, 22.7, 14.2.

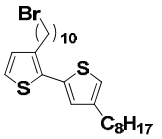

Chemical Formula: $C_{26}H_{41}BrS_2$
Molecular Weight: 497.6377

4J

To a 35 ml of dimethoxyethane solution containing **4I** (1.81 g, 5.6 mmol) and **4E'** (2.15 g, 5.6 mmol), catalyst $Pd(Pph_3)_4$ (323 mg, 0.28 mmol) was added followed by a 20 ml of 1M $NaHCO_3$. This mixture was heated to reflux for 16 h and cooled. After filtration, the organic layer was separated and the solvents were removed by vacuum evaporation. The residue was charged to a silica column (hexane as eluant) to give the product **4J** as light yellow oil: 2.28 g, yield of 82.1%. NMR δ_H (ppm) (200 MHz, $CDCl_3$): 7.15 (1H, d, J = 5.2 Hz), 6.94 (1H, d, J = 1.4 Hz), 6.93 (1H, d, J = 5.2 Hz), 6.89 (1H, d, J = 1.4 Hz), 3.41 (2H, t, J = 6.9 Hz), 2.74 (2H, t, J = 7.7 Hz), 2.60 (2H, t, J = 7.6 Hz), 1.85 (2H, mbr), 1.63 (4H, mbr), 1.30 (22H, mbr), 0.88 (3H, t, J = 6.5Hz); δ_C (ppm) (50 MHz, CDCl3): 143.6, 139.3, 135.9, 131.0, 129.9, 127.4, 123.5, 119.9, 34.0, 32.8, 31.9, 30.6, 30.3, 29.6, 29.4, 29.4, 29.1, 28.7, 28.2, 22.6, 14.1.

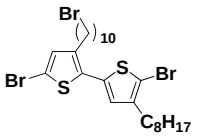

Chemical Formula: $C_{26}H_{39}Br_3S_2$
Molecular Weight: 655.4299

4K

To a solution of **4J** (2.28 g, 4.6 mmol) in 20 ml of DMF, NBS (1.63 g, 9.2 mmol) in 15 ml of DMF was added slowly. The mixture was stirred at room temperature overnight and then poured into 200 ml of water. The organic materials were extracted by dichloromethane and washed with brine and dried over anhydrous $MgSO_4$. After removal of the solvents, the crude product was purified by column chromatography on silica gel (hexane as eluant) to give **4K** as light yellow oil: 2.02 g, yield of 67%. NMR δ_H (ppm) (200 MHz, $CDCl_3$): 6.88 (1H, s), 6.74 (1H, s), 3.42 (2H, t, J = 6.9 Hz), 2.64 (2H, t, J = 7.7 Hz), 2.55 (2H, t, J = 7.7 Hz), 1.87 (2H, mbr), 1.57 (4H, mbr), 1.28 (22H, mbr), 0.89 (3H, t, J =

6.5Hz); δ_C (ppm) (50 MHz, $CDCl_3$): 142.5, 140.5, 134.3, 132.5, 131.5, 127.3, 110.7, 109.1, 34.0, 32.9, 31.9, 30.6, 29.7, 29.4, 29.3, 29.3, 29.3, 29.0, 28.8, 28.2, 22.7, 14.2.

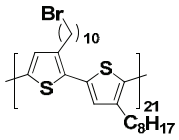

Chemical Formula (repeating unit) : $C_{26}H_{39}BrS_2$
Molecular Weight (repeating unit): 495.6217

4L

To a three-necked 50 ml flask was added **4K** (880 mg, 1.3 mmol) and 13 ml dry and oxygen-free THF. i-PrMgCl (0.67 ml, 2M in THF) was added then via syringe at 0°C. After stirring for 1 hour, Ni(dppp)Cl_2 (23 mg, 0.032 mmol) was added quickly with 1 ml of dry THF in one portion and the ice-bath was then removed. The reaction was stirring for another 3 hours and quenched by 6M HCl solution. The organic layer was extracted by chloroform and washed with brine and dried over anhydrous $MgSO_4$. After removal of the solvents, the residue was redissolved in 3 ml chloroform and precipitated in 150 ml of MeOH. The solid polymer was washed by using the Soxhlet extractor with successive solvents, first with MeOH, and then EtOH, and finally chloroform. After removal of chloroform, the polymer **4L** was dried under vacuum to give a dark-red solid. 320 mg, yield of 67%. M_n = 10 600, PDI = 1.34 (SEC-THF, polystyrene standard); DP_n (NMR) = 22; NMR δ_H (ppm) (200 MHz, $CDCl_3$): 6.97 (2H, sbr), 3.38 (2H, t), 2.79 (2H, mbr), 1.83 (2H, mbr), 1.66 (4H, mbr), 1.28 (22H, mbr), 0.89 (3H, t, J = 6.5Hz).

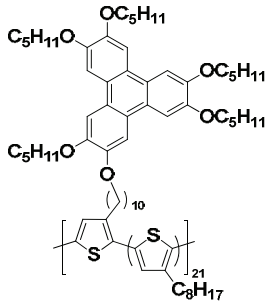

Chemical Formula (repeating unit): $C_{69}H_{100}O_6S_2$
Molecular Weight (repeating unit): 1089.6586

4M

To a solution of 2,3,6,7,10-pentakis(pentyloxy)-11-hydroxytriphenylene (**T**) (405 mg, 0.6 mmol) in 90 ml of DMF, K_2CO_3(331 mg, 2.4mmol) was added and the solution was heated up to 80°C for 1 h. Then a solution of 120 mg **4L** dissolved in 5 ml of THF was added and the mixture was heated to 120°C and the reaction was stirring for 3 days before it was poured into 200 ml of water. The organic materials were extracted by chloroform and washed with brine and dried over anhydrous $MgSO_4$. After removal of the solvents, the residue was redissolved in 5 ml chloroform and precipitated in 150 ml of MeOH. The precipitates were washed with acetone (6 h) and then EtOH (2 days) by using soxhlet apparatus, and dried under vacuum, 110mg, yield of 37%. M_n = 17800, PDI = 1.6 (SEC-THF,

polystyrene standard); M.p. 123-134°C (Lcol - Iso); NMR δ_H (ppm) (200 MHz, $CDCl_3$): 7.80 (6H), 6.96 (2H), 4.21 (12H), 2.77 (4H), 1.93 (12H), 1.70-1.20 (46H), 0.98 (15H), 0.89 (3H). Anal. Calcd for $C_{69}H_{100}O_6S_2$: C, 75.79; H, 9.22. Found: C, 74.87; H, 9.12.

CHAPTER 5 SYNTHESIS AND CHARACTERISATION OF DONOR-σ-ACCEPTOR SIDE CHAIN LIQUID CRISTALLINE π-CONJUGATED POLYMERS

5.1 Introduction

Ambipolar materials with high and balanced electron and hole mobilities would be of interest for a range of applications such as complementary-like logic circuits [62, 300] and light-emitting field-effect transistor [51, 53, 54, 234, 301, 302]. Here, to access this class of materials, we propose an approach taken advantage of the results obtained in the previous chapter.

In Chapter 4, we studied the structure-charge transport properties relationship of a p-type model liquid crystalline side-chain polymer, consisting of a regioregular (3-alkyl)polythiophene as backbone and triphenylene discotic mesogens as side-groups. This architecture allowed the formation of lamello-columnar organization. In the present chapter, we designed a new family of donor-σ-acceptor liquid crystalline side-chain polymers combining a p-type backbone and n-type side-groups in a unique self-organized polymeric architecture. More precisely, these polymers are formed by regioregular (3-alkyl)polythiophene backbones and perylene diimide side groups as presented in Figure 5.1.a. The expected self-organized structure is shown in Figure 5.1.b. This organization should lead to two distinct pathways for both charge carriers: holes in the polythiophene lamellae and electrons in perylene lamellae of columns. The self-organization properties in bulk and in thin films have been studied and preliminary results on charge transport properties, investigated in field effect transistor configuration (Figure 5.1.b), are reported.

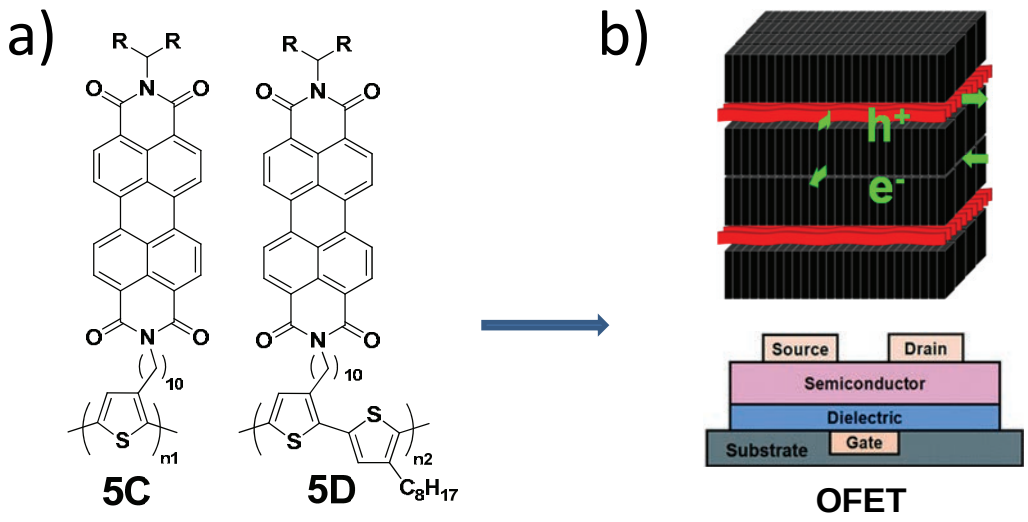

Figure 5.1: a) Chemical structures of the target donor-σ-acceptor polymers. b) Schematic representation of the expected self-organized structure and charge transport properties

5.2 Synthesis

The synthesis of side-chain polymers can be generally considered either by "direct polymerization" of a monomer bearing already the side-group [303, 304], or by "post-functionalization" of the polymeric backbone [123, 195, 305]. Considering that the perylene diimide side-groups are bulky and have a strong

tendency to aggregate, we first tested the "direct polymerization" strategy to prepare the polymers **5C** and **5D** and to ensure the complete substitution**.**

5.2.1 Synthesis by "direct polymerization"

The "direct polymerization" strategy considered for synthesizing the homopolymer **5C** consisting of regioregular (3-alkyl)polythiophene backbones and perylene diimide side groups is given in Figure 5.2. In this synthetic route, the Gabriel synthesis was performed on the 3-(ω-bromodecyl)thiophene **4D** to transform the brome on terminal alky chain to an amine before to undergo an imidification condensation to introduce the perylene diimide derivative **2M** onto the thiophene. After a mild bromination with NBS, the perylene diimide-functionalized monomer was prepared. Unfortunately, this later monomer decomposed during the final GRIM polymerization due to the Grignard Metathesis conditions and more particularly the Grignard reagent which seems incompatible with the imide functions. Consequently, no polymer was formed and the perylene diimide was found dissociated from the thiophene moiety.

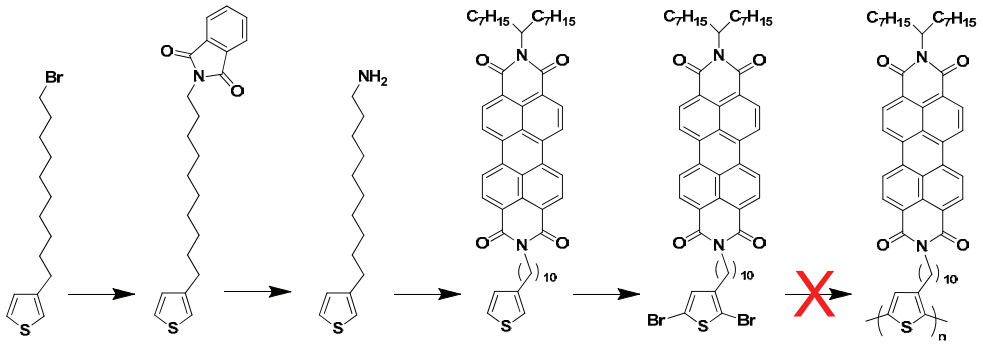

Figure 5.2 The "direct polymerization" route which did not work at the GRIM step

5.2.1 Synthesis by "post-functionalization"

Since the "direct polymerization" is not compatible with the imide function of the perylene side groupe, we secondly considered the "post-functionalization" strategy for preparing the polymers **5C** and **5D** as described in the Figure 5.3. This strategy is based on the use of the perylene diimide building bloc **2M** (see Chapter 2) which was first converted into the perylene derivative **5A** by treatment in NH_4OAc/acetic acid, and then grafted onto the precursory homopolymer and the alternating copolymer **4F** and **4L** developed in Chapter 4, with similar conditions to the triphenylene substitution. It is worth noticing that in order to avoid using an excess of base which might attack the other imide groups, **5A** was firstly reacted with the K_2CO_3 in stoichiometric condition to form its potassium salt. Then this salt was introduced to the precursory polymers **4F** or **4L** in fairly excessive quantity to reinforce the substitution ratio.

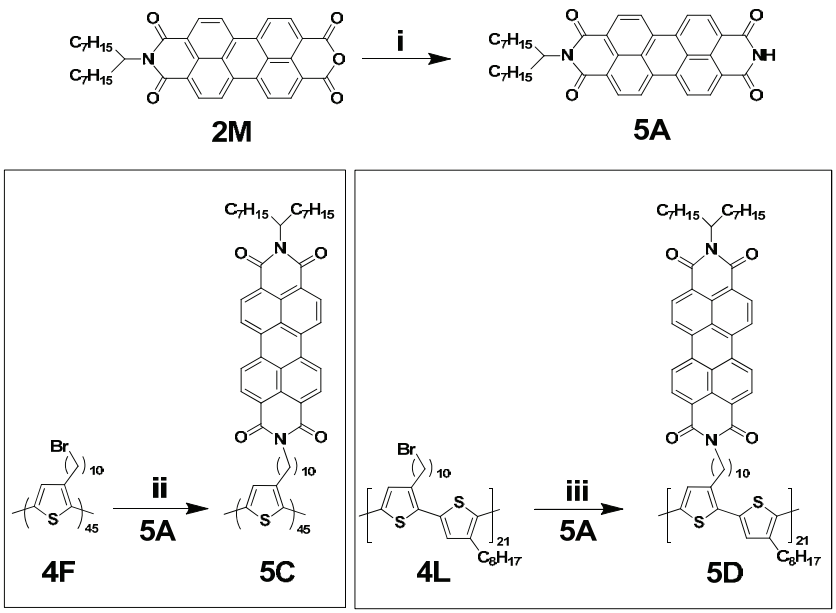

*Figure 5.3 Synthesis of the perylene diimide substituted homopolymers and alternating copolymer Conditions: (i) NH_4OAc, acetic acid, reflux, quantitative; (ii) (a) **5A**, K_2CO_3, DMF, 100°C; (b) **4F**, 130 °C, 17%. (iii) (a) **5A**, K_2CO_3, DMF, 100°C; (b) **4L**, 130 °C, 32%.*

As the excess of perylene was difficult to be removed by Soxhlet extraction and normally precipitates with the final polymers themselves, the crude polymers were then directly purified by the semi-preparative SEC (in chloroform). In both cases, the fractions from 21-28 min were collected as the target polymers **5C** and **5D** (Figure 5.4).

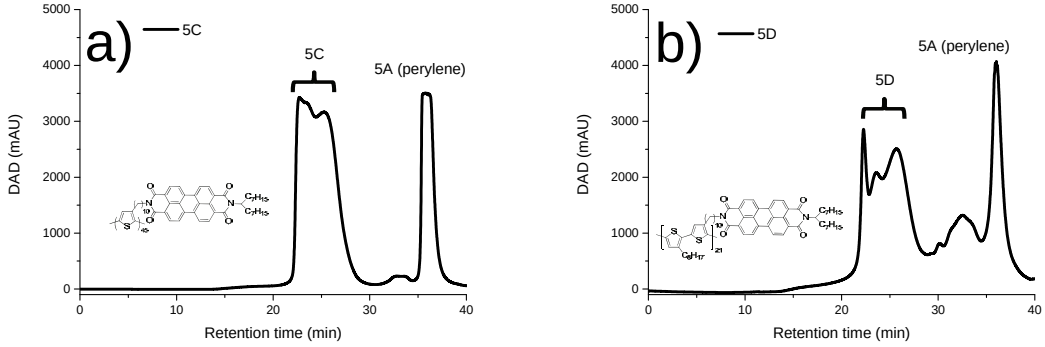

*Figure 5.4 Preparative SEC profiles of a) **5C** and b) **5D***

Then the fractionated polymers were characterized by ^{1}H NMR to evaluate the substitution ratio. In Figure 5.5, in the case of the homopolymer **5C**, it can be observed that the residual peak of the proton in α position of brome (at 3.37 ppm) persisted after the grafting reaction and based on its integration, the substitution ratio was estimated as 85%. Concerning the alternating copolymer **5D**, this signal at 3.37 almost completely vanished, confirming that the substitution is almost quantitative (considering the sensitivity of the NMR spectroscopy). It is worth noticing that, due to the bulky size of the perylene diimide side-groups and the steric hindrance induced around the terminal Br, it is not

surprising that the substitution on the homopolymer was not complete while it was complete for the alternating copolymer presenting substitution sites perfectly distributed every tow thiophenes.

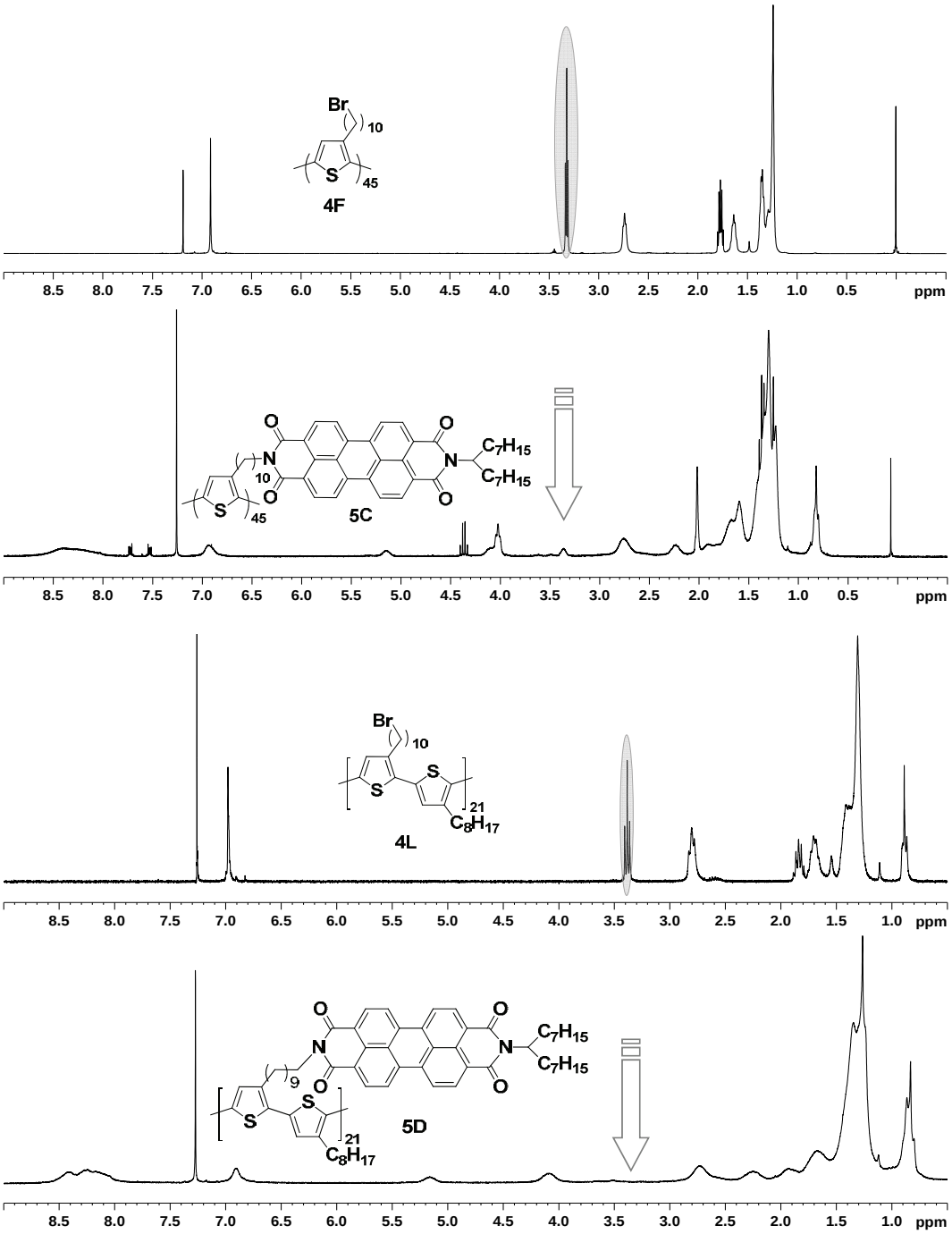

Figure 5.5 ^{1}H NMR spectra of precursory and grafted homopolymer and alternating copolymers

5.3 Thermal behavior

The thermal behavior of the homopolymer **5C** and alternating copolymer **5D** were investigated by Polarized-light Optical Microscopy (POM) and Differential Scanning Calorimetry (DSC).

5.3.1 Polarized-light optical microscopy

Under POM, the homopolymer **5C**, in its pristine state, appeared as a solid dark "plastic" showing very weak birefringence which disappeared at around 80° on heating (Figure 5.6.a). On further heating, the polymer softened gradually into a very viscous material at very high temperature (250°C). On cooling and on additional thermal treatment cycles, no birefringence was observed again.

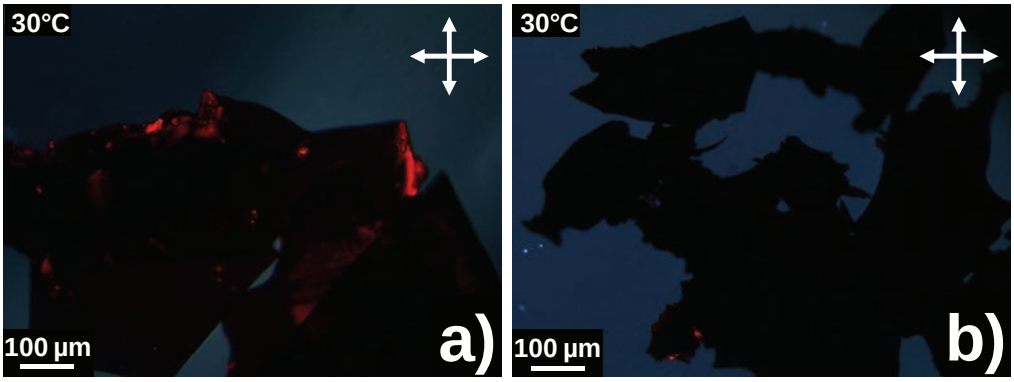

*Figure 5.6 POM images of a) **5C** and b) **5D** at 30°C*

Concerning the alternating copolymer **5D**, no birefringence was observed in this pristine state (Figure 5.6.b) during the heating and cooling cycles. Contrary to homopolymer **5C, t**he pristine dark solid melted into a very viscous liquid at around 160°C.

5.3.2 Differential scanning calorimetry

The DSC thermograms of the polymers **5C** and **5D** are given in Figure 5.7.

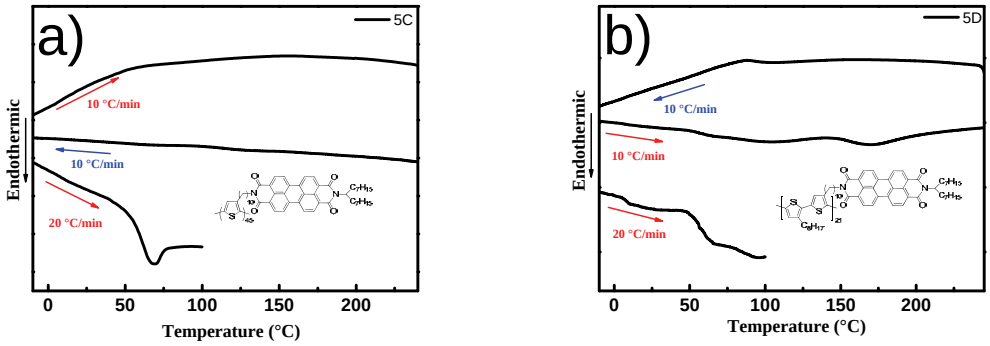

*Figure 5.7 DSC thermograms of homopolymer **5C** and alternating copolymer **5D***

The homopolymer **5C presents**, on the first heating (rate 20 °C/min), a clear glass transition ($T_{g)}$ at 53.8°C, associated with a classical volume relaxation peak which is not visible anymore on the other heating. No other evident transitions were observed at higher temperature neither on heating nor on cooling. For the alternating copolymer **5D**, a T_g was also observed at slightly higher temperature (61.8°C). On further heating, an endothermic peak at 167.7°C, associated with an enthalpy change of

4.8 Jg^{-1}, is observed, which is characteristic of the melting point (T_{mel}) of the polymer as also observed in POM. On cooling, the reversible transition is very difficult to observe and only the Tg can be really observed.

The DSC thermal analysis results are listed in Table 5.1.

Polymer	T_g [a] (°C)	Transition [b]	T_{mel} [c] (°C)	ΔH (J g^{-1})
Homopolymer 5C	53.8	Lamcol → I	-	-
Alternating Copolymer 5D	61.8	Lamcol → I	167.7	4.8

*Table 5.1. DSC results of **5C** and **5D** on heating .[a] T_g = glass transition (20°C min^{-1}); [b] Transition temperatures, Lamcol=lamello-columnar phase, I=Isotropic phase; [c] T_{mel}: melting temperature (maximum of the large peak).*

5.5 Self-organization property study

5.5.1 Temperature-dependent X-Ray Diffraction

The substituted homopolymer **5C** and alternating copolymer **5D** were studied by Temperature-Dependent X-Ray Diffraction (TDXRD) in the temperature ranges determined by DSC and POM studies. The measurements were carried out at Institut de Physique et de Chimie des Matériaux de Strasbourg (IPCMS) in cooperation with Dr. B. Heinrich and Dr. Bertrand Donnio.

The XRD patterns of the homopolymer **5C** are shown in Figure 5.8. In pristine state, the XRD pattern contains only broad scattering signals in the small and wide-angle regions which are due to the first neighbor distances between polythiophene backbones (PT), perylene diimides (PDI) and molten aliphatic segments (Figure 5.8.a). While the presence of a characteristic wide-angle maximum at 3.5 Å evidences the face-to-face piling of the PDI segments (h_{PDI}), no scattering maximum is visible at 3.80 Å (h_{PT}), what indicates that polythiophene backbones are not regularly stacked. The unique small-angle scattering around 20 Å with a correlation distance of $\xi \approx 40$ Å (evaluated from the Scherrer formula [126, 259]) is compatible with the average distance between PDI piles (D_{PDI}) evaluated from segment partial volumes. These observations indicate the amorphous character of homopolymer **5C** in the pristine state.

The annealing at 100°C (above the Tg) during 1 hour then leads to a modified pattern at room temperature (Figure 5.8.b), presenting the simultaneous appearance of numerous lamellar orders in the small-angle region and a new scattering visible at 3.80 Å (h_{PT}). That indicates now a much better segregation in sublayers with sharper interfaces and with a regular stacking of polythiophene backbones. The layer spacing around 58 Å and the intensity modulation in the small-angle harmonic series accord with two PDI and one PT electron-rich sublayers, separated by aliphatic spacers and tails which evidence a frozen lamello-columnar (Lamcol) organization as illustrated in the schematic packing model (Figure 5.8.d).

Diffractograms revealed that the annealing at higher temperature and cooling down at room temperature doesn't lead to better structured sample as proved in Figure 5.8.c and by the slightly decreasing of small angle lamellar orders and the scattering at 3.80 Å (h_{PT}).

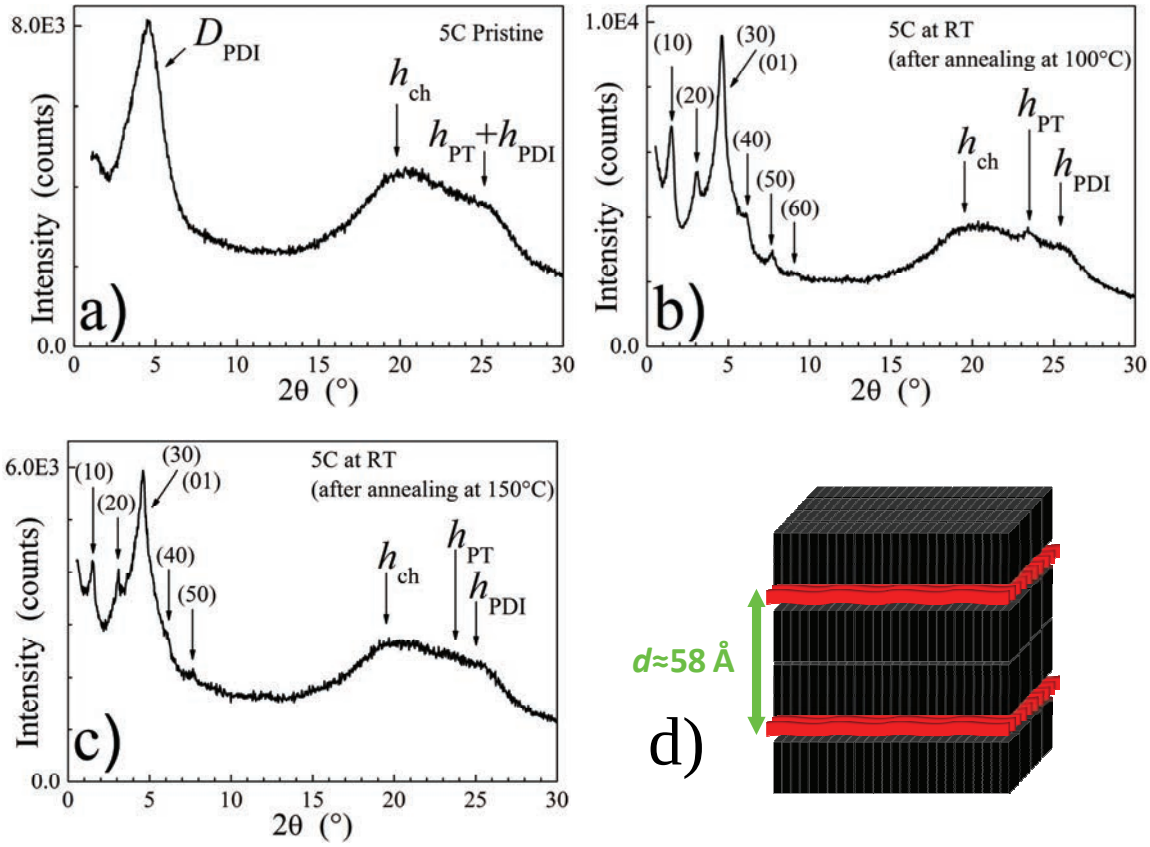

*Figure 5.8 XRD patterns of homopolymer **5C** at room temperature (RT): (a) in the pristine state; (b) after annealing at 100°C for 1 h; (c) after annealing at 150°C for 1 h; d) schematic representation of the frozen lamello-columnar organization*

The XRD patterns of the homopolymer **5D** are given in Figure 5.9. Contrary to homopolymer **5C**, the alternating copolymer **5D** already shows lamellar organization in the pristine state (Figure 5.9.a). The pristine state pattern contains numerous lamellar orders in the small-angle region and three scattering signals in the wide-angle region at 4.5 Å, 3.8 Å, 3.5 Å, corresponding respectively with molten aliphatic chain (h_{ch}), the stacking of polythiophene backbones (h_{PT}) and the stacking of perylene diimide cores (h_{PDI}). The reduced intensity of the first lamellar order confirms the presence of several high electronic density sublayers in lamellae, whose thickness (d ≈ 40 Å) is substantially smaller than in the homopolymer due to the reduction of perylene diimide number. These observations evidence a frozen lamello-columnar (Lamcol) organization very close to the previous homopolymer **5C** as illustrated in the schematic packing model (Figure 5.9.d).

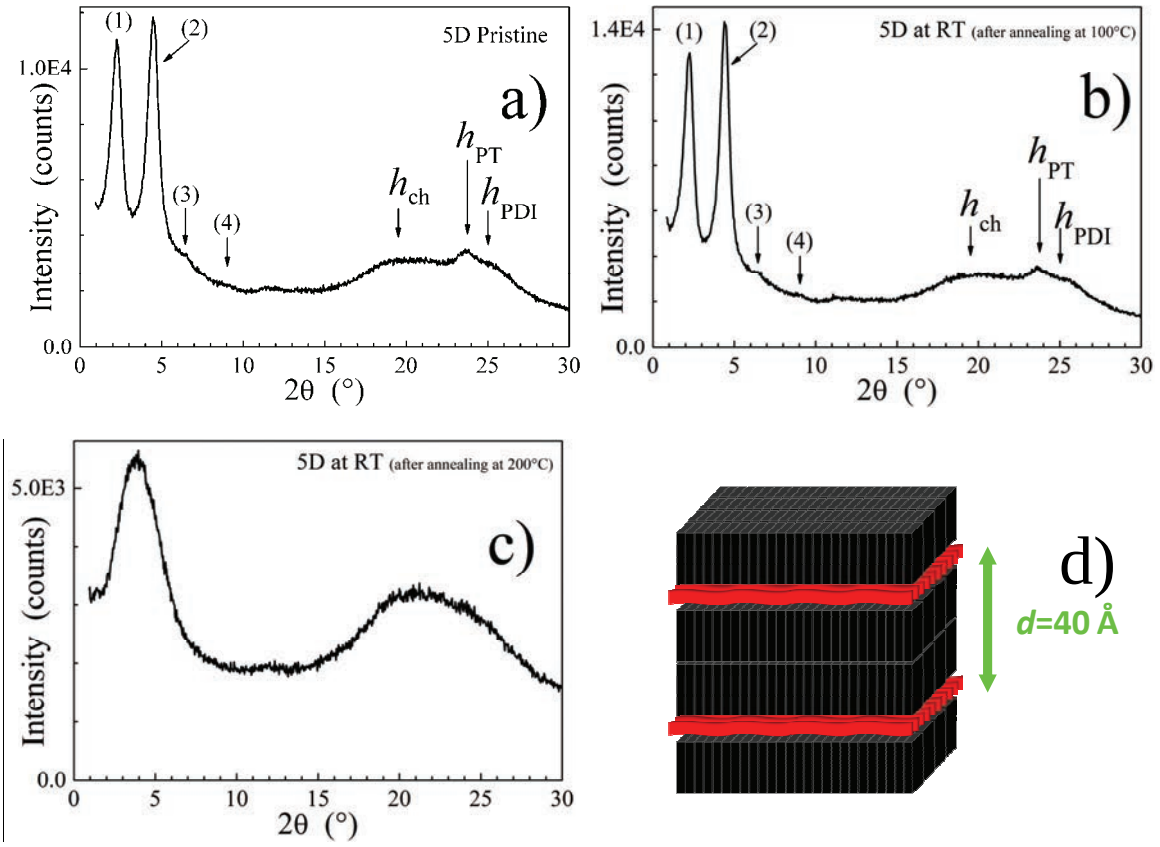

*Figure 5.9 XRD patterns of alternating copolymer **5D** at room temperature (RT): (a) in the pristine; (b) after annealing at 100°C for 1 h; (c) after annealing at 200°C for 1 h; d) schematic representation of the frozen lamello-columnar organization*

The annealing at 100°C until the T_{mel} during 1 hour does not change the structure as proved by the similar patterns obtained (Figure 5.9.b). However, the annealing at 200°C (above the T_{mel}) and cooling down at room temperature leads to an amorphous sample as shown in Figure 5.9.c: the isotropic phase seems to be frozen on cooling, considering the cooling rate used in our measurements (5-10°C/min), which is consistent with DSC observations.

5.5.2 Grazing-Incidence X-ray Scattering

The thin film structure and morphology of alternating copolymer **5D** were studied by Grazing-Incidence X-ray Scattering (GIXS). These measurements were carried out at Pohang Accelerator Laboratory (PAL), in collaboration with Prof. H-J Kim (Pusan National University). GIXS results are shown in Figure 5.10.

The **5D** film was prepared by spin coating from a chloroform solution of material (0.5% w/w. 3000 rpm) onto an OTS treated silicon wafer. The thickness of film varies from 50 to 60 nm as evaluated by profilometer. The samples were studied after annealing (150°C for 2 hours in vacuum). For more details of the sample preparation, see Paragraph 5.7.2.

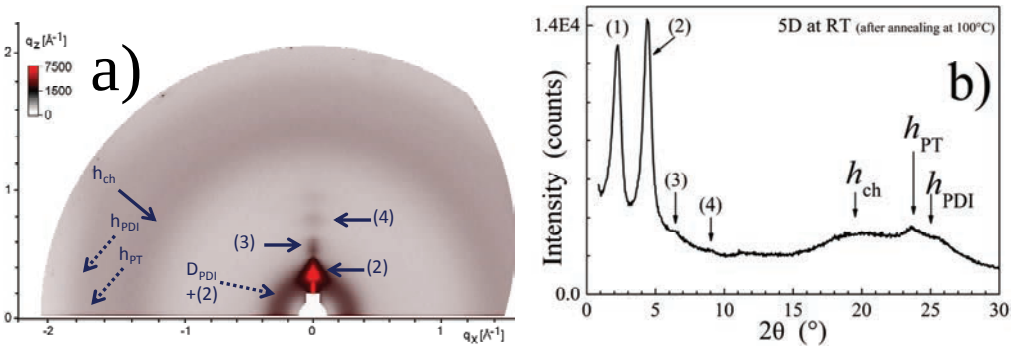

*Figure 5.10 (a) GIXS patterns (with different contras, red and black) of alternating copolymer **5D** (spun cast on silicon wafer; annealed at 150°C for 2 h); grazing angle=0.12°; (b) bulk X-ray diffraction pattern of **5D** after annealing at 100°C*

The typical two dimensional GIXS image of annealed samples of **5D** is given in Figure 5.10.a. In the small-angle region, the pattern presents several broad peaks in the specular plane (along q_z), corresponding to the (00l) reflections of the lamellar organization, as observed in the small-angle region of the bulk X-ray diffraction patterns (Figure 5.10.b). It presents also one diffuse ring at 0.3 Å^{-1} which is compatible with the average lateral distance between perylene diimide piles ($D_{PDI)}$. In the wide-angle region, in addition to the very diffuse halo around 1.4 Å^{-1} (4.5Å), corresponding to the liquid-like disorder of the aliphatic chains (h_{ch}), this pattern presents two weak broad in-plane reflections (along q_x) around 1.7 Å^{-1} and 1.82 Å^{-1} corresponding respectively to the stacking (3.8 Å) of polythiophene backbones (h_{PT}) and the π-π stacking (3.5 Å) of the segregating perylene diimide (h_{PDI}).

These results indicate a poor lamellar structure with short-correlated organizations inside sublayers. The thin film exhibits the coexistence of a disordered and Lamcol organization presenting, for the later, a weak preferential orientation of lamellae in parallel to the substrate.

5.6 Preliminary charge transport property study (OFET)

The charge transport properties of the homopolymer **5C** and the alternating copolymer **5D** were investigated in OFET configurations. These measurements were carried out at CNRS-Ewha International Research Center (CERC, Korea), in collaboration with Prof. J.-W. Wu and Prof. J.-C. Ribierre (Ewha Womans University).

All the transistors have been prepared with Bottom-Gate (BG) and Bottom-Contact (BC) configurations, and silanized (OTS) treated substrates and they have been measured in as-prepared state and annealed state. The details about the transistor fabrication and measurement parameters are given in Paragraph 5.7.3.

The as prepared transistors of homopolymer **5C** presented a nice p-channel output and transfer profiles and a hole mobility of 1.0×10^{-6} cm^{2}V^{-1}s^{-1} can be determined Unfortunately, no clear n-type behavior was observed.

After the annealing treatment (150°C, 1 hour in glove-box), the homopolymer **5C** OFET showed clearly an ambipolar behavior since n-type and p-type output and transfer profiles can be recorded (Figure 5.11). An electron mobility of 3.9×10^{-6} $cm^2V^{-1}s^{-1}$ was determined and the hole mobility increased more than one order of magnitude, to give 3.3×10^{-5} $cm^2V^{-1}s^{-1}$. The detailed OFET performances are listed in Table 5.2.

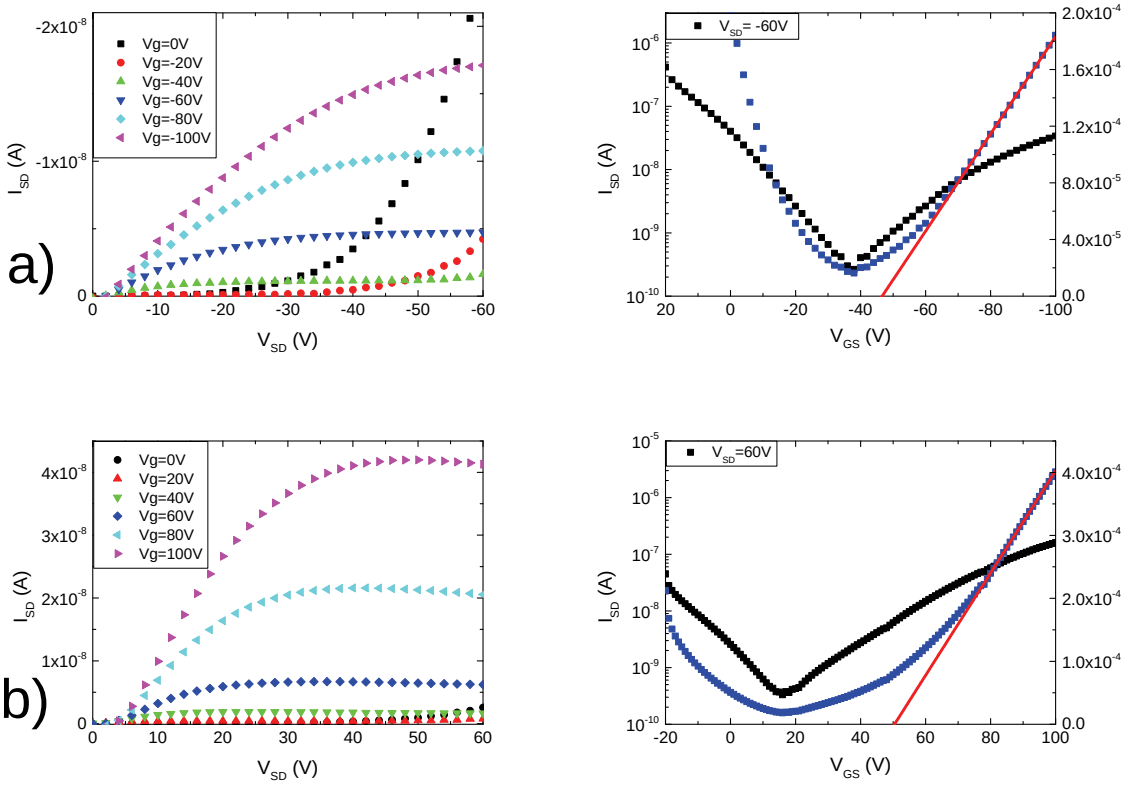

*Figure 5.11 Output and transfer characteristics for holes (a) and for electron (b) of homopolymer **5C** (annealed)*

The transistors of alternating copolymer **5D** gave a hole mobility of 4.1×10^{-6} $cm^2V^{-1}s^{-1}$. Unfortunately, as for the previous polymer **5C,** no electron mobility could be determined. In addition, similarly to **5C**, after the annealing treatment (200°C, 1 hour in glove-box), **5D** OFET **showed also** an ambipolar behavior. The hole mobility was slightly decreased of one order of magnitude from 4.1×10^{-6} $cm^2V^{-1}s^{-1}$ to 4.5×10^{-7} $cm^2V^{-1}s^{-1}$ after annealing, but more interestingly an electron mobility appeared of around 3.5×10^{-8} $cm^2V^{-1}s^{-1}$. It is worth noticing that the annealing temperature (200°C) was chosen arbitrarily before having the complete thermal behavior characterizations of the polymer **5D,** and doesn't fulfill the best conditions.

The thermal treatment conditions, charge carrier mobilities, threshold voltage and on/off current ratio about the **5C** and **5D** OFETs are listed in Table 5.2.

Polymers	Thermal Treatment	Charge Carrier Type	Mobility ($cm^2V^{-1}s^{-1}$)	Threshold Voltage (V)	I_{ON}/I_{OFF} Ratio
5C	As prepared	Hole	$1.0x10^{-6}$	-34	$6.2x10^3$
		Electron	-	-	-
	Annealed	Hole	$3.3x10^{-5}$	-49	$8.8x10^2$
		Electron	$3.3x10^{-6}$	45	$0.9x10^2$
5D	As prepared	Hole	$4.1x10^{-6}$	-41	$5.6x10^3$
		Electron	-	-	-
	Annealed	Hole	$4.5x10^{-7}$	-47	$5.8x10^2$
		Electron	$3.5x10^{-8}$	77	$2.3x10^2$

*Table 5.2 Field-effect mobility, threshold voltage and on/off current ratio of **5C** and **5D** with different conditions*

It can be observed that the annealing has an impact on the charge transport properties of polymers **5C** and **5D** since that allows to obtain ambipolar behavior with relatively well balanced mobilities, probably due to the slight improvement of the thin film structures. However, the mobilities are obviously low and the characteristic of these ambipolar transistors are quite modest (low I_{ON}/I_{OFF} ratio and high threshold voltage). That could be explained by the difficulty to master and optimize the film preparation (orientation, alignment) as suggested by the first GISX measurements. Nevertheless, these preliminary promising results show that it is possible to inject holes and electrons into a single semiconductor from the same type of electrode, by combining purely p-type and n-type entities in a unique macromolecular architecture

5.7 Conclusion

Based on the results of the previous chapter (Chapter 4) focusing on the design and charge transport properties of a p-type model liquid crystalline side-chain polymers, we developed in this last Chapter a new family of donor-σ-acceptor liquid crystalline side-chain polymers combining a p-type regioregular (3-alkyl)polythiophene backbone and n-type perylene diimide side-groups in a unique self-organized polymeric architecture.

More precisely, we functionalized the precursory homopolymer and alternating copolymer developed in Chapter 4 by perylene diimide derivatives, to reach these two perylene diimides grafted regioregular polythiophenes: a homopolymer comprising perylene diimide side-groups on each thiophene unit **5C** (85% substituted) and an alternating copolymer with a thiophene/perylene diimide ratio of 2:1 **5D**. Both polymers have a chain length around 50 (in number of thiophene units) which was controlled by the GRIM polymerization during the precursory polymer preparation.

The thermal and self-organization behaviors of these polymers were investigated by polarized-light optical microscopy, DSC, temperature-dependent X-ray diffraction and GIXS. Both the substituted homo- and copolymer self-organize into mesophases possessing intertwined lamello-columnar

structure (Lamcol mesophase), consisting in the alternation of double rows of side-groups and of polymer backbone sublayers.

The charge carrier mobility of polymers was tested in OFET configuration. The preliminary results indicate that both polymers present ambipolar charge transport properties with a hole and electron mobility up to $3.3x10^{-5}$ $cm^2V^{-1}s^{-1}$ and $3.3x10^{-6}$ $cm^2V^{-1}s^{-1}$ respectively, for the homopolymer **5C**. However, we can notice that these low mobilities are probably underestimated due to the difficulty to master the orientation and structure during the thin film elaboration, as suggested by the GIXS results.

Nevertheless, these preliminary promising results validate our approach based on two different donor and acceptor moieties combined in a unique liquid-crystalline polymeric architecture. This novel self-organized complex semiconducting materials can propose a simple and versatile strategy for producing distinct conductive channels at the nanoscale, allowing the injection of holes and electrons from the same type of electrode and leading to a new class of supramolecular ambipolar materials, easily processable, potentially suitable for electronic and optoelectronic applications.

5.7 Experimental

5.7.1 Semi-preparative SEC parameters

The semi-preparative SEC parameters were as follows: Steric exclusion was carried out on two successive columns at room temperature, PLgel mixted 10 µm 500 Å (300*25mm) and PLgel mixted 10µm 1000 Å (300*25mm), respective separation limits of 500-30000 and 500-60000 g mol^{-1}. The automative apparatus used was a model of Agilent: system GPC/SEC ChemStation 1100/1200.

5.7.2 GIXS sample preparation

The samples used in the GIXS were prepared by spin coating.

For both polymers, the films were spun cast from a filtrated (0.4µm) 0.5% wt. chloroform solution onto silanized (OTS) wafer. Spin speed=3000 rpm, ramp time=0.5s, spin time= 60s. The thickness of film was around 50±15 nm (tested by profilometer). These films were then annealed at 200°C for 2 hours in vacuum.

5.7.3 OFET sample preparation and configurations

The thin films of polymers were spun cast onto the test chips with the same parameters in GIXS.

The OFET test chips used were fabricated with MicroChemicals wafer (thermally grown 280 nm SiO_2 as dielectric layer) and the interdigitated Au electrodes. The parameters of the interdigitated transistors are as follows: channel length=25 µm, channel width=1 mm, total channel width= 2cm.

The substrate cleaning method, silanization procedures, probe-station type and transistor performance calculation methods were identical to those described in Paragraph 3.5.1.

5.7.2 Synthesis

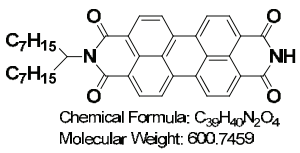

5A

A mixture of **2M** (1.0 g, 1.66 mmol) and NH_4OAc (13.0 g, 168.6 mmol) were dissolved in 50 ml of acetic acid and heated to reflux for 24 hours. Then the crude product was poured to brine and extracted by DCM, dried over anhydrous $MgSO_4$ and the solvent was then removed under reduced pressure. After a purification by column chromatography over silica gel using a 5% acetic acid solution in chloroform as eluant, **5A** was obtained as dark red solid (930 mg, quantitative); NMR, δ_H (ppm) (200 MHz, $CDCl_3$) 8.59-8.75 (m, 8H), 8.53 (br. s, 1H), 5.10-5.25 (m, 1H), 2.13-2.37 (m, 2H), 1.77-1.96 (m, 2H), 1.08-1.44 (m, 20H), 0.82 (t, 6H).

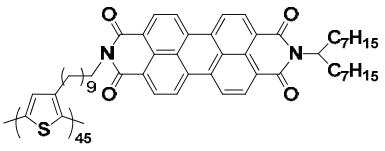

Chemical Formula(repeating unit): $C_{53}H_{60}N_2O_4S$
Molecular Weight (repeating unit): 821.1194

5C

The homopolythiophene precursor **4F** (133.8 mg, 0.444 mmol in repeating unit) was dissolved in 5 ml of DMF at 100 °C. In another flask, **5A** (800 mg, 1.33 mmol) and K_2CO_3 (184 mg, 1.33 mmol) were added in 5 ml DMF at 100°C and stirred for about 10 minutes. This suspension was added quickly (to keep the temperature) to the previous precursor polymer solution through a filter to remove the excess K_2CO_3 and stirred overnight at 130°C. The mixture was then extracted between chloroform and water, dried over anhydrous $MgSO_4$ and the solvent was then removed under reduced pressure. The crude product was precipitated from chloroform to cold MeOH and filtered through a Soxhlet thimble. After extracted in Soxhlet with MeOH and EtOH, the mixture was fractionated by the preparative SEC and gives a black solid (60 mg, 17%). NMR, δ_H (ppm) (200 MHz, $CDCl_3$): 8.40 (br m, 8H), 6.95 (br. s, 1H), 5.16 (br s, 1H), 4.03 (br s, 2H), 2.77 (br s, 2H), 2.24 (br m, 2H), 1.92-1.25 (br m, 38H), 0.82 (br m, 6H). (The NMR integrations listed are theoretical, through the residual peak at 3.37 (br s) which comes from the proton at the α position of the un-reacted brome and its integration, the substitution was estimated as 85%)

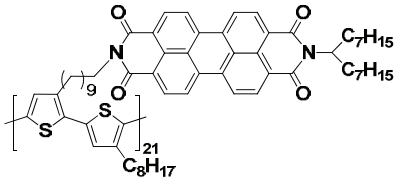

Chemical Formula(repeating unit): $C_{66}H_{78}N_2O_4S$
Molecular Weight (repeating unit): 1015.4557

5D

The copolythiophene precursor **4L** (120 mg, 0.242 mmol in repeating unit or in Brome) was dissolved in 5 ml of DMF at 100 °C. In another flask, **5A** (290 mg, 0.484 mmol) and K_2CO_3 (134 mg, 0.968 mmol) were added in 5 ml DMF at 100°C and stirred for about 10 minutes. This suspension was added quickly (to keep the temperature) to the previous precursor polymer solution through a filter to remove the excess K_2CO_3 and stirred for 4 hours at 130°C. Then another same suspension of **5A** was prepared and added in the same way and the reaction continued overnight. The mixture was extracted between chloroform and water, dried over anhydrous $MgSO_4$ and the solvent was removed under reduced pressure. The crude product was precipitated from chloroform to cold MeOH and filtered through a Soxhlet thimble. After extracted in Soxhlet with MeOH and EtOH, the mixture was fractionated by the preparative SEC and gives a black solid (79 mg, 32%). NMR, δ_H (ppm) (300 MHz, $CDCl_3$): 8.25 (br

m, 8H), 6.90 (br. s, 2H), 5.15 (br s, 1H), 4.08 (br s, 2H), 2.73 (br s, 2H), 2.25 (br m, 2H), 1.92-1.25 (br m, 52H), 0.82 (br m, 9H).

CONCLUSIONS AND PERSPECTIVES

During this work, we designed, synthesized and characterized several different self-organized semiconducting architectures incorporating different kind of electron-donor (p-type) and electron-acceptor (n-type) π-conjugated systems in unique liquid crystalline molecular or macromolecular architectures. We expect these ambipolar materials could present a spontaneous nanosegregation of p-type and n-type entities in bulk, leading to well defined distinct conductive channels for each type of charge carriers.

More precisely, we started this work with the **molecular approach**, in designing two innovative families of small molecular donor-π-acceptor liquid crystalline dyads and triads incorporating either calamitic or discotic entities (Chapters 2 and 3).

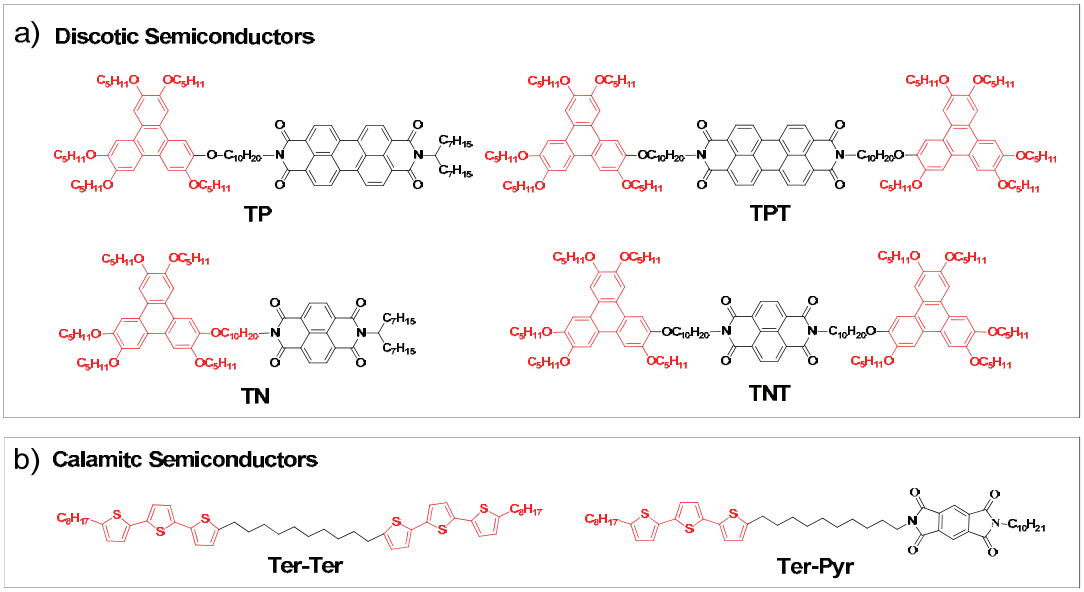

- First, we chose conventional discotic semiconductors such as triphenylene derivatives as p-type building blocks and perylene or naphthalene derivatives as n-type building blocks the linked by alkyl chain spacers (Chapter 2). Then, after developing an efficient chemical strategy, we determined and discussed their thermal behavior, self-organization, as well as the optical and electronic properties of these new molecules. In particular, it must be noticed that most of the molecules obtained, namely the triphenylene-perylene based dyad **TP** and triad **TPT** together with the triphenylene-naphthalene based triad **TNT,** are liquid crystalline, self-organizing into well defined columnar nanostructures which can even be preserved at room temperature, in glassy state. Moreover, the ambipolar properties of these molecules were confirmed by cyclic voltammetry. Among these compounds, we consequently focused essentially on the dyad **TP** and we performed AFM and GIXS measurements on solid films evidencing that this material can self-organize into hexagonal columnar structures and orientates with the columns in parallel with surface: it is indeed a favorable property when looking for efficient organic transistors where the preparation of lying columns is a key factor. Unfortunately, in the liquid crystal and/or solid state, neither TOF nor OFET charge transport studies have revealed any mobility

until now while an untypical charge transport was observed in its isotropic state which could be explained by the same photon transfer in solution absorption: a short correlation distance in the columnar and/or a non-optimized in-plane orientation of columns could be the two main reasons.

- Second, we synthesized and fully characterized two new compounds, based this time on usual calamitic semiconductors such as p-type terthiophene derivatives and n-type pyromellitic derivatives, both being linked by the same type of alkyl chain spacer (Chapter 3). Both of them revealed smectic liquid crystal mesophases, but and more interestingly through XRD, GIXS and then OFET studies, a charge transport in 2D smectic/lamellar sub-layers was confirmed. Finally, after testing and optimizing different thermal and surface treatments, a relatively high hole transport mobility of 0.1 $cm^2V^{-1}s^{-1}$ was obtained from the model terthiophene-terthiophene dyad **Ter-Ter**. Concerning the donor-σ-acceptor dyad **Ter-Pyr**, a lower hole mobility ($1x10^{-3}$ $cm^2V^{-1}s^{-1}$) was recorded and an weak electron transport was also observed. Nevertheless, the electron mobility in this donor-σ-acceptor dyad could not be evaluated from the OFET results till now, maybe due to a too important mismatching between the electrode (Au) work function and the LUMO level of the acceptor moiety and/or the non-optimized structures in the thin films: new attempts are currently in progress by modifying and adapting the transistor elaborations.

Concerning our **macromolecular approach**, we followed two different objectives:

- First (Chapter 4), based on the previous work initiated in our laboratory on a model p-type liquid crystalline side-chain polymer, consisting of a regioregular (3-alkyl)polythiophene as backbone and triphenylene discotic mesogens as side-groups, we developed and completed it in studying and evaluating the influence of the controlled dilution of the mesogenic discotic side groups (i.e. the degree of polymer lateral substitution) on the supramolecular organizations, and in correlating them with their charge transport properties obtained in field effect transistor configuration. To do so, we prepared by Grignard metathesis-based methodology one regioregular model rr-P3HT, one fully substituted homopolymer and one “diluted” substituted alternating copolymer, the chain length (in number of thiophene unities) being chosen around 50 for every polymers.

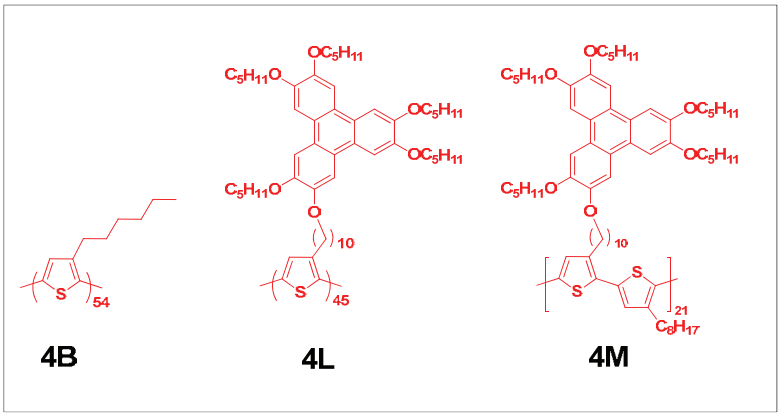

Remarkably, both the substituted homo- and copolymer self-organize into mesophases possessing intertwined lamello-columnar morphologies, resulting from the simultaneous coexistence of lamellar and columnar sublattices. Moreover, by tuning the molecular structure and thus the self-organization, the charge carrier mobility could be adjusted; the short model rr-P3HT **4B** presenting a good hole mobility value, the substituted homopolymer **4L** showing a much lower one and the substituted copolymer **4M** having intermediate values, close to model rr-P3HT **4B**.

- Second, to access to a class of ambipolar materials and in taking advantages of the precedent study in chapter 4, we propose an approach based on the design and synthesis of two donor- -acceptor liquid crystalline side-chain polymers combining a p-type backbone and n-type side-groups in a unique self-organized polymeric architecture (chapter 5). More precisely, these two polymers are formed by a regioregular polythiophene backbone and perylene diimide side groups. The first one is a homopolymer comprising perylene diimide side-groups on each thiophene unit **5C** and the second one is an alternating copolymer with a thiophene/perylene diimide ratio of 2:1 **5D**. Both polymers have a chain length around 50 (in number of thiophene units) which was controlled by the GRIM polymerization during the precursory polymer preparation. The structural characterization showed that both substituted homo- and copolymer self-organize into mesophases present an intertwined lamello-columnar structure, consisting in the alternation of double rows of side-groups and of polymer backbone sublayers.

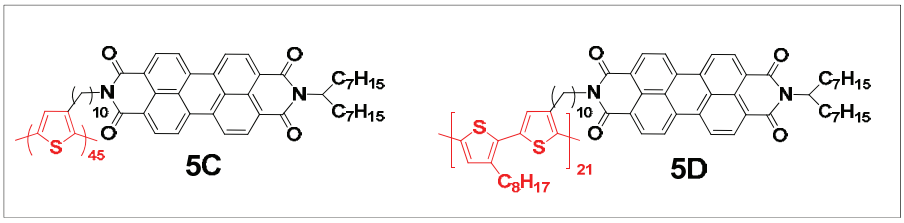

The preliminary studies of charge transport in OFET configuration indicate that both polymers present ambipolar charge transport properties with a hole and electron mobility up to $3.3x10^{-5}$ $cm^2V^{-1}s^{-1}$ and $3.3x10^{-6}$ $cm^2V^{-1}s^{-1}$ respectively, for the homopolymer **5C**. However, these low mobilities are probably underestimated due to the difficulty to master the orientation and structure during the thin film elaboration, as suggested by the GIXS results.

All this study and the preliminary results on charge transport properties are promising and validate our approach based on two different donor and acceptor moieties combined in a unique liquid-crystalline molecular or macromolecular architecture. This novel self-organized complex semiconducting materials can propose a simple and versatile strategy for producing distinct conductive channels at the nanoscale, allowing the injection of holes and electrons from the same type of

electrode and leading to a new class of supramolecular ambipolar materials, easily processable, potentially suitable for electronic and optoelectronic applications.

REFERENCES

1. Fincher, C. R.; Park, Y. W.; Heeger, A. J.; Shirakawa, H.; Louis, E. J.; Gau, S. C.; MacDiarmid, A. G.; Chiang, C. K., Electrical Conductivity in Doped Polyacetylene. *Physical Review Letters* **1977,** 39, (17), 1098-1101.
2. Forrest, S. R.; Thompson, M. E., Introduction: Organic Electronics and Optoelectronics. *Chemical Reviews* **2007,** 107, (4), 923-925.
3. Pope, M.; Swenberg, C. E., *Electronic processes in organic crystals and polymers*. Oxford University Press: 1999.
4. Mishra, A.; Bäuerle, P., Small Molecule Organic Semiconductors on the Move: Promises for Future Solar Energy Technology. *Angewandte Chemie International Edition* **2012,** 51, (9), 2020-2067.
5. Murphy, A. R.; Fréchet, J. M. J., Organic Semiconducting Oligomers for Use in Thin Film Transistors. *Chemical Reviews* **2007,** 107, (4), 1066-1096.
6. Mishra, A.; Ma, C.; Segura, J. L.; Bäuerle, P., Functional Oligothiophene-Based Materials: Nanoarchitectures and Applications. In John Wiley & Sons, Ltd: 2009; pp 1-155.
7. Forrest, S. R., The path to ubiquitous and low-cost organic electronic appliances on plastic. *Nature* **2004,** 428, (6986), 911-918.
8. Zaumseil, J.; Sirringhaus, H., Electron and Ambipolar Transport in Organic Field-Effect Transistors. *Chemical Reviews* **2007,** 107, (4), 1296-1323.
9. Wurthner, F., Perylene bisimide dyes as versatile building blocks for functional supramolecular architectures. *Chemical Communications* **2004,**, (14), 1564-1579.
10. Horowitz, G.; Bachet, B.; Yassar, A.; Lang, P.; Demanze, F.; Fave, J.; Garnier, F., Growth and Characterization of Sexithiophene Single Crystals. *Chemistry of Materials* **1995,** 7, (7), 1337-1341.
11. Shirota, Y.; Kageyama, H., Charge Carrier Transporting Molecular Materials and Their Applications in Devices. *Chemical Reviews* **2007,** 107, (4), 953-1010.
12. Pope, M.; Kallmann, H. P.; Magnante, P., Electroluminescence in Organic Crystals. *The Journal of Chemical Physics* **1963,** 38, (8), 2042-2043.
13. Vincett, P. S.; Barlow, W. A.; Hann, R. A.; Roberts, G. G., Electrical conduction and low voltage blue electroluminescence in vacuum-deposited organic films. *Thin Solid Films* **1982,** 94, (2), 171-183.
14. Tang, C. W.; VanSlyke, S. A., Organic electroluminescent diodes. *Applied Physics Letters* **1987,** 51, (12), 913-915.
15. Tang, C. W.; VanSlyke, S. A.; Chen, C. H., Electroluminescence of doped organic thin films. *Journal of Applied Physics* **1989,** 65, (9), 3610-3616.
16. Burroughes, J. H.; Bradley, D. D. C.; Brown, A. R.; Marks, R. N.; Mackay, K.; Friend, R. H.; Burns, P. L.; Holmes, A. B., Light-emitting diodes based on conjugated polymers. *Nature* **1990,**, (347), 539.
17. Baldo, M. A.; O Brien, D. F.; You, Y.; Shoustikov, A.; Sibley, S.; Thompson, M. E.; Forrest, S. R., High-efficiency fluorescent organic light-emitting devices using a phosphorescent sensitizer. *Nature* **1998,**, (395), 151.
18. Baldo, M. A.; Lamansky, S.; Burrows, P. E.; Thompson, M. E.; Forrest, S. R., Very high-efficiency green organic light-emitting devices based on electrophosphorescence. *Applied Physics Letters* **1999,** 75, (1), 4-6.
19. Lamansky, S.; Djurovich, P.; Murphy, D.; Abdel-Razzaq, F.; Lee, H.; Adachi, C.; Burrows, P. E.; Forrest, S. R.; Thompson, M. E., Highly Phosphorescent Bis-Cyclometalated Iridium Complexes: Synthesis, Photophysical Characterization, and Use in Organic Light Emitting Diodes. *Journal of the American Chemical Society* **2001,** 123, (18), 4304-4312.
20. Cleave, V.; Yahioglu, G.; Barny, P. L.; Friend, R. H.; Tessler, N., Harvesting Singlet and Triplet Energy in Polymer LEDs. *Advanced Materials* **1999,** 11, (4), 285-288.
21. O'Regan, B.; Grätzel, M., A low-cost, high-efficiency solar cell based on dye-sensitized colloidal TiO2 films. *Nature* **1991,**, (353), 737.
22. Nazeeruddin, M. K.; Kay, A.; Rodicio, I.; Humphry-Baker, R.; Mueller, E.; Liska, P.; Vlachopoulos, N.; Graetzel, M., Conversion of light to electricity by cis-X2bis(2,2'-bipyridyl-4,4'-dicarboxylate)ruthenium(II) charge-transfer sensitizers (X = Cl-, Br-, I-, CN-, and SCN-) on nanocrystalline titanium dioxide electrodes. *Journal of the American Chemical Society* **1993,** 115, (14), 6382-6390.
23. Günes, S.; Neugebauer, H.; Sariciftci, N. S., Conjugated Polymer-Based Organic Solar Cells. *Chemical Reviews* **2007,** 107, (4), 1324-1338.
24. Lilienfeld, J. E. US Patent 1745175. 1930.
25. Horowitz, G., Organic Field-Effect Transistors. *Advanced Materials* **1998,** 10, (5), 365-377.
26. Facchetti, A., Electroactive Oligothiophenes and Polythiophenes for Organic Field Effect Transistors. In John Wiley & Sons, Ltd: 2009; pp 595-646.
27. Facchetti, A.; Yoon, M. H.; Marks, T. J., Gate Dielectrics for Organic Field-Effect Transistors: New Opportunities for Organic Electronics. *Advanced Materials* **2005,** 17, (14), 1705-1725.

28. Wang, C.; Dong, H.; Hu, W.; Liu, Y.; Zhu, D., Semiconducting π-Conjugated Systems in Field-Effect Transistors: A Material Odyssey of Organic Electronics. *Chemical Reviews* **2011,** 112, (4), 2208-2267.
29. Karl, N., Charge carrier transport in organic semiconductors. *Synthetic Metals* **2003,** 133–134, (0), 649-657.
30. Coropceanu, V.; Cornil, J.; Da Silva Filho, D. A.; Olivier, Y.; Silbey, R.; Brédas, J., Charge Transport in Organic Semiconductors. *Chemical Reviews* **2007,** 107, (4), 926-952.
31. Horowitz, G.; Delannoy, P., Charge Transport in Semiconducting Oligothiophenes. In Wiley-VCH Verlag GmbH: 1998; pp 283-316.
32. Kepler, R. G., Charge Carrier Production and Mobility in Anthracene Crystals. *Physical Review* **1960,** 119, (4), 1226-1229.
33. LeBlanc, O. H., Hole and Electron Drift Mobilities in Anthracene. *The Journal of Chemical Physics* **1960,** 33, (2), 626-626.
34. Blom, P. W. M.; de Jong, M. J. M.; Vleggaar, J. J. M., Electron and hole transport in poly(p-phenylene vinylene) devices. *Applied Physics Letters* **1996,** 68, (23), 3308-3310.
35. Schouten, P. G. Charge carrier dynamics in pulse-irradiated columnar aggregates of mesomorphic porphyrins and phthalocyannines. Thesis, Delft University of Technology, 1994.
36. Schouten, P. G.; Warman, J. M.; de Haas, M. P., Effect of accumulated radiation dose on pulse radiolysis conductivity transients in a mesomorphic octa-n-alkoxy-substituted phthalocyanine. *The Journal of Physical Chemistry* **1993,** 97, (38), 9863-9870.
37. van de Craats, A. M.; Warman, J. M., The Core-Size Effect on the Mobility of Charge in Discotic Liquid Crystalline Materials. *Advanced Materials* **2001,** 13, (2), 130-133.
38. van de Craats, A. M.; Warman, J. M.; de Haas, M. P.; Adam, D.; Simmerer, J.; Haarer, D.; Schuhmacher, P., The mobility of charge carriers in all four phases of the columnar discotic material hexakis(hexylthio)triphenylene: Combined TOF and PR-TRMC results. *Advanced Materials* **1996,** 8, (10), 823-826.
39. Warman, J. M.; de Haas, M. P.; Dicker, G.; Grozema, F. C.; Piris, J.; Debije, M. G., Charge Mobilities in Organic Semiconducting Materials Determined by Pulse-Radiolysis Time-Resolved Microwave Conductivity: π-Bond-Conjugated Polymers versus π−π-Stacked Discotics. *Chemistry of Materials* **2004,** 16, (23), 4600-4609.
40. Klauk, H., Organic thin-film transistors. *Chemical Society Reviews* **2010,** 39, (7), 2643-2666.
41. Horowitz, G.; Hajlaoui, M. E.; Hajlaoui, R., Temperature and gate voltage dependence of hole mobility in polycrystalline oligothiophene thin film transistors. *Journal of Applied Physics* **2000,** 87, (9), 4456-4463.
42. Katz, H. E.; Bao, Z., The Physical Chemistry of Organic Field-Effect Transistors. *The Journal of Physical Chemistry B* **1999,** 104, (4), 671-678.
43. Sirringhaus, H., Device Physics of Solution-Processed Organic Field-Effect Transistors. *Advanced Materials* **2005,** 17, (20), 2411-2425.
44. Dimitrakopoulos, C. D.; Purushothaman, S.; Kymissis, J.; Callegari, A.; Shaw, J. M., Low-Voltage Organic Transistors on Plastic Comprising High-Dielectric Constant Gate Insulators. *Science* **1999,** 283, (5403), 822 -824.
45. Anthopoulos, T. D.; Tanase, C.; Setayesh, S.; Meijer, E. J.; Hummelen, J. C.; Blom, P. W. M.; de Leeuw, D. M., Ambipolar Organic Field-Effect Transistors Based on a Solution-Processed Methanofullerene. *Advanced Materials* **2004,** 16, (23-24), 2174-2179.
46. Rost, C.; Gundlach, D. J.; Karg, S.; Rieß, W., Ambipolar organic field-effect transistor based on an organic heterostructure. *Journal of Applied Physics* **2004,** 95, (10), 5782-5787.
47. Lindner, T.; Paasch, G.; Scheinert, S., Operation and properties of ambipolar organic heterostructure field-effect transistors. *Journal of Applied Physics* **2007,** 101, (1), -.
48. Dodabalapur, A.; Katz, H. E.; Torsi, L.; Haddon, R. C., Organic Heterostructure Field-Effect Transistors. *Science* **1995,** 269, (5230), 1560 -1562.
49. Dodabalapur, A.; Katz, H. E.; Torsi, L.; Haddon, R. C., Organic field-effect bipolar transistors. *Applied Physics Letters* **1996,** 68, (8), 1108-1110.
50. Zaumseil, J.; Sirringhaus, H., Electron and Ambipolar Transport in Organic Field-Effect Transistors. *Chemical Reviews* **2007,** 107, (4), 1296-1323.
51. Muccini, M., A bright future for organic field-effect transistors. *Nature Materials* **2006,**, (5), 605-613.
52. Sirringhaus, H.; Tessler, N.; Friend, R. H., Integrated Optoelectronic Devices Based on Conjugated Polymers. *Science* **1998,** 280, (5370), 1741 -1744.
53. Raffaella Capelli, S. T. G. G.; Muccini, A. M., Organic light-emitting transistors with an efficiency that outperforms the equivalent light-emitting diodes. *Nature Materials* **2010,**, (9), 496-503.
54. Rost, C.; Karg, S.; Riess, W.; Loi, M. A.; Murgia, M.; Muccini, M., Ambipolar light-emitting organic field-effect transistor. *Applied Physics Letters* **2004,** 85, (9), 1613-1615.

55. Loi, M. A.; Rost-Bietsch, C.; Murgia, M.; Karg, S.; Riess, W.; Muccini, M., Tuning Optoelectronic Properties of Ambipolar Organic Light- Emitting Transistors Using a Bulk-Heterojunction Approach. *Advanced Functional Materials* **2006,** 16, (1), 41-47.
56. Arias, A. C.; Corcoran, N.; Banach, M.; Friend, R. H.; MacKenzie, J. D.; Huck, W. T. S., Vertically segregated polymer-blend photovoltaic thin-film structures through surface-mediated solution processing. *Applied Physics Letters* **2002,** 80, (10), 1695-1697.
57. Meijer, E. J.; de Leeuw, D. M.; Setayesh, S.; van Veenendaal, E.; Huisman, B. H.; Blom, P. W. M.; Hummelen, J. C.; Scherf, U.; Klapwijk, T. M., Solution-processed ambipolar organic field-effect transistors and inverters. *Nature Materials* **2003,**, (2), 678-682.
58. Tang, M. L.; Oh, J. H.; Reichardt, A. D.; Bao, Z., Chlorination: A General Route toward Electron Transport in Organic Semiconductors. *Journal of the American Chemical Society* **2009,** 131, (10), 3733-3740.
59. Winder, C.; Sariciftci, N. S., Low bandgap polymers for photon harvesting in bulk heterojunction solar cells. *Journal of Materials Chemistry* **2004,** 14, (7), 1077-1086.
60. Roncali, J., Synthetic Principles for Bandgap Control in Linear ⊓-Conjugated Systems. *Chemical Reviews* **1997,** 97, (1), 173-206.
61. Xu, T.; Yu, L., How to design low bandgap polymers for highly efficient organic solar cells. *Materials Today* **2014,**, (17), 1369-7.21.
62. Anthopoulos, T. D.; de Leeuw, D. M.; Cantatore, E.; Setayesh, S.; Meijer, E. J.; Tanase, C.; Hummelen, J. C.; Blom, P. W. M., Organic complementary-like inverters employing methanofullerene-based ambipolar field-effect transistors. *Applied Physics Letters* **2004,** 85, (18), 4205-4207.
63. de Boer, R. W. I.; Gershenson, M. E.; Morpurgo, A. F.; Podzorov, V., Organic single-crystal field-effect transistors. *physica status solidi (a)* **2004,** 201, (6), 1302-1331.
64. Takahashi, T.; Takenobu, T.; Takeya, J.; Iwasa, Y., Ambipolar organic field-effect transistors based on rubrene single crystals. *Applied Physics Letters* **2006,** 88, (3), -.
65. Gray, G. W.; Demus, D.; Goodby, J.; Gray, G. W.; Spiess, H. W.; Vill, V., Introduction and Historical Development. In Wiley-VCH Verlag GmbH: 1998; pp 1-16.
66. de Gennes, P., Soft Matter (Nobel Lecture). *Angewandte Chemie International Edition in English* **1992,** 31, (7), 842-845.
67. Skoulios, A., *Annales de physique*, (3), 421.
68. Fuller, S.; Hopwood, J.; Rahman, A.; Shinde, N.; Tiddy, G. J.; Attard, G. S.; Howell, O.; Sproston, S., Amphitropic liquid crystals. Two lamellar phases in a surfactant containing thermotropic and lyotropic mesogenic groups. *Liquid Crystals* **1992,** 12, (3), 521-529.
69. Chandrasekhar, S.; Sadashiva, B. K.; Suresh, K. A., Liquid crystals of disc-like molecules. *Pramana* **1977,** 9, (5), 471-480.
70. Herrmann-Schönherr, O.; Wendorff, J. H.; Ringsdorf, H.; Tschirner, P., Structure of an aromatic polyamide with disc-like mesogens in the main chain. *Die Makromolekulare Chemie, Rapid Communications* **1986,** 7, (12), 791-796.
71. Niori, T.; Sekine, T.; Watanabe, J.; Furukawa, T.; Takezoe, H., Distinct ferroelectric smectic liquid crystals consisting of banana shaped achiral molecules. *Journal of Materials Chemistry* **1996,** 6, (7), 1231-1233.
72. Tinh, N. H.; Gasparoux, H.; Destrade, C., An Homologous Series of Disc-Like Mesogens with Nematic and Columnar Polymorphism. *Molecular Crystals and Liquid Crystals* **1981,** 68, (1), 101-111.
73. Brown, G. H.; Shaw, W. G., The Mesomorphic State - Liquid Crystals. *Chemical Reviews* **1957,** 57, (6), 1049-1157.
74. Finkelmann, H., Liquid Crystalline Polymers. *Angewandte Chemie International Edition in English* **1987,** 26, (9), 816-824.
75. Bushby, R.; Tate, D., Columnar Liquid Crystalline Semiconductors. In Bushby, R. J.; Kelly, S. M.; O'Neill, M., ^Eds. Springer Netherlands: 2013; Vol. 169, pp 65-96.
76. Adam, D.; Schuhmacher, P.; Simmerer, J.; Haussling, L.; Siemensmeyer, K.; Etzbachi, K. H.; Ringsdorf, H.; Haarer, D., Fast photoconduction in the highly ordered columnar phase of a discotic liquid crystal. *Nature* **1994,** 6493, (371), 141-143.
77. Simmerer, J.; Glüsen, B.; Paulus, W.; Kettner, A.; Schuhmacher, P.; Adam, D.; Etzbach, K.; Siemensmeyer, K.; Wendorff, J. H.; Ringsdorf, H.; Haarer, D., Transient photoconductivity in a discotic hexagonal plastic crystal. *Advanced Materials* **1996,** 8, (10), 815-819.
78. Deibel, C.; Janssen, D.; Heremans, P.; De Cupere, V.; Geerts, Y.; Benkhedir, M. L.; Adriaenssens, G. J., Charge transport properties of a metal-free phthalocyanine discotic liquid crystal. *Organic Electronics* **2006,** 7, (6), 495-499.
79. Iino, H.; Hanna, J.; Bushby, R. J.; Movaghar, B.; Whitaker, B. J.; Cook, M. J., Very high time-of-flight mobility in the columnar phases of a discotic liquid crystal. *Applied Physics Letters* **2005,** 87, (13), -.

80. Yuan, Y.; Gregg, B. A.; Lawrence, M. F., Time-of-flight study of electrical charge mobilities in liquid-crystalline zinc octakis(β-octoxyethyl) porphyrin films. *Journal of Materials Research* **2000,** 15, (11), 2494-2498.
81. Struijk, C. W.; Sieval, A. B.; Dakhorst, J. E. J.; van Dijk, M.; Kimkes, P.; Koehorst, R. B. M.; Donker, H.; Schaafsma, T. J.; Picken, S. J.; van de Craats, A. M.; Warman, J. M.; Zuilhof, H.; Sudhölter, E. J. R., Liquid Crystalline Perylene Diimides: Architecture and Charge Carrier Mobilities. *Journal of the American Chemical Society* **2000,** 122, (45), 11057-11066.
82. Hanna, J.; Funahashi, M., Fast Hole Transport in a New Calamitic Liquid Crystal of 2-(4′-Heptyloxyphenyl)-6-Dodecylthiobenzothiazole. *Physical Review Letters* **1997,** 78, (11), 2184-2187.
83. Funahashi, M.; Hanna, J., Fast ambipolar carrier transport in smectic phases of phenylnaphthalene liquid crystal. *Applied Physics Letters* **1997,** 71, (5), 602-604.
84. Funahashi, M.; Hanna, J., Anomalous high carrier mobility in smectic E phase of a 2-phenylnaphthalene derivative. *Applied Physics Letters* **1998,** 73, (25), 3733-3735.
85. Funahashi, M.; Hanna, J., High ambipolar carrier mobility in self-organizing terthiophene derivative. *Applied Physics Letters* **2000,** 76, (18), 2574-2576.
86. Iino, H.; Hanna, J., Availability of Liquid Crystallinity in Solution Processing for Polycrystalline Thin Films. *Advanced Materials* **2011,** 23, (15), 1748-1751.
87. Mery, S.; Haristoy, D.; Nicoud, J.; Guillon, D.; Diele, S.; Monobe, H.; Shimizu, Y., Bipolar carrier transport in a lamello-columnar mesophase of a sanidic liquid crystal. *Journal of Materials Chemistry* **2002,** 12, (1), 37-41.
88. Fleischmann, E.; Zentel, R., Liquid-Crystalline Ordering as a Concept in Materials Science: From Semiconductors to Stimuli-Responsive Devices. *Angewandte Chemie International Edition* **2013,** 52, (34), 8810-8827.
89. Sergeyev, S.; Pisula, W.; Geerts, Y. H., Discotic liquid crystals: a new generation of organic semiconductors. *Chemical Society Reviews* **2007,** 36, (12), 1902-1929.
90. Shimizu, Y.; Oikawa, K.; Nakayama, K.; Guillon, D., Mesophase semiconductors in field effect transistors. *Journal of Materials Chemistry* **2007,** 17, (40), 4223-4229.
91. Hanna, J.; Haarer, D.; Iino, H., Electronic and ionic carrier transport in discotic liquid crystalline photoconductor. *Physical Review B* **2005,** 72, (19), 193203.
92. Fujikake, H.; Murashige, T.; Sugibayashi, M.; Ohta, K., Time-of-flight analysis of charge mobility in a Cu-phthalocyanine-based discotic liquid crystal semiconductor. *Applied Physics Letters* **2004,** 85, (16), 3474-3476.
93. Craats, A. M. V. D.; Warman, J. M.; Fechtenkötter, A.; Brand, J. D.; Harbison, M. A.; Müllen, K., Record Charge Carrier Mobility in a Room-Temperature Discotic Liquid-Crystalline Derivative of Hexabenzocoronene. *Advanced Materials* **1999,** 11, (17), 1469-1472.
94. Shklyarevskiy, I. O.; Jonkheijm, P.; Stutzmann, N.; Wasserberg, D.; Wondergem, H. J.; Christianen, P. C. M.; Schenning, A. P. H. J.; de Leeuw, D. M.; Tomović, Ž.; Wu, J.; Müllen, K.; Maan, J. C., High Anisotropy of the Field-Effect Transistor Mobility in Magnetically Aligned Discotic Liquid-Crystalline Semiconductors. *Journal of the American Chemical Society* **2005,** 127, (46), 16233-16237.
95. Leroy, J.; Boucher, N.; Sergeyev, S.; Sferrazza, M.; Geerts, Y. H., Symmetrical and Nonsymmetrical Liquid Crystalline Oligothiophenes: Convenient Synthesis and Transition-Temperature Engineering. *European Journal of Organic Chemistry* **2007,** 2007, (8), 1256-1261.
96. van Breemen, A. J. J. M.; Herwig, P. T.; Chlon, C. H. T.; Sweelssen, J.; Schoo, H. F. M.; Setayesh, S.; Hardeman, W. M.; Martin, C. A.; de Leeuw, D. M.; Valeton, J. J. P.; Bastiaansen, C. W. M.; Broer, D. J.; Popa-Merticaru, A. R.; Meskers, S. C. J., Large Area Liquid Crystal Monodomain Field-Effect Transistors. *Journal of the American Chemical Society* **2006,** 128, (7), 2336-2345.
97. Lengyel, O.; Hardeman, W. M.; Wondergem, H. J.; de Leeuw, D. M.; van Breemen, A. J. J. M.; Resel, R., Solution-Processed Thin Films of Thiophene Mesogens with Single-Crystalline Alignment. *Advanced Materials* **2006,** 18, (7), 896-899.
98. Sonar, P.; Singh, S. P.; Sudhakar, S.; Dodabalapur, A.; Sellinger, A., High-Mobility Organic Thin Film Transistors Based on Benzothiadiazole-Sandwiched Dihexylquaterthiophenes. *Chemistry of Materials* **2008,** 20, (9), 3184-3190.
99. Meng, H.; Sun, F.; Goldfinger, M. B.; Jaycox, G. D.; Li, Z.; Marshall, W. J.; Blackman, G. S., High-Performance, Stable Organic Thin-Film Field-Effect Transistors Based on Bis-5'-alkylthiophen-2'-yl-2,6-anthracene Semiconductors. *Journal of the American Chemical Society* **2005,** 127, (8), 2406-2407.
100. Yasuda, T.; Fujita, K.; Tsutsui, T.; Geng, Y.; Culligan, S. W.; Chen, S. H., Carrier Transport Properties of Monodisperse Glassy-Nematic Oligofluorenes in Organic Field-Effect Transistors. *Chemistry of Materials* **2004,** 17, (2), 264-268.

101. Culligan, S. W.; Geng, Y.; Chen, S. H.; Klubek, K.; Vaeth, K. M.; Tang, C. W., Strongly Polarized and Efficient Blue Organic Light-Emitting Diodes Using Monodisperse Glassy Nematic Oligo(fluorene)s. *Advanced Materials* **2003,** 15, (14), 1176-1180.
102. Geng, Y.; Chen, A. C. A.; Ou, J. J.; Chen, S. H.; Klubek, K.; Vaeth, K. M.; Tang, C. W., Monodisperse Glassy-Nematic Conjugated Oligomers with Chemically Tunable Polarized Light Emission. *Chemistry of Materials* **2003,** 15, (23), 4352-4360.
103. Chen, A. C. A.; Culligan, S. W.; Geng, Y.; Chen, S. H.; Klubek, K. P.; Vaeth, K. M.; Tang, C. W., Organic Polarized Light-Emitting Diodes via Förster Energy Transfer Using Monodisperse Conjugated Oligomers. *Advanced Materials* **2004,** 16, (9-10), 783-788.
104. Zhan, X.; Facchetti, A.; Barlow, S.; Marks, T. J.; Ratner, M. A.; Wasielewski, M. R.; Marder, S. R., Rylene and Related Diimides for Organic Electronics. *Advanced Materials* **2011,** 23, (2), 268-284.
105. An, Z.; Yu, J.; Jones, S. C.; Barlow, S.; Yoo, S.; Domercq, B.; Prins, P.; Siebbeles, L. D. A.; Kippelen, B.; Marder, S. R., High Electron Mobility in Room-Temperature Discotic Liquid-Crystalline Perylene Diimides. *Advanced Materials* **2005,** 17, (21), 2580-2583.
106. An, Z.; Yu, J.; Domercq, B.; Jones, S. C.; Barlow, S.; Kippelen, B.; Marder, S. R., Room-temperature discotic liquid-crystalline coronene diimides exhibiting high charge-carrier mobility in air. *Journal of Materials Chemistry* **2009,** 19, (37), 6688-6698.
107. Oh, J. H.; Liu, S.; Bao, Z.; Schmidt, R.; Würthner, F., Air-stable n-channel organic thin-film transistors with high field-effect mobility based on N,N′-bis(heptafluorobutyl)-3,4:9,10-perylene diimide. *Applied Physics Letters* **2007,** 91, (21), 2212107.
108. Tsao, H. N.; Mullen, K., Improving polymer transistor performance via morphology control. *Chemical Society Reviews* **2010,** 39, (7), 2372-2386.
109. Akagi, K., Advances in liquid crystalline conjugated polymers. *Journal of Polymer Science Part A: Polymer Chemistry* **2009,** 47, (10), 2463-2485.
110. Akagi, K., Liquid Crystalline Conjugated Polymers – Synthesis and Properties. In Ramamoorthy, A., Ed Springer Netherlands: 2007; pp 249-275.
111. Whitehead, K. S.; Grell, M.; Bradley, D. D. C.; Inbasekaran, M.; Woo, E. P., Polarized emission from liquid crystal polymers. *Synthetic Metals* **2000,** 111–112, (0), 181-185.
112. Knaapila, M.; Stepanyan, R.; Lyons, B. P.; Torkkeli, M.; Monkman, A. P., Towards General Guidelines for Aligned, Nanoscale Assemblies of Hairy-Rod Polyfluorene. *Advanced Functional Materials* **2006,** 16, (5), 599-609.
113. Arias, A. C.; MacKenzie, J. D.; McCulloch, I.; Rivnay, J.; Salleo, A., Materials and Applications for Large Area Electronics: Solution-Based Approaches. *Chemical Reviews* **2010,** 110, (1), 3-24.
114. Redecker, M.; Bradley, D. D. C.; Inbasekaran, M.; Woo, E. P., Nondispersive hole transport in an electroluminescent polyfluorene. *Applied Physics Letters* **1998,** 73, (11), 1565-1567.
115. Sirringhaus, H.; Wilson, R. J.; Friend, R. H.; Inbasekaran, M.; Wu, W.; Woo, E. P.; Grell, M.; Bradley, D. D. C., Mobility enhancement in conjugated polymer field-effect transistors through chain alignment in a liquid-crystalline phase. *Applied Physics Letters* **2000,** 77, (3), 406-408.
116. Zhao, N.; Botton, G. A.; Zhu, S.; Duft, A.; Ong, B. S.; Wu, Y.; Liu, P., Microscopic Studies on Liquid Crystal Poly(3,3‘ ‘-dialkylquaterthiophene) Semiconductor. *Macromolecules* **2004,** 37, (22), 8307-8312.
117. McCulloch, I.; Heeney, M.; Bailey, C.; Genevicius, K.; MacDonald, I.; Shkunov, M.; Sparrowe, D.; Tierney, S.; Wagner, R.; Zhang, W.; Chabinyc, M. L.; Kline, R. J.; McGehee, M. D.; Toney, M. F., Liquid-crystalline semiconducting polymers with high charge-carrier mobility. *Nature Materials* **2006,**, (5), 328-333.
118. Baklar, M.; Barard, S.; Sparrowe, D.; Wilson, R. M.; McCulloch, I.; Heeney, M.; Kreouzis, T.; Stingelin, N., Bulk charge transport in liquid-crystalline polymer semiconductors based on poly(2,5-bis(3-alkylthiophen-2-yl)thieno[3,2-b]thiophene). *Polymer Chemistry* **2010,** 1, (9), 1448-1452.
119. Kim, D. H.; Lee, B.; Moon, H.; Kang, H. M.; Jeong, E. J.; Park, J.; Han, K.; Lee, S.; Yoo, B. W.; Koo, B. W.; Kim, J. Y.; Lee, W. H.; Cho, K.; Becerril, H. A.; Bao, Z., Liquid-Crystalline Semiconducting Copolymers with Intramolecular Donor−Acceptor Building Blocks for High-Stability Polymer Transistors. *Journal of the American Chemical Society* **2009,** 131, (17), 6124-6132.
120. Abe, S.; Kijima, M.; Shirakawa, H., Friction-induced uniaxial orientation of a liquid crystalline N-substituted polypyrrole. *Journal of Materials Chemistry* **2000,** 10, (7), 1509-1510.
121. Bao, Z.; Chen, Y.; Cai, R.; Yu, L., Conjugated liquid-crystalline polymers - soluble and fusible poly(phenylenevinylene) by the Heck coupling reaction. *Macromolecules* **1993,** 26, (20), 5281-5286.
122. Watanabe, M.; Tsuchiya, K.; Shinnai, T.; Kijima, M., Liquid Crystalline Polythiophene Bearing Phenylnaphthalene Side-Chain. *Macromolecules* **2012,** 45, (4), 1825-1832.
123. Tahar-Djebbar, I.; Nekelson, F.; Heinrich, B.; Donnio, B.; Guillon, D.; Kreher, D.; Mathevet, F.; Attias, A., Lamello-Columnar Mesophase Formation in a Side-Chain Liquid Crystal π-Conjugated Polymer Architecture. *Chemistry of Materials* **2011,** 23, (21), 4653-4656.

124. Zeng, D.; Tahar-Djebbar, I.; Xiao, Y.; Kameche, F.; Kayunkid, N.; Brinkmann, M.; Guillon, D.; Heinrich, B.; Donnio, B.; Ivanov, D. A.; Lacaze, E.; Kreher, D.; Mathevet, F.; Attias, A., Intertwined Lamello-Columnar Coassemblies in Liquid-Crystalline Side-Chain Π-Conjugated Polymers: Toward a New Class of Nanostructured Supramolecular Organic Semiconductors. *Macromolecules* **2014,** 47, (5), 1715-1731.
125. Cornil, J.; Brédas, J. L.; Zaumseil, J.; Sirringhaus, H., Ambipolar Transport in Organic Conjugated Materials. *Advanced Materials* **2007,** 19, (14), 1791-1799.
126. Schwartz, P.; Biniek, L.; Zaborova, E.; Heinrich, B.; Brinkmann, M.; Leclerc, N.; Méry, S., Perylenediimide-Based Donor–Acceptor Dyads and Triads: Impact of Molecular Architecture on Self-Assembling Properties. *Journal of the American Chemical Society* **2014,** 136, (16), 5981-5992.
127. Hayashi, H.; Nihashi, W.; Umeyama, T.; Matano, Y.; Seki, S.; Shimizu, Y.; Imahori, H., Segregated Donor–Acceptor Columns in Liquid Crystals That Exhibit Highly Efficient Ambipolar Charge Transport. *Journal of the American Chemical Society* **2011,** 133, (28), 10736-10739.
128. Guo, J.; Liang, Y.; Xiao, S.; Szarko, J. M.; Sprung, M.; Mukhopadhyay, M. K.; Wang, J.; Yu, L.; Chen, L. X., Structure and dynamics correlations of photoinduced charge separation in rigid conjugated linear donor-acceptor dyads towards photovoltaic applications. *New Journal of Chemistry* **2009,** 33, (7), 1497-1507.
129. Li, W.; Yamamoto, Y.; Fukushima, T.; Saeki, A.; Seki, S.; Tagawa, S.; Masunaga, H.; Sasaki, S.; Takata, M.; Aida, T., Amphiphilic Molecular Design as a Rational Strategy for Tailoring Bicontinuous Electron Donor and Acceptor Arrays: Photoconductive Liquid Crystalline Oligothiophene−C60 Dyads. *Journal of the American Chemical Society* **2008,** 130, (28), 8886-8887.
130. Kong, X.; He, Z.; Zhang, Y.; Mu, L.; Liang, C.; Chen, B.; Jing, X.; Cammidge, A. N., A Mesogenic Triphenylene−Perylene−Triphenylene Triad. *Organic Letters* **2011,** 13, (4), 764-767.
131. Sartin, M. M.; Huang, C.; Marshall, A. S.; Makarov, N.; Barlow, S.; Marder, S. R.; Perry, J. W., Nonlinear Optical Pulse Suppression via Ultrafast Photoinduced Electron Transfer in an Aggregated Perylene Diimide/Oligothiophene Molecular Triad. *The Journal of Physical Chemistry A* **2013,** 118, (1), 110-121.
132. Sommer, M.; Lang, A. S.; Thelakkat, M., Crystalline–Crystalline Donor–Acceptor Block Copolymers. *Angewandte Chemie International Edition* **2008,** 47, (41), 7901-7904.
133. Huettner, S.; Sommer, M.; Hodgkiss, J.; Kohn, P.; Thurn-Albrecht, T.; Friend, R. H.; Steiner, U.; Thelakkat, M., Tunable Charge Transport Using Supramolecular Self-Assembly of Nanostructured Crystalline Block Copolymers. *ACS Nano* **2011,** 5, (5), 3506-3515.
134. Miyanishi, S.; Zhang, Y.; Tajima, K.; Hashimoto, K., Fullerene attached all-semiconducting diblock copolymers for stable single-component polymer solar cells. *Chemical Communications* **2010,** 46, (36), 6723-6725.
135. Beaujuge, P. M.; Fréchet, J. M. J., Molecular Design and Ordering Effects in π-Functional Materials for Transistor and Solar Cell Applications. *Journal of the American Chemical Society* **2011,** 133, (50), 20009-20029.
136. Melucci, M.; Zambianchi, M.; Favaretto, L.; Gazzano, M.; Zanelli, A.; Monari, M.; Capelli, R.; Troisi, S.; Toffanin, S.; Muccini, M., Thienopyrrolyl dione end-capped oligothiophene ambipolar semiconductors for thin film- and light emitting transistors. *Chemical Communications* **2011,** 47, (43), 11840-11842.
137. Yassin, A.; Savitha, G.; Leriche, P.; Frere, P.; Roncali, J., A donor-acceptor-donor (D-A-D) molecule based on 3-alkoxy-4-cyanothiophene and dithienopyrrole units as active material for organic solar cells. *New Journal of Chemistry* **2012,** 36, (11), 2412-2416.
138. Facchetti, A., π-Conjugated Polymers for Organic Electronics and Photovoltaic Cell Applications†. *Chemistry of Materials* **2010,** 23, (3), 733-758.
139. Boden, N.; Borner, R. C.; Bushby, R. J.; Cammidge, A. N.; Jesudason, M. V., The synthesis of triphenylene-based discotic mesogens New and improved routes. *Liquid Crystals* **1993,** 15, (6), 851-858.
140. Kumar, S.; Manickam, M., Oxidative trimerization of o-dialkoxybenzenes to hexaalkoxytriphenylenes: molybdenum(v) chloride as a novel reagent. *Chemical Communications* **1997,**, (17), 1615-1666.
141. McKenna, M. D.; Barberá, J.; Marcos, M.; Serrano, J. L., Discotic Liquid Crystalline Poly(propylene imine) Dendrimers Based on Triphenylene. *Journal of the American Chemical Society* **2004,** 127, (2), 619-625.
142. Kumar, S.; Manickam, M., Synthesis of Functionalized Triphenylenes by Selective Ether Cleavage with B-Bromocatecholborane. *Synthesis* **1998,** 1119-1122, (8).
143. Pal, S. K.; Bisoyi, H. K.; Kumar, S., Synthesis of monohydroxy-functionalized triphenylene discotics: green chemistry approach. *Tetrahedron* **2007,** 63, (29), 6874-6878.
144. Kong, X.; He, Z.; Gopee, H.; Jing, X.; Cammidge, A. N., Improved synthesis of monohydroxytriphenylenes (MHTs)—important precursors to discotic liquid crystal families. *Tetrahedron Letters* **2011,** 52, (1), 77-79.
145. Liu, Z.; Zhang, G.; Cai, Z.; Chen, X.; Luo, H.; Li, Y.; Wang, J.; Zhang, D., New Organic Semiconductors with Imide/Amide-Containing Molecular Systems. *Advanced Materials* **2014,**, n/a-n/a.
146. Li, C.; Wonneberger, H., Perylene Imides for Organic Photovoltaics: Yesterday, Today, and Tomorrow. *Advanced Materials* **2012,** 24, (5), 613-636.

147. Jones, B. A.; Facchetti, A.; Wasielewski, M. R.; Marks, T. J., Tuning Orbital Energetics in Arylene Diimide Semiconductors. Materials Design for Ambient Stability of n-Type Charge Transport. *Journal of the American Chemical Society* **2007,** 129, (49), 15259-15278.
148. Wicklein, A.; Lang, A.; Muth, M.; Thelakkat, M., Swallow-Tail Substituted Liquid Crystalline Perylene Bisimides: Synthesis and Thermotropic Properties. *Journal of the American Chemical Society* **2009,** 131, (40), 14442-14453.
149. Kossmehl, G.; Engelmann, G., Application of Electrically Conductive Polythiophenes. In Wiley-VCH Verlag GmbH: 1998; pp 491-524.
150. Granström, M.; Harrison, M. G.; Friend, R. H., Electro-optical Polythiophene Devices. In Wiley-VCH Verlag GmbH: 1998; pp 405-458.
151. Katz, H. E.; Dodabalapur, A.; Bao, Z., Oligo- and Polythiophene Field Effect Transistors. In Wiley-VCH Verlag GmbH: 1998; pp 459-489.
152. Fichou, D.; Ziegler, C., Structure and Properties of Oligothiophenes in the Solid State: Single Crystals and Thin Films. In Wiley-VCH Verlag GmbH: 1998; pp 183-282.
153. Groenendaal, L.; Jonas, F.; Freitag, D.; Pielartzik, H.; Reynolds, J. R., Poly(3,4-ethylenedioxythiophene) and Its Derivatives: Past, Present, and Future. *Advanced Materials* **2000,** 12, (7), 481-494.
154. Groenendaal, L.; Zotti, G.; Aubert, P. H.; Waybright, S. M.; Reynolds, J. R., Electrochemistry of Poly(3,4-alkylenedioxythiophene) Derivatives. *Advanced Materials* **2003,** 15, (11), 855-879.
155. Kirchmeyer, S.; Reuter, K., Scientific importance, properties and growing applications of poly(3,4-ethylenedioxythiophene). *Journal of Materials Chemistry* **2005,** 15, (21), 2077-2088.
156. Chen, T. A.; Rieke, R. D., The first regioregular head-to-tail poly(3-hexylthiophene-2,5-diyl) and a regiorandom isopolymer: nickel versus palladium catalysis of 2(5)-bromo-5(2)-(bromozincio)-3-hexylthiophene polymerization. *Journal of the American Chemical Society* **1992,** 114, (25), 10087-10088.
157. Chen, T. A.; O'Brien, R. A.; Rieke, R. D., Use of highly reactive zinc leads to a new, facile synthesis for polyarylenes. *Macromolecules* **1993,** 26, (13), 3462-3463.
158. McCullough, R. D.; Lowe, R. D.; Jayaraman, M.; Anderson, D. L., Design, synthesis, and control of conducting polymer architectures: structurally homogeneous poly(3-alkylthiophenes). *The Journal of Organic Chemistry* **1993,** 58, (4), 904-912.
159. Horowitz, G.; Fichou, D.; Peng, X.; Xu, Z.; Garnier, F., A field-effect transistor based on conjugated alpha-sexithienyl. *Solid State Communications* **1989,** 72, (4), 381-384.
160. Garnier, F.; Horowitz, G.; Peng, X.; Fichou, D., An all-organic "soft" thin film transistor with very high carrier mobility. *Advanced Materials* **1990,** 2, (12), 592-594.
161. Geiger, F.; Stoldt, M.; Schweizer, H.; Bäuerle, P.; Umbach, E., Electroluminescence from oligothiophene-based light-emitting devices. *Advanced Materials* **1993,** 5, (12), 922-925.
162. Noma, N.; Tsuzuki, T.; Shirota, Y., αThiophene octamer as a new class of photo-active material for photoelectrical conversion. *Advanced Materials* **1995,** 7, (7), 647-648.
163. Ewbank, P. C.; Stefan, M. C.; Sauvé, G.; McCullough, R. D., Synthesis, Characterization and Properties of Regioregular Polythiophene-Based Materials. In *Handbook of Thiophene-Based Materials: Applic ations in Organic Electronics and Photonics*, John Wiley & Sons, Ltd: 2009; pp 157-217.
164. McCullough, R. D., The Chemistry of Conducting Polythiophenes: from Synthesis to Self-Assembly to Intelligent Materials. In Wiley-VCH Verlag GmbH: 1998; pp 1-44.
165. Jen, K.; Miller, G. G.; Elsenbaumer, R. L., Highly conducting, soluble, and environmentally-stable poly(3-alkylthiophenes). *Journal of the Chemical Society, Chemical Communications* **1986,**, (17), 1346-1347.
166. R. Sugimoto, S. T. H. B., Preparation of soluble polythiophene derivatives utilizing transition metal halides as catalysts and their property. *Chemistry Express* **1986,**, (11), 635-638.
167. H. Sirringhaus, P. J. B. R.; Spiering, R. A. J. J., Two-dimensional charge transport in self-organized, high-mobility conjugated polymers. *Nature* **1999,**, (401), 685-688.
168. Österbacka, R.; An, C. P.; Jiang, X. M.; Vardeny, Z. V., Two-Dimensional Electronic Excitations in Self-Assembled Conjugated Polymer Nanocrystals. *Science* **2000,** 287, (5454), 839 -842.
169. Naber, R. C. G.; Mulder, M.; de Boer, B.; Blom, P. W. M.; de Leeuw, D. M., High charge density and mobility in poly(3-hexylthiophene) using a polarizable gate dielectric. *Organic Electronics* **2006,** 7, (3), 132-136.
170. Choulis, S. A.; Kim, Y.; Nelson, J.; Bradley, D. D. C.; Giles, M.; Shkunov, M.; McCulloch, I., High ambipolar and balanced carrier mobility in regioregular poly(3-hexylthiophene). *Applied Physics Letters* **2004,** 85, (17), 3890-3892.
171. Thomas, D. S.; Köhler, A.; Wilson, J. S.; Kim, J.; Ramsdale, C. M.; Sirringhaus, H.; Friend, R. H.; Brown, P. J., Effect of interchain interactions on the absorption and emission of poly(3-hexylthiophene). *Physical Review B* **2003,** 67, (6), 064203.
172. Chen, T.; Wu, X.; Rieke, R. D., Regiocontrolled Synthesis of Poly(3-alkylthiophenes) Mediated by Rieke Zinc: Their Characterization and Solid-State Properties. *Journal of the American Chemical Society* **1995,** 117, (1), 233-244.

173. Iraqi, A.; W. Barker, G., Synthesis and characterisation of telechelic regioregular head-to-tail poly(3-alkylthiophenes). *Journal of Materials Chemistry* **1998,** 8, (1), 25-29.
174. McCullough, R. D.; Ewbank, P. C.; Loewe, R. S., Self-Assembly and Disassembly of Regioregular, Water Soluble Polythiophenes: Chemoselective Ionchromatic Sensing in Water. *Journal of the American Chemical Society* **1997,** 119, (3), 633-634.
175. Guillerez, S.; Bidan, G., New convenient synthesis of highly regioregular poly(3-octylthiophene) based on the Suzuki coupling reaction. *Synthetic Metals* **1998,** 93, (2), 123-126.
176. Liversedge, I. A.; Higgins, S. J.; Giles, M.; Heeney, M.; McCulloch, I., Suzuki route to regioregular polyalkylthiophenes using Ir-catalysed borylation to make the monomer, and Pd complexes of bulky phosphanes as coupling catalysts for polymerisation. *Tetrahedron Letters* **2006,** 47, (29), 5143-5146.
177. Zhai, L.; Pilston, R. L.; Zaiger, K. L.; Stokes, K. K.; McCullough, R. D., A Simple Method to Generate Side-Chain Derivatives of Regioregular Polythiophene via the GRIM Metathesis and Post-polymerization Functionalization. *Macromolecules* **2002,** 36, (1), 61-64.
178. Iraqi, A.; A. Crayston, J.; C. Walton, J., Covalent binding of redox active centres to preformed regioregular polythiophenes. *Journal of Materials Chemistry* **1998,** 8, (1), 31-36.
179. Liu, J.; Sheina, E.; Kowalewski, T.; McCullough, R. D., Tuning the Electrical Conductivity and Self-Assembly of Regioregular Polythiophene by Block Copolymerization: Nanowire Morphologies in New Di- and Triblock Copolymers. *Angewandte Chemie International Edition* **2002,** 41, (2), 329-332.
180. Loewe, R. S.; Khersonsky, S. M.; McCullough, R. D., A Simple Method to Prepare Head-to-Tail Coupled, Regioregular Poly(3-alkylthiophenes) Using Grignard Metathesis. *Advanced Materials* **1999,** 11, (3), 250-253.
181. Loewe, R. S.; Ewbank, P. C.; Liu, J.; Zhai, L.; McCullough, R. D., Regioregular, Head-to-Tail Coupled Poly(3-alkylthiophenes) Made Easy by the GRIM Method: Investigation of the Reaction and the Origin of Regioselectivity. *Macromolecules* **2001,** 34, (13), 4324-4333.
182. Andersson, M. R.; Mammo, W.; Olinga, T.; Svensson, M.; Theander, M.; Inganäs, O., Synthesis of regioregular phenyl substituted polythiophenes with FeCl3. *Synthetic Metals* **1999,** 101, (1–3), 11-12.
183. Yamamoto, T.; Honda, Y.; Sata, T.; Kokubo, H., Electrochemical behavior of poly(3-hexylthiophene). Controlling factors of electric current in electrochemical oxidation of poly(3-hexylthiophene)s in a solution. *Polymer* **2004,** 45, (6), 1735-1738.
184. Tamao, K.; Kodama, S.; Nakajima, I.; Kumada, M.; Minato, A.; Suzuki, K., Nickel-phosphine complex-catalyzed Grignard coupling—II : Grignard coupling of heterocyclic compounds. *Tetrahedron* **1982,** 38, (22), 3347-3354.
185. McCullough, R. D., The Chemistry of Conducting Polythiophenes. *Advanced Materials* **1998,** 10, (2), 93-116.
186. Yokoyama, A.; Miyakoshi, R.; Yokozawa, T., Chain-Growth Polymerization for Poly(3-hexylthiophene) with a Defined Molecular Weight and a Low Polydispersity. *Macromolecules* **2004,** 37, (4), 1169-1171.
187. Sheina, E. E.; Liu, J.; Iovu, M. C.; Laird, D. W.; McCullough, R. D., Chain Growth Mechanism for Regioregular Nickel-Initiated Cross-Coupling Polymerizations. *Macromolecules* **2004,** 37, (10), 3526-3528.
188. Iovu, M. C.; Sheina, E. E.; Gil, R. R.; McCullough, R. D., Experimental Evidence for the Quasi-"Living" Nature of the Grignard Metathesis Method for the Synthesis of Regioregular Poly(3-alkylthiophenes). *Macromolecules* **2005,** 38, (21), 8649-8656.
189. Iovu, M. C.; Jeffries-EL, M.; Sheina, E. E.; Cooper, J. R.; McCullough, R. D., Regioregular poly(3-alkylthiophene) conducting block copolymers. *Polymer* **2005,** 46, (19), 8582-8586.
190. Liu, J.; McCullough, R. D., End Group Modification of Regioregular Polythiophene through Postpolymerization Functionalization. *Macromolecules* **2002,** 35, (27), 9882-9889.
191. Li, Y.; Vamvounis, G.; Yu, J.; Holdcroft, S., A Novel and Versatile Methodology for Functionalization of Conjugated Polymers. Transformation of Poly(3-bromo-4-hexylthiophene) via Palladium-Catalyzed Coupling Chemistry. *Macromolecules* **2001,** 34, (10), 3130-3132.
192. Li, Y.; Vamvounis, G.; Holdcroft, S., Facile Functionalization of Poly(3-alkylthiophene)s via Electrophilic Substitution. *Macromolecules* **2000,** 34, (2), 141-143.
193. Jeffries-EL, M.; Sauvé, G.; McCullough, R. D., In-Situ End-Group Functionalization of Regioregular Poly(3-alkylthiophene) Using the Grignard Metathesis Polymerization Method. *Advanced Materials* **2004,** 16, (12), 1017-1019.
194. Jeffries-El, M.; Sauvé, G.; McCullough, R. D., Facile Synthesis of End-Functionalized Regioregular Poly(3-alkylthiophene)s via Modified Grignard Metathesis Reaction. *Macromolecules* **2005,** 38, (25), 10346-10352.
195. Miyanishi, S.; Zhang, Y.; Tajima, K.; Hashimoto, K., Fullerene attached all-semiconducting diblock copolymers for stable single-component polymer solar cells. *Chemical Communications* **2010,** 46, (36), 6723-6725.

196. Ewbank, P. C.; Loewe, R. S.; Zhai, L.; Reddinger, J.; Sauvé, G.; McCullough, R. D., Regioregular poly(thiophene-3-alkanoic acid)s: water soluble conducting polymers suitable for chromatic chemosensing in solution and solid state. *Tetrahedron* **2004,** 60, (49), 11269-11275.
197. McCullough, R. D.; Ewbank, P. C., Self-assembly and chemical response of conducting polymer superstructures. *Synthetic Metals* **1997,** 84, (1–3), 311-312.
198. Vallat, P.; Lamps, J. P.; Schosseler, F.; Rawiso, M.; Catala, J. M., Quasi-Controlled Polymerization through a Nickel Catalyst Process of a Functionalized Thiophene Monomer: Kinetic Studies and Application to the Synthesis of Regioregular Poly(thiophene-3-acetic acid). *Macromolecules* **2007,** 40, (7), 2600-2602.
199. Wang, Y.; Mills, A. A.; Euler, W. B.; Lucht, B. L., Effect of residual monomer on the spectroscopic properties of polythiophenes. *Chemical Communications* **2006,**, (20), 2121-2122.
200. Erwin, M. M.; McBride, J.; Kadavanich, A. V.; Rosenthal, S. J., Effects of impurities on the optical properties of poly-3-hexylthiophene thin films. *Thin Solid Films* **2002,** 409, (2), 198-205.
201. Hisashi, K. A. T. Y., Purification of Head-to-Tail-Type Regioregular Poly(3-hexylthiophene), HT-P3HexTh, and Investigation of the Effects of Polymer Purity on the Performance of Organic Field-Effect Transistors. *Japanese Journal of Applied Physics* **2003,** 42, (10R), 6627.
202. Yamamoto, T.; Komarudin, D.; Arai, M.; Lee, B.; Suganuma, H.; Asakawa, N.; Inoue, Y.; Kubota, K.; Sasaki, S.; Fukuda, T.; Matsuda, H., Extensive Studies on π-Stacking of Poly(3-alkylthiophene-2,5-diyl)s and Poly(4-alkylthiazole-2,5-diyl)s by Optical Spectroscopy, NMR Analysis, Light Scattering Analysis, and X-ray Crystallography. *Journal of the American Chemical Society* **1998,** 120, (9), 2047-2058.
203. Yamamoto, T.; Honda, Y.; Sata, T.; Kokubo, H., Electrochemical behavior of poly(3-hexylthiophene). Controlling factors of electric current in electrochemical oxidation of poly(3-hexylthiophene)s in a solution. *Polymer* **2004,** 45, (6), 1735-1738.
204. Wu, S.; Bu, L.; Huang, L.; Yu, X.; Han, Y.; Geng, Y.; Wang, F., Synthesis and characterization of phenylene-thiophene all-conjugated diblock copolymers. *Polymer* **2009,** 50, (26), 6245-6251.
205. Ohshita, J.; Hamamoto, D.; Kimura, K.; Kunai, A., Anodic polymerization of dithienosilole and electroluminescent properties of the resulting polymer. *Journal of Organometallic Chemistry* **2005,** 690, (12), 3027-3032.
206. Makoto, K. A. Y. I., Branched polythiophene as a new amorphous semiconducting polymer for an organic field-effect transistor. *Semiconductor Science and Technology* **2011,** 26, (3), 034004.
207. Leclerc, M.; Diaz, F. M.; Wegner, G., Structural analysis of poly(3-alkylthiophene)s. *Die Makromolekulare Chemie* **1989,** 190, (12), 3105-3116.
208. Patil, A. O.; Heeger, A. J.; Wudl, F., Optical properties of conducting polymers. *Chemical Reviews* **1988,** 88, (1), 183-200.
209. Liu, J.; Loewe, R. S.; McCullough, R. D., Employing MALDI-MS on Poly(alkylthiophenes): Analysis of Molecular Weights, Molecular Weight Distributions, End-Group Structures, and End-Group Modifications. *Macromolecules* **1999,** 32, (18), 5777-5785.
210. Holdcroft, S., Determination of molecular weights and Mark–Houwink constants for soluble electronically conducting polymers. *Journal of Polymer Science Part B: Polymer Physics* **1991,** 29, (13), 1585-1588.
211. Winokur, M. J.; Chunwachirasiri, W., Nanoscale structure–property relationships in conjugated polymers: Implications for present and future device applications. *Journal of Polymer Science Part B: Polymer Physics* **2003,** 41, (21), 2630-2648.
212. Aasmundtveit, K. E.; Samuelsen, E. J.; Inganäs, O.; Pettersson, L. A. A.; Johansson, T.; Ferrer, S., Structural aspects of electrochemical doping and dedoping of poly(3,4-ethylenedioxythiophene). *Synthetic Metals* **2000,** 113, (1–2), 93-97.
213. Heffner, G. W.; Pearson, D. S., Molecular characterization of poly(3-hexylthiophene). *Macromolecules* **1991,** 24, (23), 6295-6299.
214. Prosa, T. J.; Winokur, M. J.; Moulton, J.; Smith, P.; Heeger, A. J., X-ray structural studies of poly(3-alkylthiophenes): an example of an inverse comb. *Macromolecules* **1992,** 25, (17), 4364-4372.
215. Tashiro, K.; Kobayashi, M.; Kawai, T.; Yoshino, K., Crystal structural change in poly(3-alkyl thiophene)s induced by iodine doping as studied by an organized combination of X-ray diffraction, infrared/Raman spectroscopy and computer simulation techniques. *Polymer* **1997,** 38, (12), 2867-2879.
216. Prosa, T. J.; Winokur, M. J.; McCullough, R. D., Evidence of a Novel Side Chain Structure in Regioregular Poly(3-alkylthiophenes). *Macromolecules* **1996,** 29, (10), 3654-3656.
217. Takashima, W.; Pandey, S. S.; Endo, T.; Rikukawa, M.; Tanigaki, N.; Yoshida, Y.; Yase, K.; Kaneto, K., Photocarrier transports related to the morphology of regioregular poly(3-hexylthiophene) films. *Thin Solid Films* **2001,** 393, (1–2), 334-342.
218. Kim, D. H.; Park, Y. D.; Jang, Y.; Kim, S.; Cho, K., Solvent Vapor-Induced Nanowire Formation in Poly(3-hexylthiophene) Thin Films. *Macromolecular Rapid Communications* **2005,** 26, (10), 834-839.

219. Kim, D. H.; Han, J. T.; Park, Y. D.; Jang, Y.; Cho, J. H.; Hwang, M.; Cho, K., Single-Crystal Polythiophene Microwires Grown by Self-Assembly. *Advanced Materials* **2006,** 18, (6), 719-723.
220. Brinkmann, M.; Wittmann, J. C., Orientation of Regioregular Poly(3-hexylthiophene) by Directional Solidification: A Simple Method to Reveal the Semicrystalline Structure of a Conjugated Polymer. *Advanced Materials* **2006,** 18, (7), 860-863.
221. Bolognesi, A.; Porzio, W.; Provasoli, A.; Botta, C.; Comotti, A.; Sozzani, P.; Simonutti, R., Structural and Thermal Behavior of Poly (3-octylthiophene): a DSC, 13C MAS NMR, XRD, Photoluminescence, and Raman Scattering Study. *Macromolecular Chemistry and Physics* **2001,** 202, (12), 2586-2591.
222. Bolognesi, A.; Porzio, W.; Zhuo, G.; Ezquerra, T., The thermal behaviour of poly(3-octylthienylene) synthesized by an Ni-based catalyst: DSC, optical microscopy and XRD analyses. *European Polymer Journal* **1996,** 32, (9), 1097-1103.
223. Meille, S. V.; Romita, V.; Caronna, T.; Lovinger, A. J.; Catellani, M.; Belobrzeckaja, L., Influence of Molecular Weight and Regioregularity on the Polymorphic Behavior of Poly(3-decylthiophenes). *Macromolecules* **1997,** 30, (25), 7898-7905.
224. Samuelsen, E. J.; Mårdalen, J.; Konestabo, O. R.; Hanfland, M.; Lorenzen, M., Poly(octyl-thiophene) polymorphs under high pressure: Synchrotron X-Rays studies and the relation with spectral behaviour. *Synthetic Metals* **1999,** 101, (1–3), 98-99.
225. Pal, S.; Roy, S.; Nandi, A. K., Temperature Variation of DC Conductivity of Poly(3-alkyl Thiophenes) and Their Cocrystals. *The Journal of Physical Chemistry B* **2005,** 109, (39), 18332-18341.
226. Causin, V.; Marega, C.; Marigo, A.; Valentini, L.; Kenny, J. M., Crystallization and Melting Behavior of Poly(3-butylthiophene), Poly(3-octylthiophene), and Poly(3-dodecylthiophene). *Macromolecules* **2004,** 38, (2), 409-415.
227. Wang, Y.; Archambault, N.; Marold, A.; Weng, L.; Lucht, B. L.; Euler, W. B., Observation of Two-Step Thermochromism in Poly(3-docosylthiophene): DSC and Reflection Spectroscopy. *Macromolecules* **2004,** 37, (14), 5415-5422.
228. Inoue, Y.; Yamamoto, T.; Asakawa, N.; Yazawa, K., Twist glass transition in regioregulated poly(3-alkylthiophene). *Physical Review B* **2006,** 74, (9), 094204.
229. Cornil, J.; Dos Santos, D. A.; Crispin, X.; Silbey, R.; Brédas, J. L., Influence of Interchain Interactions on the Absorption and Luminescence of Conjugated Oligomers and Polymers: A Quantum-Chemical Characterization. *Journal of the American Chemical Society* **1998,** 120, (6), 1289-1299.
230. Cornil, J.; Beljonne, D.; Calbert, J. P.; Brédas, J. L., Interchain Interactions in Organic π-Conjugated Materials: Impact on Electronic Structure, Optical Response, and Charge Transport. *Advanced Materials* **2001,** 13, (14), 1053-1067.
231. Mena-Osteritz, E., Superstructures of Self-Organizing Thiophenes. *Advanced Materials* **2002,** 14, (8), 609-616.
232. Kiriy, N.; Kiriy, A.; Bocharova, V.; Stamm, M.; Richter, S.; Plötner, M.; Fischer, W.; Krebs, F. C.; Senkovska, I.; Adler, H., Conformation, Molecular Packing, and Field Effect Mobility of Regioregular β,β'-Dihexylsexithiophene. *Chemistry of Materials* **2004,** 16, (23), 4757-4764.
233. Katz, H. E.; Bao, Z., The Physical Chemistry of Organic Field-Effect Transistors. *The Journal of Physical Chemistry B* **1999,** 104, (4), 671-678.
234. Bao, Z.; Lovinger, A. J.; Cherniavskaya, O., Material issues for construction of organic and polymeric driving circuits for display and electronic applications. *Macromolecular Symposia* **2000,** 154, (1), 199-208.
235. Bao, Z.; Dodabalapur, A.; Lovinger, A. J., Soluble and processable regioregular poly(3-hexylthiophene) for thin film field-effect transistor applications with high mobility. *Applied Physics Letters* **1996,** 69, (26), 4108-4110.
236. Kobashi, M.; Takeuchi, H., Inhomogeneity of Spin-Coated and Cast Non-Regioregular Poly(3-hexylthiophene) Films. Structures and Electrical and Photophysical Properties. *Macromolecules* **1998,** 31, (21), 7273-7278.
237. Assadi, A.; Svensson, C.; Willander, M.; Inganäs, O., Field-effect mobility of poly(3-hexylthiophene). *Applied Physics Letters* **1988,** 53, (3), 195-197.
238. Paloheimo, J.; Stubb, H.; Yli-Lahti, P.; Kuivalainen, P., Field-effect conduction in polyalkylthiophenes. *Synthetic Metals* **1991,** 41, (1–2), 563-566.
239. Zhang, R.; Li, B.; Iovu, M. C.; Jeffries-EL, M.; Sauvé, G.; Cooper, J.; Jia, S.; Tristram-Nagle, S.; Smilgies, D. M.; Lambeth, D. N.; McCullough, R. D.; Kowalewski, T., Nanostructure Dependence of Field-Effect Mobility in Regioregular Poly(3-hexylthiophene) Thin Film Field Effect Transistors. *Journal of the American Chemical Society* **2006,** 128, (11), 3480-3481.
240. Locklin, J.; Roberts, M. E.; Mannsfeld, S. C. B.; Bao, Z., Optimizing the Thin Film Morphology of Organic Field-Effect Transistors: The Influence of Molecular Structure and Vacuum Deposition Parameters on Device Performance. *Journal of Macromolecular Science, Part C* **2006,** 46, (1), 79-101.

241. Kim, D. H.; Park, Y. D.; Jang, Y.; Yang, H.; Kim, Y. H.; Han, J. I.; Moon, D. G.; Park, S.; Chang, T.; Chang, C.; Joo, M.; Ryu, C. Y.; Cho, K., Enhancement of Field-Effect Mobility Due to Surface-Mediated Molecular Ordering in Regioregular Polythiophene Thin Film Transistors. *Advanced Functional Materials* **2005,** 15, (1), 77-82.
242. Clark, J.; Zhao, N.; Sirringhaus, H.; Breiby, D. W.; Andreasen, J. W.; Nielsen, M. M.; Giles, M.; Heeney, M.; McCulloch, I.; Chang, J., Molecular-weight dependence of interchain polaron delocalization and exciton bandwidth in high-mobility conjugated polymers. *Physical Review B* **2006,** 74, (11), 115318.
243. Cottaar, J.; Tanase, C.; Coehoorn, R.; Bobbert, P. A.; Blom, P. W. M.; de Leeuw, D. M.; Michels, M. A. J.; Pasveer, W. F., Unified Description of Charge-Carrier Mobilities in Disordered Semiconducting Polymers. *Physical Review Letters* **2005,** 94, (20), 206601.
244. Heeger, A. J., Semiconducting and Metallic Polymers: The Fourth Generation of Polymeric Materials†. *The Journal of Physical Chemistry B* **2001,** 105, (36), 8475-8491.
245. Wang, G. M.; Moses, D.; Heeger, A. J.; Dhoot, A. S., Voltage-Induced Metal-Insulator Transition in Polythiophene Field-Effect Transistors. *Physical Review Letters* **2006,** 96, (24), 246403.
246. Park, Y. D.; Kim, D. H.; Jang, Y.; Cho, J. H.; Hwang, M.; Lee, H. S.; Lim, J. A.; Cho, K., Effect of side chain length on molecular ordering and field-effect mobility in poly(3-alkylthiophene) transistors. *Organic Electronics* **2006,** 7, (6), 514-520.
247. Babel, A.; Jenekhe, S. A., Alkyl chain length dependence of the field-effect carrier mobility in regioregular poly(3-alkylthiophene)s. *Synthetic Metals* **2005,** 148, (2), 169-173.
248. Hoshino, S.; Yoshida, M.; Uemura, S.; Kodzasa, T.; Takada, N.; Kamata, T.; Yase, K., Influence of moisture on device characteristics of polythiophene-based field-effect transistors. *Journal of Applied Physics* **2004,** 95, (9), 5088-5093.
249. Hamadani, B. H.; Natelson, D., Gated nonlinear transport in organic polymer field effect transistors. *Journal of Applied Physics* **2004,** 95, (3), 1227-1232.
250. de Leeuw, D. M.; Simenon, M. M. J.; Brown, A. R.; Einerhand, R. E. F., Stability of n-type doped conducting polymers and consequences for polymeric microelectronic devices. *Synthetic Metals* **1997,** 87, (1), 53-59.
251. Abdou, M. S. A.; Holdcroft, S., Mechanisms of photodegradation of poly(3-alkylthiophenes) in solution. *Macromolecules* **1993,** 26, (11), 2954-2962.
252. Sun, Y.; Lu, X.; Lin, S.; Kettle, J.; Yeates, S. G.; Song, A., Polythiophene-based field-effect transistors with enhanced air stability. *Organic Electronics* **2010,** 11, (2), 351-355.
253. Ficker, J.; Ullmann, A.; Fix, W.; Rost, H.; Clemens, W., Stability of polythiophene-based transistors and circuits. *Journal of Applied Physics* **2003,** 94, (4), 2638-2641.
254. Rost, H.; Ficker, J.; Alonso, J. S.; Leenders, L.; McCulloch, I., Air-stable all-polymer field-effect transistors with organic electrodes. *Synthetic Metals* **2004,** 145, (1), 83-85.
255. McCulloch, I.; Bailey, C.; Giles, M.; Heeney, M.; Love, I.; Shkunov, M.; Sparrowe, D.; Tierney, S., Influence of Molecular Design on the Field-Effect Transistor Characteristics of Terthiophene Polymers. *Chemistry of Materials* **2005,** 17, (6), 1381-1385.
256. Chabinyc, M. L.; Street, R. A.; Northrup, J. E., Effects of molecular oxygen and ozone on polythiophene-based thin-film transistors. *Applied Physics Letters* **2007,** 90, (12), 123508.
257. Wescott, L. D.; Mattern, D. L., Donor−σ−Acceptor Molecules Incorporating a Nonadecyl-Swallowtailed Perylenediimide Acceptor. *The Journal of Organic Chemistry* **2003,** 68, (26), 10058-10066.
258. Würthner, F.; Thalacker, C.; Diele, S.; Tschierske, C., Fluorescent J-type Aggregates and Thermotropic Columnar Mesophases of Perylene Bisimide Dyes. *Chemistry – A European Journal* **2001,** 7, (10), 2245-2253.
259. Albouy, P. A.; Vandevyver, M.; Perez, X.; Ecoffet, C.; Markovitsi, D.; Veber, M.; Jallabert, C.; Strzelecka, H., Liquid crystalline order in Langmuir-Blodgett films of a disk-shaped heteroaromatic salt as determined by x-ray diffraction. *Langmuir* **1992,** 8, (9), 2262-2268.
260. Bury, I.; Heinrich, B.; Bourgogne, C.; Mehl, G. H.; Guillon, D.; Donnio, B., Self-assembly and liquid-crystalline supramolecular organizations of semifluorinated block co-dendritic supermolecules. *New Journal of Chemistry* **2012,** 36, (2), 452-468.
261. Pisula, W.; Menon, A.; Stepputat, M.; Lieberwirth, I.; Kolb, U.; Tracz, A.; Sirringhaus, H.; Pakula, T.; Müllen, K., A Zone-Casting Technique for Device Fabrication of Field-Effect Transistors Based on Discotic Hexa-peri-hexabenzocoronene. *Advanced Materials* **2005,** 17, (6), 684-689.
262. Levell, J. W.; Ruseckas, A.; Henry, J. B.; Wang, Y.; Stretton, A. D.; Mount, A. R.; Galow, T. H.; Samuel, I. D. W., Fluorescence Enhancement by Symmetry Breaking in a Twisted Triphenylene Derivative. *The Journal of Physical Chemistry A* **2010,** 114, (51), 13291-13295.
263. Langhals, H.; Kinzel, S., Laterally Extended Naphthalene Tetracarboxylic Bisimides. *The Journal of Organic Chemistry* **2010,** 75, (22), 7781-7784.

264. Bagui, M.; Dutta, T.; Chakraborty, S.; Melinger, J. S.; Zhong, H.; Keightley, A.; Peng, Z., Synthesis and Optical Properties of Triphenylene-Based Dendritic Donor Perylene Diimide Acceptor Systems. *The Journal of Physical Chemistry A* **2011,** 115, (9), 1579-1592.
265. Markovitsi, D.; Germain, A.; Millie, P.; Lecuyer, P.; Gallos, L.; Argyrakis, P.; Bengs, H.; Ringsdorf, H., Triphenylene Columnar Liquid Crystals: Excited States and Energy Transfer. *The Journal of Physical Chemistry* **1995,** 99, (3), 1005-1017.
266. Marguet, S.; Markovitsi, D.; Millié, P.; Sigal, H.; Kumar, S., Influence of Disorder on Electronic Excited States: An Experimental and Numerical Study of Alkylthiotriphenylene Columnar Phases. *The Journal of Physical Chemistry B* **1998,** 102, (24), 4697-4710.
267. Duzhko, V.; Shi, H.; Singer, K. D.; Semyonov, A. N.; Twieg, R. J., Controlled Self-Assembly of Triphenylene-Based Molecular Nanostructures. *Langmuir* **2006,** 22, (19), 7947-7951.
268. Ford, W. E., Photochemistry of 3,4,9,10-perylenetetracarboxylic dianhydride dyes: visible absorption and fluorescence of the di(glycyl)imide derivative monomer and dimer in basic aqueous solutions. *Journal of Photochemistry* **1987,** 37, (1), 189-204.
269. Balakrishnan, K.; Datar, A.; Naddo, T.; Huang, J.; Oitker, R.; Yen, M.; Zhao, J.; Zang, L., Effect of Side-Chain Substituents on Self-Assembly of Perylene Diimide Molecules: Morphology Control. *Journal of the American Chemical Society* **2006,** 128, (22), 7390-7398.
270. Gómez, R.; Veldman, D.; Blanco, R.; Seoane, C.; Segura, J. L.; Janssen, R. A. J., Energy and Electron Transfer in a Poly(fluorene-alt-phenylene) Bearing Perylenediimides as Pendant Electron Acceptor Groups. *Macromolecules* **2007,** 40, (8), 2760-2772.
271. İçli, S.; Alp, S.; Doroshenko, A. O.; Karapire, C.; Ertan, S.; Közb, B. In *Photoınduced energy-electron transfer studıes wıth naphthalene dıımıdes ın solutıon and ın polymer fılms (XVIII IUPAC Symposium on Photochemistry)*, XVIII IUPAC Symposium on Photochemistry, 2000; 2000.
272. Barros, T. C.; Molinari, G. R.; Berci Filho, P.; Toscano, V. G.; Politi, M. J., Photophysical properties of N-alkylnaphthalimides and analogs. *Journal of Photochemistry and Photobiology A: Chemistry* **1993,** 76, (1–2), 55-60.
273. Chen, Z.; Stepanenko, V.; Dehm, V.; Prins, P.; Siebbeles, L. D. A.; Seibt, J.; Marquetand, P.; Engel, V.; Würthner, F., Photoluminescence and Conductivity of Self-Assembled π–π Stacks of Perylene Bisimide Dyes. *Chemistry – A European Journal* **2007,** 13, (2), 436-449.
274. Thelakkat, M.; Schmidt, H., Synthesis and Properties of Novel Derivatives of 1,3,5-Tris(diarylamino)benzenes for Electroluminescent Devices. *Advanced Materials* **1998,** 10, (3), 219-223.
275. Bredas, J. L.; Silbey, R.; Boudreaux, D. S.; Chance, R. R., Chain-length dependence of electronic and electrochemical properties of conjugated systems: polyacetylene, polyphenylene, polythiophene, and polypyrrole. *Journal of the American Chemical Society* **1983,** 105, (22), 6555-6559.
276. Bauer, P.; Wietasch, H.; Lindner, S. M.; Thelakkat, M., Synthesis and Characterization of Donor−Bridge−Acceptor Molecule Containing Tetraphenylbenzidine and Perylene Bisimide. *Chemistry of Materials* **2006,** 19, (1), 88-94.
277. Seguy, I.; Jolinat, P.; Destruel, P.; Farenc, J.; Mamy, R.; Bock, H.; Ip, J.; Nguyen, T. P., Red organic light emitting device made from triphenylene hexaester and perylene tetraester. *Journal of Applied Physics* **2001,** 89, (10), 5442-5448.
278. Polander, L. E.; Tiwari, S. P.; Pandey, L.; Seifried, B. M.; Zhang, Q.; Barlow, S.; Risko, C.; Brédas, J.; Kippelen, B.; Marder, S. R., Solution-Processed Molecular Bis(Naphthalene Diimide) Derivatives with High Electron Mobility. *Chemistry of Materials* **2011,** 23, (15), 3408-3410.
279. Leight, K. R.; Esarey, B. E.; Murray, A. E.; Reczek, J. J., Predictable Tuning of Absorption Properties in Modular Aromatic Donor–Acceptor Liquid Crystals. *Chemistry of Materials* **2012,**.
280. Stich, D.; Spath, F.; Kraus, H.; Sperlich, A.; Dyakonov, V.; Hertel, T., Triplet-triplet exciton dynamics in single-walled carbon nanotubes. **2014,** 8, (2), 139-144.
281. Bäuerle, P., The Synthesis of Oligothiophenes. In Wiley-VCH Verlag GmbH: 1998; pp 89-181.
282. Pardieu, E.; Saad, A.; Dallery, L.; Garnier, F.; Vedrine, C.; Hauquier, F.; Dalko, P.; Pernelle, C., Synthesis and characterization of β-substituted 3,4-ethylenedioxy terthiophene monomers for conducting polymer applications. *Synthetic Metals* **2013,** 171, (0), 23-31.
283. Farina, V.; Krishnamurthy, V.; Scott, W. J., The Stille Reaction. In John Wiley & Sons, Inc.: 2004.
284. Leszek Mazur, A. C. K. O., Charge carrier mobility study of a mesogenic thienothiophene derivative in bulk and thin films. *Organic Electronics* **2014,**, (15), 943-953.
285. Roncali, J., Molecular Engineering of the Band Gap of π-Conjugated Systems: Facing Technological Applications. *Macromolecular Rapid Communications* **2007,** 28, (17), 1761-1775.
286. Zheng, Q.; Huang, J.; Sarjeant, A.; Katz, H. E., Pyromellitic Diimides: Minimal Cores for High Mobility n-Channel Transistor Semiconductors. *Journal of the American Chemical Society* **2008,** 130, (44), 14410-14411.

287. Castiglione, A. Liquid crystalline macromolecular architectures based on regioregular poly(3-alkylthiophene) as backbone and calamitic mesogens as side-groups: towards ambipolar materials. PhD thesis, Université Pierre et Marie Curie, Paris, 2014.
288. Tanaka, T.; Matsumoto, S.; Kobayashi, T.; Satoh, M.; Aoyama, T., Highly Oriented J-Aggregates of Bisazomethine Dye on Aligned Poly(tetrafluoroethylene) Surfaces. *The Journal of Physical Chemistry C* **2011,** 115, (40), 19598-19605.
289. Kim, H. J.; Kim, J. W.; Lee, H. H.; Kim, T.; Jang, J.; Kim, J., Grazing Incidence Small-Angle X-ray Scattering Analysis of Initial Growth of Planar Organic Molecules Affected by Substrate Surface Energy. *The Journal of Physical Chemistry Letters* **2011,** 2, (14), 1710-1714.
290. Ribierre, J.; Watanabe, S.; Matsumoto, M.; Muto, T.; Nakao, A.; Aoyama, T., Reversible Conversion of the Majority Carrier Type in Solution-Processed Ambipolar Quinoidal Oligothiophene Thin Films. *Advanced Materials* **2010,** 22, (36), 4044-4048.
291. Tang, Q.; Tong, Y.; Hu, W., Organic Circuits and Organic Single-Molecule Transistors. In Wiley-VCH Verlag GmbH & Co. KGaA: 2013; pp 171-276.
292. Tahar Djebbar, I. Architectures macromoléculaires mésomorphes élaborées à partir de poly(3-alkylthiophène)s régioréguliers. PhD thesis, Université Pierre et Marie Curie, Paris, France, 2011.
293. Osaka, I.; McCullough, R. D., Advances in Molecular Design and Synthesis of Regioregular Polythiophenes. *Accounts of Chemical Research* **2008,** 41, (9), 1202-1214.
294. Holdcroft, S., Determination of molecular weights and Mark–Houwink constants for soluble electronically conducting polymers. *Journal of Polymer Science Part B: Polymer Physics* **1991,** 29, (13), 1585-1588.
295. Zhao, J.; Swinnen, A.; Van Assche, G.; Manca, J.; Vanderzande, D.; Mele, B. V., Phase Diagram of P3HT/PCBM Blends and Its Implication for the Stability of Morphology. *The Journal of Physical Chemistry B* **2009,** 113, (6), 1587-1591.
296. Ngo, T. T.; Duc Nghia Nguyen; Van Tuyen Nguyen, Glass transition of PCBM, P3HT and their blends in quenched state. *Advances in Natural Sciences: Nanoscience and Nanotechnology* **2012,**, (3), 045001.
297. Higashi, T.; Yamasaki, N.; Utsumi, H.; Yoshida, H.; Fujii, A.; Ozaki, M., Anisotropic Properties of Aligned π-Conjugated Polymer Films Fabricated by Capillary Action and Their Post-Annealing Effects. *Applied Physics Express* **2011,** 9, (4), 091602.
298. Zen, A.; Pflaum, J.; Hirschmann, S.; Zhuang, W.; Jaiser, F.; Asawapirom, U.; Rabe, J. P.; Scherf, U.; Neher, D., Effect of Molecular Weight and Annealing of Poly(3-hexylthiophene)s on the Performance of Organic Field-Effect Transistors. *Advanced Functional Materials* **2004,** 14, (8), 757-764.
299. Kline, R. J.; McGehee, M. D.; Kadnikova, E. N.; Liu, J.; Fréchet, J. M. J., Controlling the Field-Effect Mobility of Regioregular Polythiophene by Changing the Molecular Weight. *Advanced Materials* **2003,** 15, (18), 1519-1522.
300. Kim, F. S.; Guo, X.; Watson, M. D.; Jenekhe, S. A., High-mobility Ambipolar Transistors and High-gain Inverters from a Donor–Acceptor Copolymer Semiconductor. *Advanced Materials* **2010,** 22, (4), 478-482.
301. Zaumseil, J.; Friend, R. H.; Sirringhaus, H., Spatial control of the recombination zone in an ambipolar light-emitting organic transistor. *Nature Materials* **2006,** 1, (5), 69-74.
302. Kwok, H. L.; Li, W. C., Multi-layer ambipolar light-emitting organic field-effect transistors. *Applied Physics B* **2012,** 106, (2), 425-428.
303. Pan, C.; Sugiyasu, K.; Aimi, J.; Sato, A.; Takeuchi, M., Picket-Fence Polythiophene and its Diblock Copolymers that Afford Microphase Separations Comprising a Stacked and an Isolated Polythiophene Ensemble. *Angewandte Chemie International Edition* **2014,** 53, (34), 8870-8875.
304. Huettner, S.; Sommer, M.; Hodgkiss, J.; Kohn, P.; Thurn-Albrecht, T.; Friend, R. H.; Steiner, U.; Thelakkat, M., Tunable Charge Transport Using Supramolecular Self-Assembly of Nanostructured Crystalline Block Copolymers. *ACS Nano* **2011,** 5, (5), 3506-3515.
305. Miyanishi, S.; Zhang, Y.; Hashimoto, K.; Tajima, K., Controlled Synthesis of Fullerene-Attached Poly(3-alkylthiophene)-Based Copolymers for Rational Morphological Design in Polymer Photovoltaic Devices. *Macromolecules* **2012,** 45, (16), 6424-6437.